UNIVERSITY OF SÃO PAULO
ESCOLA POLITÉCNICA
PROGRAMA DE PÓS-GRADUAÇÃO EM ENGENHARIA MECÂNICA

TOMÁS GUILLERMO MORA CHANDIA

Development of a global multistage reaction mechanism for fast pyrolysis of Chlorella Vulgaris microalgae and its application in computational fluid dynamics simulations

São Paulo - SP
2018

TOMÁS GUILLERMO MORA CHANDIA

Development of a global multistage reaction mechanism for fast pyrolysis of Chlorella Vulgaris microalgae and its application in computational fluid dynamics simulations

Doctorate Thesis presented in Programa de Pós-Graduação em Engenharia Mecânica da Escola Politécnica da Universidade de São Paulo (POLI-USP) to obtain the degree of Doctor of Science.

AREA
Mechanical Engineering of Energy and Fluids

Advisor
Prof. Dr. Jurandir Itizo Yanagihara

São Paulo - SP
2018

Este exemplar foi revisado e corrigido em relação à versão original, sob responsabilidade única do autor e com a anuência de seu orientador.

São Paulo, _____ de _____ de _____

Assinatura do autor: _____

Assinatura do orientador: _____

Catalogação-na-publicação

Mora Chandia, Tomas Guillermo

Development of a global multistage reaction mechanism for fast pyrolysis of Chlorella Vulgaris microalgae and its application in computational fluid dynamics simulations / T. G. Mora Chandia -- versão corr. -- São Paulo, 2018.

294 p.

Tese (Doutorado) - Escola Politécnica da Universidade de São Paulo. Departamento de Engenharia Mecânica.

1.Pirolise 2.Biomassa 3.Simulação 4.Analise termica 5.Cinetica I.Universidade de São Paulo. Escola Politécnica. Departamento de Engenharia Mecânica II.t.

Name: Tomás Guillermo Mora Chandía

Title: Development of a global multistage reaction mechanism for fast pyrolysis of *Chlorella Vulgaris* microalgae and its application in computational fluid dynamics simulations

Doctorate Thesis presented in Programa de Pós-Graduação em Engenharia Mecânica da Escola Politécnica da Universidade de São Paulo (POLI-USP) to obtain the degree of Doctor of Science.

Approved in:

Examination committee

Prof. Dr._____

Institution: _____

Verdict: _____

Prof. Dr. _____

Institution: _____

Verdict: _____

Prof. Dr. _____

Institution: _____

Verdict: _____

Prof. Dr. _____

Institution: _____

Verdict: _____

Prof. Dr. _____

Institution: _____

Verdict: _____

Agradezco a mi madre Javiera por todo el apoyo constante que me ha dado en toda mi vida y al emprender este trabajo.

Agradezco también el apoyo y la confianza que mi mentor y amigo el Doctor Robinson Betancourt ha depositado en mí y que ha posibilitado la consecución de esta investigación doctoral.

Agradezco al Profesor Mario Inostroza Delgado, director del Departamento de Ingeniería Mecánica de La Universidad de La Frontera de Chile por su constante apoyo.

Agradecimientos especiales a la Facultad de Ingeniería y Ciencias La Universidad de La Frontera de Chile y en especial a su Decano el Doctor Rodrigo Navia Diez por su apoyo.

Especialmente agradezco al Doctor Jurandir Itizo Yanagihara por recibirme en La Escuela Politécnica de La Universidad de Sao Paulo de Brasil para realizar esta investigación doctoral y además a la Universidad de Sao Paulo a su Pueblo y Estado por permitir que extranjeros puedan beneficiarse también de la extraordinaria calidad académica y del gran prestigio internacional que representa obtener el grado de Doctor en esta institución.

Finalmente expreso mi agradecimiento al Gobierno de Chile, que a través de su programa de becas BecasChile de Conicyt, han financiado de manera exitosa esta investigación doctoral.

RESUMO

Este documento apresenta o desenvolvimento e o resultado da modelagem matemática do processo de pirólise rápida de biomassa microalgal através da construção de um mecanismo químico de reaçãocom base nos parâmetros cinéticos de Arrhenius. O interesse na biomassa de microalgas como fonte de bio-combustíveis para produtos químicos têm crescido muito recentemente,desde a última década do século XX. Embora vários artigos relacionados à decomposição térmica tenham sido identificados na literatura, apenas alguns trabalhos estão relacionados a uma espécie específica de microalga. Em particular a microalga que possui a maior quantidade de dados experimentais encontrados na literatura é a *Chlorella Vulgaris*. Portanto, esta espécie foi escolhida nesta investigação para desenvolver o mecanismo de reação.

Os modelos matemáticos da pirólise de materiais lignocelulósicos ou de madeira foram desenvolvidos no decorrer de sessenta anos. Assim, uma grande quantidade de dados experimentais das análises TG, DTG e DSC foram acumuladas. Como consequência, foram desenvolvidos sofisticados mecanismos de reação completos para pirólise. Embora o interesse no processo de pirólise de microalgas tenha crescido, apenas alguns trabalhos reportaram dados de decomposição térmica, constantes cinéticas, composição de produtos ou mecanismos de reação completos. Como consequência, não existe na literatura,até o momento,mecanimos de reaçãoacoplados a modelos do tipo CFD que simulem pirólise rápida ou devolatilização em reatores.

Neste contexto, esta pesquisa propõe o desenvolvimento de um novo mecanismo de reação global multi-etapa (*multi-stage*) para a espécie *Chlorella Vulgaris*, baseado nas análises fundamentais TG e DTG, método iso-conversional e apoiado em conceitos e princípios bem desenvolvidos para a análise térmica da biomassa lignocelulósica. Os resultados obtidos nesta investigação mostram grande concordância quando comparadoscom os dados experimentais de TG e DTG, prevendo com precisão a complexa desvolatilização em estágios da *Chlorella Vulgaris.*

Seguindo os objetivos desta investigação, o conjunto de parâmetros cinéticos químicos obtidos foi adaptado, numa segunda etapa, para ser utilizado em uma simulação numérica hidrodinâmica (CFD). O mecanismo de reação adaptado foi aplicado para simular o processo de desvolatilização em conjunto com um reator tubular fluidizado obtido da literaturaque foi usado para estudar o processo de pirólise de *Chlorella Vulgaris*.Para resolver numericamente as equações hidrodinâmicas e a taxa de reação, foi utilizado o método dos volumes finitos considerando duas fases Eulerianas e um domínio de simetria axial.Em particular, a fase sólida composta de pó de *Chlorella Vulgaris* foi considerada como uma fase granular dispersa, descrevendo sua reologia por meio da teoria cinética do fluxo granular. O programa ANSYS Fluent 19.0 foi usado para definir e construir a malha e resolver o conjunto de equações de conservação discretizadas usando um *solver* baseado em pressão. Simulações utilizando o mecanismo de reação adaptado foram realizadas considerando uma temperatura do reator de 673 K e quatro diferentes refinamentos de malha com o objetivo de determinar a convergência da solução. Os resultados da simulação mostraram que o mecanismo de reação, cineticamente, pode prever bem a conversão de biomassa em altas taxas de aquecimento. Além disso, e como era esperado, os resultados também mostraram que a conversão da biomassa depende fortemente da temperatura local, que também está diretamente relacionada à reologia da fase granular e aos processos de transporte de massa, quantidade de movimentoe energia, que têm uma papel fundamental para controlar e limitar o processo de conversão global.

Palavras chave: microalga, análise térmica, pirólise rápida, cinética química, CFD.

ABSTRACT

This document presents a research work on the mathematical modeling of the fast pyrolysis process of microalgae biomass by means of the construction of a reaction mechanism based on Arrhenius kinetic parameters. The interest in microalgae biomass as a source of bio-fuels and chemical products has grown only very recently from the last decade of the XX century. Although several papers related to the thermal decomposition of microalgae were found in the literature, only a few works are related to specific microalgae species. In particular, the microalgae species having more experimental data found in the literature was the *Chlorella Vulgaris*. Therefore, this species was chosen in this research in order to develop a reaction mechanism.

Mathematical models for pyrolysis of lignocellulosic or woody materials have been developed for almost sixty years. Therefore, a large quantity of experimental data such as from the TG, DTG, DSC thermal analysis has been accumulated. As a consequence, sophisticated and comprehensive reaction mechanisms of pyrolysis have been developed. On the other hand, although the interest in the pyrolysis process about microalgae has grown, only a few works have reported thermal decomposition data, kinetic constants, products composition or complete reaction mechanisms in order to predict the devolatilization. As a consequence, there is currently no reaction mechanism coupled to CFD-type models that simulate rapid pyrolysis or devolatilization in reactors.

In this context, this research proposes the development of a new multi-stage global reaction mechanism for the *Chlorella Vulgaris* species, based on the fundamental analysis TG and DTG and supported by well developed concepts, methodologies and principles for lignocellulosic biomass thermal analysis. The results obtained in this research have evidenced that the reaction mechanism has a very good agreement compared to experimental data of TG and DTG, accurately predicting the complex devolatilization of *Chlorella Vulgaris* in several steps. Following the objectives of this research, in a second stage, the set of chemical kinetic parameters were adapted to be used in a hydrodynamic numerical simulation (CFD).

The adapted reaction mechanism was applied to simulating the devolatilization process in conjunction with a tubular fluidized reactor obtained from the literature which was used in studying the fast pyrolysis process of the *Chlorella Vulgaris*. In order to numerically solve the hydrodynamics and the rate equations, the finite volume method was used considering two Eulerian phases and an axis-symmetric domain. In particular, the solid phase, composed by the *Chlorella Vulgaris* powder was considered as a dispersed granular phase describing its rheology by means of the kinetic theory of granular flows. ANSYS Fluent 19.0 software package was used in defining and constructing the mesh and solving the set of discretized conservation equations using a transient pressure-based solver. Simulation using the adapted reaction mechanism for a reactor temperature of 673 K was performed for four different grid refinements in order to determine the solution convergence. Simulation results showed that the reaction mechanism can predict well the kinetics of the biomass conversion at high heating rates. Furthermore, and as expected, the results also showed that the biomass conversion depends strongly on the local temperature that is related to the granular rheology and transport processes of mass, momentum, and energy that have a fundamental role to control and to limit the overall biomass conversion.

Keywords: microalgae, thermal analysis, fast pyrolysis, chemical kinetics, CFD.

FIGURES LIST

TABLES LIST

ACRONYM LIST

2D	Modeling in two dimensions
2-DAEM	Double Distributed Activation Energy Method
3D	Modeling in three dimensions
ANSYS Fluent 19.0	Computational Fluid Dynamics Software package version 19.0
BR	Biorefinery
CFB	Continuous fluidized bed reactor
CFD	Computational Fluid Dynamics
CHAR	Sold residue after pyrolysis
CV	*Chlorella Vulgaris*
DAEM	Distributed Activation Energy Method
DKP	Diketopiperazine compund
DSC	Differential Scanning Calorimetry
DTG	Differential Thermogravimetric
FB	Fluidized Bed
FTIR	Fourier Transform Infrared
FWO	Ozawa, Flynn and Wall method
HHV	High Heating Value
KAS	Kissinger-Akahira-Sunose method
KTGF	Kinetic Theory of Granular Flows
NG	*Nannochloropsis Gaditana*
GC	Gas Chromatography
IKR	Isokinetic relationship
GCI	Grid Convergence Index
GRR	Grid Refinement Ratio
LVG	Levoglucosan compound
MF	Model Free method
MS	Mass Spectrometry
SC	*Scenedesmus Almeriensis*
TAR	Bio-oil produced during pyrolysis
TG	Thermogravimetric
UDF	User Defined Function

SYMBOLS LIST

A_i	Pre-exponential factor of Arrhenius equation for component i
$A^{\alpha\beta}$	Interface surface metric tensor
A_P	Coefficient of discretized field equation
$\hat{A}_i$	Cell area
$\bar{\bar{A}}_i$	Interfacial area concentration
B	Total instantaneous balance over all phases and interfaces.
B_s	Instantaneous balance of a field variable over the interface
B_V	Instantaneous balance of field variable over a phase
C_D	Drag coefficient
c_i	Mass fraction coefficient of rate of reaction for component i
$\hat{c}$	Random velocity of particles
$\bar{c}$	Stoichiometric coefficient of char in devolatilization reaction
c_p	Specific heat
$D_{k,i}$	Diffusion coefficient of species i in phase k
$D^*_{i,k}$	Total diffusion coefficient of species i in phase k
d_i	Particle diameter of solid phase i
E_i	Activation energy of Arrhenius equation for component i
e	Particle-particle restitution coefficient
$\hat{e}_k$	Internal energy
e_{ss}	Particle-particle restitution coefficient
e_a^{21}	Relative normalized error between two numerical solutions
F_k	Field variable volumetric basis of phase k
$\bar{F}$	Averaged Field variable in volumetric basis
$\bar{F}^w$	Averaged Field variable volumetric basis as a function of weighting factor w
$\bar{\bar{F}}_k$	Averaged effective Field volumetric basis variable for phase k
$f_{GAS-100kg}$	Mass conversion factor from arbitrary mass of biomass to 100 kg
$\vec{F}_q$	External body forces
$\vec{F}_{lift,q}$	Lift force
$\vec{F}_{wl,q}$	Wall lubrication force
$\vec{F}_{vm,q}$	Virtual mass force
$\vec{F}_{td,q}$	Turbulent dispersion force

$f(\alpha)$	Differential form of reaction model
f_i	Frequency distribution of activation energy of component i
$\hat{f}_s$	Drag function
$f_{h=0}$	Asymptotic solution
$\hat{f}_i$	Numerical solution of a field variable i
G	Solid stress modulus
$\vec{g}$	Acceleration of gravity or generalized body force
$g(\alpha)$	Integral form reaction model
g_{ln}	Space metric tensor
g_0	Radial distribution
$\hat{g}_k$	General body force
$\bar{g}_i$	Stoichiometric coefficient of gaseous species in devolatilization reaction
H_R°	Heat of reaction
$\bar{h}_{f,i}^\circ$	Specific standard molar enthalpy of formation
h_q	Specific enthalpy
$\hat{h}_{pq}$	Convection heat transfer coefficient
h	Effective grid length
$\bar{h}$	Grid length criteria
I	Unitary tensor
$\bar{\bar{J}}_k$	Effective averaged diffusion flux of phase k
J^D	Mixture diffusion Flux
J_k^T	Diffusion turbulent flux of phase k
J^T	Mixture turbulent diffusion flux
J_α^l	Surface flux expressed in interface space coordinates
j_i^q	Diffusion coefficient for the species i in phase q
j_k	Volumetric flux of phase k
k'	Fluctuating granular energy conduction coefficient
K_{ls}, K_{gs}	Momentum exchange coefficient between phases l to s or g to s
k_i	Kinetic constant of component i
$\hat{k}_q$	Thermal conduction coefficient
M_k	State density functions
M	Molar mass
$M_{graphite}$	Molar mass of graphite specie

$M_{GAS,i}$	Molar mass of specie i in eq.(219)
$Moisture$	Mass fraction of moisture in biomass in wet basis
$\dot{m}$	Mass rate in volumetric basis
m_{GAS_i}	Mass of specie i in eq.(219)
$m_{GAS_i-100kg}$	Amount of mass of gas I considering 100 kg of mixture
Nu_p	Nusselt number of phase p
n	Order of reaction model
n_k	Unitary vector of surface of phase k
P	Pressure
P^*	Current pressure (for numerical calculation with SIMPLE algorithm)
P'	Pressure correction (for numerical calculation with SIMPLE algorithm)
$\bar{P}_k$	Averaged pressure of phase k
P_s	Solid pressure
Pr	Prandlt number
$p(x)$	Approximation of temperature integral function
$\hat{p}$	Effective rate of convergence
$\hat{Q}_{pq}$	Heat exchange between phase *p* and *q*.
Q_{vb}	Volumetric heat of reaction
q'	Fluctuating granular energy flux
$\vec{q}_q$	Heat flux
q_k	Conductive heat flux phase k
q_k^T	Turbulent convection and turbulent mechanical work
R	Universal gas constant J/mol/K
$\dot{R}$	Rate of reaction volumetric basis
R^2	Statistical coefficient of determination
R_{pq}, R_{gs}	Interaction forces between phase p and q; g and s respectively
Re	Reynolds number
r_{21}	Grid refinement ratio between grid 1 and 2
$S_k^{\psi,I}$	Interfacial source term for phase k
$S_m^{\psi,I}$	Interfacial source term for mixture
S^{ϕ}	Source term of generic field variable ϕ
$\dot{S}$	Net rate of intra-phase production of specie i
SS_{resid}	Sum of squares

S^2	Statistical variance
s	Sign parameter of effective rate of convergence in equation 275
Δs	Distance between particles
T	Temperature in Celsius or Kelvin
ΔT	Large scale time interval
Δt	Time interval
t_α^n	Hybrid tensor of interface
U	Independent variable value for fitting procedure
V	Volumen
$\hat{V}$	Cell volume
V_i^*	Initial Volume fraction of component i
V_i	Instantaneous Volume fraction of component i
$\boldsymbol{V_{km}}$	Mass diffusion velocity
$\boldsymbol{V_{kj}}$	Drift velocity
$\boldsymbol{v_m}$	Mixture center of mass velocity
$\boldsymbol{v_r}$	Relative velocity
v_{ni}	Normal velocity of surface of phase k
v_i	Velocity of phase i
w_i	Mass concentration of component i
X_i	Volume fraction of phase i
x	Argument of exponential function in Arrhenius rate equation
x_0	Arbitrary point in space
Δx	Finite spatial length
Y_i	Mass fraction of component i
Z	Dependent variable to be fitted in fitting procedure

GREEK LETTERS LIST

$(\ \ )_\beta$	Surface covariant derivative
α	Extent of reaction
β	Heating rate
γ	Collisional energy dissipation of granular phase
γ_v	Volume available for the total flow
Γ^ψ	General diffusion coefficient of generic field variable ψ
δ	Interface thickness
δt_1	Finite time interval
ε_i	Volume fraction of phase i
$\hat{\varepsilon}_{21}$	Difference of numerical results for field variables
ϵ	Characteristic time interval of interface related with it thickness
$\hat{\theta}$	Relaxation factor
Θ	Granular temperature
κ_s	Diffusion coefficient
λ_s	Bulk viscosity
μ_i	Dynamic viscosity of gas phase i
ρ	Instantaneous density
$\bar{\rho}$	Averaged phase density
$\bar{\bar{\rho}}_k$	Effective averaged density of phase k
$\rho_k^{'}$	Fluctuation density component
ρ_m	Mixture density
$\sigma_{E01}, \sigma_{E02}$	Standard deviation of frequency distribution of activation energy of component i
τ_k	Stress tensor of phase k
$\bar{\tau}_k$	Averaged stress tensor of phase k
$\bar{\tau}_k^T$	Averaged turbulent stress tensor of phase k
φ_{gs}	Energy exchange term between phases
Φ_{ext21}	Asymptotic solution obtained from Richardson extrapolation
χ^2	Sum of square
ψ	Generic field variable in mass basis
$\hat{\psi}_k$	Averaged Generic field variable in mass basis

$\bar{\omega}_k$	Weight factor for phase k
Ω_i	Conversion factor for gas phase distribution in reaction equation
ψ_m	Instantaneous generic field variable in mass basis

INDEX

1. INTRODUCTION

In the way of the so called "green energy", thermal and biological conversions of biomass are two alternatives used to transform this sustainable energy source into suitable fuels and chemical substances. However and unfortunately, the economic factor is a fundamental criterion about the feasibility of new potential source as non-conventional source of energy. Of course for developed countries higher costs in energy can be handled and green taxes can be applied too, however for non-developed countries higher costs in energy can mean a slowdown in growth. Direct production cost comparison between the reference fossil fuel and biofuel energy can be made in where the costs of biomass conversion to bio-fuel is similar or superior to petroleum fuel. Seth (2011) calculates that the production cost per liter of biodiesel from canola is between 0.94 and 1.13 USD$/l with a vegetable oil cost between 0.64 and 0.83 USD$/l, respectively. On the other hand, the cost to produce biodiesel from soy oil is between 0.40 to 0.60 USD$/l, with a vegetable oil cost between 0.14 and 0.33 USD$/l, respectively. It should be noted that these costs are only production costs, neither taxes nor transport costs or profit margins are included. The former and latter biofuels can be compared with the cost of one gallon of ultra low sulfur diesel in USA of 1.07 USD$/l (Source http://www.eia.gov), so the final costs can be similar.

Opdal and Skreiberg (2006) summarizes information and comments that the cost of producing synthetic diesel from forest biomass using the Fischer Tropsch process, is 0.96 USD$/l (according to 2012 exchange information Norwegian coin/U.S. dollar), compared with production cost of conventional diesel of 0.52 USD$/l (data compiled by Opdal and Skreiberg (2006)). In this case the conversion process to transform forest biomass into liquid fuels is not favorable.

Two observations can be mention here. First, the direct cost differences are not as high; however, soy biodiesel is a first generation bio-fuel and therefore has the drawback that it competes for lands dedicated for food production. This issue is critical and limits the countries in where the industry can be developed. Secondly, the economic assessment does not include the additional costs involved. For example, if the hypothesis of that the human being produced CO_2 is the cause of the global

warming and the subsequent environmental disasters produced by, the associated costs of fossil fuel production can be incalculable.

As mentioned before, the problem of energy obtained from biomass is that in several cases it competes for land surface required to produce food. That is the reason that motivates the research about new sources and technologies in order to produce fuels of second and third generation, being the second, those that come from waste biomasses, and third generation, those that are grown in areas not suitable for crops or not destined for food (AHMAD et al., 2011) such as microalgae.

This doctoral thesis has been proposed to complement the research relative to the processing of microalgae biomass at an industrial scale in order to obtain useful chemical products and fuels. The Desert Bioenergy Consortium, a technological company, was created in Chile in 2010 with the objective to research and develop processes based on this sustainable resource producing food for humans and animals, chemical substances, and fuels like biodiesel and biogas. The beginning of this entrepreneurship was decided due to the fact that Chile has a vast desert, with more than 105.000 km^2, and with a generous solar radiation throughout the year, that is, a suitable condition for microalgae culture.

Additional specific reasons that motivate this doctoral research proposition are:

The potential attributed to microalgae production is enormous. Chile has a vast ground extension that is not utilized, and cannot be utilized, for alimentary culture and with an intense solar radiation all year around. The latter is the key factor, as stated by several authors, owing to the fact that there are several drawbacks related to the sustainability of bio-fuels obtained from raw material cultivated on agricultural lands useful for crops for humans and animals.

Microalgae biomass is a source of potential fuels, food and highly value-added substances for the chemical industry (DEMIRBAS, 2010).

Since research for production of bio-fuels derived from microalgae has been recently considered once again, twenty years worldwide, and six in Chile, the amount of raw

material available to perform experiments and research is limited. Consequently, research with the current support of a mathematical model is very important to optimize time, and resources.

Processes to obtain biogas through anaerobic digestion and biodiesel by transesterification of microalgae have been studied quite enough. However, on the other hand, there is not much work and data related to fast pyrolysis of microalgae (SHUPING et al., 2010), with the exception of some work at laboratory scale. Therefore, there is an open field for research.

In addition to the reasons described above, there are more general motivations to carry out this research regarding the energy situation in the world and its direct relationship with the environment and our lives.

The latter is the main reason that motivates the DB consortium and this thesis, the use of micro algal biomass as a feedstock for third generation bio-fuels, which in the case of Chile, can be produced in the desert, without freshwater, and in where, virtually no food can be exploited efficiently.

1.1. RESEARCH PROBLEM DEFINITION

This doctoral research belongs to a more general project called the Desert Bioenergy Consortium DB, mentioned before. One of the main objectives proposed by the DB consortium is the development of the Biorefinery concept (BR), using the microalgae species such as *Nannochloropsis gaditana*, *Botryococcus braunii* and *Chlorella Vulgaris* or any other suitable and useful species as the raw material. The BR productive scheme must be defined in order to support the economic activity around the microalgae production and processing. Currently, the extraction of proteins and lipids; and bio-digestion to produce bio-methane has been researched. However, the DB consortium, in 2013 proposed the addition of the fast pyrolysis process, in order to improve the valorization of the microalgae biomass. This additional process can increase the pool of chemical substances, including bio-fuels; to be synthesized in the BR. Figure 1 shows an approximated BR production scheme including the fast pyrolysis process and the potential outputs.

Figure 1 – Process scheme of Biorefinery.

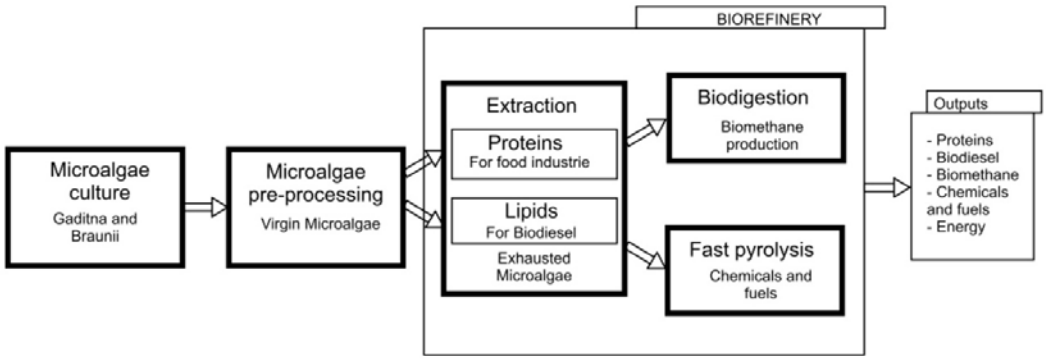

As can be observed, the pre-processed microalgae material (almost dry) produced in the crop plant is transported to the BR for further processing. It is worth noticing that this raw material can have different amounts of components that depend on growth conditions, therefore a variable in the BR scheme. The first stage is the extraction of proteins followed by the extraction of lipids to produce raw material for food industry and biodiesel respectively. The second stage can be a parallel step. The extraction process produces the exhausted microalgae, being that the composition of this material differs from the virgin biomass. The relative amounts of microalgae components i.e. carbohydrates, lipids, proteins; and probably other new substances (due to the extraction process), depend on the type of extraction and its intensity. Therefore, the composition of exhausted microalgae depends on the upstream parameters. A fraction of the exhausted microalgae is conveyed to the bio-digestion, and the remaining to the fast pyrolysis process, therefore, the mass fraction is an additional variable in the BR scheme, and it must be determined in order to optimize the whole process.

As a consequence of aforementioned, the range of the operation parameters for the BR is wide, and the determination of a set of suitable parameters implies solving an optimization problem. A criterion is required to determine a set of constraints in order to determine the operating parameters for all sub-processes. Therefore, the DB consortium needs a tool that allows systematic evaluation of all sub-processes.

This optimization problem can be addressed in three different ways: empirically, theoretically, or by a combination of both. How the other processes (lipid and protein extraction and transesterification and anaerobic digestion) will be assessed is out of

the scope for this doctoral research, and it is assumed here, and it is probable, that this information already exists. However, in the case of fast pyrolysis of microalgae, the situation is different.

Research about fast pyrolysis of microalgae, has not been performed in detail or fully implemented yet, neither by DB consortium nor by other research or industrial groups. The scientific interest about this process, with this raw material, is recent, and there is not much information available. Therefore, a reasonable way to obtain a tool, at least at an engineering level, in order to assess the fast pyrolysis process, taking advantages of the current computational power is by means of a mathematical modeling.

As a consequence of the aforementioned, the focus of this doctoral research is only on fast pyrolysis process, although it must be taken into account that the results must be integrated as a sub-process in the BR scheme. The research scope is delimited as shown in Figure 2. There are two input parameters: i) composition of exhausted biomass; and ii) mass flow rate. These parameters, as aforementioned can vary, and the integrated tool must handle this variation. On the other hand, the outputs, circle in Figure 2, are a set of undermined variables. This set of variables is composed by potential chemicals and fuels that belong to the liquid phase of the pyrolysis products. Furthermore, the composition and relative amount of substances depends on: i) microalgae species, ii) intensity of extraction process (relative fraction of components) iii) input parameters (mass rate, temperature, moisture content among others); ii) the reactor type, and iii) the process conditions.

Once the scope of this investigation has been defined, a more detailed overview about this simulation tool must be developed. The mathematical model must correlate the inputs with the outputs, i.e. virgin or exhausted (extracted biomass) raw material with the liquid fraction, and also, in order to integrate the sub-process in the BR, the net energy consumed or released must be determined. The level of detail of the model is determined by the following factors: *i)* detail in the prediction of char and gas, *ii)* availability of theories or methodologies involved in the description; and *iii)* availability of experimental data

Figure 2 – Research scope of the doctoral research.

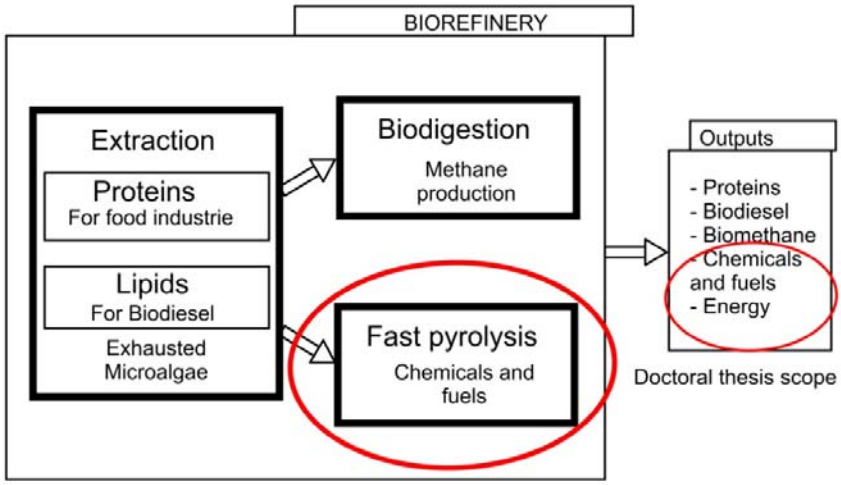

.

In order to define the main objective of this research, a mathematical model of the fast pyrolysis or more specifically a model of devolatilization, in conjunction with a simulation using CFD (Computational Fluid Dynamics) is proposed. For clarity sake, the whole task is sub-divided in a work diagram, shown in Figure 3.

Figure 3 – Stages of mathematical modeling for pyrolysis of microalgae biomass.

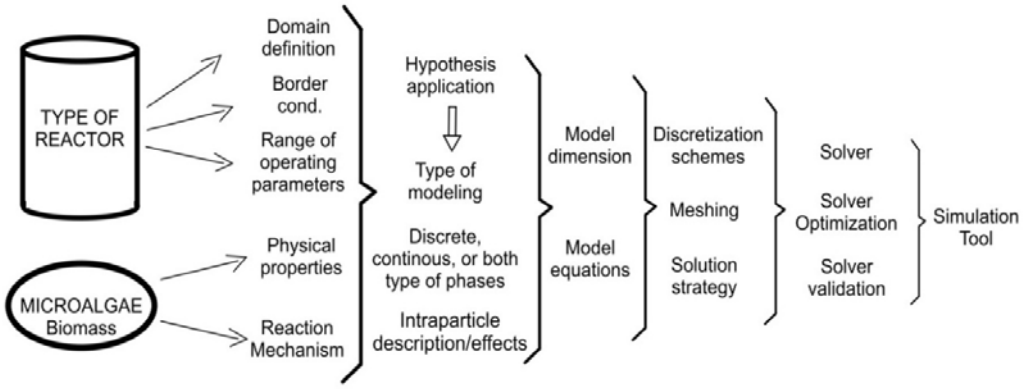

The first level (on the left) defines two groups, one group related with the reactor type, and the second related with the biomass. There are four types of reactors commonly used for fast pyrolysis of lignocelluloses biomass: *i)* fluidized bed reactor, that operates with a solid or gaseous energy carrier, *ii)* the ablatives; cone type; and *iii)* vacuum reactors (BASU, 2010). These four types of reactors operate, essentially, different. Therefore, from the modeling and CFD point of view, the domain and the boundary conditions will be, a priori, different. However, the type of reactor to be

described mathematically is constrained to those in which the experimental data are available.

On the other hand, the second group is composed of the physical properties and the reaction mechanism related to the chemical dynamics of thermal decomposition. The development of the reaction mechanism is a challenging task in this research owing to the fact that there are no comprehensive mechanisms for pyrolysis of microalgae that have been reported in literature. So far, there is only partial information about the thermal decomposition of microalgae, being this information related with the weight loss rate, with the products identification and only three reports about partial reaction mechanisms based on thermal analysis and one semi-theoretical work consisted in detailed but limited study about the chemistry of devolatilization. As will be seen in the literature review, the amount of information needed to construct a detailed reaction mechanism can be large and needs efforts of the scientific community. The information about thermal decomposition about microalgae biomass is scarce and scattered too, in other words, there are several experiments the microalgae group, nonetheless, for different microalgae species, with different composition, and there is not enough data in detail, so far, about one species in particular. This is a challenge considering that for lignocellulosic biomass there is a vast amount of research, experience and data available, and even so, there are only a few suitable reaction mechanisms for reactor calculations, and in general, with debatable wide applicability. The reason is that the thermal decomposition of composite materials (woody, polymers or microalgae biomasses) is not completely known or is very complex to describe (DI BLASI, 2008), (MOLDOVEANU, 1998). Microalgae is also a complex material, and as the lignocelluloses biomass, it is composed by organic or biologic co-polymers i.e. carbohydrates, lipids and proteins, that can have different sub-components. For example, the protein co-polymer can be formed by different sequences of one or several of the 20 different essential amino acids known (MOLDOVEANU, 1998).

Considering the aforementioned, the development of a comprehensive reaction mechanism for microalgae, with suitable detail for research, will take time. However, a reaction mechanism for engineering purposes is a reasonable objective for this doctoral research. Taking as reference the research done about the pyrolysis of

lignocellulosic biomass, the elements needed to obtain a reaction mechanism are: TG analyzers, substance detectors MS, GC or FTIR; a suitable number of experiments; availability of raw material; and knowledge about their composition. This doctoral research does not have full access to equipment and the availability of raw material is restricted to very few grams in the case of *N. Gaditana* and *B. Braunii*, however not for *Chlorella Vulgaris* that is commercially available. Therefore, in order to develop a reaction mechanism for microalgae biomass a good candidate is the *Chlorella Vulgaris*.

The BR objectives and the availability of the elements of research suggest the following points: *i)* the BR concept and the need of a tool to assess the pyrolysis of microalgae biomass at an engineering level; *ii)* there is no comprehensive reactions mechanism for pyrolysis of microalgae reported in literature, and *iii)* although only a few, data about microalgae thermal decomposition are available in form of: TG, mass loss and mass loss rate and analysis of pyrolytic substances for various microalgae species. Considering these four points this doctoral research proposes the development of a global reaction mechanism (kinetic model), *Chlorella Vulgaris*, in order to take advantage of the information published by different research groups, and then couple this kinetic model to a mathematical description of a reactor and simulate both models using CFD.

As aforementioned, the microalgae species that has been chosen to develop the kinetic model is the *Chlorella Vulgaris*. More information about these species is described later in this document. The reason to choose these species owes to the fact that there are good numbers of papers presenting experimental results about its thermal decomposition. Other species such as *B. Braunii* has also a generous number of papers published; however, related to pyrolysis, this number is less than for *Chlorella Vulgaris*. It is worth noticing that not only TG and DTG are available for chlorella, but there is also available experimental data about final yields of pyrolysis products and specific thermal analysis for two of its components.

1.2. OBJETCTIVES

The main and specific objectives are presented in the next two subsections.

1.2.1. MAIN OBJECTIVE

Develop a global multi-stage reaction mechanism for fast pyrolysis of *Chlorella Vulgaris* microalgae applicable in simulations using computational fluid dynamics.

1.2.2. SPECIFIC OBJECTIVES

1. Development of the global multi-stage reaction mechanism

- Perform a set of thermal analysis, TG, for *Chlorella Vulgaris* microalgae.
- Determine a set of kinetic parameters for the devolatilization process based on thermal analysis, TG and calculated DTG for *Chlorella Vulgaris*.
- Determine experimentally the relative amount of carbohydrates, proteins and lipids of *Chlorella Vulgaris* in order to associate it with the DTG data.
- Validate the global multistage reaction mechanism against the experimental data.

2. Laboratory-scale Reactor simulations

- Adapt and apply the global multi-stage reaction mechanism for pyrolysis of *Chlorella Vulgaris* in a CFD simulation using ANSYS Fluent 19.0.
- Chose a representative gas distribution for *Chlorella Vulgaris* volatiles from the literature in order to construct a reaction equation for CFD simulations.
- Perform a grid convergence study in order to evaluate the accuracy of the solution.
- Determine the biomass conversion index and made a comparison with the literature values.

- Develop a global multi-stage reaction mechanism for fast pyrolysis of *Chlorella Vulgaris* microalgae applicable in simulations using computational fluid dynamics.

2. GENERAL ASPECTS AND BIBLIOGRAPHY REVIEW OF THERMAL DECOMPOSITION OF LIGNOCELLULOSIC AND MICROALGAE BIOMASSES

The present section is divided in seven parts. Section 2.1 contains the basic definitions about the pyrolysis and fast pyrolysis processes. The methodology of this work takes as a guideline the development of reaction mechanisms and models of pyrolysis for lignocellulosic biomass and cellulose. Therefore in section 2.2 are presented works related only with the thermal analysis in which the objective is to develop a kinetic model in order to describe a reactor behavior for lignocellulosic biomass.

The third part, section 2.3, will present the current reported works related to kinetic and thermal analysis for pyrolysis of *Chlorella Vulgaris* using the techniques TG (thermogravimetric analysis), DTG (differential thermogravimetry), DSC (differential scanning calorimetry), and detection techniques by FTIR, GC and MS. Section 2.4 presents the current research reported in the literature about advances in the fast pyrolysis of *Chlorella Vulgaris* microalgae in laboratory-scale reactor. Later, more details are presented in section 2.5 about the types of reaction mechanisms for lignocellulosic biomass and it applicability on reactor modeling using CFD. Finally, section 2.6 presents briefly reported works showing the application of CFD to modeling of FB and CFB reactors for one a two dimension considering cold flow and reactive flows for fast pyrolysis.

2.1. BASIC DEFINITIONS OF MICROALAGAE AND FAST PYROLISIS PROCESS

Following paragraphs define the main factors affecting the conversion process in pyrolysis and in fast pyrolysis, in general, and basic definitions about the microalgae biomass.

2.1.1. PYROLYSIS

Pyrolysis process is one of various processes which belong to a more general group called thermal conversion processes, which also include combustion, iron ore reduction, gasification and fine ore sintering among others (WURZENBERGER, 2001). If raw material is biomass, it is possible to define the term biomass thermal

conversion or decomposition and then biomass pyrolysis. Di Blasi (2008) defines pyrolysis as a possible thermochemical route for thermally decomposing a material in absence of oxidizing agents to produce many different products. Other authors like Diebold (1997), Basu (2010) and Bridgwater and Boocock (1997) define pyrolysis in a similar manner.

Basu (2010) and Bridgwater and Boocock (1997) classify pyrolysis as slow and fast depending on the heating rate. Pyrolysis process often takes place from 300°C up to 650 °C. Alternatively, Moldoveanu (1998) defines temperature for fast pyrolysis above250°C up to 800°C. Factors like heating rates, particle size, type of biomass, reactor temperature and residence time affect directly the char, liquids and gas yields (BASU, 2010).

The main objective of DB Consortium is to implement the Biorefinery concept based on microalgae as raw material. Four processes are researched in this way, protein and lipids extraction for food and fuel respectively; biogas production through anaerobic digestion for bio-methane, and recently fast pyrolysis. While protein extraction and biogas production has good perspectives, lipids extraction to produce biodiesel by transesterification has not demonstrated good results. Therefore, in order to obtain better results in the BR framework, fast pyrolysis has a good perspective, considering the latest results (MUÑOZ et al., 2015).

2.1.2. FAST PYROLYSIS

The purpose and the definition of fast pyrolysis, given by Diebold (Diebold, 1997), is thermal conversion of biomass to produce mainly condensable organic vapors and minimizing the char and gas. As stated by Basu (2010) the primary goal of fast pyrolysis is to maximize the production of liquids. The heating rate is more severe than that of slow pyrolysis, reaching 10.000°C/s. Due to the high heating rates, biomass is inside the reactor less time than compared with slow pyrolysis. For lignocellulosic the typical process maximum temperature is 500°C, very high heating rate, short residence times, i.e. below 1 second, reaching a yield of up to 85% of liquids.

2.1.3. PARTICLE SIZE

Since thermal conductivity of lignocellulosic biomass is very low, and due to the fact that fast pyrolysis needs very high heating rates, the size of the particle must be reduced and has to be very small (BRIDGWATER; BOOCOCK, 1997). Particle sizes also influence intraparticle gas flow resistance. For example, in cellulose pyrolysis levoglucosan (LVG) is decomposed exothermally producing char before vaporize (ARSENEAU, 1971), that is, if there is a resistance to flow outward, the liquids precursor (LVG) decreases and then the char increases.

2.1.4. PYROLYSIS TEMPERATURE

Temperature of pyrolysis is defined as the maximum temperature that can be reached by a biomass particle. For fast pyrolysis temperatures between 425 to 600°C increase the liquid yields for lignocellulosic biomass (BASU, 2010). More specifically, Bridgwater and Boocock (1997) states that to maximize liquids the temperature process inside a reactor must be around 500°C (with high heating rates and very short residence times) for lignocellulosic biomass.

2.1.5. HEATING RATE

High heating rate must be reached for fast pyrolysis. Relatively high heating can reach from 455 K/s (DI BLASI, 2002). Debdoubi and Colacio (2005) experimented with heating rate from 400 to 500 °C/min, and observed an increase in the liquid yield using Esparto, up to 68.5%. For large particle size, over 2 mm, char removal is needed to maximize the heat transfer (BRIDGWATER; BOOCOCK, 1997), due to the low thermal conductive of char (0.27 kW/m-K, (XIONG et al., 2014)).

2.1.6. RESIDENCE TIME

Residence time is a critical factor in maximizing liquids. Bridgwater (1997) states that in order to freeze secondary reactions i.e. cracking of volatiles in presence of char, the residence time must be below 1 s, being typically a range between 100 to 300 micro seconds. However, the same author (BRIDGWATER; BOOCOCK, 1997) comments that for fuel applications the residence time can reach around 6 s.

2.1.7. MICROALGAE BIOMASS

Demirbas (2010) defines algae as a photosynthetic organism growing in aquatic environments that need to grow sunlight, carbon dioxide and nutrients from the water. There are two types of algae biomass, macroalgae and microalgae.

Microalgae biomass can live and grow in a number of environments. Ahmad et al. (2011) resumes from other authors that microalgae can grow in places that are unsuitable for others crops, like brackish, salt water or even in non-arable lands, while Costa (2011) reports that microalgae can be grown on land unsuitable for agriculture and farming activities.

Microalgae have a good potential for energy, alimentary and can be a source of high valued chemicals, due to the fact that its substances can convert into energy. The conversion of microalgae biomass may be performed through several processes. The Desert Bioenergy Consortium is mainly developing processes to produce biogas by anaerobic digestion and biodiesel by transesterification. However, the production of energy from fast pyrolysis process has been proposed.

2.2. BIBLIOGRAPHIC REVIEW OF PYROLYSIS AND THERMAL ANALYSIS FOR LIGNOCELLULOSIC BIOMASS AND CELLULOSE

Since the thermal decomposition of materials such as lignocellulosic biomass is very complex (DI BLASI, 2008), researchers have developed a methodology to obtain the named lumped kinetics parameters, necessary to construct a mechanism, and based mainly on experimental data obtained from thermal analysis i.e. TG and DTG analysis. Thermal analysis can be made with different devices i.e. tubular furnaces, entrained and fluidized bed reactors, screen heaters and drop tubes (DI BLASI, 2008), however, the most used is TG apparatus. TG and DTG analysis consists mainly in carrying out a continuous measurement of the weight of a material sample during the thermal decomposition process until no gases are released. In order to avoid additional chemical reactions an inert or low reactivity gas (frequently molecular nitrogen) is used to sweep out rapidly the pyrolysis gases.

Lignocellulosic and woody materials are complex substances, composed of cellulose, hemicellulose, lignin, extractives and ashes (DI BLASI, 2008). The TG analysis of this type of material reveals the complexity of the reaction mechanism, showing more than one zone. A zone is a part of the weight loss curve in which there is an increase of the volatile mass rate, thus indicating that one or more components have started to decompose. For low heating rates lignocellulosic biomass shows more than one zone. This zone corresponds to cellulose, hemicellulose and lignin decomposition. Hemicellulose starts to decompose almost at lower temperature. Lignin-cellulose start to decompose at higher temperatures and in a narrow range, while the range of thermal decomposition of pure lignin is extended to higher temperatures.

Caballero et al. (1997) performed a study in order to determine a reaction mechanism and kinetic parameters for *almond shells* and *olives stones*. The author conducted a TG and DTG analysis to determine the kinetic parameters, with heating rates of 2, 10 and 25 K/min, low pressure and with sample weight of 3-4 mg. Two kinetic models were applied, one with two parallel reactions and the other with three parallel reactions. However, a model consisting of three parallel and independent reactions, showed the best results. The model could fit the experimental results due to the characteristics of the process. Figure 4 shows the TG and DT curves for *almond shells* obtained by the author.

In the TG analysis it is possible to see two little shoulders on the weight loss curve. On the other hand, the DTG curve shows the same effect but in enhanced form. Two reaction zones can be seen in the DTG curve indicating, at least, that two reactions are present in the process. Caballero et al. (1997) explained that the two peaks in the DTG curve correspond to the simultaneous decomposition of cellulose and lignin and hemicellulose and lignin. Therefore, the author suggested that a mechanism for these two pseudo components could be applied. However, based on observation of other authors, that state that lignin decomposes before hemicellulose, and the fact that there is a competition between the char and tar products, a three model mechanism was applied with better results, and as can be seen in Figure 5, the latter model fitted better both materials and for all heating rates.

Figure 4 – TG (a) and DTG (b) analysis and model predictions for almond shells (Model: continuous line, experimental data: points).

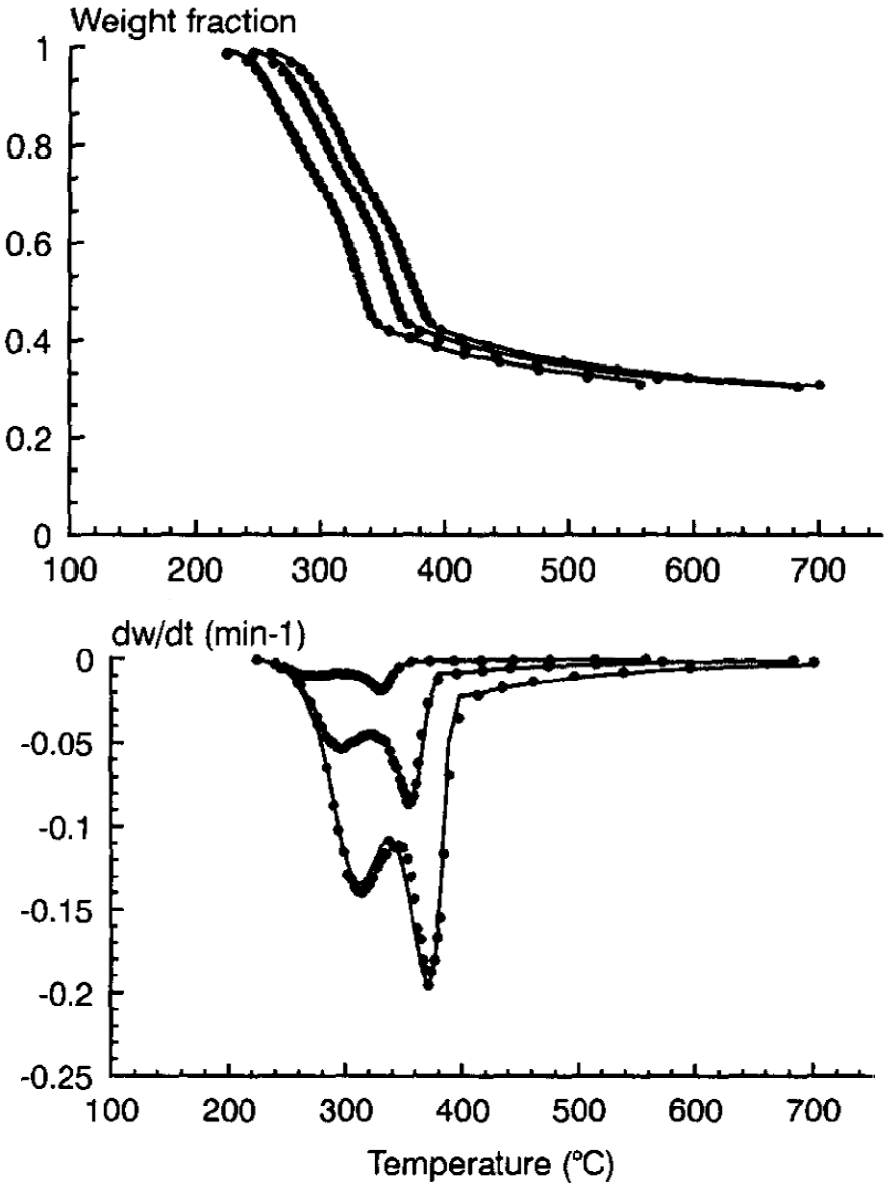

Source: Caballero et al. (1997).

As stated by Di Blasi (2008), the weight loss curve is not a simple summation of single components. As described in the latter reference the two peaks observed in DTG chart is caused by a contribution of all components in raw material. Authors Di Blasi (2008) and Manya; Velo and Puigjaner (2003) define the pseudo-components with the same name of the components: cellulose, hemicellulose, and lignin, and stated that a reaction mechanism can be constructed by means a linear contribution of these pseudo-components instead of components.

Figure 5 – TG (a) and DTG (b) analysis and model predictions for olive stones (Model: continuous line, experimental data: points).

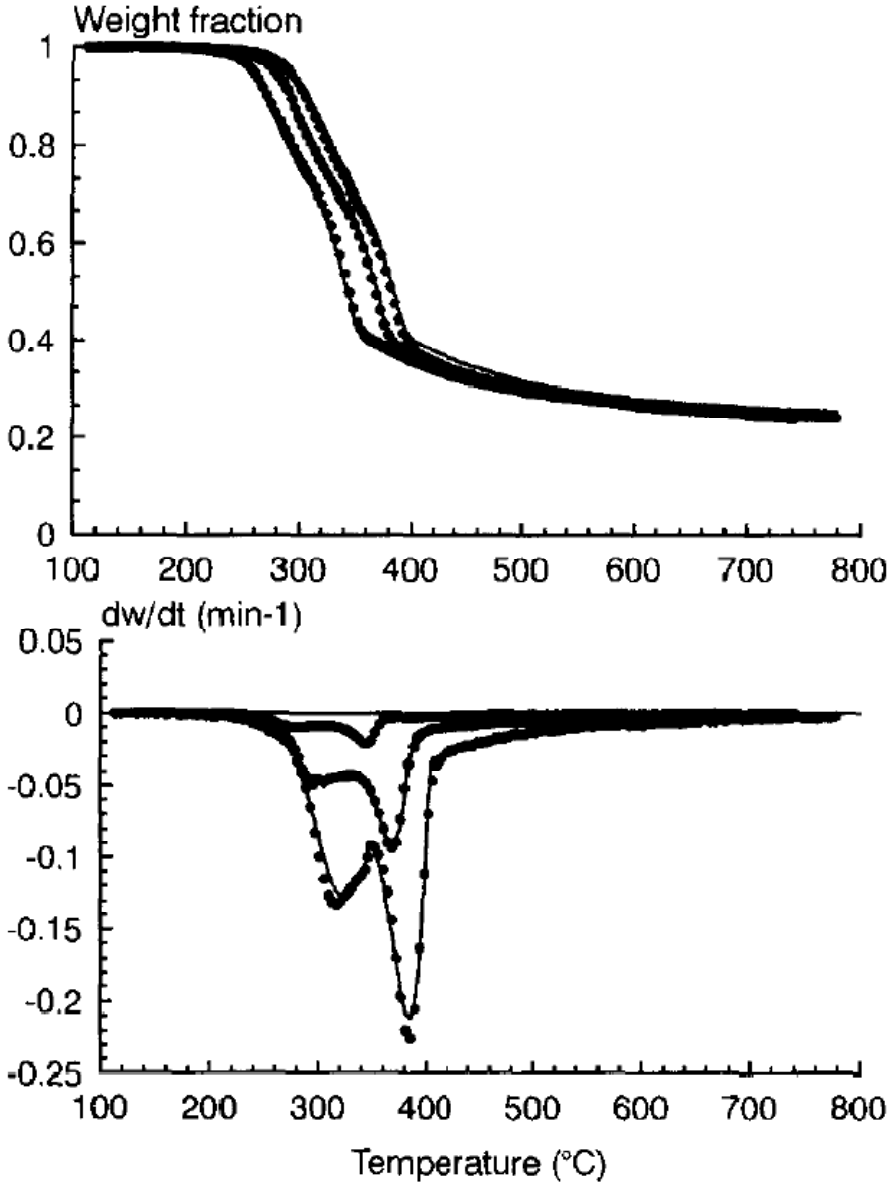

Source: Caballero et al. (1997).

Manya; Velo and Puigjaner (2003) performed a study to obtain a reaction mechanism for pyrolysis of virgin and treated *Sugar Cane Bagasse* and waste wood samples using TG and DTG analysis. The experimental conditions were: heating rates of 2, 10 and 20 K/min; maximum temperature of 900 °C; sample weight of 10 mg; and using nitrogen to sweep the volatiles. Figure 6 shows the TG and DTG charts for each sample. Two peaks in the DTG chart can be observed in Figure 6. As mentioned by Manya; Velo and Puigjaner (2003) these peaks correspond to: the lignin decomposition over a wide range of temperature; the decomposition of

hemicellulose-lignin pseudo-component manifested in the first peak, and the decomposition of cellulose-lignin pseudo-component reaching the second peak. Therefore there is an overlapping effect.

The decomposition of lignin is not evident in Figure 6, but the author assumed this based on that the thermal decomposition of kraft alkali lignin (similar to lignin) decomposes in a wide range of temperature.

Manya; Velo and Puigjaner (2003) proposed a mechanism considering three pseudo-components to account the overlap i.e. hemicellulose, cellulose and lignin. Three first order parallel reaction models were defined with one reaction for each pseudo-component.

Figure 6 – DTG for treated and untreated *Sugar Cane Bagasse* (Treated continuous line, untreated: points).

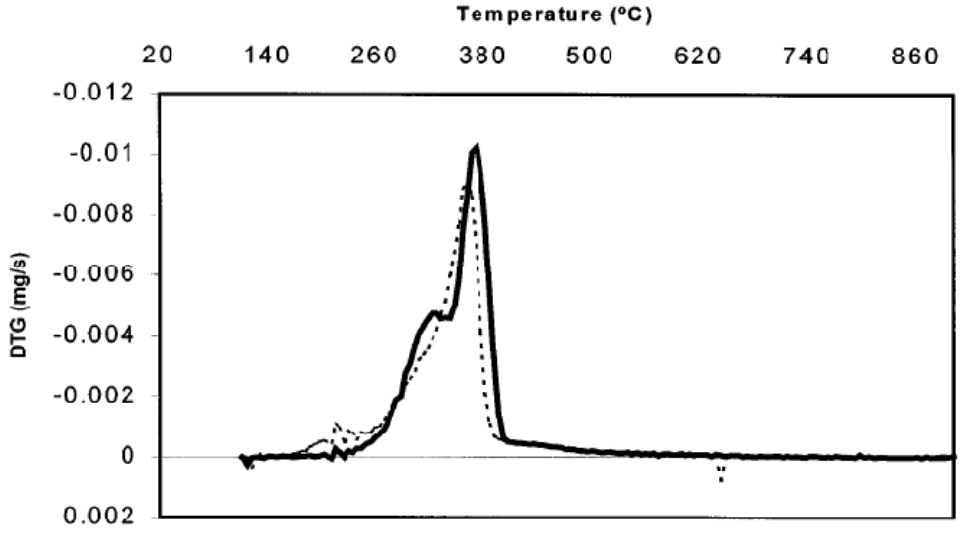

Source: Manya; Velo and Puigjaner (2003).

First, the reaction model (eq.(1)) was applied to determine the kinetic parameters of hemicellulose, which is supposed to decompose mainly near the first peak. Experimental data points near the latter peak were used to obtain the kinetic parameters.

$$\frac{d\alpha}{dt} = K(1-\alpha) \qquad (1)$$

However, due to the overlapping effect, the prediction of hemicellulose pseudo-decomposition was over-estimated. In order to discount the effect of lignin, Manya;

Velo and Puigjaner (2003) applied a procedure to assess the discrepancies between the simulated and experimental data, comparing the maximum value of simulated curve with the experimental DTG curve; the ratio between these two values was the correction factor for hemicellulose rate equation.

Points near the second peak were used to obtain the rate equation for cellulose using eq.(1) as a reaction model and applying the same correction procedure used for hemicellulose pseudo-component. Experimental data points toward the right side, but far away, from the second peak are used to determine the kinetic parameters for lignin pseudo-component using also the model of eq.(1). Therefore, the whole scheme for the devolatilization of *Sugar Cane* can be described by a liner contribution of all pseudo-components (eq.(2)).

$$\frac{dV}{dt} = \sum_{i=1}^{3} A_i exp\left(\frac{-E_i}{RT}\right)(V_i^* - V_i) \qquad (2)$$

The results have shown a good agreement for cellulose and hemicellulose pseudo-component, however, no satisfactory results were obtained for lignin. The author supposed that the first order model, $(1-\alpha)$, was not suitable for the description of lignin decomposition. Therefore a reaction of an *n-order* model was proposed (eq.(3)). This reaction model is expressed also as non-dimensional degree of conversion α.

$$f(\alpha) = (1-\alpha)^n \qquad (3)$$

A new estimation of kinetic parameters for lignin decomposition shown a better fit with the experimental data as can be seen in Figure 7.Two important aspects have revealed the latter two works. Firstly, due to the overlapping, for pyrolysis of complex materials or composites at low heating rates the mathematical description can be conducted by means parallel reactions, one reaction for each pseudo-components. Also, it is worth mentioning that DTG charts do not reveal, a priori, the number of pseudo-components. In the case of these two works indeed the description using three pseudo-components were proposed due to the observed behavior of lignin. As mentioned by Manya; Velo and Puigjaner (2003) the TGA for kraft alkali lignin (similar to lignin) shows a thermal decomposition in a wide range of temperature, and in view of this information it was possible to recognize the overlapping effect, and therefore introduce a correction factor for both hemicellulose and cellulose.

Figure 7 – TG for treated and untreated *Sugar Cane Bagasse*.

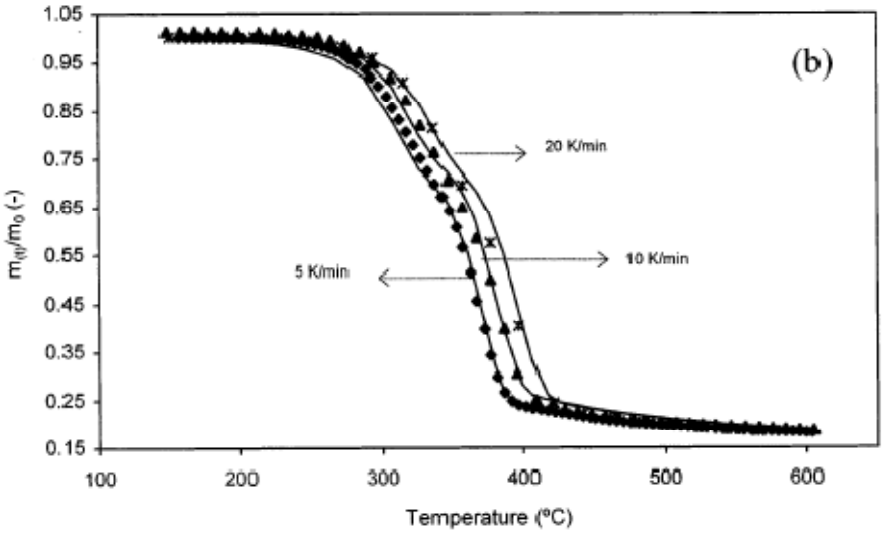

Source: Manya; Velo and Puigjaner (2003).

The second aspect is related with a type of model for reaction. Manya; Velo and Puigjaner (2003) firstly supposed a first order reaction for lignin devolatilization, however, best results were obtained using an *n*-order reaction model. The latter kinetic component is related to the structure of solid phase, and in the case of pyrolysis, as the devolatilization proceeds, the internal structure of the raw material undergoes a change, affecting any variable related to the structure, or, from the point of view of the experimental results, related with the shape of the curve in the TG and DTG charts. As mentioned by Xin et al. (2015), char characteristics can vary from unchanged or barely pyrolyzed at low temperature, to a highly carbonized material at high temperature. The results obtained by Manya; Velo and Puigjaner (2003) suggest that can be different mechanism for the different components.

Xin et al. (2015) conducted a detailed study about the char evolution during pyrolysis of crystalline cellulose in a bench-scale fixed bed reactor. The author performed a series of analysis using: FTIR spectroscopy to assess the char surface functionality; 2D correlation spectroscopy method; and X-ray diffraction, in order to observe changes in the structure of crystalline cellulose. The author showed, based on the H/C and O/C analysis that cellulose undergoes a dehydration below 300°C, while at 330°C a sharp decrease in the same parameter indicated a significant decomposition of cellulose. It is interesting that the author mentions that a value for H/C of 0.78 suggests that non-condensed aromatic structure or aromatic nucleus with aliphatic chain can be formed in the residual char. At temperatures above 330°C, ring opening

(pyranose rings), aromatization, decarbonylation (-C=O functional group) and more dehydration seemed to occur. Near 430°C results suggest that deoxygenation reactions predominate. As the process proceeds, the characteristic crystallinity of cellulose disappears owing to dehydration. The decomposition produces oligosaccharides, aliphatic hydrocarbons and aromatics, linked together and forming three dimensional disordered networks. As the temperature increases the char undergoes significant deoxygenation and dehydrogenation increasing the amount of aromatic rings grouped in clusters of more than six members. The work of Xin et al. (2015) is highly illustrative and confirms other experimental observations such as early dehydration of hydroxyl groups bonded at the pyranose rings of glucose.

It is worth mentioning that the first two studies revised here do not account for any aspects relating neither to the structure nor to the composition of the remaining solid or volatile released. Further, nothing was mentioned about the pyrolysis products, only about the weight loss of the whole sample or pseudo-components.

Always related with lignocellulosic biomass and in order to evaluate a reactor, separately from the consumption of the raw material, the quantification of pyrolysis products is necessary. In the case of fast pyrolysis the product of interest is the bio-oil (the liquid fraction before condensation). In fast pyrolysis the heating rate is higher than in slow pyrolysis. Another definition of fast pyrolysis is provided by Basu (2010) that defines it as when the characteristic reaction time of pyrolysis is longer than the necessary time to reach maximum pyrolysis temperature reaching heating rates as high as 1000 or 10000 K/min. As mentioned in section 2.1 fast pyrolysis improves the liquid yield if, as mentioned above, the heating rate is high; the maximum temperature is about 500°C; and if the residence time is quite short in order to reduce secondary cracking reactions. With the aim to study the pyrolysis process inside a reactor, kinetics must be described in order to calculate the rate of consumption of solids and the rate of formation of: char, gas and liquids. Although char formation is reduced in fast pyrolysis, it can catalyze secondary cracking reaction of heavier liquids molecules (BASU, 2010), (Moldoveanu, 1998). Thermal conditions in fast pyrolysis are different compared to the first two works revised (Caballero et al. (1997) and Manya; Velo and Puigjaner (2003)). If maximum temperature is reached almost instantly (delaying time) the process is near to isothermal conditions. When

isothermal conditions or fast heating rates are applied overlapping is more sever and only one single peak can emerge (Di Blasi, 2008).

Thurner and Mann (1981) obtained kinetics parameters to predict the evolution of the three main pseudo-products of wood, that is, lumped products i.e. char, liquid and gas. In order to obtain the kinetic parameters a especial reactor was constructed capable of obtaining mass weight loss, gas and liquids evolutions as a function of time. The type of wood used was oak sawdust, with mean length size of 0.615 mm, elemental composition of: 40.7% C, 5.6% H and 41.8% O (weight basis).

The experiments were performed at isothermal conditions. It is important to note that fully isothermal condition are never reached due to the inertial effects, and an approximate behavior is obtained with high heating rates and small sample size (DI BLASI, 2008). In order to verify effectively the isothermal condition the author performed a quantitatively procedure, discarding significantly inertia effects and a suitable control over temperature. To determine the kinetic parameter for each pseudo-products, experiments were performed at 354, 369 and 392°C. The reaction mechanism proposed is showed in Figure 8. This reaction mechanism is suggested by the work of Shafizadeh and Chin (1977). Figure 8 shows that the three lumped pseudo-products are produced, in parallel, with different kinetics constants.

Figure 8 – Reaction mechanism used by Thurner and Mann et al. (1981). Parallel and serial mechanism was proposed to path to produce gas (secondary cracking reaction) and char.

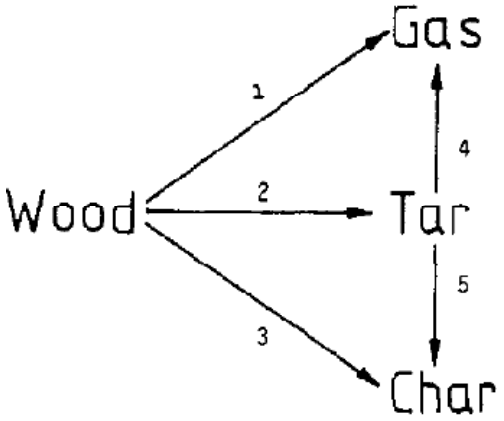

Source: Thurner and Mann et al. (1981).

As can be seen, tar can be converted by reactions 4 and 5 in more char and gas as a secondary reaction. The author commented that if the tar is removed faster from the pyrolysis zone only reaction 1-3 remains. Rate equations for pseudo-products are:

$$\frac{dw_G}{dt} = k_1 w_w(t) \quad (4)$$

$$\frac{dw_T}{dt} = k_2 w_W(t) \quad (5)$$

$$\frac{dw_C}{dt} = k_2 w_W(t) \quad (6)$$

Where w_W, w_G, w_T and w_C are the masses of wood, gas, tar and char respectively. The author demonstrated that for isothermal conditions the final residue ($w_R = w_w + w_C$) can be related with the kinetics constant k_1, k_2 and k_3.

$$k_3 = \frac{w_{R(t\to\infty)}}{1 - w_{R(t\to\infty)}}(k_1 + k_2) \quad (7)$$

According to Thurner and Mann (1981) the evolution of char is difficult to obtain, but indeed is possible knowing the kinetic constants for gas and liquids. Considering this reaction scheme the author performs the experiments recording the data of the time evolution of the gas and liquids fractions along the pyrolysis process. The kinetic constants were obtained using equations 8 and 9.

$$k_1 = \frac{1}{w_{W(t)}}\left[\frac{dw_G(t)}{dt}\right] \quad (8)$$

$$k_2 = \frac{1}{w_{W(t)}}\left[\frac{dw_T(t)}{dt}\right] \quad (9)$$

Figure 9 presents the best curve fitted to experimental data. Figure 10 shows, as the author confirms a quite well agreement with the experimental data for 354°C.

Other results of these works are related with the composition of volatiles (gas and liquids) obtained using chromatographic techniques. The gas fraction consisted of carbon dioxide, carbon monoxide, oxygen and compounds with more than three atoms of carbon. Also, traces of acetylene, ethylene and methane were indentified. In bio-oil (liquids), three compounds were detected, two unknowns and the other one, probably, Levoglucosan (LVG).

Figure 9 – Best curve fitting at 354°C.

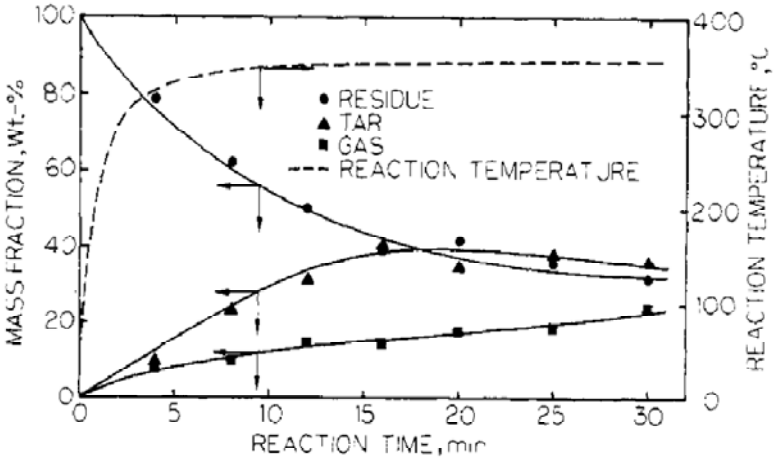

Source: Thurner and Mann (1981).

The work of Thurner and Mann (1981) shows important details about the determination of kinetic constant, that are, isolating the kinetic nature and the possibility to obtain the rate of products without a large amount of experimental data. The former is related with the procedure (pre-experimental assessments) to identify the maximum amount of mass in order to avoid the thermal inertia and transport effects (DI BLASI, 2010). The latter is related with the possibility to obtain the rate of production for the three main pyrolysis pseudo-products, assuming, arbitrarily, a reaction model and satisfying the isothermal conditions, being necessary to determine experimentally two of the three kinetics constants.

Figure 10 – Experimental results compared with model results at 354°C.

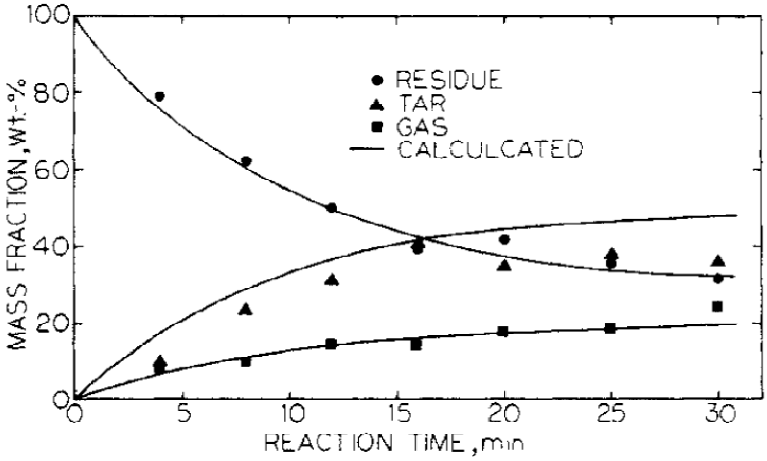

Source: Thurner and Mann (1981).

Di Blasi and Branca (2001) performed a study to determine the kinetic parameters of primary pyrolysis of thin layers of beech (*Fagus sylvatica*) wood powder, with

composition of: 45% celullose, 33% hemicellulose, 20% lignin and 2% of extractives. In order to determine the kinetic parameters of the primary products of pyrolysis, experiments were carried out in a fast thermogravimetric system and in a laboratory scale reactor, in order to obtain the mass weight loss and the final yield of products respectively.

The author performed a pre experimental stage in order to determine the dependence of the char yield on the reaction temperature. Considering a heating rate of 1000 K/min and final temperature of 708 K, the char yield was reduced from 14.5 to 11% as the wood layer thickness was decreased from 500 to 200 μm. Thinner layers up to 100 μm did not give any variation in the amount of char produced. For experimental tests, the layer thickness was set to 150 μm (9 mg), with heating rate of 1000 K/min and with a range of maximum temperature from 573 to 708 K. Similarly to Thurner and Mann (1981) Di Blasi and Branca (2001) use the mechanisms suggested by Shafizadeh and Shin (1977) (Figure 11).

Figure 11 – Reaction mechanism proposed by Di Blasi and Branca (2001).

$$\begin{array}{l} \overset{k_C}{\nearrow} CHAR \\ W \overset{k_L}{\rightarrow} LIQUIDS \qquad (a1-a3,) \\ \overset{k_G}{\searrow} GAS \end{array}$$

$$k = k_G + k_L + k_C, \quad k_j = A_j e^{-E_j/(RT)}, \; j = G, L, C \qquad (1-2)$$

Source: Di Blasi and Branca (2001).

Kinetic constants have the same meaning as in the work of Thurner and Mann (1981). However as can be observed in Figure 11, the objective is to determine the Arrhenius kinetic parameters: A_0 (frequency factor) and E_a (activation energy) rather than only the constants. To obtain the parameters, the author used the following mathematical equations, based on the assumption of isothermal conditions.

$$Y_G = \frac{k_G}{k} \qquad (10)$$

$$Y_L = \frac{k_L}{k} \qquad (11)$$

$$Y_C = \frac{k_C}{k} \qquad (12)$$

Where Y_g, Y_l and Y_c are the final yields of gas, liquids and char. Final yield of carbon can be obtained directly from the weight loss curve. Other relations were used (eq.(13) - eq.(17)), and also defining Y_v, total volatile yield ($Y_g + Y_l$).

$$Y_V = 1 - Y_C \quad (13)$$

$$Y_V = \frac{k_V}{k} \quad (14)$$

$$K_V = K_G + K_L \quad (15)$$

and

$$Y_G = \frac{\alpha_{gl}}{1 + \alpha_{gl}} Y_V \quad (16)$$

$$Y_L = \frac{1}{1 + \alpha_{gl}} Y_V \quad (17)$$

$$\alpha_{gl} = \frac{Y_G}{Y_L} \quad (18)$$

In equations 15 to 17 α_{gl} is the ratio between the gas and the liquid final yields. Both yields were determined by the author from the experiments in the laboratory-scale reactor.

Seven runs were conducted in isothermal conditions with the aim to obtain the data to determine the kinetic parameters A_0 and E_a. The author distinguished two zones in the devolatilization chart of the sample, then two sets of Arrhenius parameters were fitted. Other sets of runs were conducted in order to obtain the final yields of gas, liquids and char fractions as a function of the maximum temperature. Table 1 shows the parameters obtained by Di Blasi and Branca (2001).

Table 1 – Kinetics parameters for global parallel reaction mechanism obtained by Di Blasi and Branca (2001) (Error interval has been ommited).

	E [kJ/mol]	ln (A [1/s])
(a) k	94.4	12.4
(b) k	141.2	22.2
k_c	111.7	15.0
k_v	148.6	23.4
k_G	152.7	22.2
k_L	148.0	23.1

Source: Di Blasi and Branca (2001).

The author concluded that the better set of parameters is: k = 141.2 kJ/mol, k_c = 111.7 kJ/mol, k_V = 148.6 kJ/mol, k_g = 152.7kJ/mol, k_l =1 48.0 kJ/mol. The author highlighted that: a) the model does not have applicability for slow heating rate and low temperature, due to the fact that is obtained from data near the central part of the weight loss curve, leaving the data of tails of the curves out. b) the global kinetic

model developed can be coupled with the mathematical transport description with the objective not only to predict the conversion time, but also the variation of the distribution of pseudo-products.

The work of Di Blasi and Branca (2001) shows that with the assumption of certain mechanisms and with the isothermal condition, it is possible to obtain a global model with the capability to give the rate of consumptions of the solid and the rate of production of the lumped pyrolysis products, apparently without any knowledge of the species composition of the lumped products. As mentioned by Di Blasi (2008), global models are suitable for engineering calculations due the capability to predict products yields, however no information is available about the composition of the condensable and non-condensable products. To obtain a more detailed reaction mechanism it is necessary to observe the solid at a molecular level. However, not only the elemental analysis is necessary, but also the structure, due to its properties that play a fundamental role about the reaction pathways (CAREY, 2006). On the other hand, the chemical structures are composed by functional groups, where each functional group give molecular properties, and also are the key factor on chemical reactions (CAREY, 2006). Therefore the detailed description of the pyrolysis process must take into account the structure and the functional groups in order to propose a set of chemical reaction to predict the char, the gas, and the liquids products.

Figure 12 – Reaction mechanism proposed by for cellulose pyrolysis.

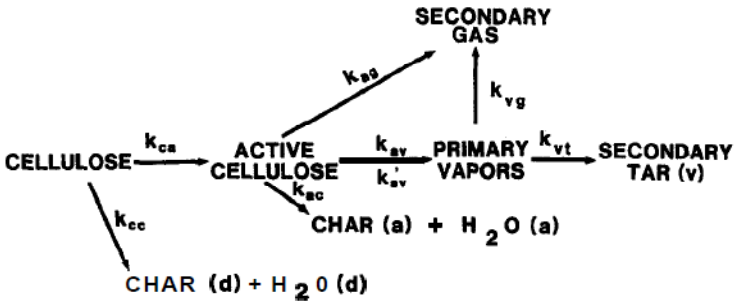

Source: Diebold (1994).

In the decade of the nineties, Diebold (1994) proposed a multi-step semi-global reaction mechanism for cellulose thermal decomposition. The mechanism is shown in Figure 12, and consists of a set of parallel and serial reactions to produce char, water steam, gas and tar. However, unlike the mechanism proposed by Shafizadeh and Chin (1977) the present scheme defines one path for primary vapors and tars; two

possible paths for gases; and also two paths to produce char, directly from cellulose and from the intermediate product called activated cellulose, no secondary cracking was considered for *TAR V* as can be seen in Figure 12.

The model was constructed using results and kinetics parameters from other authors, being the main objective to incorporate the competitive reaction between the char and liquids observed experimentally in cellulose pyrolysis by means different kinetic parameters for each reaction. This competition can be observed between the reactions to form primary vapors and the reaction to form char and water. As can be observed in the mechanism, water is explicitly defined as a product. The author comments that this reaction is due to a process related to the structure of cellulose and the influence of its functional groups, according to Carey (2006). It is worth to note that Cellulose is a *carbohydrate*, a regular polymer of glucosidic monomers with the molecular formula $(C_6H_{10}O_5)_n$ (RANZI et al., 2008). The monomers are glucose (α-glucopyranose) residuals bonded together by glycosidic bonds (CAREY, 2006). Cellulose is classified as an isotactic polymer i.e. due to that its different structural polymer chains can be packed together and very tightly. Further, another structural-functional property is that the 2-hydroxyl (Figure 14) groups can form an H-bonding with an accessible oxygen in a contiguous chain, an intermolecular bond (CAREY, 2006). The latter property gives the strong characteristic of the cellulose fibers. Water formed directly from cellulose is due to the dehydration (elimination of OH group in the pyranose ring shown in Figure 14), a reaction favored at low temperatures. When the pyrolysis process is more severe a chain cleavage reaction competes with the latter reaction producing the dehydro-cellulose, carbon oxides and additional water. As the author comments, the chain cleavage are preceded by another reaction that produces activated cellulose. This reaction is proposed due to the fact that other authors (BRADBURY; SAKAI AND SHAFIZADEH, 1979) observed an induction time before the main volatile production during pyrolysis, especially at high heating rates.

Figure 13 – Cellulose polymer chain depicted by Carey (2006).

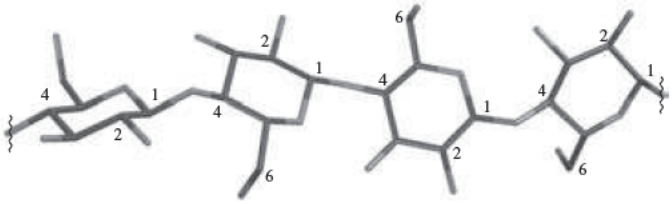

Source: Carey (2006).

Figure 14 – Cellulose polymer chain depicted by Moldoveanu (1998), in where there are two hydroxyl groups OH per monomer.

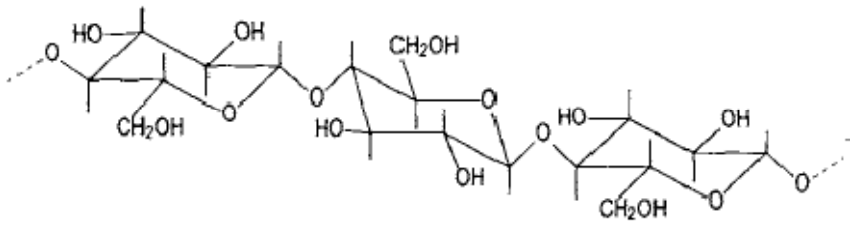

Source: Moldoveanu (1998).

Diebold (1994) also mentioned that active cellulose has DP (degree of polymerization) of 200 and is not very stable, therefore it tends to degrade very rapidly to a polymer thermally stable i.e. char. The tar fraction is composed by vaporized substances from the condensed phase (activated cellulose), that vaporize when its vapor pressure approaches to ambient pressure. At atmospheric pressure the vaporized substances are identified and correspond to monomers and fragment of monomers rather than oligomers, indicating an almost complete cleavage of chains. However, some oligomers are present in the vapor phase therefore the depolymerization process may continue. Competitive cleavage, decarboxylation and dehydration can break these oligomers and monomers to produce non-condensable gases i.e. CO, H_2, CH, CO_2, C_2H_4, and higher olefins, but also phenolic and other polycyclic aromatics compounds.

All aforementioned reactions were observed by researchers in the cellulose pyrolysis, however these observations must be included in the kinetic model. In the mechanism developed by Diebold (1994) two reactions compete for the cellulose material, the cleavage reaction to form oligomers and the dehydration reaction to form char and water (char (d) and H_2O (d) in Figure 12). The author comments that some carbon dioxide is observed in a reduced amount during the dehydration. However in the mechanism this little amount is included as water. As can be seen in Figure 12 activated cellulose can react competitively to produce more char, water (char (a) and H_2O (a) in Figure 12), tarry vapors and non-condensable secondary gases. Similar to the first char and water reaction some by-product gases formed in the second charring reaction are included in water. In the reaction to form secondary tar, any gaseous by-product or water formed are included in the compound. This treatment is defined as the lumped approach.

As mentioned above, the reaction mechanism constructed by Diebold (1994) used kinetic parameters taken from the literature at that time. The criteria applied to choosing some kinetic parameters and not others, was according to the relative rates, choosing those with the highest rate. According to the author this criteria comes from the experimental facts that is related to the sample temperature and can affect the kinetic constant. Table 2 shows a summary of the kinetic parameters selected by Diebold (1994).

The author mentioned that the kinetic parameter k_{ag}, that produces gas directly from activated cellulose, could not be determined, and, in order to resolve this lack of information, the author used the same parameter as for k_{vg}. Related with the kinetic parameters Diebold (1994) mentioned that in order to apply the model to a wide range of pyrolysis conditions, the kinetic parameters had to be extrapolated. The model was applied, for example, to simulate the TGA curves and compare the results with the actual values obtained by other authors. Figure 15 shows one of these verification for Avicel PH-102 (microcrystalline cellulose).

Table 2 – Kinetics parameters selected by Diebold (1994) from other authors.

Reaction	**k**	**A [1/s]**	**E [kJ/mol]**	**Source**
Cellulose to char + H_2O	k_{cc}	6.70E5	110	Stamm*
Cellulose to active cellulose	k_{ca}	2.8019	240	Bradbury*
Active cellulose to primary vapors at 1 atm	k_{av}	6.79E9	140	Lewellen*
Active cellulose to primary vapors at 1.5 Torr	k_{av}	3.20E14	200	Bradbury*
Active cellulose to char + H_2O	k_{ac}	1.30E10	150	Bradbury*
Active cellulose to secondary gases	k_{ag}	3.60E21	200	Antal*
Primary vapors to secondary gases	k_{vg}	3.60E11	200	Antal*
Primary vapors to secondary tars	k_{vt}	1.80E03	61	Antal*

* Sources are referenced by Diebold (1994).
* Table 2 present a summary of table presented in Diebold (1994).
* Kinetic coefficient equation: k = A exp(-E/R/T). Source: Diebold (1994)

Other verifications were made with simulations at different heating rates, from 0.01 to 100,000 °C/min (Figure 16). The author mentioned the good agreement with the experimental data that predicts a decreasing char yield as the heating rate increase. A slight offset between the simulated and actual curves for simulation at 1000°C and with a heating rate of 100 °C/min is mentioned. Nonetheless at low temperature, the author confirms a good agreement with the experimental data.

The revision of the work of Diebold (1994) revealed two important aspects. The first is related with the possibility to propose a kinetic model for complex materials based on the result published by other authors obtaining from suitable to good results compared against experimental data. The second aspect is related to the necessity of detailed information about the chemistry of complex materials, such as cellulose, hemicellulose, lignin, (biopolymers (MOLDOVEANU, 1998)) other regular polymers, carbohydrates in general, proteins or lipids. The additional information needs to be at least related to the structure and functional groups that is studied in organic chemistry and have an important role in chemical reactions (CAREY, 2006). Therefore, a detailed knowledge about the structure and functionality is essential in order to propose a detailed reaction mechanism for substances from which there is no as much information about its thermal decomposition.

Figure 15 – Model results compared with actual experimental TGA using microcrystalline cellulose Avicel ph-102.

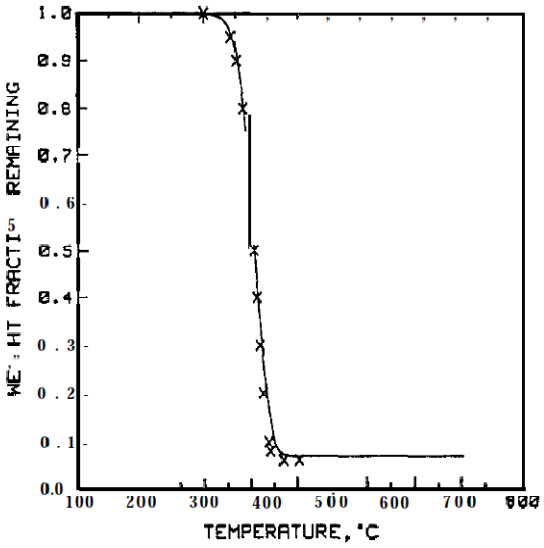

Source: Diebold (1994).

In the case of lignocellulosic materials, as mentioned by Diebold (1994), research has been performed from around 1960, therefore, there are more than fifty years of research efforts producing a generous amount of data and information, on the contrary, in the case of microalgae biomass, research about pyrolysis is relatively recent with no more than 20 years and indeed the data available are limited.

Figure 16 – Additional results compared with experimental TGA data using microcrystalline cellulose Avicel ph-102.

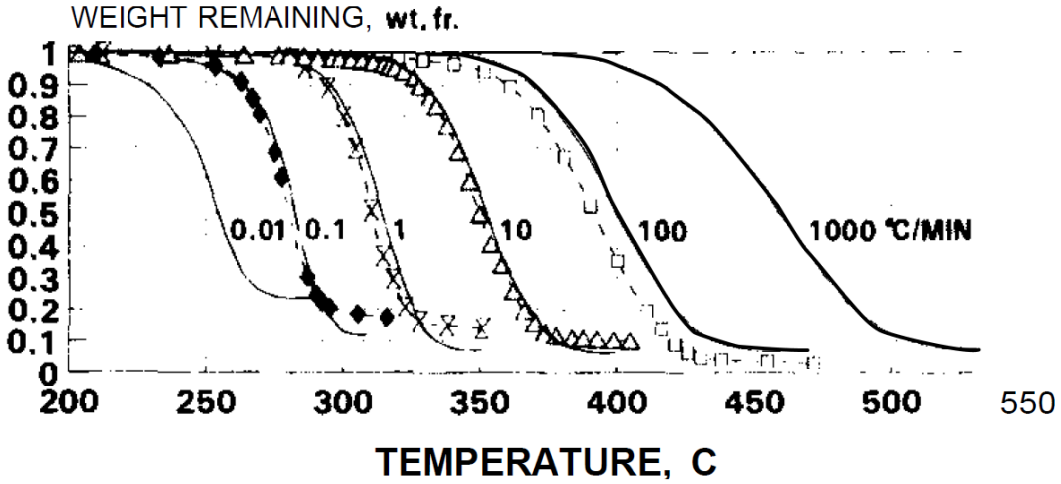

(Symbols: experimental data; continuous line: model data).
Source: Diebold (1994).

2.3. LITERATURE REVIEW OF PROLYSIS AND THERMAL ANALYSIS FOR CHLORELLA VULGARIS AND OTHER MICROALGAE BIOMASSES

In section 2.2 works were presented about the thermal analysis related to pyrolysis of lignocellulosic biomass and a more detailed work of Diebold about pure cellulose. In the current section a series of works related to thermal analysis for *Chlorella Vulgaris* are presented in conjunction with other articles related to the partial developments of reaction mechanisms about different microalgae species. Some of these articles are related only on TG and DTG analysis; however the remaining papers include also substances identification.

The interest about the thermal decomposition of microalgae biomass is recent, as can be seen in Figure 17; in the final of the past century only fourteen papers were published (considering a search in http://www.sciencedirect.com web site). Further, in the first decade of the XXI century, there was little more interest with only fifteen papers. However, only in the first five years of the decade of 2010, there are 70% more papers related to the microalgae pyrolysis, revealing an increasing interest about this material and its thermal decomposition. Most works related to thermal decomposition of microalgae are in the stage of primary characterization and analysis of only Arrhenius kinetic parameters and substance identification.

Figure 17 - Papers published in the last 40 years about microalgae pyrolysis (Sciencedirect.com).

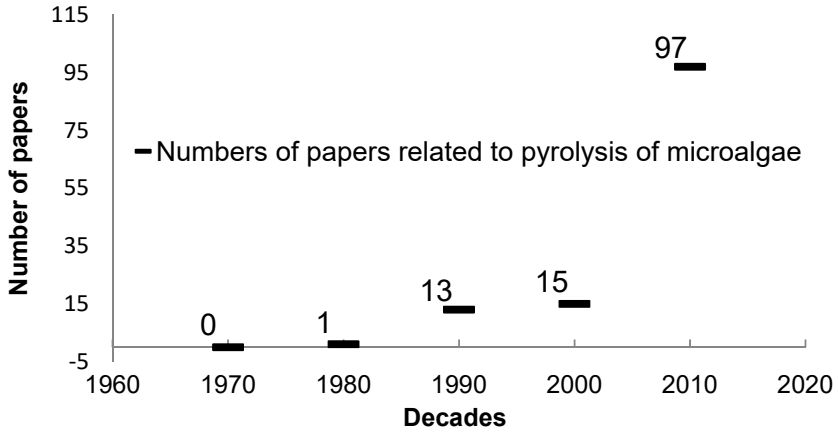

For *Chlorella Vulgaris* there are no papers that contain efforts related to the proposition of a chemical kinetic reaction mechanism for fast pyrolysis in order to evaluate reactor hydrodynamics.

Non-complete, therefore, partial kinetic schemes have been developed mainly for oxidative pyrolysis, weight loss and without rate equations for pseudo-products. Only two works related to thermal decomposition *of Chlorella Vulgaris* were found in which the complete kinetic parameters were determined in conjunction with partial reactions, however, a global reaction mechanism was not reported. In addition, three other articles were found where a partial reaction mechanism was proposed, but for species different from Chlorella Vulgaris. In order to take a picture about the following paragraphs shows relevant articles related to the thermal analysis, for *Chlorella Vulgaris* and other microalgae species.

Agrawal and Chakraborty (2013) performed a TG, DTG and DSC analysis for *Chlorella Vulgaris* microalgae, in an inert (molecular nitrogen) and oxidative (combustion) atmosphere. Five heating rates, in non-isothermal conditions, were applied: 5, 10, 20, 30, 40 °C/min in order to heat up a sample of 10 mg (size 10 μm) from 50°C to 800°C.

The size and weight of the samples were chosen in order to avoid the transport effects and thermal inertia. Arrhenius kinetic parameters were obtained from the TG and DTG data using an iso-conversional method i.e. FWO and KAS. An iso-conversional method (model free method (ALI; RAZZAK; HOSSAIN, 2015)) is a

procedure that has the advantage that a reaction model is not arbitrarily selected (VYAZOVKIN; DOLLIMORE, 1996). Composition of microalgae was reported and shown in Tables 3, 4, and 5, for elemental composition, proximate and components analysis, respectively.

Table 3 – Elemental composition of *Chlorella Vulgaris* obtained by Agrawal and Chakraborty (2013).

Elemental composition% by weight			
C	**H**	**N**	**S**
14.90	2.09	1.70	1.84

Source: Agrawal and Chakraborty (2013).

Table 4 – Proximate analysis of *Chlorella Vulgaris* obtained by Agrawal and Chakraborty (2013).

Proximate analysis% by weight			
Vol. Matter	**Ash**	**Moisture**	**Fixed Carbon**
37.3	48.6	9.1	5.0

Source: Agrawal and Chakraborty (2013).

Table 5 – Components of *Chlorella Vulgaris* obtained by Agrawal and Chakraborty (2013).

Components% by weight		
Lipids	**Carbohydrates**	**Proteins**
29.0	12.0	51.0

Source: Agrawal and Chakraborty (2013).

Figure 18 shows the results obtained by the author for heating rate of 10 °C/min. DTG curve was separated in three stages. First stage is mainly for moisture release, while most of the weight loss takes place in stage 2, from 200 to 500°C. Stage 2 is subdivided in two zones.

The strong peak in zone 1 of stage 2 is attributed to the decomposition of proteins and carbohydrates, releasing volatiles. The second zone 2, with a weaker peak is attributed to lipids decomposition. The author states that the strong peak in stage 3 is due to the gasification process of the carbonaceous compounds, releasing mainly CO and CO_2.

Other details in Figure 12, mentioned by the author, are that the slight endothermic peak in stage 1 is due to evaporation of moisture, while in stage 2 the volatile formation has a net production of heat, instead of an endothermic reaction. In stage 3, the gasification of the carbonaceous fraction needs energy to decompose. Another

effect detected by the author, but not shown in Figure 18, is the shift experimented by weight loss curves toward higher temperatures as the heating rate is increased. The author attributes this effect to the temperature detected by the measuring system.

Explanation provided is that is the temperature of the purge gas, and for high heating rates, the residence time of the sample inside the reactor decreases to a value in which it does not have enough time to reach thermal equilibrium. This explanation is reasonable however reveals a disadvantages for experiments using high heating rates. Nonetheless, as was presented in the Section 2.2, in the case of lignocellulosic biomass, inertia effects or induction is expected, and the proof is the inclusion of the activated cellulose in the reaction mechanism presented in the work of Bradbury; Sakai and Shafizadeh (1979). Therefore, shift effect could not be due to only experimental condition but also due to a physical process due to characteristics of the material, being necessary more studies about this phenomenon.

Figure 18 - TG, DTG and DSC for *Chlorella Vulgaris* obtained at 10 °C/min.

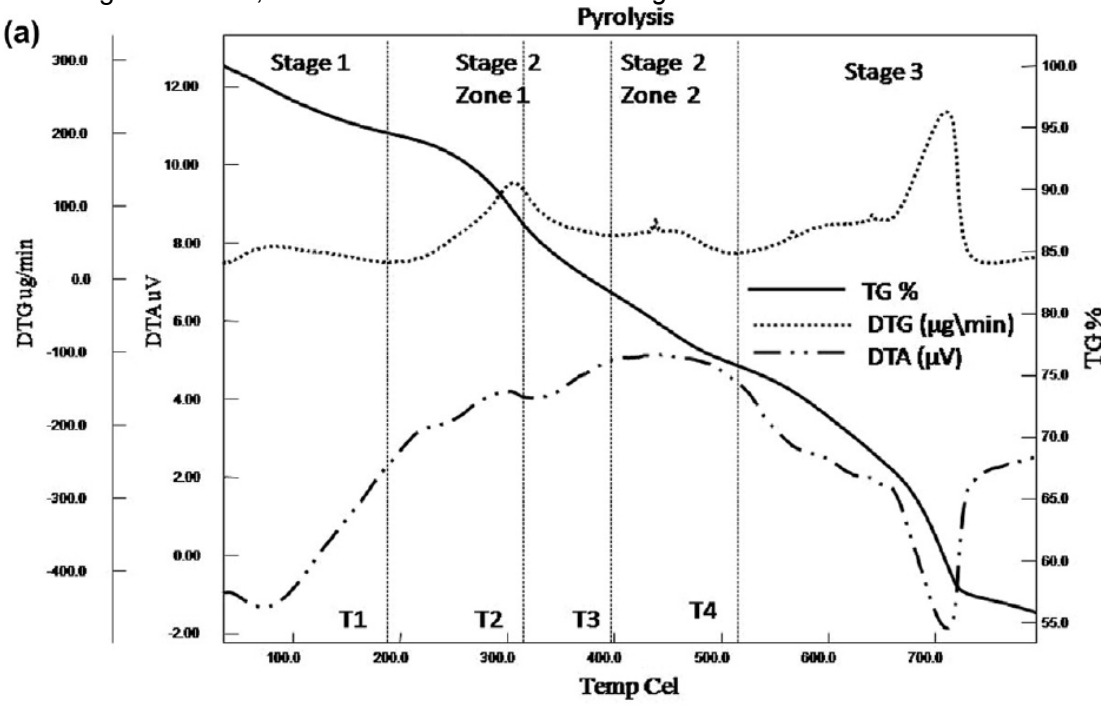

Source: Agrawal and Chakraborty (2013).

Two sets of kinetic parameters were determined owing the two reaction zones on stage 2, one for proteins and carbohydrates and another for lipids. The mean kinetic constants obtained were: A_0 = 172.8 - 758.4 s^{-1}; E_a = 51.0 kJ/mol and A_0 = 403.2 -

1159.0 s^{-1}, Ea = 64.0 kJ/mol for carbohydrates and proteins (lumped) and lipids respectively. The frequency factors are expressed as a range in order to introduce a variation as a function of the heating rate. The author concludes that: a) lipids require more energy to decompose than proteins and carbohydrates, b) the rate and yield of volatiles were increased as the heating rate is increased; and c) kinetic parameters shall be used in additional works in order to maximize the liquid yield, showing a possible future development of a reaction mechanism.

Other study of kinetics related to *Chlorella Vulgaris* was performed by De Filippis et al. (2014). In this paper the kinetics parameters for thermal decomposition of microalgae were obtained by applying the Distributed Activation Energy Model, DAEM. However, and due to the results obtained from the TG analysis, the author decided to apply an alternative methodology named Double DAEM or 2-DAEM in order to improve the kinetic model. The characterization of the microalgae by elemental composition, proximate and components analysis are shown in Tables 6, 7 and 8 respectively. Three heating rates applied were: 10, 20 and 40 K/min. Maximum experimental temperature were 1223 K, maintained for 10 minutes. Sample weight was 7 mg, with a particle diameter range between 50 to 100 μm.

Table 6 – Elemental composition of *Chlorella Vulgaris* obtained by De Filippis et al. (2014).

Elements				
C	**H**	**N**	**O**	**S***
41.1	6.4	7.3	40.5	-
% by weight				

Source: De Filippis et al. (2014). *Not meausured

Table 7– Proximate analysis of *Chlorella Vulgaris* obtained by De Filippis et al. (2014).

Vol. Matter	Ash	Moisture*	Fixed Carbon
73.4	4.7	-	21.9
% by weight Dry			

Source: De Filippis et al. (2014).*Not Measured

Table 8 – Components of *Chlorella Vulgaris* obtained by De Filippis et al. (2014).

Components		
Lipids	**Carbohydrates**	**Protein**
16.2	38.2	45.6
% by weight Dry		

Source: De Filippis et al. (2014).

As the author commented, DAEM methodology was developed in order to describe the weight loss curve, or any other product of the pyrolysis, considering the existence

of many or infinite parallel reactions that evolve simultaneously. Each parallel reaction has its own activation energy; however, all have the same frequency factor. If the number of parallel reactions is infinite, then mathematically an activation energy distribution is defined. With the aim to obtain a simultaneous contribution of all parallel reactions, an integration considering a probability density function for the activation energy must be calculated (eq.(19)). In order to calculate the integral, a distribution must be supposed being chosen the Gaussian distribution. In consequence, the parameters needed to determine the model are the mean activation energy E_0 and the standard deviation σ for the Gaussian distribution.

$$1 - \frac{v}{v^*} = \int_0^{\infty} exp\left[-\frac{k_0}{\alpha}\int_0^{T} exp\left(\frac{-E}{RT}\right)dT\right] f(E)\,dE \qquad (19)$$

Figures 19 and 20 shows the TG and DTG analysis obtained by the author for the three heating rates defined. From the DTG curve in Figure 20, a first step occurred at low temperature (450 to 700 K, or 177 to 477 °C), while the second at higher temperature (500 to 850 K or 227 to 577 °C). The author attributes the first step to primary pyrolysis, where almost all volatiles are released, and the second step to the secondary pyrolysis, where the solid residue is further decomposed, but releasing a lower amount of volatiles.

Figure 19 – TG analysis of *Chlorella Vulgaris*.

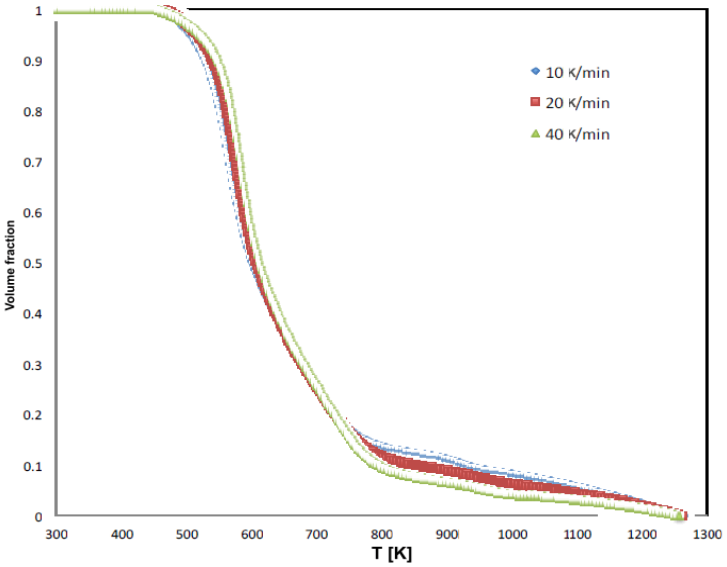

Source: De Filippis et al. (2015).

De Filippis et al. (2014) assumed that two reactions are evolved simultaneously and in series. However, the DAEM methodology (eq.(19)) is defined for only one set of infinite parallel reactions, being necessary two different Gaussian activation energy distributions (f_1 and f_2), one for each lumped reaction (eq.(20)).

$$1 - \frac{v}{v^*} = \int_0^\infty exp\left[-\frac{k_0}{\alpha}\int_0^T exp\left(\frac{-E}{RT}\right)dT\right][wf_1(E) + (1-w)f_2(E)]f(E)\,dE \qquad (20)$$

Figure 20 - DTG analysis of *Chlorella Vulgaris*.

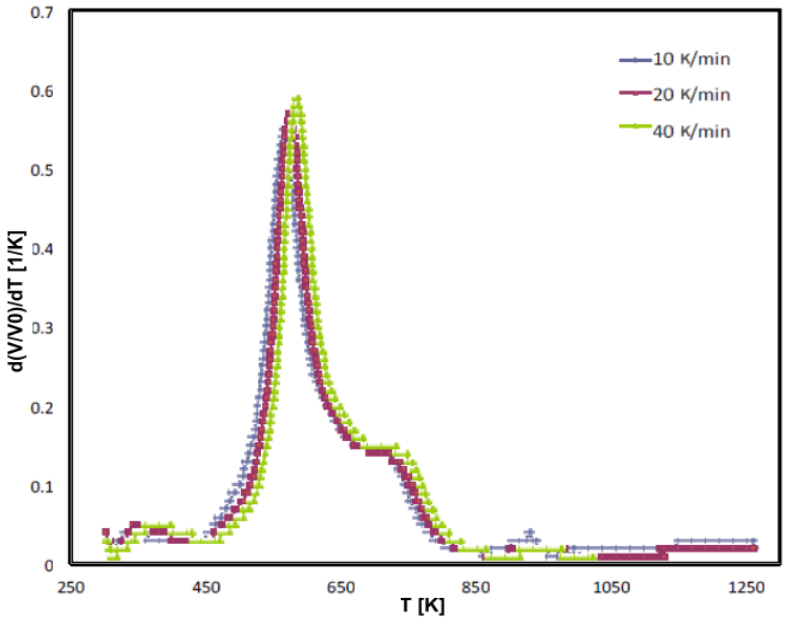

Source: De Filippis et al. (2015).

Since both reactions can be defined in the entire temperature domain, the total volatiles can be divided in two fractions, *w* and *1-w*. With the aim to demonstrate the suitability of the 2-DAE method, a comparison was made with the DAE method, being necessary the determination of two sets of parameters. Results comparing the fitting process using both methods are presented in Figures 21 and 22.

This article shows that the results with the 2-DAE methodology give better results compared to the DAE methodology, due to the 2-DAEM model fits better the experimental values depicted in red points in both Figures. The kinetic parameters determined by the De Filippis et al. (2014) are listed in Table 9, including the dispersion σ associated to the assumed normal distribution,

Figure 21 – DAE method results compared with experimental data (Experimental data: red points, model: black curve).

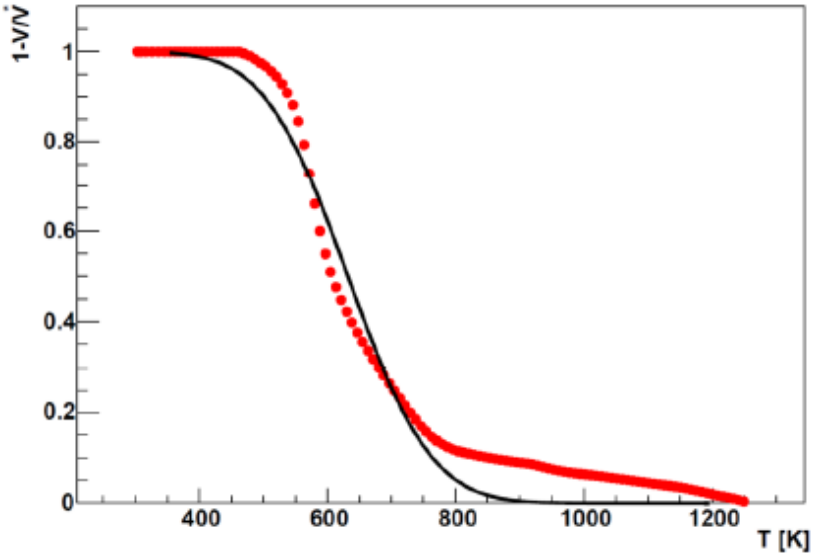

Source: De Filippis et al. (2015)

Figure 22 – 2-DAEM method results compared with experimental data. (Experimental data: red points, model: black curve).

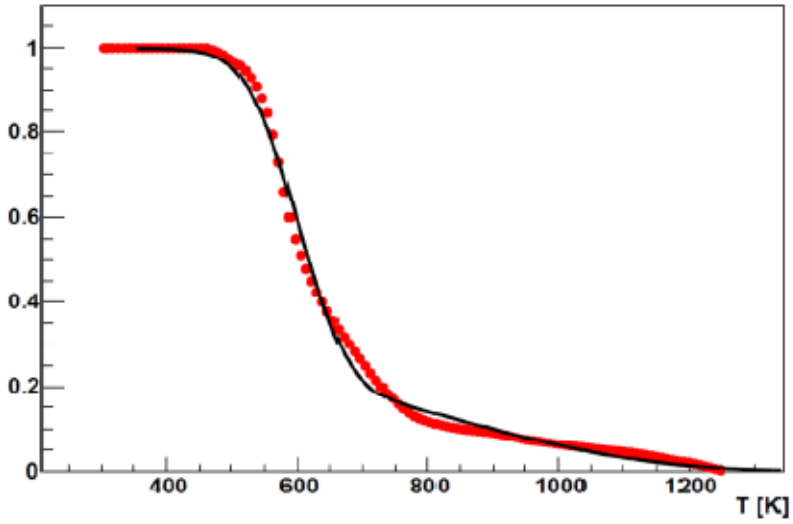

Source: De Filippis et al. (2015).

Table 9 – Kinetic parameters obtained by the author with a heating rate of 20 K/min obtained by De Filippis et al. (2014).

	1-DAEM	2-DAEM
A [1/s]	1.00E14	1.00E14
E_{01} [kJ/mol]	184	174.5
σ_{E01} [kJ/mol]	30	17.3
E_{02} [kJ/mol]		258.5
σ_{E02} [kJ/mol]		63.5
w		0.78

Source: De Filippis et al. (2015).

It is worth to mention the calculated error obtained from both methodologies. Table 10 shows the residual sum of squares indicating the better performance of the 2-DAE methodology.

Table 10 – Residual sum of squares for DAEM and 2-DAEM methodologies obtained by De Filippis et al. (2014).

1-DAEM	0.067
2-DAEM	0.002
χ^2 (1-DAEM)/χ^2 (2-DAEM)	33

Source: De Filippis et al. (2015).

Finally, the author concludes that the first step of the pyrolysis process dominates, and takes place with a low activation energy and in a narrow range expressed by the dispersion obtained (σ_{E01} = 17.3 kJ/mol). Also, concludes that the two reactions are overlapped and the second reaction take place in a wider temperature range (σ_{E02} = 63.5 kJ/mol).

Gong et al. (2014) performed a very descriptive and useful study about the pyrolysis behavior of *Chlorella Vulgaris* and *Dunaliella Salina.* Kinetic constants determination and an analysis of product released during pyrolysis (char, liquids and non-condensable) at various temperatures were conducted, using TG, DTG, GC-MS, and proximate and elemental analysis. Kinetic analysis was conducted in a TG analyzer while all experiments related to the product characterization were conducted in a lab-scale quartz pyrolyzer. The following heating rates were used for TG analysis: 5, 10, 20, and 40 K/min, with a sample in the range of 45 to 150 μm. Characterization of biomass is shown in tables 11, 12 and 13.

From the proximate, elemental and thermal analysis the author has commented some characteristics. Microalgae shows a higher concentration of nitrogen (N) and sulfur (S) compared with lignocellulosic biomass, owing the content of proteins and its peptides bonds.

Table 11 – Proximate analysis and high heating value for *Chlorella Vulgaris* and *Dunaliella Salina* microalgae species obtained by Gong et al. (2014).

	Moisture	**Ash**	**Volatile matter**	**Fixed carbon**	**HHV [MJ/kg]**
Chlorella Vulgaris	4.40	11.40	75.20	9.00	19.30
Dunaliella Salina	4.00	7.20	76.30	12.50	21.20

Source: Gong et al. (2014)

Table 12 – Elemental and empirical molecular formula for *Chlorella Vulgaris* and *Dunaliella Salina* microalgae species obtained by Gong et al. (2014).

	C	H	O	N	S	Molecular formula
Chlorella Vulgaris	44.7	6.5	24.0	7.6	1.4	$CH_{0.15}\ O_{0.54}$
Dunaliella Salina	48.1	7.1	23.3	9.4	0.8	$CH_{0.15}O_{0.49}$

Source: Gong et al. (2014)

Table 13 – Component analysis for *Chlorella Vulgaris* and *Dunaliella Salina* microalgae species obtained by Gong et al. (2014).

	Protein	Lipid	Carbohydrate	*$mf_{carbohydrate}$
Chlorella Vulgaris	47.4	15.6	13.2	21.2
Dunaliella Salina	58.8	10.5	11.9	19.5

*Obtained by difference
Source: Gong et al. (2014)

The author also comments the low oxygen content based on C/O and H/O ratios compared with lignocellulosic biomass. From the observation of the component analysis the low lipids content is highlighted, which is as expected due to the fact that *Chlorella Vulgaris* and *D. Salina* are not suitable for biodiesel production. Two values for carbohydrates content are shown in table 13. Values in column labeled as carbohydrates are obtained by the phenolic-sulfuric method, while values in column labeled as $mf_{carbohydrates}$ (mass fraction carbohydrates) are obtained by difference. Figures 23 and 24 show the experimental results of TG and DTG analysis. Three zones have been distinguished by Gong et al. (2014).

Figure 23 – TG and DTG analysis for *Chlorella Vulgaris* and *Dunaliella Salina* microalgae at 10 K/min.

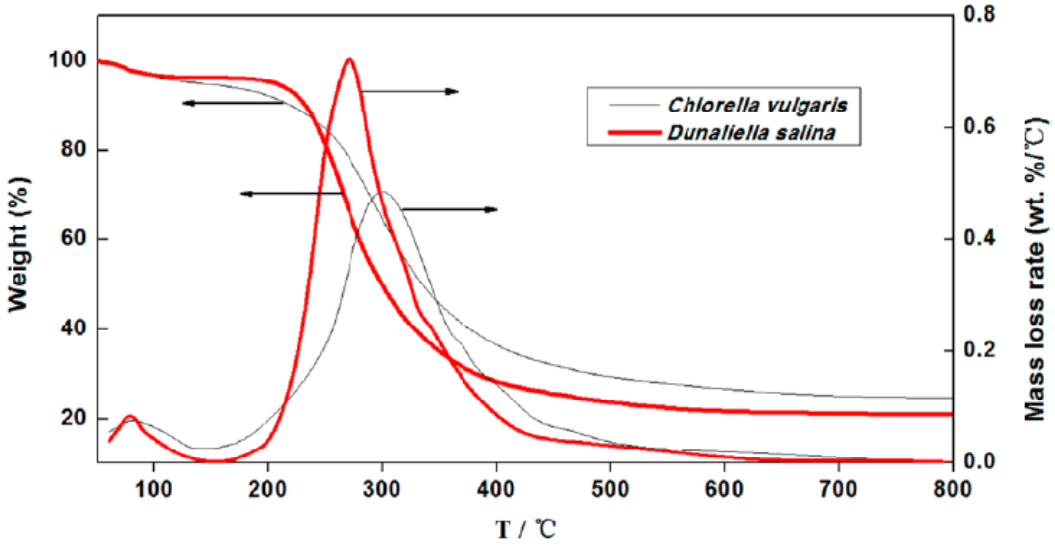

Source: Gong et al. (2014)

The author attributes the first peak (first zone), below 100°C, to the moisture evaporation. Evident differences are present in TG plots in zone two, in which a severe weight loss takes place. *D. Salina* and *Chlorella Vulgaris* has a maximum weight loss, of 3.7%/min and 2.5%/min, respectively, and a different starting temperature for devolatilization of 270°C 3 and 00°C respectively. Gong et al. (2014) attributes the lower starting temperature of *D. Salina* to the higher protein content than of *Chlorella Vulgaris*. The third zone is attributed to bonds cleavage of C-H inside the remaining residue. The author comments that the maximum weight loss is shifted toward higher temperatures as the heating rate is increased as a common behavior in dynamic TG experiments, attributing the phenomenon to the mass and heat transport issues.

Gong et al. (2014) has obtained kinetic parameters from TG and DTG data. An *n-th* order model was applied to describe the dynamics. Table 14 shows Arrhenius and exponential parameters obtained. Highlights are: the activation energy decreases as the heating rate increases; due to the higher content of proteins of *D. Salina* compared to *Chlorella Vulgaris*. The latter has a higher activation energy for all heating rates; correlation coefficients for all samples and conditions were larger than 0.94, that is, a good agreement between the model and experimental data.

Figure 24 – All DTG analysis for *Chlorella Vulgaris* and *Dunaliella Salina* microalgae.

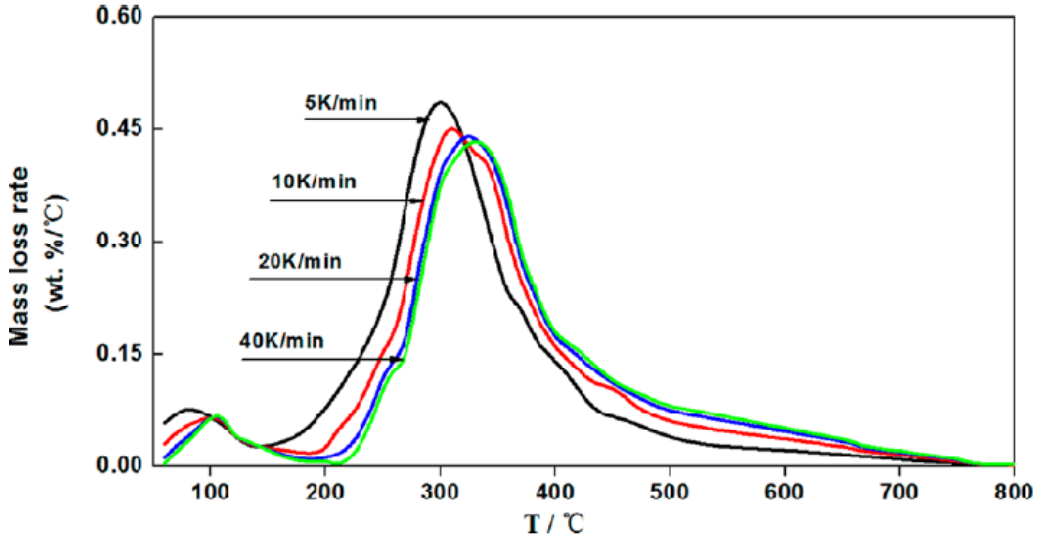

Source: Gong et al. (2014)

Figure 25 and 26 shows the products yields as a function of temperature. The author comments that, as the final temperature is increased from 300 to 700°C, the gas

yield is increased and char yield decreased. Pyrolytic gas from *Chlorella Vulgaris* pyrolysis was higher than *D. Salina* in all experimental conditions. The oil yield increases as the temperature increases from 300 to 500°C. Maximum liquids yields (wet basis) were 60.7 and 64.9% for *Chlorella Vulgaris* and *D. Salina* at 500 °C, respectively.

Table 14 – Kinetic parameter for *n-th* order model for both species obtained by Gong et al. (2014).

	Heating rate [K/min]	E [kJ/mol]	A [min^{-1}]	n	R^2
Chlorella Vulgaris	5	48.4	1.80E4	2.05	0.94
	10	45.2	1.60E4	1.92	0.97
	20	43.6	1.30E4	1.83	0.95
	40	42.9	1.00E4	1.86	0.96
Dunaliella Salina	5	43.8	9.20E3	1.95	0.98
	10	41.1	6.60E3	1.86	0.94
	20	39.3	7.60E3	1.85	0.97
	40	38.8	6.20E3	1.88	0.95

Source: Gong et al. (2014)

Pyrolytic gas analysis shows that (Table 15) reveal that methane (CH_4) was the only constituent detected at for experiments at 300°C. Also, the fraction of methane decreases rapidly with an increment in temperature up to 700 °C. No H_2 was detected when the temperature was lower than 500°C, and just 24 to 26% at 700 °C. As C_nH_m content increases volume fraction of carbon dioxide (CO_2) decreases faster. Content of gases such as C_2H_6, C_2H_4, and C_2H_2 caused that the Q_v (theoretical calorific value) of the pyrolytic gas of *D. Salina* was higher than that of *Chlorella Vulgaris* due the higher heating value of its components.

Figure 25 – Char, liquids and gas yields for *Chlorella Vulgaris* at 10 K/min.

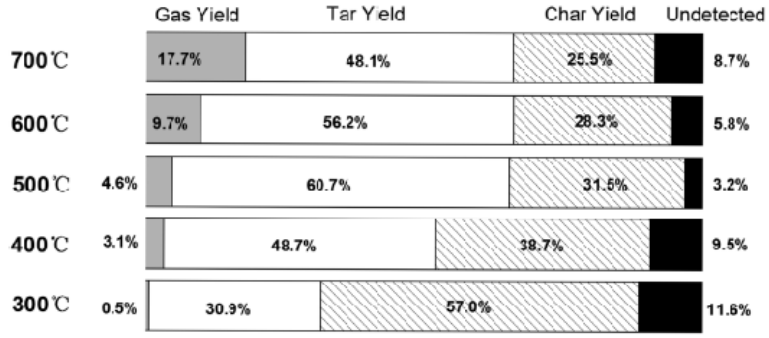

Source: Gong et al. (2014)

The author also has reported the proximate and elemental analysis for the liquids and char produced during pyrolysis. In summary the elemental carbon content of the

liquids increase while the carbon content of char decreases as the pyrolysis temperature increases. On the other hand, the hydrogen and oxygen content of char and liquids decreases as the pyrolysis temperature increases, for both microalgae species.

Figure 26 – Char, liquids and gas yields for *Dunaliella Salina* at 10 K/min.

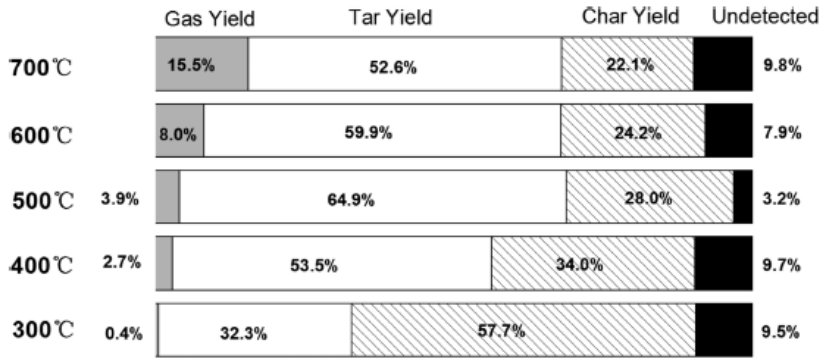

Source: Gong et al. (2014)

Table 15 – Analysis of pyrolytic gases for *Chlorella Vulgaris* obtained by Gong et al. (2014).

	Temperature [°C]				
	300	**400**	**500**	**600**	**700**
H_2	nd	nd	22.2	25.5	25.9
CH_4	100	36.5	34.9	22.8	21.5
CO	nd	nd	nd	24.5	29.9
CO_2	nd	61.6	39.6	22.1	14.5
C_2H_4	nd	nd	nd	2.4	5.8
C_2H_6	nd	1.9	4.3	2.8	2.3
C_2H_2	nd	nd	nd	nd	0.2
Q_{vb} (MJ/Nm^3)	35.9	14.3	17.7	17.2	19.3

Nd: not detected
Formula for heating value: $Q_{vb} = 12.64V_{CO} + 10.79V_{H2} + 35.88V_{CH4} + 59.44V_{C2H4} + 56.49V_{C2H2} + 64.35V_{C2H6}$
Source: Gong et al. (2014).

GC-MS analyses of both species show the following results. *Chlorella Vulgaris* produces less carbohydrate-derived compounds than D. Salina. The author mentioned that the ash contained in *Chlorella Vulgaris* could promote a catalytic decomposition of carbohydrate, producing gases with low molecular weight.

Finally, Gong et al. (2014) concludes the following. The protein derivatives in the pyrolytic oil include: phenols, nitrogen containing aromatic derivatives, nitriles, amides, pyrrole, nitrogen compounds, pyridine, amine compounds, among others.

Many of these products were evolved from the original amino acid structure in microalgae proteins. The main phenols and alkyl-phenols detected by GC and spectrometry in the liquids from both microalgaes were: phenol, 4-methylphenol, and 3-ethylphenol. Heterocyclic rings compounds with one nitrogen atom were also detected. The author suggests that they come mainly from the primary pyrolysis of amino acids. Other organic compounds detected in the pyrolysates were a straight-chain alkanes, alkenes, alkynes, fatty acids, aldehydes, and esters with a number of carbon atoms in the range from 12 to 20, as it mentioned by the author, derived from lipids. *Chlorella Vulgaris* present a higher amount of lipid derived substances compared to *D. Salina*. An important characteristic revealed in this paper is that the main fatty acids in both oils are straight-chain fatty acids, such as palmitic, linolenic, myristic, and linoleic acids.

Xu et al. (2014) performed a TG analysis and has obtained the kinetic parameters in order to study the effects of alkaline earth and alkali metal compounds on catalytic thermal decomposition of *Chlorella Vulgaris* with particle size was of 200 μm. Only one maximum temperature and heating rate were applied, 1000°C and 30 K/min respectively. The microalgae were characterized by an elemental and proximate analysis and results were: C=47.84, H=6.41, O=25.00, N=9.01 and S=1.46; and volatile=55.37, ash=10.28 and fixed carbon=34.35 (wt. %) respectively. Additionally, low heating value was determined accounting for 21.88 MJ/kg. Catalyst used was MgO, CaO, $BaCO_3$, K_2CO_3, Na_2CO_3. Kinetic parameters were determined using two iso-conversional methods, FWO and KAS. Only one stage of the whole thermal decomposition process was considered in the analysis and the kinetic parameters determined were between 99.60 to 134.05 kJ/mol. The author concluded that the catalyst improved the thermal degradation of *Chlorella Vulgaris* with a significant reduction of the remaining char. In descending order of effectiveness of the catalyst was 1.35 mg (with no additive), 1.05 mg (K_2CO_3), 0.82 mg (Na_2CO_3), 1.11 mg ($BaCO_3$), 1.15 mg (CaO) and 1.35 mg (MgO).

Kebelmann et al. (2013) studied the thermal decomposition of microalgae *Chlamydomonas Reinhardtii* (wild type, and with cell wall deficiencies), C*. Reinhardtii* CW15 and *Chlorella Vulgaris*. The proteins and lipids were extracted and studied under conditions of intermediate pyrolysis. Extracted lipid fractions were analyzed in

a TG apparatus and substances detections was performed using spectrometry analysis Py-GC-MS. Proteins for all microalgae species accounted for almost 50% and lipids 16-22% of dry weight of cells with little difference in the lipid compositions for *C. Reinhardtii.* Author observed three stages in pyrograms, identifying: dehydration, devolatilization and decomposition of carbonaceous solids. Spectrometry analysis show that lipid pyrolysis products derived from *C. Reinhardtii and C. Reinhardtii CW15* were very similar. Major products identified were phytol and phytol derivatives formed from the terpenoid chain of chlorophyll, benzoic acid, alkyl ester derivatives, benzenedicarboxylic acid alkyl ester derivatives and squalene. In the case of lipids extracted from *Chlorella Vulgaris* the author identified: octadecanoic acid octyl ester, hexadecanoic acid methyl ester and hydrocarbons including heptadecane, 1-nonadecene and heneicosane. A significant amount protein derived compounds from all microalgae were detected such as: toluene, phenol, 4-methylphenol, 1H-indole, 1H-indole-3methyl. An interesting aspect about the work of Kebelmann et al. (2015) is that the pyrolysis profiles of proteins and lipids were determined separately. The difference in the peak of maximum rate loss for both components and how the pattern was replicated were almost at the same when the intact microalgae was pyrolyzed. This facts with the addition of the analysis of products, performed by Kebelmann et al. (2015), are useful in order to elucidate particular characteristics of component thermal decomposition.

Yuan; Tahmasebi and Yu (2015) studied and determined the pyrolysis characteristics of four algal and lignocellulosic biomass samples by using a thermogravimetric analyzer and a fixed-bed reactor. Yuan; Tahmasebi and Yu (2015) used a vertical fixed-bed tubular quartz reactor with an internal diameter of 2.0 cm heated in an electric furnace. The quartz reactor was designed in a way that the volatile matter could leave the reactor quickly during pyrolysis. About 3 g. of biomass were used in each experimental run. The effects of pyrolysis temperature and biomass type on the yield and composition of pyrolysis products were investigated. The liquid fraction from *Chlorella Vulgaris*, obtained from pyrolysis, showed higher contents of nitrogen containing compounds, as several authors have commented before. Yuan; Tahmasebi and Yu (2015) observed an increase in aromatics compounds such as phenol (aromatic compound) and its derivatives as the temperature increases up to 700°C. Spectrometry analysis using FTIR showed that the concentration of OH, C-H,

C=O, O-CH_3 and C-O functional groups in char decreases markedly as pyrolysis maximum temperature increases. It is highlighted in this study that the final yields for all biomasses were obtained as a function of the temperature. It is worth to note that this of experiments and of data in addition to the kinetic parameters obtained, can allow the development of a lumped global with one stage and three parallel mechanism for the lumped pseudo-products, char, tar and gas, however this possibility is no mentioned in this article.

All works analyzed have been performed in order to obtain preliminarily information about kinetics, mainly the activation energy *E*, and in some reports the pre-exponential factor A, obtained from non-free model approach as a consequence of an arbitrary assumption of the reaction model. All kinetic values show a wide range of variation for *Chlorella Vulgaris* that denote differences based on origin and crop cycle. Also, very important information has been obtained about the amount and the characteristics of devolatilized species released during the pyrolysis. However, efforts to develop a reaction mechanism are seldom reported and a scheme useful for CFD application has not been developed so far. Most advanced articles toward the development of a reaction mechanism are presented in the following paragraphs for *Chlorella Vulgaris* and other microalgae species.

Hu et al. 2015 performed TG analysis for *Chlorella Pyrenoidosa.* TG experiments were performed with particles size less than 125 μm and weights between of 2.5 to 5.0 mg. TG data was obtained for heating rates of 20, 40 and 60 K/min. The kinetic triplet was determined in this work. Activation energy E was determined by using the iso-conversional method of Starink, pre-exponential factor A by means the compensation effect method and the reaction model by using the master plot technique. TG analysis results obtained by Hu et al. (2015) shown a complex devolatilization with at least three different zones, including one for moisture elimination. However, a complete analysis to determine the kinetic triplet was performed only for the main devolatilization process. Several reaction models were evaluated. Diffusion type reaction model give the best match. Activation energy found in this article was in the range between 85.85 to 241.70 kJ/mol while the pre-exponential factor between 3.62E4 and 8.89E14 1/min. Although the authors determined the complete set of kinetic parameters for the most important reaction of

the devolatilization process, additional parameters or a chemical reaction to complete the reaction mechanism were not defined.

Gai et al. (2013) have performed TG and kinetic analysis for *Chlorella Perynoidosa*. TG methodology account for samples of 15 ± 0.1 mg and heating rates of 10, 20, 40 and 80 k/min. In this work the kinetic triplet was determined. Activation energy E was determined using the KAS method, and the reaction model and activation A were determined simultaneously using the universal integral method, an arbitrarily method that can produce compensated kinetic parameters. A relatively low complex devolatilization was obtained from the TG analysis consisting in one peak for moisture elimination, a second peak for the main devolatilization zone and a shoulder at higher temperature. However, kinetic analysis was only performed for the main devolatilization zone. An average activation energy of 77.02 kJ/mol was determined however, a wide range was revealed from 58.85 kJ/mol for $\alpha = 0.2$ to 114.5 kJ/mol for $\alpha = 0.8$. Diffusional reaction models give a good fitting however with significant deviation. Instead the n-order models were reported by the authors as the most suitable reaction models. A one complete kinetic triplet was found for the devolatilization of *Chlorella Perynoidosa* by Gai et al. (2013), however moisture elimination and the additional zone represented by shoulder were not analyzed and therefore the reaction mechanism was only partially determined.

Lopez-Gonzalez et al. (2014) performed model estimation parameters for oxidative pyrolysis of *Chlorella Vulgaris* based on TG thermal analysis. A multistage approach was proposed and the kinetic triplet i.e. E, A and the reaction model, was obtained applying a non-free method using an arbitrary reaction model of n-order. Specific kinetic parameters are not informed for every reaction considered and no iso-conversional analysis was reported in order to obtain the effective activation energy.

Other parameters such as heat of reaction, specific het capacity and mass of each component are not informed. Lopez-Gonzalez et al. (2014) performed the research with the objective to study the pyrolysis behavior of three different microalgae species: *Scenedesmus Almeriensis* (SC), *Nannochloropsis Gaditana* (NG) and *Chlorella Vulgaris* (CV). A pre-experimental procedure was conducted with the objective to avoid the mass transport effects inside the samples during pyrolysis. As a consequence, particle sizes between 100 and 150 mm were pyrolyzed.

Proximate, elemental and component analysis, are shown in Tables 16, 17 and 18 respectively. In an Argon atmosphere and in order to eliminate the moisture a heating rate of 40 °C/min was applied up to 105 °C and maintained for 10 minutes. Then, with a ramp of 40°C/min the samples reach 1000°C, and this temperature was kept during 10 minutes, all.

Table 16 – Biomass Proximate analysis (in wt.% basis) obtained by Lopez-Gonzalez et al. (2014).

	M	Ash	VM	FC
Chlorella Vulgaris	4.4	15.9	67.2	12.4
Scenedesmus Almeriensis	2.9	19.4	67.9	9.7
Nannochloropsis Gaditana	3.5	6.4	79.8	10.2

M: Moisture content,
VM: Volatile matter
FC: Fixed carbon.
Source: Lopez-Gonzalez et al. (2014).

Table 17 – Elemental analysis (in wt.% basis) obtained by Lopez-Gonzalez et al. (2014).

	C	H	N	S	O
Chlorella Vulgaris	44.8	6.8	7.0	1.0	40.4
Scenedesmus Almeriensis	41.9	6.7	5.9	0.8	44.7
Nannochloropsis Gaditana	49.4	7.7	7.0	1.1	34.7

Source: Lopez-Gonzalez et al. (2014).

A parallel multi-stage kinetic model for the pseudo-components was developed based on data obtained from TG analysis. A multi-stage reaction kinetic scheme was defined consisting of several independent reactions (Figure 27).

Table 18 – Component analysis (in wt.% basis) obtained by Lopez-Gonzalez et al. (2014).

	Proteins	Lipids	Carbohydrates
Chlorella Vulgaris	58.1	13.5	12.4
Scenedesmus Almeriensis	44.2	24.6	25.2
Nannochloropsis Gaditana	40.5	26.3	25.1

Source: Lopez-Gonzalez et al. (2014).

Figure 27 – Multi-stage reaction mechanism proposed by Lopez-Gonzalez et al. (2014).

$$A\ (Biomass) \rightarrow V_1(Volatiles_1) + C_1(Biomass_1)$$
$$C_1(Biomass) \rightarrow V_2(Volatiles_2) + C_2(Biomass_2)$$
$$\dots$$
$$B_{x-1}(Biomass_{x-1}) \rightarrow V_x(Volatiles_x) + C(Char)$$

Source: Lopez-Gonzalez et al. (2014)

The sub-index (1,2, …, x_1 and x) refers to each of the decomposition stages, in which a pseudo-component decomposes and it is determined by the number of DTG peaks

observed during process. Considering *n* pseudo-components and parallel nth-order reactions, the kinetic coefficients are related by the following equations:

$$\frac{d\alpha}{dt} = \sum_{i=1}^{n} c_i k_{i0} exp\left(\frac{-E_{ia}}{RT_s}\right)(1-\alpha_i)^{n_i} \quad (21)$$

$$\frac{d\alpha_i}{dt} = k_{i0} exp\left(\frac{-E_{ia}}{RT_s}\right)(1-\alpha_i)^{n_i} \quad (22)$$

Where α is the degree of conversion of the material, k_{io} and E_{ia} are the frequency factors and the activation energy respectively. The initial concentration of each pseudo-component is related through constant c_i. In order to determine all the kinetic parameters an ODE system must be solved in conjunction with a linear regression using numerical techniques.

The TG and DTG results for the three species are shown in Figure 28. In reference to the results obtained, the author indicates good agreement with the results reported in the literature, due to the fact that the main pyrolysis process of the different species of microalgae took place at temperatures between 150 °C and 550 °C.

In this temperature range, that the author defines as the devolatilization stage, NG microalgae produced a higher amount of gases (71.9 wt.%) than samples of SC (64.5 wt.%) and CV (64.6 wt.%), suggesting a correlation with the proximate analysis results. Lopez-Gonzalez et al. (2014) indicates that this stage was characterized by different overlapped steps and generally, these steps were described as the decomposition of lipids, carbohydrates and proteins.

All samples showed a similar weight loss: 11.4, 8.0 and 6.9 wt.% for NG, CV and SC, respectively. However, the author could identify several differences attributed to the distribution of components. In this sense, sample of SC started its decomposition at a lower initial temperature (142°C) than samples NG (160°C) and CV (178°C). Also a shoulder at low decomposition temperature was only observed for samples NG and SC. This behavior can be attributed to the higher content of carbohydrates on samples of NG and SC.

On the other hand, the higher peak in pyrograms is attributed to the protein decomposition. Finally, the amount of char residual was higher for CV and SC (27.4 and 28.4 wt.%/°C, respectively) than for sample NG (16.7 wt.%/°C). Lopez-Gonzalez et al. (2014) attributes this behavior to the higher ash content in the former ones.

Figure 28 – TG and DTG obtained by Lopez-Gonzalez for CV, NG and SC biomasses.

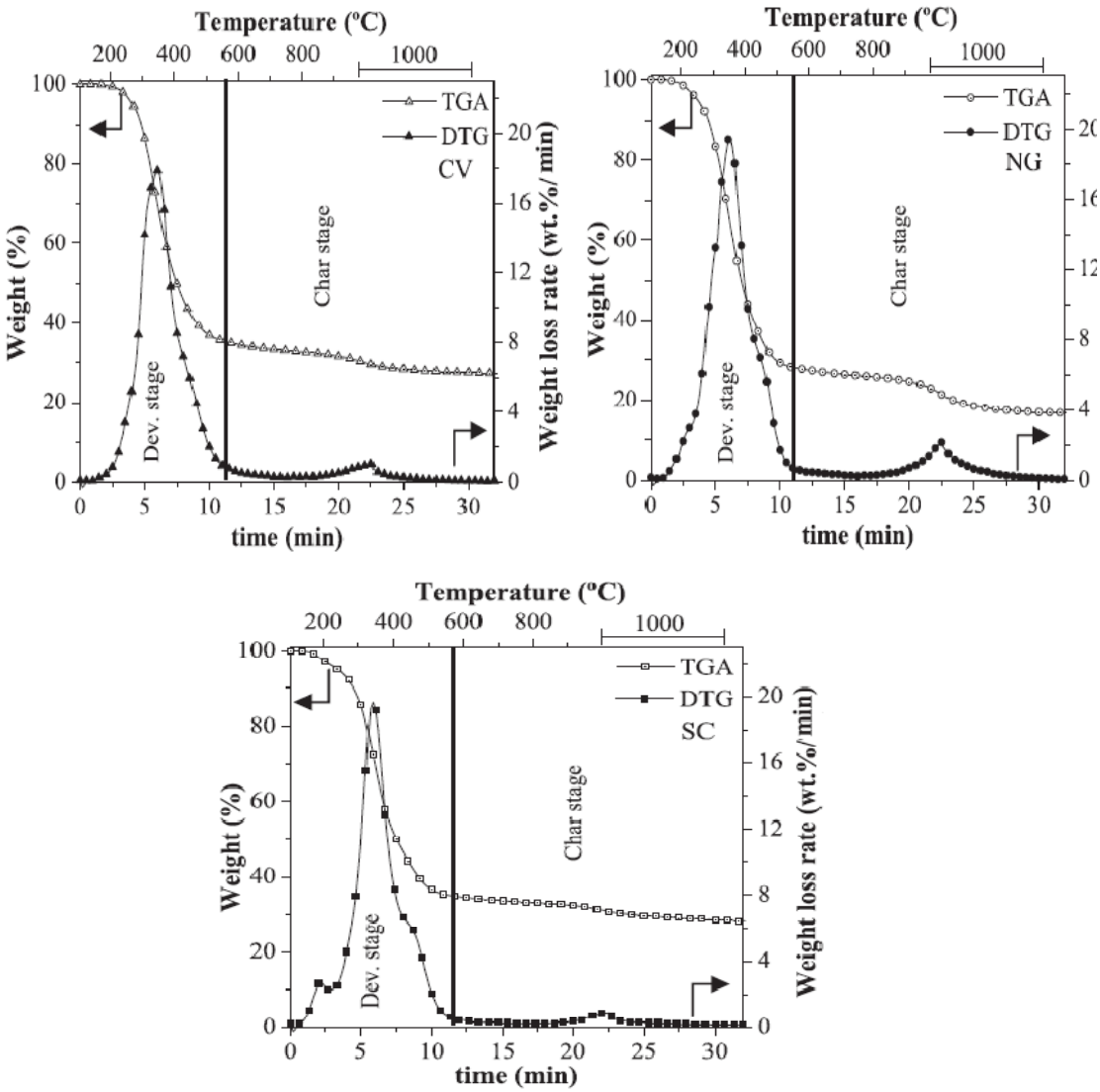

Source: Lopez-Gonzalez et al. (2014).

Figure 29 shows the model results obtained by Lopez-Gonzalez et al. (2014). As it is said by the author a good agreement was obtained. Four reactions were defined for SC and Ng microalgae species, three reactions for the devolatilization stage, and only one for carbonaceous decomposition stage. On the other hand, considering that

CV did not present a low temperature shoulder, only three reactions were defined. Details of the parameters are presented in Table 19.

Table 19 – Kinetic parameters for devolatilization and oxidation processes obtained by Lopez-Gonzalez et al. (2014).

		Devolatilization		Oxidation	
		1st sh	**Peak**	**2nd sh**	**Peak**
Nannochloropsis gaditana	E_A [kJ/mol]	59.8	128.1	32.4	231.1
	A [min^{-1}]	2.60E6	2.70E9	2.80E13	2.60E83
	n	1	1		
Scenedesmus Almeriensis	E_A [kJ/mol]	64.7	79.6	41.3	173.8
	A [min^{-1}]	2.20E5	4.30E51	1.35E34	6.80E63
	n				
Chlorella Vulgaris	E_A [kJ/mol]		63.5	82.5	135.3
	A [min^{-1}]		1.20E5	3.30E53	1.70E52
	n		1		

Sh: Temperature at shoulder.
Source: Lopez-Gonzalez et al. (2014).

Figure 29 – Predictions of kinetic model v/s experimental results.

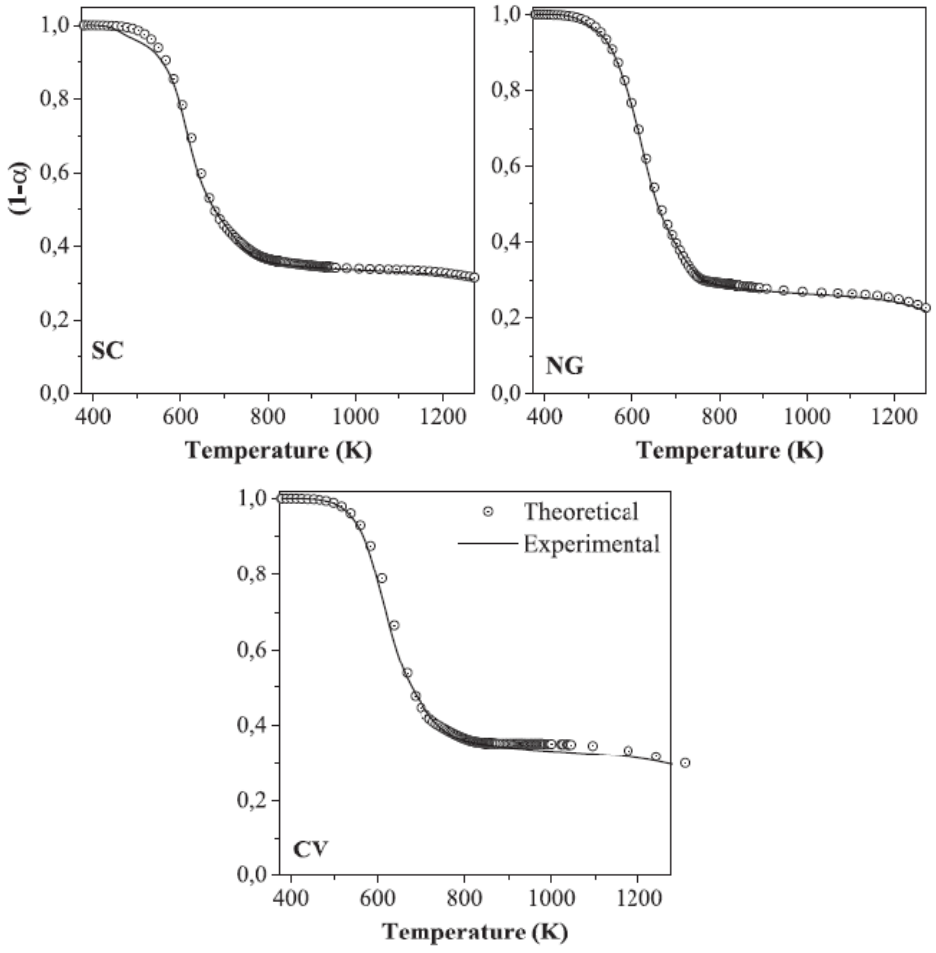

Source: Lopez-Gonzalez et al. (2014).

Analysis made in GC is described by the author. Compounds detected were divided in the following groups: light volatiles (V) as H_2 and H_2O; HC (hydrocarbons) as CH_3, CH_4, C_2H_5, C_4H_6 and C_4H_7; nitrogen compounds (N), mainly released as amines and cyanides (HCN, CH_4N and C_3H_8N; sulfur compounds (S) such as, H_2S, CH_3SH and S_2H_2; alcohols (AL) as CH_2OH and C_2H_5OH; carbon oxides (C-O) as CO and CO_2 ; ketones (K) as C_2H_2O and C_4H_4O; carboxylic acids (CA) such as COOH and CH_2OOH; and AC (aromatic compounds) such as C_4H_4, C_4H_5, C_5H_4, C_5H_5, C_6H_6 and C_7H_8. Also the author mentioned a possible reaction path, consisting in a dehydration followed by the depolymerization of the HC chains of the species carbohydrates. The breakdown of this molecule produced a large variety of low molecular weight products such as carbon monoxide and dioxide, aldehydes, ketones and primary alcohols in the range of temperatures from 150 to 300°C.

Finally for non-condensable gases Lopez-Gonzalez et al. (2014) mentioned a high production of oxygenated gases such as CO, CO_2 and H_2O. Hydrocarbons released in the main devolatilization stage were in three emission peaks at 190, 330, 500°C. Methane (CH_4) peaked at 510°C whereas linear HC (C_2H_5, C_4H_6 and C_4H_7) at lower temperatures possibly linked to the decomposition of lipids. Another important gas, the H_2 started its evolution at temperatures around 384°C, with a wide peak between 384 and 1000 °C. Finally, nitrogen compounds divided in amines and cyanides were found in higher proportions than sulfur ones. The evolution of amines (CH_4N and C_3H_8N) was associated to the decomposition of proteins which took place at temperatures below 400 °C, as mentioned by the Lopez-Gonzalez et al. (2014) in reference to other authors.

Raheem et al. (2017) presented an article about the kinetics developing a reaction based on thermal analysis. TG and DTG data reported by Raheem et al. (2017) shows three separated peaks near 100°C, 250°C and near 300°C attributing the first peak to elimination of moisture and the second and third to the devolatilization of protein and carbohydrates, and at higher temperature to lipids, respectively. Nevertheless the thermograms have shown a shoulder near the second peak that suggests a different overlapped reaction. A reaction mechanism with three separate reactions for the decomposition of three pseudo-components defined by the author was proposed and a fourth for char oxidation. TG and DTG thermal analysis were

performed in order to obtain the kinetic triplet. Effective activation energy was not calculated and an arbitrary reaction model were used to determine the reaction mechanism. Very low activation energies and pre-exponential factors were obtained from 1.1 to 41.0 kJ/mol and 0.003 to 3.9981 1/s respectively. No more parameters for the construction of the reaction mechanism were reported.

Kim et al. (2015) performed a work to develop a reaction mechanism for *Dunaliella Tertiolecta* microalgae considering two parallel reactions for char and volatiles production with an additional reaction for secondary cracking of the volatiles. Free model iso-conversional procedure was applied to calculate the effective activation energy as a function of the extent of reaction α, however, an arbitrary reaction model was used to obtain a compensated pre-exponential factor A. Activation energy found by the author was in the range of 35.25 to 269.68 kJ/mol for a extent reaction α between 0.05 to 0.95 respectively, and no more information about the reaction mechanism was reported.

Sharara et al. (2014) performed a thermal analysis TG and DTG for two types of microalgae species, different from *Chlorella Vulgaris*, in the Arkansas Biological and Agricultural Engineering Research Lab. A fine set of iso-conversional analysis was performed using the Friedman, FWO, KAS and Kissinger methods reporting values for the activation energy ranging roughly from 150 to 550 kJ/mol. Four first order reactions were proposed in order to fit the experimental data and a deconvolution analysis was performed in order to identify the reaction zones. Kinetic triplet was obtained for each reaction with a multistage fitting process. The results reported by the author have shown that the activation energy obtained from the multistage procedure differs significantly with those values obtained from the model free iso-conversional process and no more parameters for the reaction mechanism were reported.

Finally Salmon et al. (2009) performed a semi-theoretical analysis to study the thermal decomposition of *botryococcus braunii* microalgae using the software package ReaxFF for molecular dynamics simulations. A study for a detailed reaction mechanism was performed by the author for aliphatic chain esters and aldehydes components of the microalgae specie. Although a detailed analysis was performed

revealing important insights about the devolatilization process no useful reaction mechanism for CFD application was reported.

As can be seen in this review, most of the works published for thermal decomposition of *Chlorella Vulgaris* reported in the literature, show preliminary data of kinetics, mainly, activation energy. Authors such as Sharara et al. (2014) and Xu et al. (2014) have reported results for the effective activation energy obtained from the iso-conversional method. However, the pre-exponential factors are not estimated in a free-model sense, in order to avoid the compensation effect between the parameters of the kinetic triplet. Only four articles were found with a mechanistic proposition of devolatilization, two for *chorella vulgaris* and other two for different microalgae species. Each article proposed a reaction mechanism scheme. However, no complete dynamic model was reported in order to describe the whole process helpfully for the use in CFD applications. This review indicates that advances in the study of pyrolysis of microalgae biomass are in their first stages. Therefore, additional research and studies must be accomplished in order to obtain a reaction mechanism such as the development conducted through several years for the lignocellulosic biomass. However, a complete and detailed reaction mechanism is impossible to be obtained nowadays, instead, a straightforward approach can be a reasonable starting point. In this sense a step-wise development can be applied to obtain a limited but otherwise useful global reaction mechanism for engineering applications and step-wisely increase the details and complexity in order to improve the accuracy. The present work propose this type of straightforward reaction mechanism developing a complete global and lumped reaction mechanism for the *Chlorella Vulgaris* microalgae ready for its use in CFD package software such as ANSYS Fluent 19.0 or Open Foam, based on thermal analysis of TG and with limited information and data obtained so far.

2.4. EXPERIMENTAL FAST PYROLYSIS OF CHLORELLA VULGARIS IN LABORATORY-SCALE REACTORS

Author Mellin has reported two articles in where reactor for pyrolysis of lignocellulosic biomass has been simulated verifying the experimental results. The author in a first article (Mellin et al., 2013) uses a lumped one-stage global reaction mechanism to

predict the devolatilization of biomass, and in a second paper (MELLIN; KANTARELIS; YANG, 2014), authors used a global multi-stage semi-detailed reaction mechanism in order to obtain a prediction of the volatile distribution. It is clear that for modeling and simulating the thermal decomposition process is mandatory the experimental counterpart in order to verify the results. In the case for microalgae, as mentioned before, no models for fast pyrolysis in reactor simulations have been developed. However, experiments of fast pyrolysis in a reactor environment of *Chlorella Vulgaris* have been performed by several authors and it is presented in the following section.

Belotti et al. (2014) performed fast pyrolysis of *Chlorella Vulgaris* using a quartz tubular reactor with 40mm in diameter and 300 mm length, equipped with a quartz frit on the bottom side and heated by an external electric resistance. An amount of 15 g of biomass was loaded forming a 3 cm layer. Pyrolysis tests were performed at 400, 500, 600 and 700°C. Grierson et al. (2009) has been conducting pyrolysis of Chlorella Vulgaris using an apparatus that consists of an infrared furnace and an arrangement of internals for heating of a packed bed of sample. Heating rate applied was 10°C/min from room temperature until the furnace reached 500°C. Wang et al. (2013) performed the thermal decomposition of *Chlorella Vulgaris* with a lab scale, atmospheric-pressure fluidized bed reactor. The reactor consisted of a steel tube with 0.31 m in length and 38.1 mm in diameter. Solid was 100 g of silica particles with an average diameter of 0.55 mm. A constant reactor temperature of 500°C was applied. Biomass rate was 100 g/h and comprehensive analysis of products was conducted. Yuan; Tahmasebi and Yu (2015) used a vertical fixed-bed tubular quartz reactor with an internal diameter of 2.0 cm heated in an electric furnace. The quartz reactor was designed in a way that the volatile matter could sweep out faster from the reactions zone. About 3 g of biomass was used in each experimental run. The pyrolysis experiments were carried out under isothermal conditions. As has been mentioned in Section 2.3, Gong et al. (2014) carried out experiments on a quartz fixed-bed reactor using an atmospheric flow of N_2 (purity > 99.99 vol%). The inner diameter of the reactor was 40 mm. The outlet of the reactor was only 6 mm, which can minimize the secondary reaction of volatile. The range of temperature investigated were from 300 to 700°C. The author stated that a relatively fast heating rate could be achieved by

pushing the sample crucible into the center of the reaction zone after the temperature had reached the set value.

As can be concluded, not all authors performed their pyrolysis experiments at the same experimental conditions; however the authors, Yuan; Tahmasebi and Yu (2015) and Gong et al. (2014) mentioned that the experiments were performed with high heating rate and with short residence time. Also, it is worth to note that both authors only reported the final yields and the respective temperature however did not reported any variable during the process. As a consequence, no comparison can be made between the results of the simulation proposed in this research and the published articles. However, experimental conditions such as high heating rates and short residence time must be satisfied and a qualitative comparison between final yields of char and volatiles can be performed, such as the decreasing amount of char obtained as the pyrolysis temperature is more severe. Under these circumstances a suitable equipment is the fluidized bed reactor (FB) in which as reported by the author, this type of reactor can reach a heating rate of 1000°C/s and the residence time, in the case of their specific work, can be as low as 2 s. The methodology is presented and described in Mellin; Zhang, Kantarelis and Yang (2013) and Mellin et al. (2014) can be a suitable starting point in order to apply a reaction mechanism coupled with hydrodynamics applying different conditions inside a reactor such as precisely maximum pyrolysis temperature and residence time.

2.5. REACTION MECHANISMS TYPES APLICABLE TO REACTOR MODELLING

Reaction mechanisms developed for pyrolysis can be specific for one species or can be more universal. For example the one-stage parallel mechanism developed by Di Blasi and Branca (2001) (section 2.2) is only for a specific material, however, on the other hand, the mechanism developed by Ranzi et al. (2008) has the objective to be applied for a lignocellulosic biomass with different relative amounts of components, then more universal. Therefore the degree of sophistication is quite important and depends on the application and the availability of information and data.

As seen in the latter section pyrolysis process can be described from the point of view of the mass loss and mass loss rate, where kinetics describes the rate of reaction at which the virgin biomass is devolatilized. The kinetic parameters, frequently of Arrhenius type, are obtained from the experimental TG and DTG runs. As has been described by the authors cited in Section 2.2 and 2.3 a best fitting procedure, linear on non-linear regression (VARHEGYI et al. 1989), is commonly applied in order to determine the frequency factor *A* and the activation energy *E* from dynamic or isothermal TG and DTG analysis. Only one TG curve is necessary to determine a *global reaction mechanism*, being the latter those of black box type, in where all reaction of a certain chemical process are summarizes or condensed in only one whole reaction without parallel or serial reactions. However, it does not give any information about the pyrolysis products and the reproducibility of experimental data can be poor especially for complex materials. Only if the entire volatile phase (tar/liquids + non-condensable gases) is approximated by only one lumped substance, with specific averaged thermodynamic and transport properties, it should be possible to integrate it into a global-lumped reaction mechanism for reactor calculations. Therefore, an advantage of this type of model is the minimum of experimental data required, and a drawback is the inability to describe in detail the volatile phase and the inaccuracy for complex materials and competitions.

Other type of reaction mechanism is the *semi-global* type in where a description of a certain chemical process provides more details than the global scheme and in where, however, the set of reaction are not necessarily elementary reactions (HURT; CALO, 2001). Other characteristic about semi-global mechanism is that it can provide a competitive sense as the products can be predicted independently by different set of kinetic parameters evolving in parallel competing for the reactant. An example of this type of reaction mechanism is the model developed by Diebold (1994) that is more suitable when studying a reactor. Parallel-independently reaction mechanisms are commonly encountered for lignocellulosic biomass, in where the superimposed principle (MILLER; BELLAN, 1996) is assumed and that considers that each of pseudo-components (reactants) react independently and in parallel of each other components without cross effects. Since the pseudo-components can react in different temperature ranges is possible to find in the literature this type of mechanism named as *multi-stage* or *multi-step reaction mechanisms*. Considering

the definition presented here a multi-stage reaction mechanism can be composed by global or semi-global sub-mechanisms. In the case of lignocellulosic biomass parallel reactions are defined for cellulose, hemicelluloses and lignin, in where, for example the semi-global reaction mechanism of Diebold (1984) can be used for cellulose. Despite that the semi-global reaction mechanisms provide more details than the global ones a straight forward approach forces the treatment of the products as a lumped products.

For lignocellulosic biomass as in the case of the model of Diebold (1984) or Shafizadeh-Chin (1977), three pseudo-products are defined i.e char, tar and non-condensable gases. As described in Chapter 2 by Di Blasi and Branca (2001) isothermal conditions gives a set of ODE to determine the kinetic parameters necessary for mechanism construction. In the case when the experiments take place with varying temperature is suggested by Font et al. (1990) that other expressions are available in order to determine the rate equations for pseudo-products. With the objectives to obtain the rate equations, the mass loss rate data is necessary in conjunction with the final yields of the lumped pseudo-products, either, char and total volatiles; char, tar (liquids) and non-condensable gases. Due to the sample size, final fractions of pseudo-products frequently are obtained from a lab-scale reactor rather than with TG equipment. As a consequence of mass conservation, knowing the initial mass of virgin material, mass loss is determined by a linear relation of the three pseudo-products. The model obtained can predict the mass loss and pseudo-products rates, and furthermore, if the final yield of pseudo-products is known as function of process temperature, then a model with variable product distribution as a function of temperature is available (DI BLASI, 2008). Therefore, a more suitable description is obtained with a parallel *semi-global, parallel and lumped reaction mechanism* in order to simulate a reactor behavior.

The detailed or semi-detailed reaction mechanisms are models with parallel and serial reactions with competitive characteristics are further suitable than global semi-global reaction models. However, this type of model needs more information in order to construct the scheme. Not only kinetic parameters must be obtained, but also, additional information about, the structure, functional groups and reaction pathways. The detailed or semi-detailed reaction mechanisms are more sophisticated. These

reaction mechanism is based on theoretical knowledge (possible reaction paths according to structure and functional groups) and on experimental observations (TG and DTG in addition to substance identification using CG-MS-FTIR or other procedures including those for structural analysis i.e X-ray for crystals, Ramman spectroscopy (XIN et al., 2015). Commonly, this type of mechanism has one sub-mechanism for each component of complex materials. Each mechanism can have two or three stages with competitive and serial reactions, and can include secondary heterogeneous reactions for intermediaries species in order to predict additional char formation or lighter gases (non-condensable). The competitive characteristic again gives the possibility to apply the mechanism over a wide range of temperature. The detailed or semi-detailed reaction mechanisms can predict the devolatilization of large species and the subsequent decomposition to species with lower molecular weight, therefore, this type of mechanism can predict liquid and gas compositions.

The sophistication of this type of model has been increased in the last years. Nowadays, a frequently used reaction mechanism for the decomposition of general lignocellulosic biomass was proposed by Ranzi et al. (2008) that was used by Mellin et al. (2014). The model is a semi-detailed mechanism based on the Broido-Shafizadeh (BRADBURY; SAKAI AND SHAFIZADEH, 1979) reaction scheme. Although this reaction scheme, proposed by Bradbury; Sakai and Shafizadeh (1979) in 1979, was only for cellulose, the structure has been extended in order to describe hemicelluloses and lignin thermal decomposition. Similar to the model developed by Diebold (1994), some of the parameters used by Ranzi et al. (2008) were obtained from other authors and also a series of experimental observation about the structure and pathways are included in order to improve the model predictions. Also, Ranzi et al. (2008) has mentioned the incorporation of the results from semi-detailed and detailed kinetic models developed by Marongiu et al. (2007a) and Marongiu et al. (2007b), respectively. Finally, the application of this type of reaction mechanism is virtually direct in CFD, and it is not unusual to use other kinetic software package, such as Chemkin or CANTERA to solve the chemical evolution. Several mechanisms of this type are identified in the literature with different configurations and levels of detail (BANYASZ et al, 2001), (LIN; ZHU; TAVLARIDES, 2009), (TEGELAAR; DE LEEUW; HOLLOWAY, 1989), (VARHEGYI et al, 1997), (LIAO; WANG; MA, 2004), (WANG et al., 2011) and (RANZI et al., 2008).

The aforementioned has the objective to show the different alternatives related to the pyrolysis of complex material such as lignocellulosic biomass. This brief description about the kinetic modeling of lignocellulosic has the following objectives for this research: to understand how detailed the microalgae reaction mechanism model can be, considering the current knowledge about the thermal decomposition of microalgae and considering the methodologies developed and the knowledge accumulated so far for the similar material, the lignocellulosic biomass, that can serve as a guide lines to study new materials such as microalgae biomass. One of the most commonly used methodologies in determining a reaction mechanism for complex material, is a combination of the theoretical assumption and hypothesis about the devolatilization process in conjunction with experimental results.

In this section a search was conducted in order to identify mathematical models for chemistry, the reaction mechanisms, were found for lignocellulosic biomass, and for bio-polymers such as cellulose suitable for CFD simulation. However, CFD applications neither for *Chlorella Vulgaris* nor for other microalgae were found. The reason is due to the lack of reactions mechanisms that describe the thermal decomposition process and the prediction of volatiles for this type of material. Nonetheless, as has been commented in Section 2.3 several authors have obtained the Arrhenius kinetics parameters for the mass loss rate, assuming an arbitrary reaction model, and also in some cases such as the work of Gong et al. (2014) identifying only one kinetic triplet for the entire devolatilization process. Therefore the information and data surveyed in the literature are very limited and can only be used, at least, in models with only one lumped gaseous substance, from which there is no information about its physical properties and therefore it seems unsuitable to develop a reactor simulation with CFD.

2.6. ONE AND TWO DIMENSION MODEL EXAMPLES FOR GRANULAR PHASES APPLIED FOR A FLUIDIZED REACTORS

Multiphase flow modeling has been applied for pyrolysis of lignocellulosic biomass for example by Mellin et al. (2014), Mellin; Zhang, Kantarelis and Yang (2013), Xiong et al. (2014), Xue; Heindel and Fox (2011), and Yu et al. (2014). As an introduction in

the current section a formulation of the transport equations for multiphase flows is introduced and presented for a one dimension problem.

Gidaspow (1994) developed and simulated a multiphase flow model in order to study the axial distribution of solids in a circulating fluidized riser, which consists of a straight tube with an inlet of gas and particles. Particles are entrained by the gas and then the mixture leaves the unit at the top. Transport equation for mass and momentum are the basic equations in modeling and is used in this cold flow reactor type analysis.

Equations 23 to 26 are the averaged transport field equations for both phases (particles and gas). The first and third equations, eq.(23) and eq.(25), are the mass conservation balances for the gas and solid (dispersed phase) phase respectively. These equations do not have a source term related to mass e chemical reactions are not considered.

$$\frac{\partial(\rho\varepsilon)_g}{\partial t}+\frac{\partial(\rho\varepsilon v)_g}{\partial x}=0 \tag{23}$$

$$\frac{\partial(\rho\varepsilon v)_g}{\partial t}+\frac{\partial(\rho\varepsilon vv)_g}{\partial x}=-\frac{\partial P}{\partial x}+K_{gs}\left(v_s-v_g\right)+\frac{2f(\rho\varepsilon v)_g v_g^2}{D}+\rho_g\vec{g} \tag{24}$$

$$\frac{\partial(\rho\varepsilon)_{\mathrm{s}}}{\partial \mathrm{t}}+\frac{\partial(\rho\varepsilon v)_{\mathrm{s}}}{\partial \mathrm{x}}=0 \tag{25}$$

$$\frac{\partial(\rho\varepsilon v)_s}{\partial t}+\frac{\partial(\rho\varepsilon vv)_s}{\partial x}=K_{gs}\left(v_s-v_g\right)-G\frac{\partial\varepsilon_s}{\partial x}+\frac{2f_s(\rho\varepsilon v)_s v_s^2}{D}+\left(\rho_s-\rho_g\right)g \tag{26}$$

Equations 24 and 26 are the averaged momentum conservation equations, for the gas and solid phase respectively. On the right side of the gas momentum equation, the first term is the pressure gradient, the second term the rate of momentum dissipation due to relative velocity between the phases. Term K_{gs} represents the friction coefficient obtained from the Ergun, Wen and Yu referenced by (GIDASPOW, 1994). Third term in eq.(24) is the momentum loss due to the wall friction factor based on Fanning's or modified Hagen-Poiseuille f term (GIDASPOW, 1994).

In the averaged momentum conservation equation for the solid phase pressure derivative respect the volume fraction ε_s is expressed by the modulus of elasticity G that accounts for the solid-solid collisions (JAKOBSEN, 2008). An empirical expression was obtained by Rietma and Mutsers (GIDASPOW, 1994) in fluidized bed experiments in order to obtain the powder modulus for cracking catalysts, glass beads and polypropylene. Finally the friction factor f_s related to the wall momentum losses in eq.(26) is obtained by the expression of Konno (GIDASPOW, 1994).

The model developed by Gidaspow (1994), consisted in the description of hydrodynamics of two phases, solid and gaseous inside the riser, however, without chemical reactions. Taking a further step towards the modeling and simulation of the pyrolysis process Trendewicz et al. (2015) performed a study about the pyrolysis of lignocellulosic biomass inside a circulating fluidized bed reactor using a one dimensional model. The author used the same model as Gidaspow (1994) with minor changes, nonetheless, the same constitutive equations, but considering an additional phase composed by biomass particles. Due to an additional phase and the inclusion of chemical reactions, additional source terms were added. Furthermore, three energy conservation equations were defined for each phase, with the corresponding source terms for the gas and biomass phases to account for the chemical reactions and with a model based on the Nusselt number for the heat transfer.

Since there are no simulations to be taken as starting point for microalgae pyrolysis and in order to achieve a good agreement between experimental and simulated data, flexibility is necessary. This flexibility can be reached by using other constitutive relations that can be obtained from the literature. For example, from Syamlal et al. (1993) for drag modeling. Furthermore, model customization can allow better fit by means of the model parameter adjustment. These alternatives can be useful for the pyrolysis simulation of microalgae. For example, the model developed and used by Trendewicz et al. (2015) is based on a particle diameter of 500 μm for biomass and sand, and on the other hand, for microalgae biomass the maximum particle diameter studied by Gong et al. (2013) was 150 μm. Therefore, starting from the setup of other works, the sub-models can be changed or adjusted according to the microalgae parameters.

In the context of pyrolysis of lignocellulosic biomass another good example of a comprehensive model describing the behavior inside a CFB reactor for fast pyrolysis are described in Mellin et al. (2014) and in Mellin; Zhang, Kantarelis and Yang (2013). In these works conservation equations and constitutive relations for multiphase flow were solved in conjunction with a semi-detailed and a simple chemical kinetic schemes for a two-dimensional reactor domain.

The Euler–Euler multiphase flow framework with three phases is applied in the computation; one gas phase and two granular phases: sand and biomass. No drying process was included in the description. Reaction mechanism used was the scheme developed by Ranzi et al. (2008) and no turbulence was accounted for since the author assumed a laminar flow. Mass for each phases and species conservation equations was defined, considering a source from chemical reactions for the gaseous and biomass solid phases. Convective heat transfer was modeled based on the *Ranz-Marshall* and Nusselt number and different convective transfer coefficients were calculated. Mechanical energy is accounted for and a source term for heat of reaction was added. For the momentum equation different constitutive relations were applied for drag between sand-gas, sand-biomass and gas-biomass interactions.

This chapter has presented examples of reaction mechanisms applied to the pyrolysis of lignocellulosic biomass showing the way to determine the kinetic energy parameters of: the activation E and the pre-exponential factor A, in addition to the third element the reaction model. The complexity achieved by the Diebold model (1994) is the product of extensive research that has included the characterization and study of the products of pyrolysis collected from several authors. However, it has also been shown that with the results of TG and DTG it is possible to construct useful reaction mechanisms to describe the devolatilization process.

In the second part of the chapter, results of the thermal analysis applied to the Chlorella Vulgaris species have been shown verifying that mainly only the activation energy E of the devolatilization process has been determined in both inert and oxidative environments. Works were also reviewed where the set of the three important kinetic parameters E, A and the reaction model have been determined, however, only partially and without an associated reaction equation which is the

minimum information necessary in conjunction with hydrodynamics to be applied in reactor modeling. An additional set of articles were found where fast pyrolysis experiments have been carried out in laboratory-scale reactors for Chlorella Vulgaris. In these articles the total conversion of the biomass in conjunction with the partial determination of the products of pyrolysis has been evaluated, showing the large amount of condensable gases that can be produced. This information turns out to be relevant to extend, in the future, the preliminary reaction mechanism of devolatilization of Chlorella vulgaris, a global reaction mechanism, towards a semi-global one that can includes the production of condensable and non-condensable gases as well as incorporating competitive and parallels processes between the gases and the formation of char.

Finally in the final part some aspects of the modeling of the hydrodynamics in pyrolysis reactors have been mentioned, and in where the possibility of describing a phase composed of particles from a continuous description, including chemical reactions, starting from the fundamental conservation equations is highlighted. In the next two chapters will be introduced the procedures and methodologies in order to obtain the kinetic parameters for the reaction mechanism in addition to the methodology to associate a reaction equation. Regarding hydrodynamics, the formulation of the multiphase flow theory and associated sub-models to describe the rheology of the granular phase will be introduced in detail; finalizing with the description of the application of both the reaction mechanism and the conservation equations in the numerical solver software ANSYS Fluent 19.0.

3. THEORETICAL FRAMEWORK

This chapter presents and describes the characteristic aspects about microalgae biomass and the theory behind the development of reaction mechanisms and multiphase flow dynamics and its application in CFD. The chapter starts with the description of the microalgae components and its properties including references with current research about microalgae pyrolysis. The second part presents the methods used in order to obtain reaction mechanisms schemes starting from thermal analysis data TG and DTG. Finally, basis of the multi-phase flow dynamics theory is presented specifying a point of view about the continua and the development of the basic conservation equation of mass, momentum and energy. In addition, in the final part of the chapter other aspect are outlined related in general with fluid flows dynamics such as the finite volume (FV) method for numerical solution.

3.1. STRUCTURE OF CHLORELLA VULGARIS AND ITS COMPONENTS

From the revision of the literature performed in sections from Chapter 2 it can be concluded that the thermal decomposition of *Chlorella Vulgaris* can be described as a function of its biological components in the same way as for lignocellulosic biomass. This conclusion is obtained from the works of De Filippis et al. (2014), Gong et al. (2013) and Kebelmann et al. (2013). The first two authors has been identified in pyrograms the existence of more than one reaction that evolve simultaneously during the process, attributing this to the thermal decomposition of pseudo-components.

On the other hand, Kebelmann et al. (2013) has presented more reliable evidence. Kebelmann et al. (2013) has extracted the lipid and protein fractions in order to perform the thermal analysis in separated manner. The pyrograms showed that the isolated thermal profiles for the lipids and the proteins started to decompose at near the same temperature as the thermal decomposition of virgin microalgae. These facts suggest that is necessary to analyze with more detail the specific types of components and sub-components. The latter in order to elucidate the starting point in which the information and data about microalgae can allow the construction of the reaction mechanism and the determination of the kinetic parameters.

3.1.1 CARBOHYDRATES

Chlorella Vulgaris is a green algae that growths in fresh water, belongs to the phyliumchlorophyta, has a spherical shape and has cell size about 2-10 μm. This type of microorganism is very versatile, for example, if the microalgae are stressed with a nitrogen depletion, the microorganisms respond with an increment in the lipid content due to this external effect that forces them to transform proteins or peptides to lipids and carbohydrates. The same is reported by Choix; De-Bashan and Bashan (2002) that conclude that there is an increase in storage of starch at cell wall due to an autotrophic condition caused by the treatment with the *Azospirillumbrasilense* bacteria. The latter indicates that even for the same species of microalgae the relative amount of components can change as a function of the medium condition. For example in a study conducted by Park et al. (2014), orange peel was used as nutrient component for *Chlorella Vulgaris* resulting in a significant increase in the fatty acids content. Ho et al, (2013) comments that under nitrogen starvation microalgae can store energy in cell walls and plastids in the form of cellulose and starch. However, Nemcova and Kalina (2000) reported that microalgae without stress has a cell wall rich in monosaccharide and glucosamine (2-Amino-2-Deoxy-D-Glucopyranose) shown in Figure 30. The same author comments that other sub-species can content mannose and glucose as the main constituents of their rigid cell wall.

Takeda (1988a) and Takeda (1988b) found that major components of carbohydrates of a certain *Chlorella Vulgaris* strain are galactose, glucose (Figure 31), mannose (Figure 32), and glucosamine. The author performs a study, in two different papers in order to classify the different strains of *Chlorella Vulgaris* based on the carbohydrate contents in the cell wall. Results of two works showed that *Chlorella Vulgaris* has a rigid cell wall composed by hemicellulose with high content of glucosamine. It is worth noting that Takeda (1988a) cited in his work that Iriki found that the cell wall of green algae is composed by mannan or xylan (Figure 34). The latter species is an aldopentose, a carbohydrate that forms a pyranose ring, different than glucose, mannose and galactose that are aldohexoses. The latter four molecules are enantiomers and are composed by 6 carbon atoms rather than 5 carbon atoms for other carbohydrate like the xylose (Figure 35). Xylan and xylose are similar; however, xylan has an additional oxygen atom. Therefore, xylan is a xylose molecule in which a hydrogen atom has been substituted by a hydroxyl group and the orientation of the substitutes groups are

changed. The latter is a key factor because in substitutions process the resulting molecule can inherit some properties from the original base molecule (CAREY, 2006). Another author, Blumreisinger; Meindl and Loos (1983) performed an analysis about the carbohydrates content for various microalgae microorganism including *Chlorella Vulgaris*. The author concluded and reported high amounts of glucosamine rhamnose, arabinose, xylan and galactose.

Figure 30 – Glucosamine (2-Amino-2-Deoxy-D-Glucopyranose).

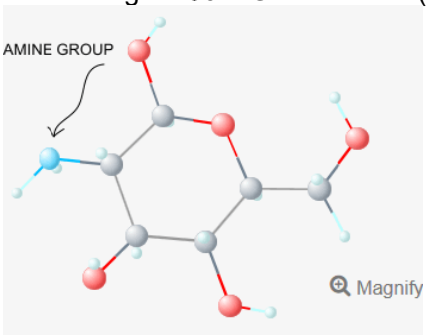

Figure 31 – Glucose C5H10O5 (D-Glucopyranose).

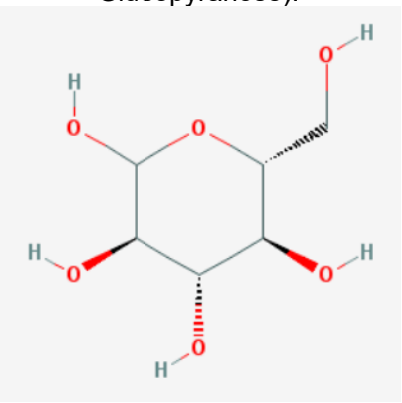

Figure 32 – Mannose C6H12O6 (D-Mannopyranose).

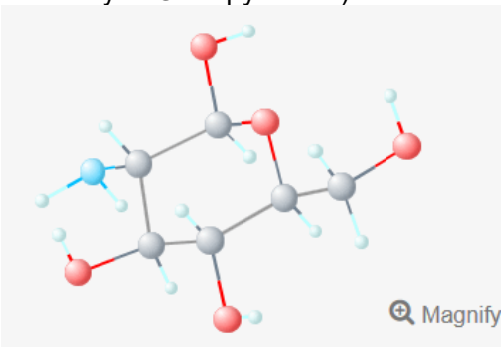

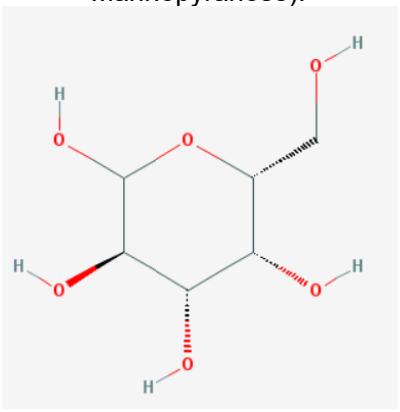

Source: http://pubchem.ncbi.nlm.nih.gov.

As can be seen in the latter paragraph there are some similarities between lignocellulosic and microalgae biomass. One similarity is the cell wall composition. Cellulose (in lignocellulosic biomass) is composed by unit of glucose residues, a molecule similar to glucosamine. Species in Figures 33 and 34 are very similar, however the spatial arrangement of its atoms is very different. These molecules are chiral structures and belong to the group of the pyranose rings (CAREY, 2006). On the other hand, glucosamine that has the formal name of IUPAC 2-Amino-2-Deoxy-D-Glucopyranose, receives this name because the skeleton of the molecule is the

glucose, and the unique difference is that have an amino group substituted in the second carbon.

Figure 33 – Xylose $C_5H_{10}O_5$ (D-xylopyranose).

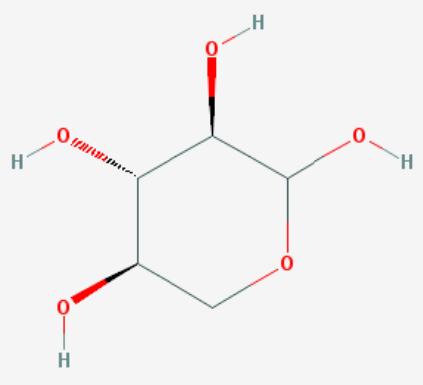

Figure 34 – Xylan $C_5H_{10}O_6$.

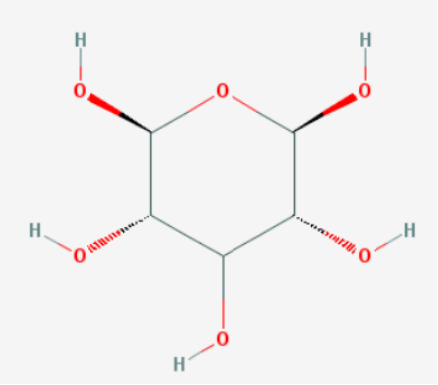

Source: http://pubchem.ncbi.nlm.nih.gov.

3.1.2 PROTEINS

The protein content of *Chlorella Vulgaris* is significant. A mean value over all works revised, (Table 20) shows that the protein content is about 57% (%wt. free of moisture and ashes), although this value can vary largely. Also, as can be seen in Chapter 2 proteins are decomposed at relatively low temperatures, before the other two components. Proteins are very complex molecules and very important for animals and humans, and may be involved in almost all biological activities (CAREY, 2006). Proteins are constituted by polypeptides, which are formed by amino-acid units (Figure 35), and further, the amino-acid molecule is constituted by one amide group and by one carboxylic acid function (CAREY, 2006). Large groups of amino acids linked form a chain. One or several chains can form protein that can be very large and with a complex structure (Moldoveanu, 1998).

One characteristic of amino groups is that contains a nitrogen atom and because of this is that the authors cited in Chapter 2 have attribute the nitrogenous compounds produced during pyrolysis to the proteins. Since *Chlorella Vulgaris* is a microalgae used for food industries, its characterization has been done in order to identify its specific content of proteins and amino-acids. For example Ursu et al. (2014) has reported 19 different amino-acids for *Chlorella Vulgaris* that compose 8 different proteins: P7, P12, UFPe7, UFRe7, UFPe12, UFRe12, Na-CN and SPI.

Table 20 – Averaged content of components in *Chlorella Vulgaris*. (%wt. free of dry and ashes, extracted microalgae is not included).

	Lipids	Carbohydrates	Proteins
Belotti[e]	16.99	35.15	47.84
De Filippis[a]	16.20	38.20	45.60
Du[g]	13.34	32.20	54.44
Gong[b]	20.52	17.36	62.10
Kebelmann[c]	19.49	11.44	69.05
Lopez-Gonzalez[d]	16.07	14.76	69.16
Wang[f]	20.04	26.85	53.10
Mean	**17.52**	**25.14**	**57.33**
σ	**2.61**	**10.64**	**9.61**

[a]De Filippis et al. (2015), [b]Gong et al.(2013), [c]Kebelmann et al.(2013), [d]Lopez-Gonzalez et al. (2014), [e]Belotti et al.(2014), [f]Wang et al. (2013), [g]Du et al. (2013)

Figure 35 – Dipeptide, formed by two peptides.

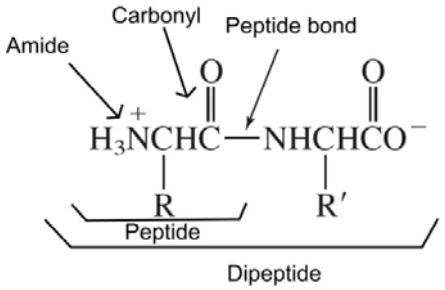

Source: Carey (2016).

3.1.3 LIPIDS

Two of the three components of microalgae, such as the lignocellulosic biomass, are complex organic co-polymers. However, lipids can be polymers or simple straight molecules (MOLDOVEANU, 1998).

As can be seen in table 20, lipids are the minor component present in *Chlorella Vulgaris*. In the BR scheme, lipids can be extracted in a previous step; therefore, the amount of lipids for pyrolysis would probably not be significant. However, in order to develop a more universal mechanism for *Chlorella Vulgaris*, lipids must be considered. There are not many reports about the sub-components of lipids. Although, Chia et al. (2013) has reported directly lipids, the identification was only for a group, not for a specific unit. The author reported a high content of AMPL (acetone mobile polar lipids, a class of lipids), that can include chlorophyll, glycolipid and monoacyglycerol. When lipids extraction is performed, the product obtained are fatty acids, therefore, frequently, the lipid content is informed by the fatty acids distribution, such as is reported by Gong et al, (2014) Choi et al. (2014) Park (2014) and Kebelmann et al. (2013).

Information about lipid content of *Chlorella Vulgaris* can be obtained from work of (GONG et al., 2013) who reported the presence of palmitic, linolenic, myristic, and linoleic acids. Kebelmann et al. (2013) found the following distribution of fatty acids: α-linolenic (33.4%), palmitic (27.9%), oleic (21.1%) and linoleic (10.0%). Also Choi et al. (2014) that reported the following fatty acids: myristic, palmitic, palmitoleic, stearic, oleic, lonoleic, lonilenic acids, however those with the higher concentration were: palmitic (22.6%), linoleic (19.4%) and Oleic (18.0%) acids. Finally, Park (2014) that used OPE as (Orange Peel Extract) a nutrient reports the following concentrations: linoleic (34%), palmitic (18%), oleic (13%) and palmitoleic (10%) acids. And for microalgae without OPE nutrient, higher concentrations were: linoleic (40%) and palmitic (33%) acids. Figures 36, 37, 38 and 39 show the Lewis structures for linoleic, oleic, linonlenic and palmitic fatty acids.

Figure 36 –Linoleic acid, $C_{18}H_{32}O_2$.

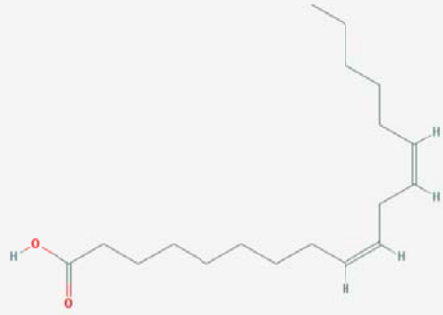

Figure 37 – Oleic acid, $C_{18}H_{34}O_2$.

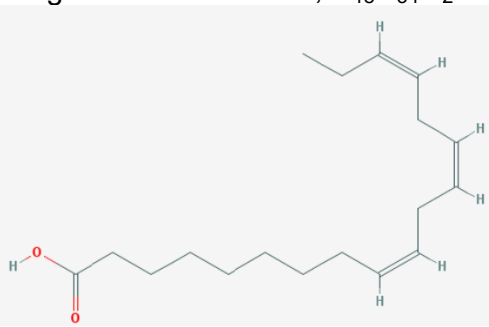

Figure 38 – Linolenic acid, $C_{16}H_{32}O_2$.

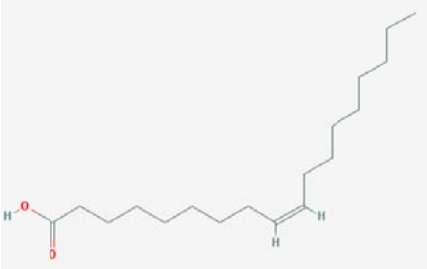

Figure 39 – Palmitic acid, $C_{16}H_{32}O_2$.

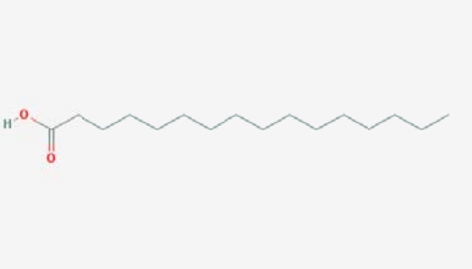

Source: http://pubchem.ncbi.nlm.nih.gov.

3.2 ORGANIC CHEMISTRY AND ANALITICAL PYROLYSIS RELATED TO CHLORELLA VULGARIS COMPONENTS

The examination of the literature about analytical pyrolysis shows that the thermal decomposition mechanisms of materials can be very complex. For the case of such as materials there are many reactions involved in the reduction of large molecules.

However the mechanisms of pyrolysis developed and used in the literature, for engineering purposes, do not contain this level of detail. And even in this way these mechanisms has demonstrated be suitable for CFD simulations, achieving a good agreement with experimental data. For example Moldoveanu (1998) has developed a comprehensive mechanism for cellulose thermal decomposition with several compounds, on the other hand, Couci (2007) developed a semi-detailed mechanism for cellulose, hemicellulose and lignin for woody materials with 60 species and 400 reactions, however, only few lumped substances and reactions are used in practice in the mechanism developed by other author Ranzi et al. (2008).

3.2.1 CARBOHYDRATES

Pyrolysis of carbohydrates is frequently related to the pyrolysis of cellulose. A generous number of scientific articles can be found specifically for pyrolysis of cellulose. As mentioned in section 2.2 almost all mechanisms have been developed for cellulose and then adapted for other complex substances such as hemicellulose or lignin.

Moldoveanu (1998) presented and described the main reaction mechanism for decomposition of carbohydrates, although, in general the mechanism is for a more general group, the polymers. The author has mentioned that thermal decomposition starts with reactions in condensed phase, in which the mechanism for primary decomposition can consist in: β elimination, with E_1, E_2 and E_i reaction mechanisms.

One of the specific mechanisms is the side group elimination. This type of mechanism includes the dehydration, mentioned also by Ranzi et al. (2008), as the predominant reaction at low temperature in cellulose pyrolysis. Other mechanism is the combined reaction, in which a radical produced by side group reaction or by a chain scission interact with another part of the macromolecule. This type of reaction can lead to char formation (MOLDOVEANU, 1998).

Other type of reaction is depolymerization. One of them is the polymeric chain scissions through transglycosidation in which an ether bond breaks producing oligomers or monomers. Other type is polymeric chain scissions by radicals. This type is a chain reaction mechanism that begins with a random scission on a weaker bond

(Moldoveanu, 1998). In 3.1 has mentioned that xylan (Figure 40) and other sugars are present in the cell wall of *Chlorella Vulgaris*, and these substances are a component of hemicellulose. Shen, Gu and Bridgwater (2010) performed a study about the thermal decomposition of xylan. The raw material used was O-acetyl-4-O-methylglucorono-xylan. DTG chart is shown in Figure 41. The important result obtained from this work is that although the analysis shows two peaks for the xylan material, the temperature range of the decomposition is the expected for lignocellulosic hemicellulose.

Figure 40 – O-acetyl-4-O-methylglucorono-xylan specie.

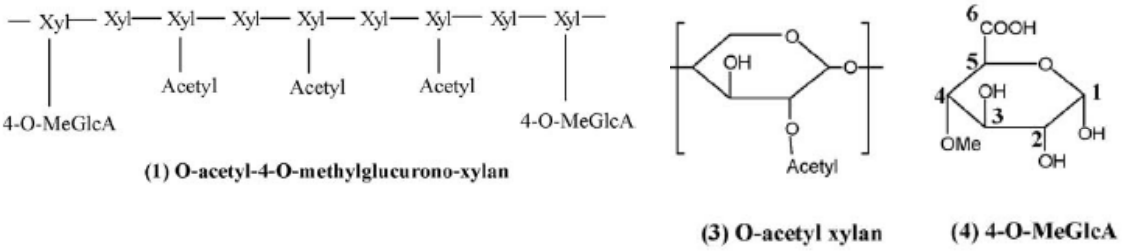

Source: Shen, Gu and Bridgwater (2010).

Figure 41 - DTG analysis, obtained by Shen, Gu and Bridgwater (2010) using O-acetyl-4-O-methylglucorono-xylan.

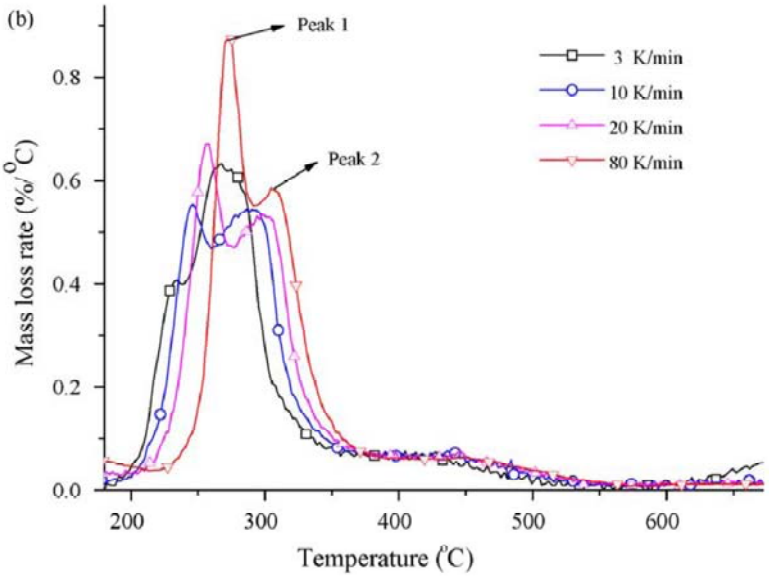

Source: Shen, Gu and Bridgwater (2010).

3.2.2 PROTEINS

Moldoveanu (1998) mentioned that the amino-acid pyrolysis is relevant for protein pyrolysis because certain compounds in the pyrolysate are the same when the substance to be pyrolyzed is a specific amino acid. Therefore, it is suggested that the

pyrolysis products from proteins can be conserved if the pyrolysis severity is not high. This argument is in line with the mentioned by Carey (2006), who commented that the delocalized electrons pairs of the nitrogen in the amide functional group diminish the positivity of the carbonyl carbon, reducing the reactivity to nucleophilic attacks.

Moldoveanu (1998) described a common reaction involving peptides (a cluster of amino-acids linked) (Figure 42). The main mechanisms are the decarboxylation by CO_2 elimination, or water elimination with the formation of a dipeptide anddiketopiperazines DKPs. By Strecker degradation, amino acids may also be converted to aldehydes.

Figure 42 – Reaction scheme for thermal decomposition of a simple peptide.

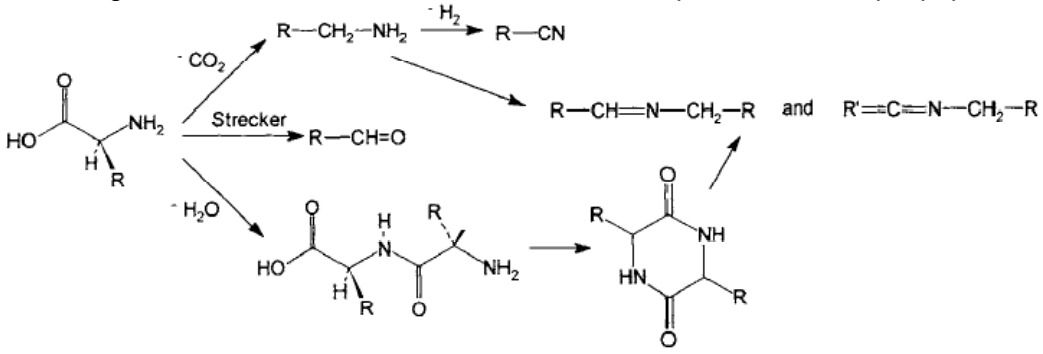

Source: Moldoveanu (1988).

The same author mentioned that R-H type compounds may be generated, and this is a characteristic mainly for the aromatic amino acids. Smaller molecules, some unsaturated, are also formed by further decompositions. The compounds of the type R-CH=N-CH_2-R and R'=C=N-CH_2-R are formed mainly from aliphatic amino acids (Ala, Val, Leu, lie) (MOLDOVEANU, 1998).

One type of compound generated by pyrolysis of simple peptides consists of small molecules similar to those obtained from the pyrolysis of component amino acids such as hydrocarbons (aromatic hydrocarbons from peptides containing Phe or Tyr), aldehydes, pyrrole, pyrroline, indole (from peptides containing TRP) and some aliphatic amines (MOLDOVEANU, 1998). The same substances, pyrrole, indole and aliphatic amines, were reported in section 2.4 for *Chlorella Vulgaris* pyrolysis.

As mentioned above another type of pyrolysis products for peptides includes the DKPs (Figure 44) and their secondary fragmentation products. The formation of DKPs from

oligopeptides showed that its generation always takes place from neighboring amino acids. The mechanism is showed in Figure 43.

Figure 43 – Diketopiperazine (DKP) formation.

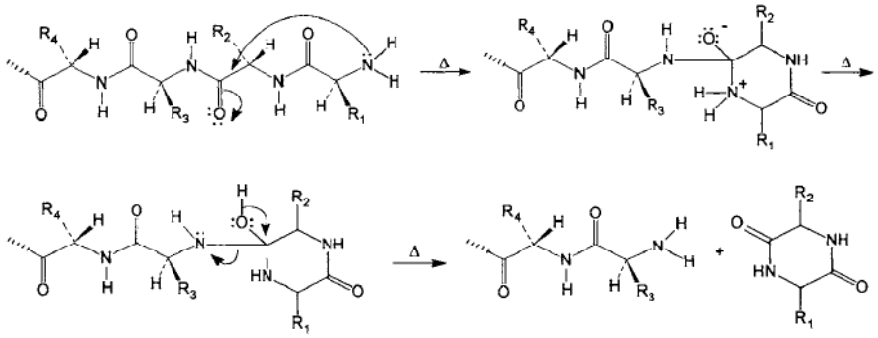

Source: Moldoveanu (1988).

For dipeptides the eliminated molecule is water, for tripeptides it is an amino acid, from tetrapeptides a dipeptide, and so on. The author mentioned that the pyrolysis conditions were found to influence the amount of DKPs. Milder pyrolytic conditions i.e. pyrolysis with moderated temperatures, favored more DKPs formation, while higher temperatures of pyrolysis generated more small molecules, as expected (MOLDOVEANU, 1998) .

Figure 44 – Diketopiperazine $C_4H_6N_2O_2$ a heteromolecule.

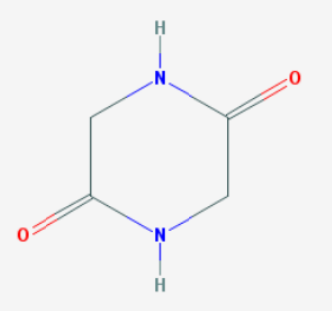

Source: http://pubchem.ncbi.nlm.nih.gov).

Moldoveanu (1998) commented that DKPs can be present in the pyrolysis liquids. However, Kebelmann et al. (2013) performed a study characterizing the pyrolysis products of lipids and protein extracted from *Chlorella Vulgaris* and did not report DKP's.

As can be seen in Table 21 several types of compounds were detected by Kebelmann (2013), however, there are no DKPs, possibly due to that Kebelmann et al. (2013) performed its pyrolysis experiments at 500°C a more severe pyrolysis condition. There

are 8 compounds with an aromatic groups, and two of them have a concentration of more than 6% i.e. 1H-indole and toluene (Figures 45 and 46), however one of them has a nitrogen atom possibly derived from the proteins structure.

Table 21 – Derived compound from protein of *Chlorella Vulgaris* obtained by Kebelmann et al. (2013).

Type	Compound	%	Nitrogen
Chain	1-Hexadecene	7.21	
Aromatic	1H-Indole	6.60	Yes
Aromatic	Toluene	6.24	
Alcohol	Trans-Phytoland Isomers	4.27	
Aromatic	2-Propenoic acid, 3-(4-methoxyphenyl)-, 2-ethylhexyl ester	3.34	
Aromatic	Phenol	3.03	
Aromatic	Phenol, 4-methyl-	2.76	
Aromatic	1H-Indole, 3-methyl-	1.76	Yes
Chain	Octadecanoic acid, octyl ester	1.69	
Chain	Hexadecanamide	1.66	Yes
Aromatic	Styrene	1.52	
Aromatic	3-Phenylpropionitrile	1.36	Yes

Source: Kebelmann et al. (2013)

Figure 45 – 1H-indole.

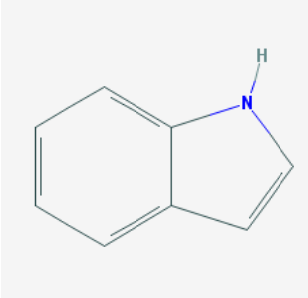

Figure 46 – Toluene.

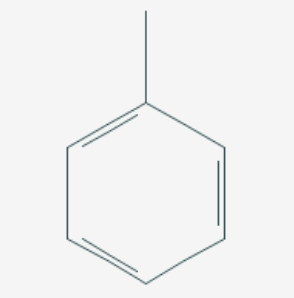

Source: http://pubchem.ncbi.nlm.nih.gov

As mentioned before, Ursu et al. (2014) performed a study in order to indentify proteins and amino-acids contents of *Chlorella Vulgaris*. She obtained the following set of amino-acids listed in Table 22. In this table only phenylalanine, tyrosine and tryptophan have an aromatic group (Figures 47 to 49), representing the 10.4% of the total mass of proteins. Results obtained by Kebelmann et al. (2013) shown that a 23% in weight are compounds with aromatic rings. The direct comparison cannot be made due to the fact that the aromatic rings are linked with other groups, and it affects the molar mass, avoiding the comparison in mass basis. Also in the work of Kebelmann et al. (2013) there are a 58.5% of substances not identified. However, the fact is that if some structures such as benzene can be preserved during the pyrolysis of proteins, because it could be a key factor in the establishment of the reaction mechanism for proteins.

Table 22 – Amino-acids identified by Ursu et al. (2014).

Amino acids	%	Amino acids	%
Alanine	10.70	Proline	5.00
Glutamic acid	10.30	Serine	4.40
Aspartic acids	8.60	Tyrosine	4.40
Leucine	8.20	Isoleucine	3.40
Arginine	7.40	Methionine	2.60
Glycine	7.00	Histidine	1.60
Valine	6.70	Cystenine	1.30
Phenylalanine	6.00	Ammonia	1.30
Threonine	5.50	Tryptophan	0.20
Lysine	5.40		

Source: Ursu et al. (2014)

Figure 47 – Phenylalanine.

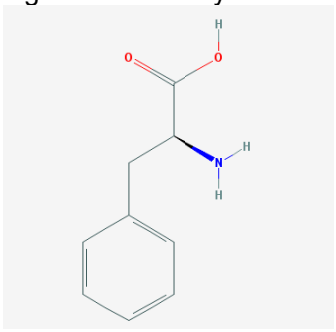

Figure 48 – Tyrosine.

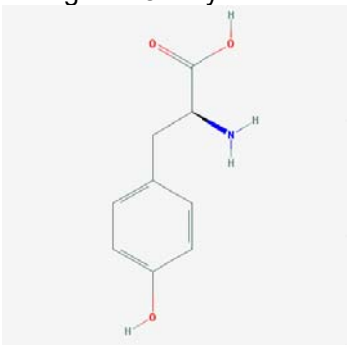

Figure 49 – Tryptophan.

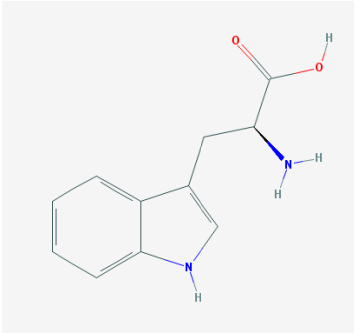

Source: http://pubchem.ncbi.nlm.nih.gov

It is worth noting that tryptophan is one of the substances detected by Kebelmann et al. (2013), and can be a precursor of the 1H-indole, due to the fact that this molecule is a part of the tryptophan structure, as can be seen comparing Figures 45 and 49. However, Ursu et al. (2014) reports minimum amounts of tryptophan with only 0.2%. On the other hand it can be seen that the benzene ring of Phenylalanine (Figure 47), with 6% reported by Ursu et al. (2014) potentially can produce a toluene rings, and this

compound is reported with the highest concentration in the work of Kebelmann et al. (2013).

The hypothesis that aromatic compounds can be preserved during pyrolysis can be assumed considering two factors. The first is obtained from organic chemistry that state benzene is an important molecule due to its properties. One of this property of benzene and aromatics in general is its stability due to the hexa-ring, conjugated double bonds and SP^2 orbital bond hybridization, which give a strong structure without tensions (CAREY, 2006). Aromatic compounds can react easily, but the ring is conserved, the effect of benzene ring frequently is to stabilize an ion or a radical species during the reaction. The second factor is related with the first factor. Although the aromatic structure is strong, high temperatures can break the ring, however, as mentioned in section 2.3, proteins are decomposed at relatively low temperatures in pyrolysis, and considering that in fast pyrolysis the volatiles must be swept out rapidly, in order to avoid secondary cracking, the aromatic ring can be conserved due to the low temperature and short residence time. Therefore a possible pathway to be proposed for proteins pyrolysis is one in which the amino-acids break into benzene and substitutes producing mainly 1H-indole and toluene.

Du et al. (2013) performed an interesting study in order to investigate the effects of microalgae components on pyrolysis products. However, Du et al. (2013) did not extract the lipids, proteins or carbohydrates from *Chlorella Vulgaris*. Instead, the author used three natural substitutes in order to investigate the pyrolysis characteristics and then compare the results with the pyrolysis of whole *Chlorella Vulgaris*. Substitutes were: cellulose for carbohydrates; egg whites for proteins and canola oil for lipids. Du et al. (2013) performed several experiments at different temperatures in a Pyroprobe coupled to a GC-MS. Table 23 shows the component analysis.

Table 23 – Components analysis for *Chlorella Vulgaris*, cellulose, white eggs and canola oil.

Components		
Lipids	**Carbohydrates**	**Proteins**
29.0	12.0	51.0
% by weight		

Source: Du et al. (2013).

Table 24 shows the results obtained by Du et al. (2013). As in the work of Kebelmann (2013), it is reported almost the same aromatics compounds such as toluene, phenol 4-methyl, indole and indole with substitutes, and as can be seen pyrolysis of egg white produces the same compounds but with different concentration.

Table 24 – Compounds identified by Du et al. (2013) from pyrolysis of *Chlorella Vulgaris* and proteins (egg whites).

Bio-oil compounds	*Chlorella Vulgaris*				Egg whites			
	Temperature [°C]							
	450	500	550	600	450	500	550	600
Toluene	0.35	0.38	0.37	0.40	0.48	0.62	0.70±0.11	0.73
Ethylbenzene					0.03	0.04	0.05	0.06
Styrene	0.09	0.12	0.10	0.09	0.08	0.09	0.09	0.10
1-nonene								
1-Undecene								
Phenol	0.47±0.19	0.43±0.13	0.38	0.43	0.08	0.87	0.79	0.86±0.14
Phenol, 4-methyl-	0.85±0.27	1.03±0.20	0.98±0.12	0.99±0.23	0.64	0.85±0.11	0.84	0.98
Pyridine								
Benzil nitrile	0.12	0.13	0.14	0.17	0.12	0.16	0.14	0.18
Pyrrole								
Benzenepropanenitrile	0.09	0.11	0.13	0.10	0.19	0.17	0.21	0.24
Indole	0.22	0.21	0.20	0.17	0.38	0.41±0.13	0.39	0.42
1H-Indole, 3-methyl-	0.11	0.13	0.15	0.16	0.10	0.14	0.15	0.14
Furfural	0.17	0.23	0.18	0.19				
Levoglucosan								
Hexadecanoic acid								
Oleic acid								
Residue	22.10	22.00	18.60	17.60	23.50	23.00	22.80	21.40

Values with more than 0.1 of uncertainty are specified.
Source: Du et al. (2013).

Comparing the *Chlorella Vulgaris* with the egg whites is possible to observe that the compounds with higher concentrations are the same, toluene, phenols and indole. It is worth noting that all of these substances do not have a nitrogen atom bonded. On the other hand, nitrogenated compounds have a lower concentrations in both, *Chlorella Vulgaris* and egg whites i.e: benzonitrile and benzenepropanenitrile. Possibly, the remaining nitrogen compounds of amino-acids are in the fraction not identified by GC-MS.

Besides of the interesting results reported for the substitutes components, the author gives important insights about the stability of benzene. In table 24 is possible to observe that the aromatic compounds toluene, phenol 4-methyl, indole and indole with substitutes just has a minor changes in the range of temperature of 450 to 640°C.

Several research has been reported in the literature regarding the pyrolysis of amino-acids including products analysis by FTIR and GC-MS. These reports presented here include the amino-acids with higher concentration reported by Ursu et al. (2014) i.e Alanine, Glutamic acid, Aspartic acid and Leucine.

Ren et al. (2011) pyrolyzed Glutamatic acid, Aspartic acid and Leucine separately in order to study the effect in the production of NO_x and N_2O precursors NH_3 (Amonia) and HCN, and several pyrolysis profiles were obtained.

Choi and Ko (2011) pyrolyzed and analyzed 20 amino-acids, among others, Alanine, Glutamatic acid, Aspartic acid and Leucine, mixed with silica and tetramethylammonium hydroxide (TMAH) to catalyze pyrolysis of amino-acid monomers. The pyrolysis products were divided into cyclic and non-cyclic products. Among the 20 amino-acids the glutamic acid (branched chain without rings), produced cyclic compounds during pyrolysis from the monomers generated. Variations of the relative intensities of the cyclic pyrolysis products with the pyrolysis temperature and amino acid concentration were also investigated. Authors propose several mechanisms for hetorocycles formation from the originial amino-acids structure based in their investigations.

Sharma; Chan and Hajaligol (2006) performed the pyrolysis of aliphatic a-amino acids, glutamine, glutamic and aspartic acids, and formation of heterocyclic and polycyclic aromatic hydrocarbons (N-PACs and PAHs) were studied. Tars and char of each amino-acids were produced at 300°C and then between 700 and 800°C in order to study secondary reactions. Tars were analyzed by gas chromatography/mass spectrometry. Glutamic acid and glutamine underwent significant decomposition to volatile products at 300°C but aspartic acid required higher temperature. The heterocyclic compounds were primarily single-ring compounds comprised of five or six member heterocycles in the absence of secondary reactions, and up to four rings after the secondary pyrolysis.

Wanjun; Cunxin and Donghua (2006) investigated the thermal behavior of some aliphatic amino acids, including alanine, and leucine, using thermogravimetry (TG) in the range of temperatures within 30–400°C. Pyrolysis of these amino-acids was performed at various heating rates under inert conditions. A kinetic analysis was carried out using a composite procedure involving the iso-conversional method. It is highlighted that the author states that the iso-conversional method suggest that the pyrolysis reaction can be described with a model comprised by only one reaction. The master plots method suggested that the phase boundary reaction model best describe the pyrolysis of alanine and leucine. Also, for each amino acid, the kinetic parameters, such

as activation energy and pre-exponential factor were determined. Kinetic parameters obtained for alanine and leucine were: E=175.10±5.16 kJ/mol; A=5.92E13 1/s; n=2.2; and reaction model $1-(1-\alpha)\text{^}(1/n)$ for alanine, and E = 151.28±0.75 kJ/mol; A = 4.29E11 1/s; n = 1.3; and reaction model $1-(1-\alpha)\text{^}(1/n)$ for leucine.

3.2.3 LIPIDS

As mentioned in Chapter 2 the lipid content in *Chlorella Vulgaris* is seldom informed, and instead what it is commonly reported is the fatty acids contents, because this organic compounds are the products of the lipid extraction process. Moldoveanu (1998) described some insights about analytical pyrolysis for lipids. The author mentioned that in order to analyze the lipids, frequently a previous step using hydrolysis must be made with the objective of separating the different fatty acids. Therefore information about lipids are expressed through fatty acids relative amounts. There is not much information about pyrolysis of single fatty acid. Almost all works related to the pyrolysis of lipids include a mixture of various fatty acids. Therefore the contribution of all of them are overlapped in the pyrograms.

More details about the work performed by Kebelmann et al. (2013) is presented here related to the lipids or fatty acids pyrolysis. The author studied the pyrolysis of the fatty acids extracted from three species of microalgae, one of them *Chlorella Vulgaris*. The part of the work highlighted at this point is the weight loss curves obtained by Kebelmann et al. (2013) for: proteins, extracted lipids (in form of fatty acids) and for untreated *Chlorella Vulgaris*. Figures 50, 51, 52 and 53 show these results.

Figure 50 – TG analysis for lipids (Fatty acids) of Chlorella Vulgaris microalgae species.

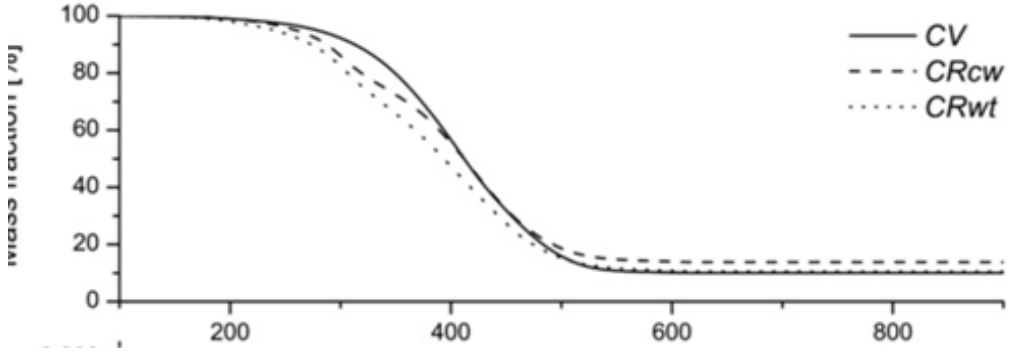

Source: Kebelmann et al. (2013)

Figure 51 – DTG analysis for lipids (Fatty acids) of Chlorella Vulgaris microalgae species.

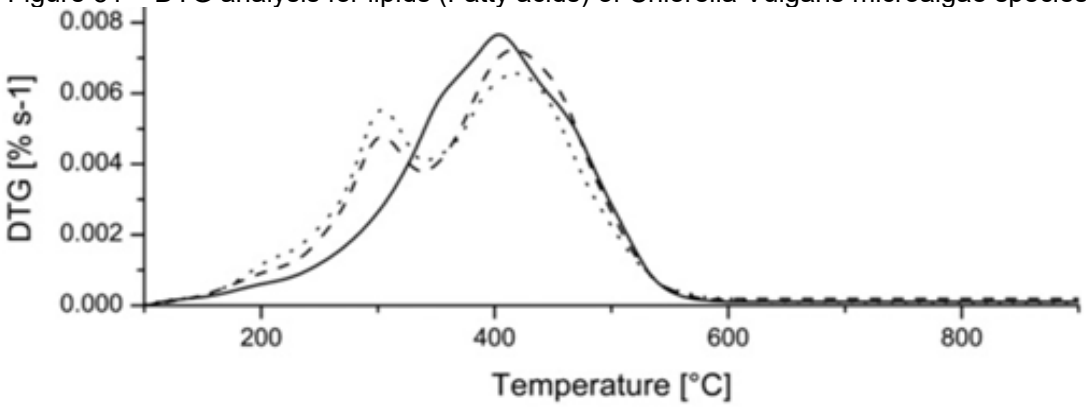

Source: Kebelmann et al. (2013)

As can be seen in Figures 51 lipids (Fatty acids) are decomposed in wide range of temperature, while proteins, shown in Figure 52, are decomposed in a narrow range in agreement with other works for thermal decomposition of *Chlorella Vulgaris* reported in section 2.3.

Figure 52 –TG and DTG analysis for proteins of Chlorella Vulgaris microalgae species.

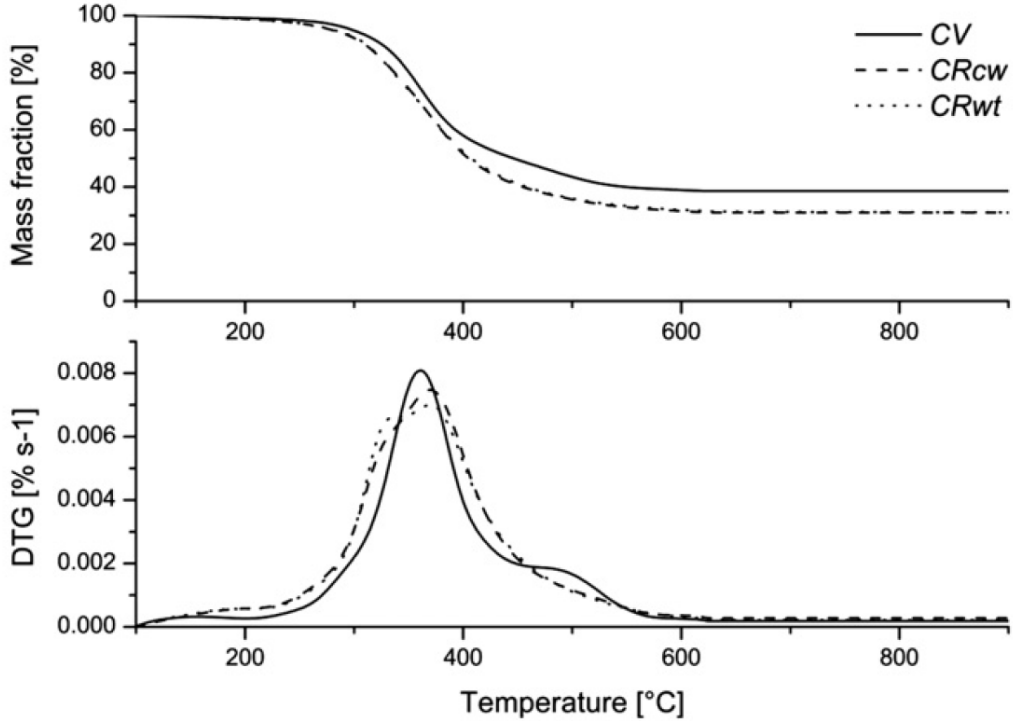

Source: Kebelmann et al. (2013)

Lipids have the temperature peak at 410°C, and proteins at lower temperature between 350-360°C.Another important aspect is that the char formation is higher for proteins than lipids. Figure 53 shows the TG and DTG analysis for the untreated *Chlorella Vulgaris*. In the Figure is possible to observe two peaks in the DTG chart. The first peak can be attributed to proteins and carbohydrates and the second peak to lipids. The first peak has a higher devolatilization rate, and it is possible due to the higher content of proteins in the raw material (54.9% wt.) and due to the volatile part of proteins that has a lower energy to decompose compared to lipids. In short, two conclusions can be obtained from this work: a) a correspondence is suggested between the pyrolysis of fatty acids and lipids; and b) lipids produce less char than proteins, only for *Chlorella Vulgaris*.

As it was mentioned in Chapter 1, there is no reaction mechanism, useful for CFD applications, reported neither for microalgae biomass nor for *Chlorella Vulgaris*. The revision of literature has revealed that the microalgae thermal decomposition can be described as a function of its biological components. However, no mechanism are developed so far. In the search of a starting point to construct a mechanism, an examination has been performed in order to investigate with more detail the structure of the different components of microalgae.

The results of this review reveals that the levels of detail needed to describe a component can be different. In order to formalize the information four levels of details are defined and presented in Table 25 with the objective to guide for further development of a reaction mechanism. The levels of detail are: components, subcomponents, basic subcomponents and organic subcomponents. For example in the case of carbohydrates, the literature revision has shown that this component can be composed by hemicellulose.

Considering that a mechanism for hemicellulose already exists for lignocellulosic biomass, the level of detail for its description is at the subcomponent level. In the case of proteins no specific mechanism has been found. However, there are thermal analysis for single amino-acids and peptides, including mechanisms and kinetic parameters. Further, the description of the reaction pathways of amino-acids pyrolysis include the description of its organic components is currently reported in the literature. Therefore in

the case of proteins the level of detail needed for its description is at organic subcomponents level.

Figure 53 – TG and DTG analysis for untreated *Chlorella Vulgaris* microalgae species.

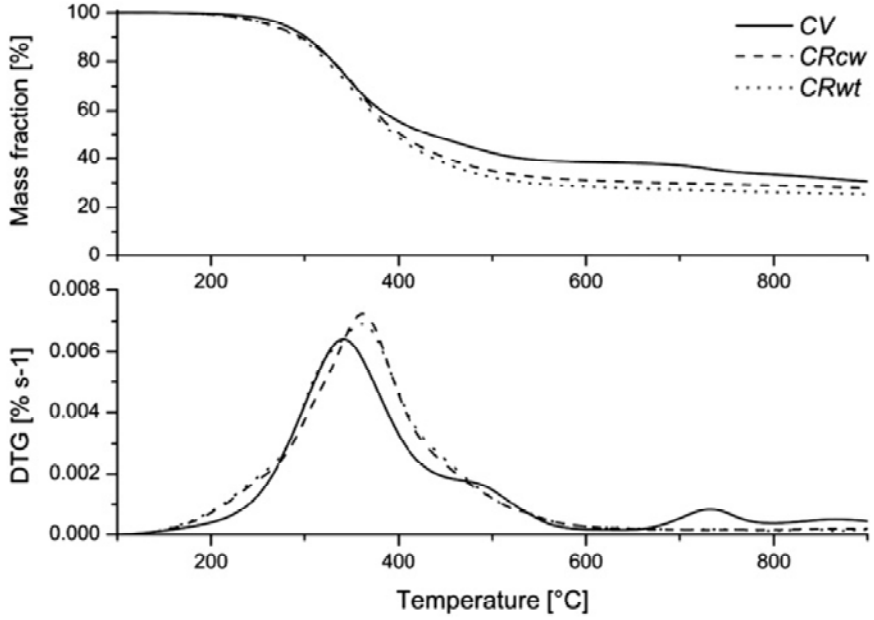

Source: Kebelmann et al. (2013)

Table 25 – Level of detail for description of *Chlorella Vulgaris* components.

DESCRIPTION LEVELS			
COMPONENT	**PROTEINS**	**LIPIDS**	**CARBOHYDRATES**
SUB-COMPONENTS	P7 P12 UFPe7 UFRe7 UFPe12,among others	SCARCE INFORMATIION	POLISACHARIDES hemicellulose cellulose starch
BASIC SUB-COMPONENTS	AMINO-ACIDS Alanine Glutamic acid Aspartic acids Leucine Arginine, among others	FATTY ACIDS* Palmitic acid Oleic acid Linoleic acid Linolenic acid among others	SUGARS glucose manose arabinose glucosamine
ORGANIC SUBCOMPONENTS	Amine groups, carboxylic acids	Carboxylic acids, alkanes, alkenes	Basic sugar heterocycles,organic and inorganic substitutes

3.3. DEVELOPMENT OF REACTION MECHANISM FROM THERMAL ANALYSIS DATA

Considering the literature reviewed in Chapter 2 related to comprehensive development of reaction mechanisms in the last sixty years for lignocellulosic materials and the

knowledge about the complex structure of the microalgae main components, the conclusion at the time is not possible to obtain a detailed reaction mechanism for microalgae biomass. This conclusion is supported on the fact that the models for pyrolysis of lignocellulosic biomass are a sum of contributions of several authors through the years, proposing hypothesis, developing methodologies with its respective verification against experimental data, giving at each step of the way more knowledge, details and accuracy. In the case of pyrolysis of microalgae biomass the framework given by this body of knowledge can accelerate the development; however a starting point from basic schemes is logically the way to improve in stepwise sense the level of detail and at the same time allowing the application for research or engineering as the case of Biorefinery concept assess.

The basic brick in a reaction mechanism for devolatilization is a one step reaction as shown in eq.(27). In general, in devolatilization there is one reactant, generally biomass or a biomass component, which is decomposed by thermal energy.

$$A \xrightarrow{k} bC + cD \tag{27}$$

In dynamic chemistry, an additional equation is defined which provides a rate of reaction for the consumption of the reactant A, or equivalently the rate of production of C and D.

$$\frac{dA}{dt} = -k\, f(A) \tag{28}$$

eq.(28) shows the rate equation for A as a function of the kinetic constant k and model function $f(A)$. In terms of devolatilization observed in TG and DTG analysis, the rate equation is called the mass loss or mass decay equation. Amore suitable form to describe the process is with the use of the non-dimensional concept of extent of reaction α. This concept relates undimensionally and linearly the mass loss due to devolatilization with a parameter ranging from 0 to 1, then

$$\alpha = \frac{w - w_0}{w_f - w_0} \tag{29}$$

Where w, w_0 and w_f are the actual mass at time t, the initial mass and the final residue respectively. With the concept of extent of extent of reaction eq.(29) can be expressed non-dimensionally as

$$\frac{d\alpha}{dt} = k\, f(\alpha) \tag{30}$$

The kinetic constant $k$is frequently expressed by means the Arrhenius equation

$$k = A\, exp\left(\frac{-E}{RT}\right) \tag{31}$$

Where A, E, R and T are the pre-exponential factor, activation energy ($Joule/mol$), universal gas constant ($Joule/mol/K$)and absolute temperature (K). The pre-exponential factor is time dimensional and the factor n depends on the reaction model order. Therefore, a chemical process described dynamically can be expressed by combining eq.(30) and eq.(31).

$$\frac{d\alpha}{dt} = A\, exp\left(\frac{-E}{RT}\right) f(\alpha) \tag{32}$$

The kinetic parameters *A* and *E* give the main loss rate as a function of temperature of the one step reaction. However, it is worth noting that mathematically, two sets of kinetic parameters can give the same mass loss rate as a function of temperature due to compensation between the parameters. The third element in the rate equation is the model function $f(\alpha)$ that provides the shape of the mass loss curve or the mass loss rate curve. The model $f(\alpha)$ is related to the reaction itself and considers physical processes aspects of the reaction. For thermal analysis of pyrolysis there is a set of reaction models typically encountered in devolatilization of lignocellulosic biomass or in homogenous polymers. Table 26 shows 12 models suggested by Vyazovkin et al. (1998) in addition of reactions 1 and 14 provided by Zhou et al. (2003) which are the commonly reaction models used in order to study the devolatilization of complex materials.

In Table 26 $f(\alpha)$ and $g(\alpha)$ the differential and integral forms of the reaction model are found. It is worth to note that the most common reaction mechanism used in CFD simulation of lignocellulosic biomass pyrolysis is the reaction model 7, the Mampel first order reaction, as can be verified in works of Mellin et al. (2014), Xion et al. (2014), Ranzi et al. (2008) Trendewicz et al. (2014) and Xue; Heindel and Fox (2012). These three elements constitute the kinetic triplet that must be determined for a single step reaction. As was reviewed in Chapter 2, generally, devolatilization reaction for complex

materials has more than one competitive, parallel or serial reaction. Hence, for complex devolatilization behavior a separation between different steps must be elucidated in order to isolate different processes. However, there are cases in where the isolation of each reaction is unfeasible due to the number of reactions needed to describe the whole reaction. In these cases an apparent kinetic triplet can be fitted in order to approximate the experimental curve with the lack of accuracy, however, a different approach can be applied using a scheme with a distributed activation energy *E* (DE FILIPPIS et al., 2015).

Table 26 - Differential and integral forms of common reaction models used to study the devolatilization of solids.

	Reaction model	$f(\alpha)$	$g(\alpha)$
1	Zero order*	1	α
2	Power law	$\alpha^{3/4}$	$\alpha^{1/4}$
3	Power law	$3\alpha^{2/3}$	$\alpha^{1/3}$
4	Power law	$2\alpha^{1/2}$	$\alpha^{1/2}$
5	Power law	$2/3\,\alpha^{-1/2}$	$\alpha^{3/2}$
6	One-dimensional diffusion	$1/2\,\alpha^{-1}$	α^{2}
7	Mampel (first order)	$1-\alpha$	$ln(1-\alpha)$
8	Avrami-Erofeev	$4(1-\alpha)[-ln(1-\alpha)]^{3/4}$	$[-ln(1-\alpha)]^{1/4}$
9	Avrami-Erofeev	$3(1-\alpha)[-ln(1-\alpha)]^{2/3}$	$[-ln(1-\alpha)]^{1/3}$
10	Avrami-Erofeev	$2(1-\alpha)[-ln(1-\alpha)]^{1/2}$	$[-ln(1-\alpha)]^{1/2}$
11	Three dimensional diffusion	$2(1-\alpha)^{2/3}\left[1-(1-\alpha)^{1/3}\right]^{-1}$	$\left[1-(1-\alpha)^{1/3}\right]^{2}$
12	Contracting sphere	$3(1-\alpha)^{2/3}$	$1-(1-\alpha)^{1/3}$
13	Contracting cylinder	$2(1-\alpha)^{1/2}$	$1-(1-\alpha)^{1/2}$
14	Second order*	$(1-\alpha)^{2}$	$1/(1-\alpha)-1$

Source: Vyasovkin (1998) and *from Zhou et al. (2003).

3.3.1. DETERMINATION OF THE ACTIVATION ENERGY E FROM EXPERIMENTAL DATA

For each reaction the kinetic triplet must be determined. Generally, data obtained from TG, DTG DSC analysis is used in conjunction with a fitting procedure performing experiments in isothermal and in non-isothermal conditions. The more straightforward method in fitting experimental data, one heating rate method (OHR), a non-isothermal method, uses only one experimental DTG run with a programmed linear heating rate β,

$$\beta = \frac{dT}{dt} \tag{33}$$

The mass loss rate as a function of extent of reaction α is converted by means of eq.(33). Linearized form of eq.(32) is obtained by applying the neperian logarithm in time basis

$$ln\left[\frac{d\alpha}{dt}f^{-1}(\alpha)\right] = ln(A) - \frac{E}{RT} \quad (34)$$

Or in temperature basis

$$ln\left[\beta\frac{d\alpha}{dT}f^{-1}(\alpha)\right] = ln(A) - \frac{E}{RT} \quad (35)$$

Assuming an arbitrary reaction model from Table 26, the activation energy *E* and the pre-exponential factor *A* can be determined as the slope and intercept respectively applying a linear fitting procedure to $\frac{d\alpha}{dt}f^{-1}(\alpha)$ v/s $1/T$ or $\beta\frac{d\alpha}{dT}f^{-1}(\alpha)$ v/s $1/T$ combined data. As stated by Vyazovkin (1998), there is a compensation effect between the three elements of the kinetic triplet, *A, E* and$f(\alpha)$, therefore, practically all models in Table 26 fit the experimental data causing an ambiguously set of kinetic parameters.

Two more disadvantages has the OHR method: i) if only the TG data is available, that gives the mass loss rate curve, a numerical differentiation must be computed introducing noisy data, and even more so, in the case that DTG data is available, the inherent noise of experimental data forces a filtering procedure, introducing more uncertainty of the predictions. And ii) the procedure do not covers and relates data for more than one run. In order to avoid this cumbersome issue another approach was developed by researchers modifying eq.(34) or eq.(35), frequently named the Model Free methods.

3.3.2. MODEL FREE METHODS

Model free method (MF) is composed by a set of procedures to give an unambiguously kinetic triplet. The fundamental concept is to solve eq.(35) in a different form as a function of the mass rate only and applying neperian logarithm again.

$$ln\left[\beta\frac{d\alpha}{dT}\right] = ln(A)f(\alpha) - \frac{E}{RT} \quad (36)$$

Equation 36 allows fitting the data without an arbitrary selection of the reaction model and determining the activation energy E, theoretically, unambiguously. The disadvantage is that the pre-exponential factor is undeterminable if a reaction model is

not chosen; hence, an additional procedure must be applied. As stated by Vyazovkin et al. (1998) Kujirai and Akahira suggest the first method to process TG data considering more than one experimental run. Later the same author formalized the procedure as the iso-conversional method.

3.3.3. ISO-CONVERSIONAL METHOD

The iso-conversional method starts from the hypothesis that the reaction rate at a constant extent of conversion is only a function of the temperature. The hypothesis is a direct consequence of the rate eq.(32). Deriving eq.(36) respect to $1/T$ at a constant extent of reaction α

$$\left\{\frac{d}{d(1/T)}\right\}_{\alpha}\left\{ln\left[\beta\frac{d\alpha}{dT}\right]\right\}=\left\{\frac{d}{d(1/T)}\right\}_{\alpha}\left\{ln(A)f(\alpha)-\frac{E}{RT}\right\} \tag{37}$$

gives

$$\left[\frac{dln(d\alpha/dT)}{d(1/T)}\right]_{\alpha}=-\frac{E_{\alpha}}{R} \tag{38}$$

Equation 38 states that it is possible to determine the activation energy E using more than one experimental run even in isothermal or in non-isothermal conditions. The Friedman method is based on this concept and takes the linearized form of eq.(36) on a time or temperature basis,

$$ln\left[\beta_i\left(\frac{d\alpha}{dT}\right)_{\alpha,i}\right]=ln(A)f(\alpha)-\frac{E_{\alpha,i}}{RT_{\alpha,i}} \tag{39}$$

Considering mass loss data and temperature for constant α at, at least three different heating rates, the slope of the curve gives the activation energy *E.* It is worth to note that the iso-conversional method yields the activation energy as a function of the extent of reaction, instead of apparent activation energy for an entire run, which allows the discrimination about the variation of these values as the reaction proceeds. This characteristic is useful in order to elucidate a complex reaction mechanism composed of more than one single step reaction. Therefore, the iso-conversional method provides a distribution of the activation energy while the OHR method only provides an ambiguous and apparent activation energy.

The iso-conversional method gives the effective value of the activation energy for a one step reaction; however, the other two kinetic parameters, pre-exponential factor A and the model $f(\alpha)$ are still unknown. As mentioned above, the differential method has the

disadvantages of noise and being that the data of DTG is not always available, a numerical differentiation of TG data from the thermal analysis is necessary. In order to address this issue another method frequently used is the integral method, described in the next section.

3.3.4. INTEGRAL METHODS

In order to avoid noisy data and numerical differentiation the integral form of eq.(32) can be used.

$$\int_0^1 \frac{d\alpha}{f(\alpha)} = g(\alpha) = A\int_0^t exp\left(\frac{-E_\alpha}{RT}\right)dt \tag{40}$$

In eq.(40) the integral of the model is replaced by the function $g(\alpha)$ listed in Table 26. Temperature basis is used due to the fact that the integral is representative even for isothermal and non-isothermal conditions. The integral is frequently named the *temperature integral* (VYAVZOVKIN et al., 1988) and there is no analytical solution for it. For non-isothermal analysis the following substitution is used

$$x = \frac{-E_\alpha}{RT} \tag{41}$$

Hence eq.(40) becomes

$$g(\alpha) = \frac{AE_\alpha}{\beta R}\int_{x_0}^{x}\frac{exp(x)}{x^2}dx = \frac{AE_\alpha}{\beta R}p(x)\Big|_{x_0}^{x} \tag{42}$$

Lyon (1996) mentions that different researchers have been approximating the integral term $p(x)$ analytically with an asymptotical expansion starting from the integration by part procedures such as

$$p(x) = \frac{exp(x)}{x^2}\left(1 + \frac{2!}{x} + \frac{3!}{x^2} + \frac{4!}{x^3} + \cdots\right) \tag{43}$$

Or with

$$p(x) = \frac{exp(x)}{x(x-1)}\left(1 + \frac{2}{(2-x)(3-x)} - \frac{4}{(2-x)(3-x)(4-x)} + \cdots\right) \tag{44}$$

In order to obtain more than 95% of accuracy, values of $-x > 30$ or $-x < 10$ are necessary. As referenced by the same author and by Vyazovkin et al. (1988) a more usable empirical approximation is proposed by Doyle

$$p(x) = (7.03E - 10\ )exp[xB(x)] \tag{45}$$

In which $B(x)$ can range between 1.195 and 1.034 with an average value of 1.052 for $x = [-10, -60]$. This equation is commonly used in thermal analysis as the Ozawa, Flynn and Wall (FWO) iso-conversional method. Combining eq.(45) with the temperature integral approximation eq.(42) gives

$$g(\alpha) = 7.03E - 10\frac{AE_\alpha}{\beta R}\ exp\left[-1.052\frac{E_\alpha}{RT}\right] \tag{46}$$

Rearranging

$$\beta = 7.03E - 10\frac{AE_\alpha}{Rg(\alpha)}\ exp\left[-1.052\frac{AE_\alpha}{RT}\right] \tag{47}$$

and taking the neperian logarithm gives

$$ln(\beta_i) = constant\ - 1.052\frac{E_\alpha}{RT_i} \tag{48}$$

The latter equation is the Ozawa, Flynn and Wall iso-conversional method (FWO method) mentioned by Vyavzovkin et al. (1988). In order to obtain the distribution of the activation energy E as a function on the extent of reaction α, at least three experimental runs must be performed at different heating rates β_i. The linear regression procedure must be calculated considering constant conversion α, and plotting $ln(\beta_i)$ v/s $1/T$. An additional advantage from the use of eq.(48) is that only the TG analysis is enough at three different heating rates in order to obtain the activation energy distribution. The disadvantages of the method reside in the crude approximation of Doyle.

As explained by Vyazovkin et al. (1988) approximation of the temperature integral is truncated. If the temperature integral is expressed as the function S,

$$S(T) \approx \int_0^T exp\left(\frac{-E_\alpha}{RT}\right)dT \tag{49}$$

And in order to reduce the complexity, the traditional method approximates and truncates the integral to

$$I(E,T) \approx S(T) - S(T_0) \tag{50}$$

Where T_0 is the typical starting temperature of a thermal analysis. The hypothesis is that for processes starting at T_0 the deviation from a process starting on $T = 0$ is negligible. In other words, the amount of mass lost in the temperature interval $[0, T_0]$ is minimal as the activation energy E is higher. As a consequence, the aforementioned limit of $x = [-10, -60]$ is stated. For processes with lower activation energy, a more accurate temperature integral is required.

Another approximation for temperature integral is developed by taking another the approximation of eq.(42) (Lyon, 1996)

$$p(x) = \frac{exp(x)}{x(x-1)}\left(1 + \frac{2}{(2-x)(3-x)} - \frac{4}{(2-x)(3-x)(4-x)} + \cdots\right) \quad (51)$$

That for $-x > 30$ the series terms as a function of x can be neglected obtaining a 95% of accuracy. The truncation gives the following integral form of the rate equation

$$g(\alpha) = \frac{ART^2}{\beta E_\alpha}\ exp\left[-\frac{E_\alpha}{RT}\right] \quad (52)$$

Linearized form for regression procedure becomes

$$ln\left(\frac{\beta}{T^2}\right) = constant\ - \frac{E_\alpha}{RT} \quad (53)$$

This equation is known as the Kissinger-Akahira-Sunose method (KAS method). Both the FWO and KAS methods are the iso-conversional method procedures commonly used in the modern thermal analysis to obtain the model free and effective activation energy *E.* Also an alternative equation is the Starink in where the only difference with the KAS and FWO is that the exponent of the temperature inside the logarithm is 1.92, and as mention by Vyazovkin et al. (1988) yields better results compared with the other two methods presented here.

A more accurate approximation for temperature integral is developed by taking the substitution (LYON, 1997)

$$y = \frac{exp(x)}{x^2} \quad (54)$$

Therefore, the integral form of the rate equation becomes

$$g(\alpha) = \frac{AE_\alpha}{\beta R}\int_{y_0}^{y} f(y)dy \tag{55}$$

Integration by parts yields

$$g(\alpha) = \frac{AE_\alpha}{\beta R}\left\{\left[\frac{exp(x)}{x(x-2)}\right]_{x_0}^{x} + 2\int_{x_0}^{x}\frac{exp(x)}{x^2(x-2)^2}dx\right\} \tag{56}$$

And repeating the integration by parts

$$g(\alpha) = \frac{AE_\alpha}{\beta R}\frac{exp(x)}{x(x-2)}\left[1 + \frac{2}{x(x-2)} + \frac{8}{x(x-2)^2} + O(x^{-4}) + O(x^{-5})\right]_{x_0}^{x} \tag{57}$$

As mentioned by Lyon (1997) for temperatures commonly encountered in thermal analysis, the lower limit of the last term in RHS of eq.(63) can be neglected and for values of $-x > 10$ only the first term of the RHS is relevant. Combining eq.(57) with eq.(42) yield

$$g(\alpha) = \frac{ART^2}{\beta(E_\alpha + 2RT)}exp\left(\frac{-E}{RT}\right) \tag{58}$$

A difference between eq.(58) compared with eq.(53) is that when the neperian logarithm is applied to eq.(64), the temperature will remain coupled with the activation energy. Therefore, simple linear regression is not possible as can be seen in eq.(59), however this more accurate approximation can be used in conjunction with the non-linear iso-conversional methods explained in the next section.

$$ln\left[\frac{g(\alpha)}{T^2}\right] = \frac{AR}{\beta(E_\alpha + 2RT)} - \frac{E}{RT} \tag{59}$$

3.3.5. NUMERICAL METHOD FOR ISO-CONVERSIONAL PROCEDURE

The methods FWO and KAS provide a straightforward procedure in order to determine the activation energy E and the pre-exponential factor A if the reaction model is known or suggested. However, these methods reside on approximations of the temperature integral introducing inaccuracies and in cases when the reaction rate is significantly at low temperatures; the approximations are even less accurate. Nowadays, the increased computational power allows the use of numerical techniques in order to calculate the temperature integral for the iso-conversional method.

With the application of numerical methods to the thermal analysis data Vyazovkin and Dollimore (1996) presents a different iso-conversional procedure in order to determine the activation energy. The traditional method presented in the above section resides on the linear regression technique, instead. Vyazovkin and Dollimore (1996) proposes a non-linear method starting from the temperature integral. Recalling the eq.(40) in temperature basis

$$g(\alpha) = \frac{A}{\beta}\int_0^T exp\left(\frac{-E_\alpha}{RT}\right)dT \tag{60}$$

And identifying the temperature integral as

$$I(E,T) = \int_0^T exp\left(\frac{-E_\alpha}{RT}\right)dT \tag{61}$$

Gives the following rate equation

$$g(\alpha) = \frac{A}{\beta}I(E,T) \tag{62}$$

Using the iso-conversional principle the following equality is valid for a constant extent of conversion α and different heating rates β_i

$$g(\alpha)_{\beta_1} = g(\alpha)_{\beta_2} = \cdots = g(\alpha)_{\beta_n} \tag{63}$$

Then using eq.(62)

$$\frac{A}{\beta_1}I\left(E_\alpha, T_{\alpha,1}\right) = \frac{A}{\beta_2}I\left(E_\alpha, T_{\alpha,2}\right) = \cdots = \frac{A}{\beta_n}I\left(E_\alpha, T_{\alpha,n}\right) \tag{64}$$

Dividing eq.(64) by the first term of the equality

$$1 = \frac{\frac{A}{\beta_2}I\left(E_\alpha, T_{\alpha,2}\right)}{\frac{A}{\beta_1}I\left(E_\alpha, T_{\alpha,1}\right)} = \frac{\frac{A}{\beta_3}I\left(E_\alpha, T_{\alpha,2}\right)}{\frac{A}{\beta_1}I\left(E_\alpha, T_{\alpha,1}\right)} = \cdots = \frac{\frac{A}{\beta_n}I\left(E_\alpha, T_{\alpha,n}\right)}{\frac{A}{\beta_1}I\left(E_\alpha, T_{\alpha,1}\right)} \tag{65}$$

Performing a summation of all terms with the exception of the first that is identically 1 yields

$$\frac{\frac{A}{\beta_2}I\left(E_\alpha, T_{\alpha,2}\right)}{\frac{A}{\beta_1}I\left(E_\alpha, T_{\alpha,1}\right)} + \frac{\frac{A}{\beta_3}I\left(E_\alpha, T_{\alpha,2}\right)}{\frac{A}{\beta_1}I\left(E_\alpha, T_{\alpha,1}\right)} + \cdots + \frac{\frac{A}{\beta_n}I\left(E_\alpha, T_{\alpha,n}\right)}{\frac{A}{\beta_1}I\left(E_\alpha, T_{\alpha,1}\right)} = \sum_{i=2}^{n}\frac{\frac{A}{\beta_i}I\left(E_\alpha, T_{\alpha,i}\right)}{\frac{A}{\beta_1}I\left(E_\alpha, T_{\alpha,1}\right)} = (n-1) \tag{66}$$

Performing the same procedure for all terms, in general

$$\sum_{\substack{i=1 \\ i\neq k}}^{n} \frac{\frac{A}{\beta_i} I\left(E_\alpha, T_{\alpha,i}\right)}{\frac{A}{\beta_k} I\left(E_\alpha, T_{\alpha,k}\right)} = (n-1) \tag{64}$$

Performing a summation over the n summations of type of eq.(64) yields

$$\sum_{j=1}^{n} \sum_{\substack{i=1 \\ i\neq j}}^{n} \frac{I\left(E_\alpha, T_{\alpha,i}\right)\beta_j}{I\left(E_\alpha, T_{\alpha,j}\right)\beta_i} = n(n-1) \tag{65}$$

Equation 65 is a non-linear relation between the temperature integral and the following condition

$$\sum_{j=1}^{n} \sum_{\substack{i=1 \\ i\neq j}}^{n} \frac{I\left(E_\alpha, T_{\alpha,i}\right)\beta_j}{I\left(E_\alpha, T_{\alpha,j}\right)\beta_i} - n(n-1) = 0 \tag{66}$$

However, as mentioned by Vyazovkin et al.(1996) eq.(66) it is not identically 0 for experimental data, then applying eq.(66) to an experimental data set

$$\sum_{j=1}^{n} \sum_{\substack{i=1 \\ i\neq j}}^{n} \frac{I\left(E_\alpha, T_{\alpha,i}\right)\beta_j}{I\left(E_\alpha, T_{\alpha,j}\right)\beta_i} - n(n-1) = min \tag{67}$$

Therefore, eq.(67) is a constraint condition that reaches a minimum if the correct values of the activation energy is used. Considering that the iso-conversional method is applied for the interval of α from 0.01 to 0.99 and with the recommended step of 0.02, it is necessary to perform several iterative calculations in order to minimize eq.(67). Traditional approximations such as of the Doyle can be used in the evaluation of eq.(67). However, the method is flexible due to the fact that a more accurate analytical approximation can be applied. On the other hand, direct integral numerical schemes can be used as an alternative. This method is named as flexible procedure because it permits the evaluation of activation energy E at the time that the temperature integral is evaluated with different schemes or approximations.

At this point, three methods are presented in order to obtain effective activation E and pre-exponential factor A by using an arbitrary model assumption yielding an ambiguous kinetic triplet. Later, the iso-conversional method was presented, allowing the determination of effective activation energy E. However, being it impossible to obtain the pre-exponential factor A without the assumption of a reaction model. The following

section presents a method in order to determinate this element of the kinetic triplet independently of the reaction model.

3.3.6. ESTIMATION OF THE PRE-EXPONENTIAL FACTOR A

Iso-conversional methods do not provide a straightforward way to determine the pre-exponential factor A of the Arrhenius equation, and any evaluation using the OHR method produce a different kinetic triplet (VYAZOVKIN; WIGHT, 1998). It is supposed that one of the reaction models in Table 26 or their derivates is the correct model for a certain one step reaction, and the other models fits the same experimental data compensating the activation energy E and the pre-exponential factor A. The work of Vyazovkin and Wight (1998) and Vyazovkin and Lesnikovich (1988) postulates that the compensation produced by the estimation of the kinetic parameters A and E assuming different reaction models obey a linear relationship between them called the *compensation equation* (VYAZOVKIN; LINERT, 1995)

$$ln(A_x) = aE_x + b \tag{68}$$

This idea resides on the fact that an intersection point of the Arrhenius lines obtained from the linearized Arrhenius equation exists

$$ln(k) = ln(A_x) - \frac{E_x}{RT} \tag{69}$$

where the factor x is a perturbation factor (VYAZOVKIN; WIGHT,1998). This intersection point is named as the *Isokinetic Relationship* IKR. An alternative definition of IKR can be obtained by combining eq.(69) and eq.(36)

$$ln(k_{iso}) = ln\left\{[f(\alpha)]^{-1}\beta\frac{d\alpha}{dT}\right\}_x \tag{70}$$

This equation states that the IKR point reside in the space $ln(k_{iso})$ v/s $1/T$, and the temperature T_{iso} that correspond to $ln(k_{iso})$ is the isokinetic temperature, in where RHS of eq.(70) is least dependent of factor x. This definition permits the search for an IKR point directly from the experimental data.

Considering the linear nature of the Arrhenius lines, the IKR exists only if there is an intersection of the lines. Also, the intersection point is unique. The most important is that the factor x can be any of model in Table 26 used in the estimation of kinetic

parameters that has been demonstrated by Vyazovkin and Wight (1998). This method in named the compensation method since the use of different reaction models produce an incorrect value of E compensating with the value of A.

An IKR exists when the type of model is the factor that produces a change in the reaction allowing a method to determine the pre-exponential factor *A* using the value of E estimated by any iso-conversional method. Besides, the fact that iso-conversional method can provide a distribution of the activation energy, the compensation method provides a distribution of the pre-exponential factor A as a function of activation energy, giving a comprehensive overview of the devolatilization of a process.

3.3.7. REACTION MODEL IDENTIFICATION

For one step reaction of solid materials, one of the reaction models of Table 26 probably fits the experimental data as suggested by Vyavzovkin and Wight (1998) or supposed by Zhou et al. (2003) or Arshad et al. (2017) with the kinetic parameters obtained from any of the iso-conversional and compensation methods. In order to determine the correct model or the best fitted model a graphic method can be applied to identify the best one. However, a statistical analysis using the sum of squares is the discriminative quantity to determine the correct model.

In order to identify the suitable reaction model a reconstruction with kinetic the parameters obtained with any method are processed using the following equations derived from the differential form of eq.(36) (VYAZOVKIN, 2015)

$$f(\alpha) = \beta \left(\frac{d\alpha}{dT}\right)_{\alpha} \left[A_{\alpha} exp\left(\frac{-E_{\alpha}}{RT_{\alpha}}\right)\right] \tag{71}$$

Or in integral form (VYAZOVKIN, 2015)

$$g(\alpha) = \frac{A_{\alpha}}{\beta} \int_{0}^{T_0} exp\left(\frac{-E_{\alpha}}{RT_{\alpha}}\right) dT \tag{72}$$

The functions $f(\alpha)$ and $g(\alpha)$, listed en Table 26 are compared graphically with the reconstructed data identifying the proper curve. An example is presented in Figure 54 that shows the reconstruction of a two steps mechanism data in where the first reaction

well fits a zero order reaction (reaction 1 in table 26), while the second step, the dehydration falls between reaction model D2 and D3 as can be seen in the Figure.

Figure 54. Reconstructed curves for the two step mechanism of dehydration of *nedocromil sodium trihydrate.*

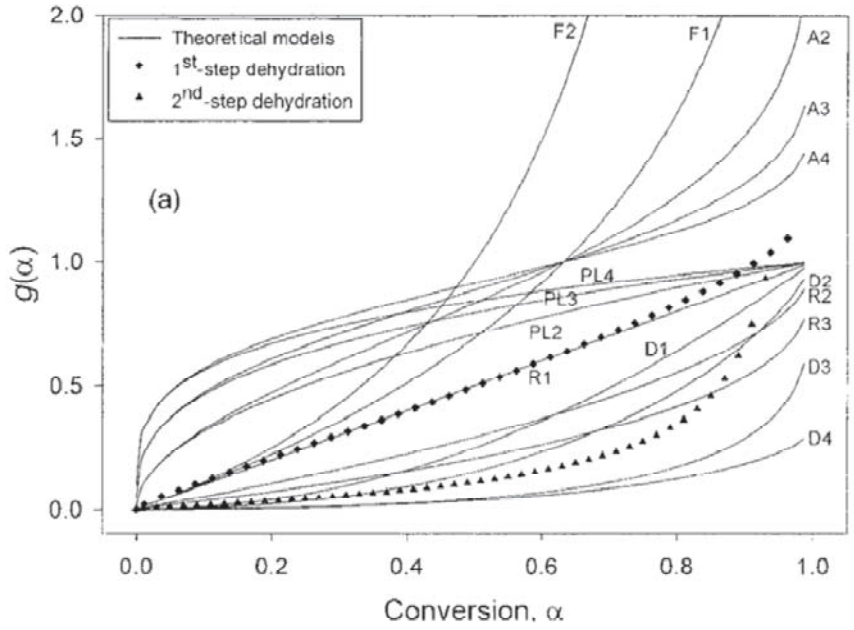

Source: Vyazovkin (2015).

As shown by Vyazovkin (2015) exact match is not plausible in every cases and experimental data will not be well predicted using of any rigid model presented in Table 26. In order to develop a reaction mechanism for further studies as in the case of the application on CFD, a generalized structure of reaction models presented in Table 26 is proposed in order to determine parameters that fit more accurately the experimental data. Khawam et al. (2006) references the equation proposed by Sestak and Berggren that provides a generalized from of the models presented in Table 26

$$g(\alpha) = \alpha^m(1-\alpha)^n[-ln(1-\alpha)]^p \qquad (73)$$

Where m, n and p are constant to be fitted. It is worth to note that eq.(73) solves the lack of accuracy when using the best statistic reaction model of Table 26, and allows the work in other applications. However, reaction models in Table 26 are those obtained from the theory that imply physical and geometric characteristics, on the other hand the use of the eq.(73) give no physical meaning to the reaction model but can fit well the experimental data.

At this point, three methods have been described in order to determine the kinetic triplet that fits the experimental data obtained from thermal analysis TG and DTG. However,

complex materials is composed by more than one component or pseudo-component that is devolatilized in separated steps or even in several steps. As a result, experiments can evidence complex thermal behavior especially observed in DTG charts such as for lignocellulosic and microalgae materials as were presented in Chapter 2. Therefore, an analysis for complex material must include the discrimination of different processes in order to obtain a useful reaction mechanism for CFD applications.

3.3.8. THERMAL ANALYSIS OF COMPLEX MATERIALS

Complex materials can be decomposed by serial, parallel and/or competitive reactions. The evidence of that process can be seen in direct observation of the DTG analysis. Figures 55 and 56 show examples for lignocellulosic material, *almond shells,* and for *Chlorella Vulgaris* microalgae, respectively. In both charts the authors (CABALLERO et al., 1997, RAHEEM et al., 2015) have identified different zones with a notorious different devolatilization process. In the work of Caballero et al. (1997), two peaks were detected at different heating rates, the first near 300°C and the second near 400°C evidencing two different processes.

Frequently in lignocellulosic devolatilization the different peaks detected are attributed to the devolatilization of the cellulose, hemicelluloses and lignin and the reaction mechanisms are constructed using the superimposed principle (MILLER; BELLAN, 1997) separating the devolatilization of the three components. Therefore, from the point of view of the thermal analysis and the determination of kinetic triple, two different sets of kinetic triplet and models must be determined. In this case there is a well defined separation of the two peaks, however, it is not guaranteed that each peak corresponds to a one single reaction step as is stated by Vyavzovkin et al. (1995).

On the other hand, the TG and DTG analysis reported by Raheem (Raheem et al., 2015) shows three separated peaks near 100°C, 250°C and another near 300°C. The author attributes the first peak to elimination of moisture. The second and third peaks are attributed to the devolatilization at low temperature of proteins and carbohydrates and at higher temperature to lipids. Nevertheless, near the second peak (from left to right) there is a shoulder that suggests a reaction of another and different pseudo-component. As a consequence, considering the first observation of the chart suggests a reaction mechanism with at least four one step single reactions with their respective

kinetic triplet. However, as mentioned before, there is no guarantee that four one step reactions will be enough to well fit the experimental data.

Figure 55 - DTG analysis for almond shells obtained by Caballero et al. (1997).

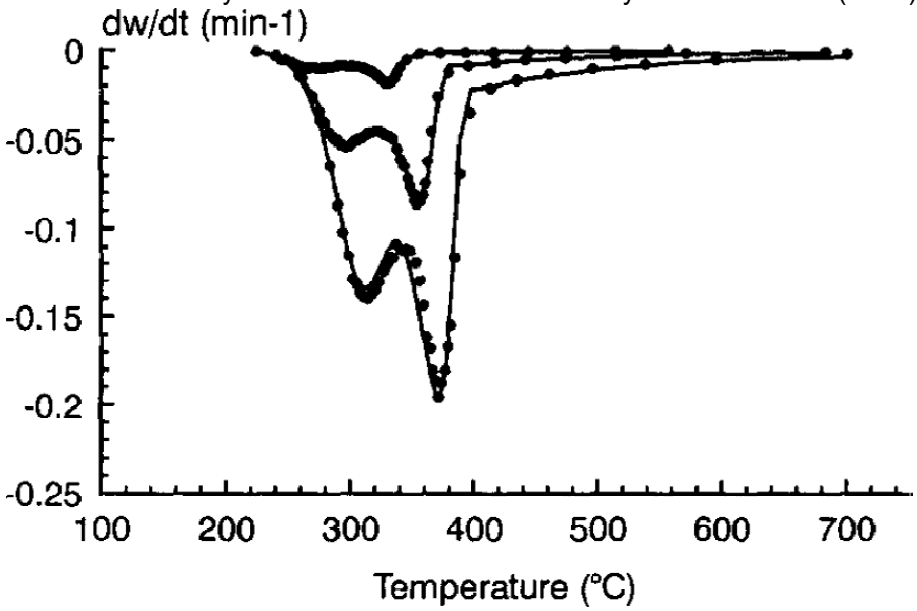

Source: Caballero et al. (1997).

Figure 56 - TG and DTG analysis for *Chlorella Vulgaris* microalgae obtained by Raheem et al. (2015).

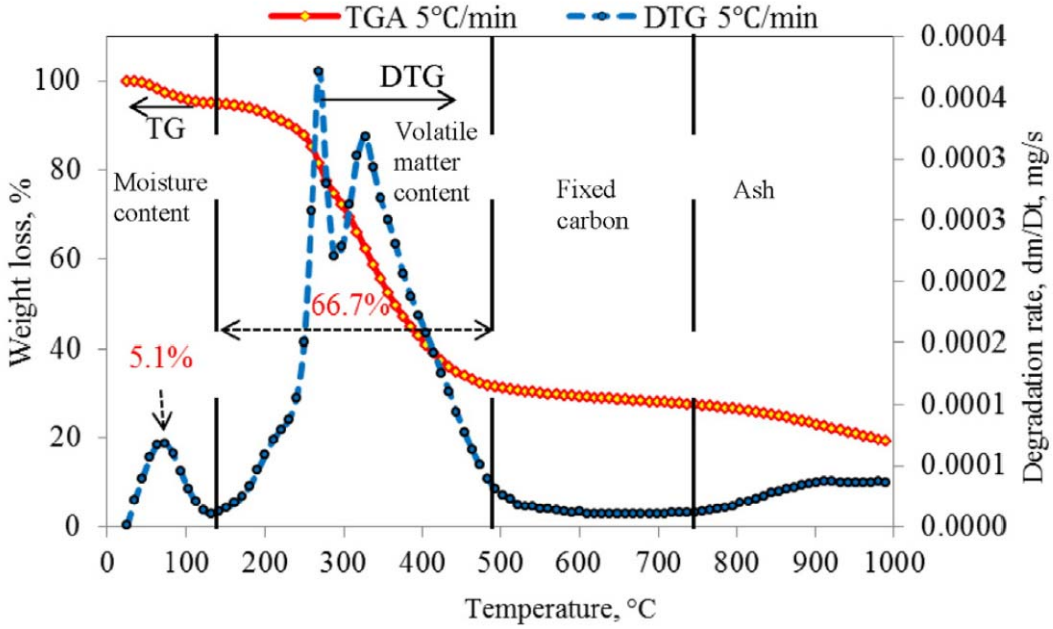

Source: Raheem et al. (2015).

In order to elucidate in more detail the mechanism, the iso-conversional method serves as a useful tool to discriminate the distribution of the activation energy E. Since the activation energy depends only on temperature, it serves as a discriminator to know at

the peaks if there is reasonably one activation energy value. Therefore, one single step reaction can be considered. On the contrary, a more complex process can exist such as two overlapped and or competitive processes. A good example is shown in Figure 57 of a reaction with two separate steps with a reasonable constant value of the activation energy as referenced by Vyazovkin (VYAVZOVKIN, 2015) for the dehydration of *nedocromil sodium trihydrate.* If the compensation effect of eq.(70) is used, it allows the pre-exponential factor to be determined reasonably well based on the linearly relationship.

Figure 57 - Two step iso-conversional method applied to the dehydration of *nedocromil sodium trihydrate* (VYAVZOVKIN, 2015) (step one described by diamond symbols and step two is described with triangles symbols).

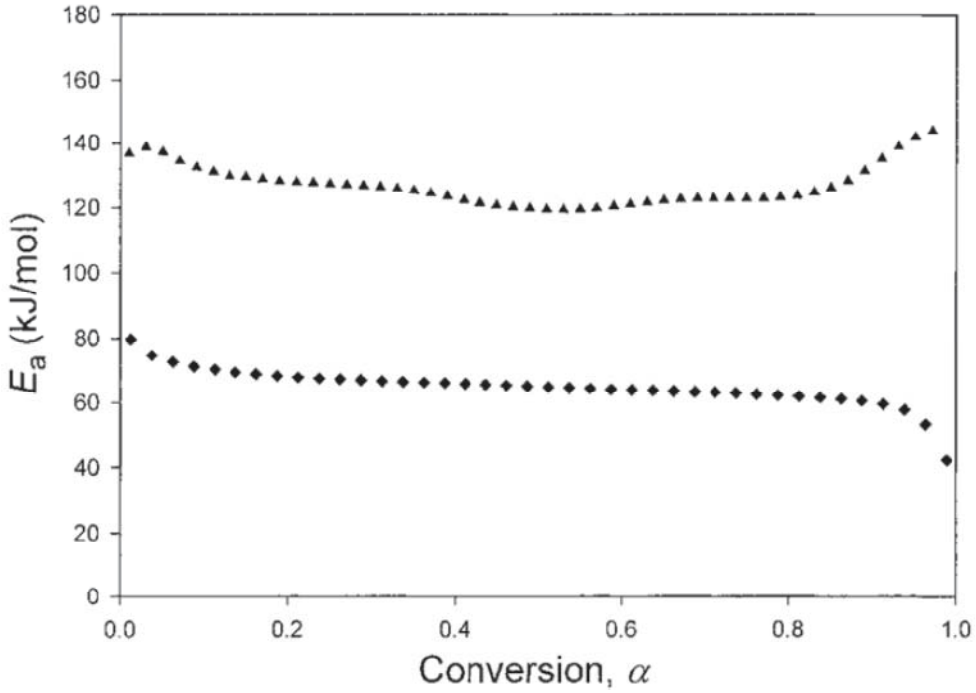

Source: Vyazovkin (2015).

For complex materials with supposedly more than one single reaction step, it is possible to perform a multi-step simultaneously fitting process in order to determine the kinetic triplet for each reaction starting from the generalized reaction model presented in eq.(73). This method accounts for a minimization problem and tries to fit several kinetic parameters such as *n*, *m and p* of eq.(73) and also *component mass fraction* to determinate the reaction models in conjunction of the kinetic parameters E and A. Since there is an optimization problem, constraints must be supplied. One constraint is the mass conservation that states that the sum of the total mass devolatilized by each reaction must correspond with overall mass devolatilized by the whole process. This

constraint is calculated as the integral value of the rate eq.(32). There are software packages such as TDPro and its module FK (Formal Kinetics) capable to fit up to six independent reactions. However, direct processing of thermal analysis data with this software does not guarantee that the kinetic triplet and specifically the kinetic parameters are the effective ones. Therefore, the use of this type of package is useful if a previous iso-conversional is made.

The simultaneous multi-step fitting process is a procedure that needs a numerical method in order to determine several parameters of eq.(73), and the convergence is not always guaranteed, and in the case of the software packages TDPro is useless for more than six independent reactions. A different approach that uses this type of software and its capability for minimization is to isolate each peak of thermal analysis. Then, perform an iso-conversional analysis to determine the kinetic parameters E and A and finally identify the model parameters *m*, *n* and *p.* This method accounts for a deconvolution of the DTG curve.

3.3.9. DECONVOLUTION TECHNIQUE

In order to determine several reactions using the iso-conversional procedure a deconvolution technique can be applied to DTG data. The basic idea behind the method consists in proposing a parameterized shape function for each reaction in where the sum of the contribution of each, results in an overall curve that minimizes the sum of square error matching the experimental curve. It is worth to note that the rate equation eq.(32) is obviously a function capable of fitting the data, however, the parameters of this equation are not shape parameters, instead, they are physical parameters.

The parameterized function may have parameters that allow the definition of shape characteristics such center, height, width and symmetry. These four parameters permit a straightforward modeling of the overall curve as a contribution of single ones. Also, an optimization process can be performed in order to refine the approximation. The advantage and the main difference between the deconvolution and the simultaneous optimization is that the latter must process a vast amount of data of different heating rates in order to determine all the parameters of eq.(73) for each reaction. On the contrary, the deconvolution technique allows each reaction to be isolated for further independent kinetic analysis.

Perejón et al. (2011) presents in its work three parameterized shape functions in order to perform a deconvolution: Gauss normal, Weibull, Lorentzian and an additional fourth, the Fraser-Suzuki shape function. The author states in his work that the Fraser-Suzuki equation is the best one to model the thermal analysis data because of the fact that it can deal with asymmetries and avoid false overlapping. The former comes from the fact that the Fraser-Suzuki equation has a built-in asymmetry parameter while the Gaussian and Lorentzian have no such parameter. The latter comes from the fact that the Gauss function can be useless due to the fact that for one set of kinetic parameters $E = 150\ kJ/mol$ and $A = 6E13\ 1/min$ with an Avrami-Eforeev reaction model (reaction models 8 to 10 in Table 26) is necessary three Gauss shape functions in order to fit the data as showed in Figure 58, resulting in false deconvolution.

Figure 58 - Reconstruction with Gauss shape function of simulated data for first order model reaction with kinetic parameters $E = 150\ kJ/mol$ and $A = 6E13\ 1/min$

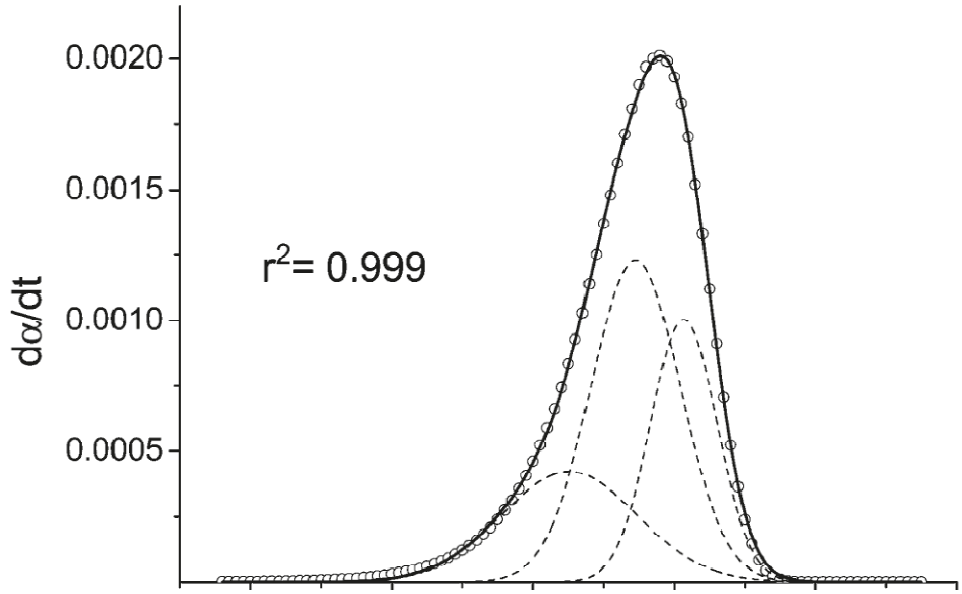

Source: Perejón et al. (2011).

On the other hand, the use of Fraser-Suzuki fits the data, with the same kinetic parameters and reaction model with only one shape function and with value of the correlation coefficient $r = 0.999$ as is showed in Figure 59.

The deconvolution technique thus provides a useful path to analyzing complex thermal devolatilization isolating, as a guess, the different reactions that compose the whole

process. In the case of devolatilization and pyrolysis of *Chlorella Vulgaris* this technique can provide in the future a tool to analyze the complex process as was presented in Chapter 2, in where practically all the works reviewed have shown more than one peak in DTG char.

Figure 59. Reconstruction with Fraser-Suzuki shape function of simulated data Avrami-Eforeev model reaction with kinetic parameters $E = 150\ kJ/mol$ and $A = 6E13\ 1/min$ (Pajerón et. al, 2015).

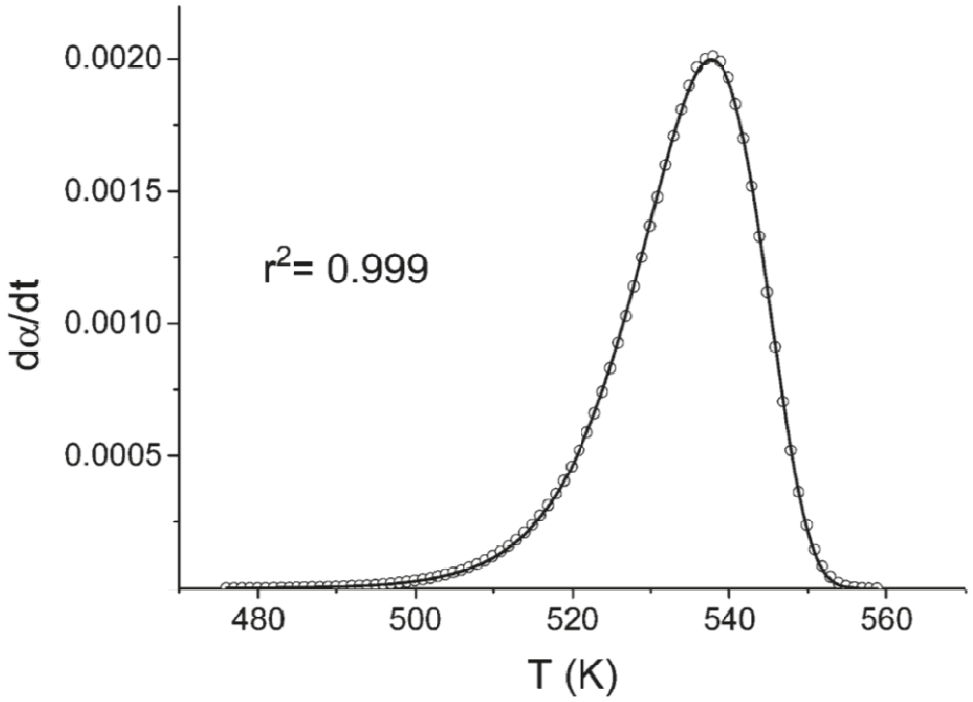

Source: Perejón et al. (2011).

3.3.10. NUMERICAL SOLUTION FOR RATE EQUATIONS

The objective of this work is to develop a reaction mechanism for the primary pyrolysis of *Chlorella Vulgaris* in order to use it in a CFD application. Section 3.1 introduces information about the composition of the microalgae that helps with the discrimination about the kinetics involved in the process while sub-sections from 3.3.1 to 3.3.9 presented the principles and methods to determine these kinetic parameters for complex materials. Pyrolysis process inside a reactor is controlled in part by chemical kinetics in conjunction with the hydrodynamics. Even thought chemical kinetics are coupled with hydrodynamics, the reaction mechanism can be solved locally and a numerical solution different than the solution procedure for hydrodynamics is needed.

The following section presents the procedure in order to solve a set of rate equations by means a numerical method.

Figure 60 – Proposed global multi-stage reaction mechanisms for *Chlorella Vulgaris* components.

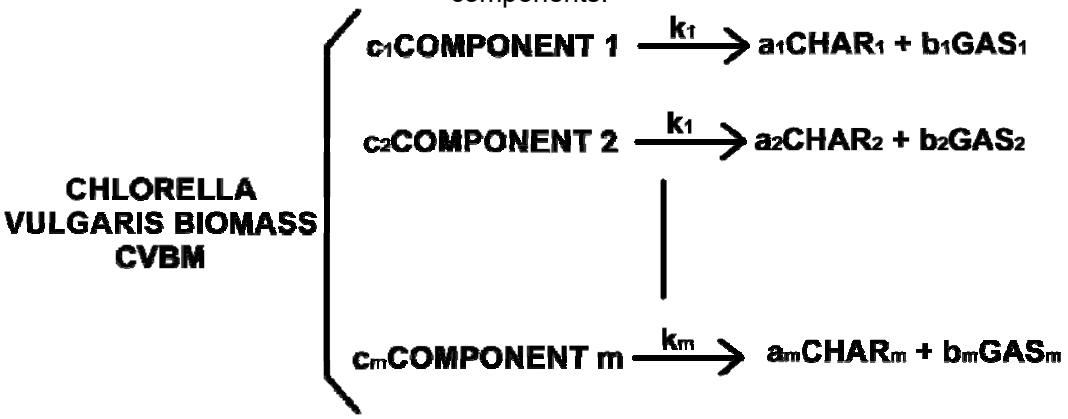

Following the scheme presented in Figure 60, two assumptions are introduced. First, the rate coefficients k_1, to k_m, are defined following the basic Arrhenius expression i.e. (DAVIS; DAVIS, 2012, p 54):

$$k_i = A_{0,i} exp\left(\frac{-E_i}{RT}\right) \tag{74}$$

Where the kinetic parameters A_0 and E must be determined. And secondly, the superimposed principle is applied (MILLER; BELLAN, 1997), then *m* independent reaction of order n_i is considered (See Figure 60). By applying the latter assumption, the rate equation for any number of pseudo-components of a complex material can be described in general by

$$\frac{d(CVBM)}{dt} = \sum_{i=1}^{m} \frac{d(Comp_i)}{dt} = \sum_{i=1}^{m} c_i k_i COMP^{n_i} \tag{75}$$

Where $CVBM$is the acronym of *Chlorella Vulgaris* Biomass. Considering that the sum of coefficients a and b in the reaction template is equal to the mass fraction of c

$$c_i = a_i + b_i \tag{76}$$

The products can be calculated form the following equation

$$\frac{d(Products)}{dt} = \sum_{i=1}^{m} \frac{d(Char_i)}{dt} + \frac{d(Gas_i)}{dt} = \sum_{i=1}^{m} a_i \frac{d(Comp_i)}{dt} + \sum_{i=1}^{m} b_i \frac{d(Comp_i)}{dt} \quad (77)$$

Therefore, solving system of non-linear eq.(77), the mass loss and the product release can be calculated. The kinetics constant is expressed under the basic Arrhenius structure; therefore, a set of kinetic parameters must be determined. In order to solve the system, $4m$ kinetic sets must be supplied i.e. c_i, A, E and n_i. The system of equation can be solved independently because of the application of the superimposed principle that neglect the cross effects.

With the objective of determining the reaction rate of the microalgae biomass and the release rate of gases and char, a numerical solution for the following generic equation must be solved.

$$\frac{dComp}{dt} = -Aexp\left(\frac{-E_i}{RT}\right) Comp^n \quad (78)$$

The most simple solution method for types of non-linear ordinary differential equations is the explicit Euler scheme

$$Comp^{t+\Delta t} = Comp^t + \left[Aexp\left(\frac{-E_i}{RT}\right) Comp\right]^t \Delta t \quad (79)$$

However, the explicit scheme can produce negative mass and therefore inconsistencies. A better and more stable scheme is the totally implicit Euler scheme

$$Comp^{t+\Delta t} = Comp^t + \left[Aexp\left(\frac{-E_i}{RT}\right) Comp\right]^{t+\Delta t} \Delta t \quad (80)$$

In where the derivative is evaluated in the time point $t + \Delta t$, a time in where neither the mass nor temperature of $Comp$ is known. To solve this issue the approach named the predictor-corrector can be used and is explained as follow. The first step is to predict the value with a low order estimator such as the explicit Euler method and then correct it with a more stable and accurate method. Other robust method, frequently used is the Runge-Kutta method, which has several schemes that can improve significantly the convergence rate and the accuracy. Finally, often in kinetic calculations issues can arise due to the large difference in the reaction rates, so, special solvers named stiff solvers

must be applied. However, since the reaction mechanism developed in this work does not account for a secondary cracking reaction, the order of the rate of reaction of the decomposition of the different component is expected to be similar. Therefore, the use of a stiff solver is not to be used.

3.4. MULTI-PHASE FLOW DYNAMICS

The multi-phase theory can found described in detail in the very useful books of Jakobsen (2008), Ishii and Hibiki (2010) or in Wallis (1969) for one, two or three dimensions. In this section are presented the topics related to the multi-phase flow approach and the background for the numerical solution using the finite volume method (FV) in conjunction with other components for general fluid dynamics. The section starts with the formal procedure developed by Ishii and Hibiki (2010) in order to establish the conservation equations when two different phases flow together. The objective is to obtain an approximate model that can capture the main characteristics of the flow considering two continuous flowing fields, that in the rigorous sense, at least one of the fields is a dispersed phase. Remaining sub-sections are dedicated to show the concepts behind the Granular Kinetic Theory, turbulence, radiative heat transfer and the basis of the finite volume method.

As aforementioned through this document, no papers were found related to the modeling of a fast pyrolysis in a reactor using neither for the microalgae biomass nor for the *Chlorella Vulgaris.* The lack of works is probably due to a comprehensive reaction mechanism for microalgae pyrolysis is not developed so far.

One of the objectives of this research is to demonstrate the applicability of the reaction mechanism in a CFD simulation of fast pyrolysis of microalgae, and to predict the final char yield and the total lumped gas produced. Therefore, in order to simulate the thermal decomposition of microalgae, a process scheme must be proposed based on fluid dynamics of two different phases i.e. a solid phase of microalgae powder and a gas phase composed of a mixture of several gases.

As mentioned before, authors Grierson et al. (2009), Belotti et al. (2014), Wang et al. (2013), Yuan; Tahmasebi and Yu (2015) and Gong et al. (2014) performed studies about the thermal decomposition of *Chlorella Vulgaris* using a lab-scale pyrolyzer. The

type of reactor used by the authors was different, and a full specification about the pyrolysis parameters, in general, were not provided. However, Yuan; Tahmasebi and Yu (2015) and Gong et al. (2014) provided a brief description of their experiments and it can be concluded that these experiments were performed with high heating rate and with short residence time, a characteristic strongly related with hydrodynamics.

From the point of view of mathematical modeling, a continuous fluidized bed reactor (CFBR) presents a challenge about the degree of accuracy obtained from approximate description of the flow fields provided form the multiphase flow theory. The lack of a better accuracy provided by the multiphase flow theory relay on the treatment of discontinuities due to the existence of an interface between the phases. However, despite this issue several papers have been published describing the thermal decomposition of complex materials using the multiphase theory and a CFD codes with good results.

Mellin et al. (2013), Mellin; Zhang, Kantarelis and Yang (2013) , Xiong et al. (2014), Xue; Heindel and Fox (2011), Rostami;Hajaligol and Wrenn (2004) and Yu et al. (2014) have developed simulations and sub-models for CFD considering: one, two and three dimensions, multi-phase flow and turbulence descriptions for fluidized bed reactors. These three characteristics add complexities to the modeling. Considering the characteristics of fast pyrolysis short residence times can be achieved with high velocities inside the reactor in order to bring out the volatiles from the reaction zone. Also, high heating rates can be achieved due to the heat transfer caused by the intense mixing between the biomass particles and hot sand or gas and/or with heat transfer from reactor walls. Therefore, the combination of high velocities and intensive mixing are characteristic for fluidized bed and circulating fluidized bed reactors, FB and CFB respectively, and cannot be avoided in a mathematical description.

3.4.1. BASES OF MULTI-PHASE FLOW THEORY

Fast pyrolysis is commonly performed in FB and in CFB reactors and as has been mentioned, high velocities and high heating rates are common characteristics of both types of reactors. Other common characteristics between these types of reactors is that there is a mixture of solids i.e. biomass and sand flowing together with gas, or only

biomass and gas flowing together. The dynamic description of two phases or components that flow together interactively can be generally classified as the Eulerian-Eulerian and the Lagrangian-Eulerian approaches. In the Lagrangian-Eulerian approach the solid phase is treated as a set of discrete particles and each particle needs to be tracked in order to describe its dynamics with a set of equations of motion. The Lagrangian-Euler approach is feasible only when the solid phase can be considered diluted. In the Eulerian-Eulerian approach the solid phases are treated as a continuous phase but dispersed, and the diluted condition is not necessary (JAKOBSEN, 2008).

Since multi-phase flows have, at least two phases, the conservation equations must be developed for each phase and may include an interface description, in which mass momentum and energy are exchanged. There are several approaches and procedures to obtain a set of suitable equations for different applications, as mentioned by Ishii and Hibiki (2010, p. 58). For example, Jakobsen (2008, p. 429) starts from a microscopic description in order to obtain the conservation equation for two-phase flows averaging over time, volume or using the statistical ensemble approach. The mathematical formulation of the local instantaneous equations starts with the integral balance principle applied on a fixed control volume (CV), through which the fluid flows, containing two continuous phases separated by an interface across which the physical properties are discontinuous and may jump. The integral equations are then transformed by using the Leibniz rule and the Gauss theorem to obtain a sum of two volume integrals and a surface integral.

In order to define a suitable model for a CFB reactor or similar systems, considering physical properties of biomass, it is necessary to understand all the terms and its meanings in the set of conservation equations. It is possible only understanding the basic assumptions and approximations applied. A systematic and detailed description was provided by Ishii and Hibiki (2010, p. 67), named the two-fluid model, in order to develop a general set of conservation equations, starting from the fact that there are discontinuities i.e. an interface in the flow field.

Three types of models can be developed from the two-fluid theory, each with its own suitable characteristics to describe specific processes, the complete two-fluid model, and two reduced models: the mixture and the drift models. A flow with two phases or

components is the basic system of multi-phase flows, and the starting point to describe systems for *n* phases or components.

3.4.1.1. AVERAGING

Averaging can be made over space, over time or by considering a pure statistical approach. Statistical type of averaging is named the ensemble method and is not mentioned here. The objective of the space averaging or volume and time averaging is to obtain a smooth and continuous function of the transported properties. Since multi-phase flows can have a dispersed phase such as sand and/or biomass particles, by definition, discontinued phases, the averaging produces a smooth and continuous function that describes the dispersed phase. However, the jump conditions are also averaged in order to obtain the relations to account for the exchanges through interfaces. The procedure to obtain averaged field equations starts with the application of the Leibnitz's rule and the Gauss's theorem for phases and interfaces (JAKOBSEN, 2008, p. 404). Then, an averaging operator is applied for both transport equation and jump conditions. Averaged products of variables are obtained; however, as a consequence a covariance term arises coupling the transport equations.

The time averaging procedure is similar to the space procedure and it is applied to the microscopic instantaneous transport equation. The macroscopic multi-phase models resulting from the local averaging procedures must be combined with state equations, constitutive equations, boundary and initial conditions. The constitutive equations (closure laws) specify how the phases interact with themselves and with each other. Finally as stated by Jakobsen (2008) the accurate modeling of multiphase flows requires that the phase interaction terms given by the jump conditions and the turbulent like effects are correctly parameterized.

3.4.1.2. TIME AVERAGING

As mentioned by Ishii and Hibiki (2010) there is an obvious fact that in flows with two or more phases there is one and only one phase or interface passing on a fixed point $\boldsymbol{x_0}$ in a time t_0. This means that in one point $\boldsymbol{x_0}$ cannot coexist two phases and/or a phase and an interface simultaneously. It is worth to note that the point $\boldsymbol{x_0}$ and the space surrounding it, is conceived in terms of the hypothesis of the continuum (WHITE, 1999).

Viewing the $\boldsymbol{x_0}$ point along a time ΔT it is possible to detect the alternative switching between phases and eventually the passing of an interface thin layer (Figure 61). This layer can produce sharp changes on field variables, i.e. discontinuities, or jumps from the value of one phase to the value of another phase. This discrete description may cause the impossibility to apply a sufficiently smooth continuous description.

Figure 61 - Alternating phases and interface passing on a fixed point in space.

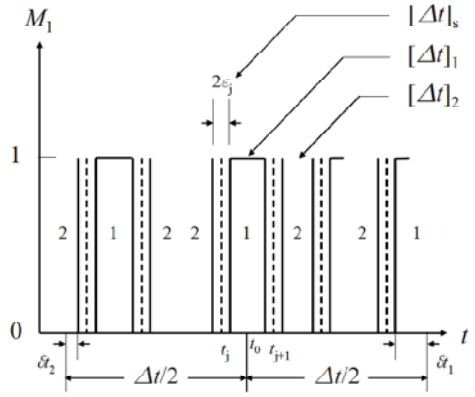

Sourcer: Ishii and Hibiki (2010).

In order to obtain a continuous field description, including the phases and the interactions through the interface, and average over the time interval ΔT is applied. The purpose of the averaging procedure is to reduce the local instant fluctuations caused by the phase switching and turbulence, providing smooth mean values of field quantities whether they are variables or fluid properties. The averaging over the time implies that the differential time interval will be larger than the infinitesimal time interval provided by the hypothesis of continuum, therefore, the time scale will depend on the structure of the flow field. In other words, the first assumption made is that the time averaging procedure describes a real field of two phase flows that cannot occupy the same place at the same time, in terms of two continuous flow fields that can coexist in $\boldsymbol{x_0}$ at the same time t_0.

This approximated description is developed using the scheme of Figure 61. In the time interval ΔT alternatively passes the phase 1, 2 and the interface in a random motion. It is worth to note that if an observer can view a comprehensive set of fixed points $\boldsymbol{x_0}$ at the time t_0, the observer may view several points in which an interface is passing through. This global view of various points gives to the observer information about the

structure of the flow showing the usefulness of this approach. The entire interval ΔT can be divided in subintervals such that

$$\Delta T = [\Delta T]_s + [\Delta T]_1 + [\Delta T]_2 \tag{81}$$

Where $[\Delta T]_1$ and $[\Delta T]_2$ are the total time, over ΔT, in which one and only one of the phases was at the point $\boldsymbol{x_0}$. The width of $[\Delta T]_s$ can be defined as

$$[\Delta T]_s = \left[t_j - \epsilon_j; t_j + \epsilon_j\right] \tag{82}$$

A further definition is suggested by Ishii and Hibiki (2010) for the faces time intervals

$$[\Delta T] = [\Delta T]_1 + [\Delta T]_2 \tag{83}$$

Therefore, the total time interval can be expressed by the following

$$\Delta T = [\Delta T]_s + \sum_{k=1}^{2} [\Delta T]_k \tag{84}$$

For the case of two phases, Ishii and Hibiki (2010) define the *state density functions* M_k and M_s, with the following properties:

$$M_k(\boldsymbol{x}, t) = 1 \; and \; M_s(\boldsymbol{x}, t) = 0 \; if \; a \; point \; x \; is \; ocupied \; by \; the \; k^{th} \; phase \tag{85}$$

And

$$M_k(\boldsymbol{x}, t) = 0 \; and \; M_s(\boldsymbol{x}, t) = 1 \; if \; a \; point \; x \; is \; ocupied \; by \; the \; interface \tag{86}$$

If a general function *F* is defined and associated to each phases and outside the time interval δ for the interface, then F_k can be defined as

$$F_k(\boldsymbol{x_0}, t) = \; M_k(\boldsymbol{x_0}, t)F = \begin{cases} F(\boldsymbol{x_0}, t) \; if \; t \in [\Delta t]_k \\ 0 \quad if \; t \; not \in [\Delta t]_k \end{cases} \tag{87}$$

It is worth noting that *F* and F_k are the instantaneous values of fields. If the interphase time interval δ tends to 0, it is possible to take the following limit

$$\Delta t_1 = \lim_{\delta \to 0} \left\{ \sum\nolimits_j \left[\left(t_{j+1} - \epsilon_{j+1}\right) - \left(t_j + \epsilon\right) \right] + \delta \mathrm{t}_1 \right\} \ldots\ldots \; j = 2m - 1 \tag{88}$$

$$\Delta t_2 = \lim_{\delta \to 0} \left\{ \sum\nolimits_j \left[\left(t_{j+1} - \epsilon_{j+1}\right) - \left(t_j + \epsilon_j\right) \right] + \delta \mathrm{t}_2 \right\} \ldots\ldots \; j = 2m$$

Where m is a counter that indicates an even and odd consecutive shifts of interfaces on the point x_0. Therefore

$$\Delta t = [\Delta t]_1 + [\Delta t]_2 \tag{89}$$

Then it is possible to define the *averaged phase density function* if the interface has a normal velocity v_{ni} different from 0, that means a moving interface. Averaged phase density function is defined by the following equation

$$\varepsilon_k(\boldsymbol{x_0}, t) \equiv \lim_{\delta \to 0} \frac{1}{\Delta t} \int_{[\Delta t]} M_k(\boldsymbol{x_0}, t) dt \tag{90}$$

Where ε_k is the temporal void fraction (or volume fraction) of the phase *k*. It is defined here as the averaged presence of phase *k* on the point $\boldsymbol{x_0}$ in the time interval Δt. It is worth to note that if Δt is the time interval for rapid fluctuations, then Δt can be considered an infinitesimal time interval, then ε_k is the instantaneous volume fraction of the phase *k* in a volume around the point $\boldsymbol{x_0}$. Accordingly, ε_k can give information about the instantaneous structure of the flow, and therefore it is a field property. From the definiton of the *phase density functions* the void fraction can be expressed as

$$\varepsilon_k = \frac{\Delta t_k}{\Delta t} = \bar{M}_k \tag{91}$$

And therefore due to eq.(90)

$$\varepsilon_1 + \varepsilon_2 = 1 \tag{92}$$

In the same way as eq.(90), other field variables can be averaged over the time interval Δt. By taking the generic function *F*

$$\bar{F}(\boldsymbol{x_0}, t) \equiv \lim_{\delta \to 0} \frac{1}{\Delta t} \int_{[\Delta t]} F(\boldsymbol{x_0}, t) dt \tag{93}$$

and

$$\bar{F}_k(\boldsymbol{x_0}, t) \equiv \lim_{\delta \to 0} \frac{1}{\Delta t} \int_{[\Delta t]} F_k(\boldsymbol{x_0}, t) dt \tag{94}$$

$\bar{F}$ and $\bar{F}_k$ are the Eulerian averaged in the time interval $[\Delta t]$ and its means that the averaged is performed with the assumption that only the $\bar{F}$ and $\bar{F}_k$ were present in the

point $\boldsymbol{x_0}$ at the time interval. Since other phases could be on the point at the same time interval, the averaged value is an apparent value, named as *superficially mean value* due to the fact that it has been obtained as if only the phase *k* had been in volume in the time interval. It is worth to note that the instantaneous *F* values is averaged in time but related to the volume around the point $\boldsymbol{x_0}$, it is mean that *F* is a volumetric based quantity. As a consequence of eq.(90) and eq.(92).

$$\bar{F}(\boldsymbol{x_0}, t) \equiv \lim_{\delta \to 0} \frac{1}{\Delta t} \int_{[\Delta t]} F_1(\boldsymbol{x_0}, t) dt + \lim_{\delta \to 0} \frac{1}{\Delta t} \int_{[\Delta t]} F_2(\boldsymbol{x_0}, t) dt \tag{95}$$

And

$$\bar{F} = \overline{F_1} + \overline{F_2} \tag{96}$$

Ishii and Hibiki (2010) defines a generic weighted mean value for *F*

$$\bar{F}^{\omega} = \frac{\overline{\omega F}}{\bar{\omega}} \tag{97}$$

And

$$\bar{F}_k^{\omega} = \frac{\overline{\omega_k F_k}}{\bar{\omega}_k} \tag{98}$$

If *w* is not normalized. The weighted function w is defined in the same way as *F*, as a volumetric based quantity. If w is the density, a volumetric based quantity, a weighted equation can be obtained using eq.(96), eq.(97) and eq.(98), then it is possible to state that

$$\bar{F}^{\omega} = \frac{\sum_{k=1}^{2} \overline{\omega_k F_k}}{\bar{\omega}} = \frac{\sum_{k=1}^{2} \bar{\omega}_k \bar{F}_k}{\sum_{k=1}^{2} \bar{\omega}_k} \tag{99}$$

That relates the mixture quantity mean value $\bar{F}^{\omega}$ with the superficial phase mean value. The $\bar{F}_k$ term is the apparent mean value, therefore the specific mean value $\bar{\bar{F}}_k$ of $F_k$can be defined by taking the integral over the time interval $[\Delta t]_k$. Following the definition on weighted mean value and since M_k can only be 1 in the interval $[\Delta t]_k$, and using eq.(91)

$$\bar{\bar{F}}_k \equiv \frac{\overline{M_k F_k}}{\overline{M_k}} = \frac{\bar{F}_k}{\varepsilon_k} \tag{100}$$

And using the integral mean value definition

$$\bar{\bar{F}}_k \equiv \frac{\overline{M_k F_k}}{\overline{M_k}} = \frac{\bar{F}_k}{\varepsilon_k} = \int_{[\Delta t]} F_k \, dt \tag{101}$$

Therefore $\bar{\bar{F}}_k$ can be considered the effective mean value of F_k. As a consequence

$$\bar{F}_k = \varepsilon_k \bar{\bar{F}}_k \tag{102}$$

And

$$\bar{F} = \sum_{k=1}^{2} \varepsilon_k \bar{\bar{F}} \tag{103}$$

eq.(103) relates an effective quantity mean value of any phase with the apparent superficial value. The transformation provided by the eq.(103) is useful for experiments, since when there is a dispersed phase with a high time-spatial fluctuations, the measures of local quantities based on the phase specific flow area is difficult, however the measure based on the local total area is more suitable experimentally.

If the instantaneous volumetric *F* function is expressed by means a mass based quantity

$$F = \rho\psi \tag{104}$$

Then

$$\overline{\rho\psi} = \sum_{k=1}^{2} \overline{\rho_k \psi_k} \tag{105}$$

Since the density ρ is a volume based quantity it is possible to define a mass weighted mean value according to Ishii and Hibiki (2010)

$$\hat{\psi}_k = \frac{\overline{\rho_k \psi_k}}{\bar{\rho}_k} = \frac{\frac{\overline{\rho_k \psi_k}}{\varepsilon_k}}{\frac{\bar{\rho}_k}{\varepsilon_k}} = \frac{\overline{\overline{\rho_k \psi_k}}}{\bar{\bar{\rho}}_k} \tag{106}$$

therefore

$$\overline{\rho\psi} = \sum_{k=1}^{2} \bar{\rho}_k \hat{\psi}_k = \sum_{k=1}^{2} \varepsilon_k \bar{\bar{\rho}}_k \hat{\psi}_k \tag{107}$$

And since by definition of weighted mean

$$\overline{\rho\psi} = \bar{\rho}\hat{\psi} \tag{108}$$

Then

$$\bar{\rho}\hat{\psi} = \sum_{k=1}^{2} \varepsilon_k \overline{\overline{\rho_k}}\hat{\psi}_k \tag{109}$$

All this relation allows expressing mixture quantities based on mass by means of a sum of specific or apparent values for each phase. As mentioned before in view of averaging and of the concept of simultaneously presence of two phases at the same point and at the same time, the time interval can be considered an infinitesimal time interval, in which both phases coexist simultaneously as a continuous function allowing for example, the differentiation. Therefore, as stated by Ishii and Hibiki (2010)

$$\overline{(\bar{F})} = \bar{F}(x_0, t_0) \tag{110}$$

That means that $\bar{F}(x_0, t_0)$ is the instantaneous value of the field quantity $\bar{F}$ in the point x_0 at the time t_0 in the averaged scale time. The development of the concept of averaged in time allows defining field conservation equations for multiphase flows like a single phase flow. However, the interface can exchange of quantities like mass, momentum and energy coupling both phases, therefore a term related to the interface balance must be developed to close these equations.

3.4.2. BALANCE EQUATIONS FOR PHASES AND JUMP CONDITIONS

Based on the fundamental relations reviewed in the past section the balance equations can be derived including the effect of the interface. The first step in order to obtain the balance equation for volume centered in the point $\boldsymbol{x_0}$ is to compute the derivative of a volumetric based quantity in the Eulerian context, including the simultaneous existence of two phases and the interface. According to Ishii and Hibiki (2010) the derivative of a mean field quantity, results from the applying the partial time derivative to the generic volume based mean quantity, and considering the interface as a thin layer of width δ

$$\frac{\partial}{\partial t}\bar{F} = \frac{1}{\Delta t}\lim_{\delta \to 0}\left\{\int_{\Delta t} \frac{\partial F(x_0, t)}{\partial t} dt + \sum_j F\left(x_0, t_j + \epsilon_j\right) - F\left(x_0, t_j - \epsilon_j\right)\right\} \tag{111}$$

Where by definition yield the derivative for the interface. From Figure 61 when $\delta \to 0$ then $t_j \pm \epsilon_j \to t_0$, then is defined

$$\lim_{\epsilon_j \to 0} F\left(x_0, t_j + \epsilon_j\right) = F\left(x_0, t_j^{\pm}\right) \equiv F^{\pm}\left(x_0, t_j\right) \tag{112}$$

And eq.(111) can be expressed as

$$\overline{\frac{\partial F}{\partial t}} = \frac{\partial \bar{F}(x_0, t_0)}{\partial t} - \frac{1}{\Delta t}\sum_j F^{+}\left(x_0, t_j\right) - F^{-}\left(x_0, t_j\right) \tag{113}$$

And the space derivative

$$\overline{\nabla F} = \lim_{\delta \to 0} \frac{1}{\Delta t}\left\{\int_{[\Delta t]_T} F(x_0, t)\, dt\right\} \tag{114}$$

And expanding considering the interface

$$\begin{aligned}\overline{\nabla F} = \lim_{\delta \to 0}\Bigg\{\nabla\left[\frac{1}{\Delta t}\int_{[\Delta t]_T} F(x_0, t)\, dt\right] + \frac{1}{\Delta t}\sum_j -\nabla\left(t_j - \epsilon_j\right)F\left(x_0, t_j - \epsilon_j\right) \\ + \nabla\left(t_j + \epsilon_j\right)F\left(x_0, t_j + \epsilon_j\right)\Bigg\}\end{aligned} \tag{115}$$

Yields

$$\overline{\nabla F} = \nabla \bar{\mathrm{F}}(x_0, t_0) + \frac{1}{\Delta t}\frac{1}{v_{ni}}\sum_j \mathrm{n}^{+}F\left(x_0, t_j^{+}\right) + \mathrm{n}^{-}F\left(x_0, t_j^{-}\right) \tag{116}$$

In where a relation of eq.(117) is used for a moving interface provided by Ishii and Hibiki (2010) that relates the gradient of the moving interface with the normal displacement velocity vector v_{ni}.

$$\nabla \mathrm{t_j} = \frac{n}{\boldsymbol{v_{ni}} \cdot n} \tag{117}$$

Where$\nabla \mathrm{t_j} = \nabla\left(t_j + \epsilon_j\right)\epsilon_j \to 0$ and n is the instantaneous normal vector of the moving surface. Using the definition of the normal displacement

$$\boldsymbol{v_i} \cdot n \equiv v_{ni} \tag{118}$$

The derivatives for time and space are

$$\overline{\frac{\partial F}{\partial t}} = \frac{\partial \bar{F}(x_0, t_0)}{\partial t} - \frac{1}{\Delta t}\sum_j \frac{1}{v_{ni}}[F^+ n^+ \cdot v_i + F^- n^- \cdot v_i] \tag{119}$$

$$\overline{\nabla F} = \nabla \bar{\mathrm{F}}(x_0, t_0) + \frac{1}{\Delta t}\sum_j \frac{1}{v_{ni}}(\mathrm{n}^+ F^+ + \mathrm{n}^- F^-) \tag{120}$$

eq.(119) and eq.(120) express the mean of a derivative of a mixture quantity in terms of a derivative of a mean mixture quantity. For each phase derivatives for time and space are

$$\overline{\frac{\partial F_k}{\partial t}} = \frac{\partial \bar{F}_k(x_0, t_0)}{\partial t} - \frac{1}{\Delta t}\sum_j \frac{1}{v_{ni}}[F_k n_k \cdot v_i] \tag{121}$$

$$\overline{\nabla F_k} = \nabla \bar{\mathrm{F}}_\mathrm{k}(x_0, t_0) + \frac{1}{\Delta t}\sum_j \frac{1}{v_{ni}}(F_k n_k) \tag{122}$$

3.4.3. MIXTURE CENTER OF MASS VELOCITY FIELD

The *mixture center of mass velocity* is defined using eq.(109)119a, and state that it is a velocity based on the momentum of an amount of mass in a volume centered in $\boldsymbol{x_0}$

$$\boldsymbol{v_m} = \frac{\sum_{k=1}^{2} \varepsilon_k \overline{\overline{\rho_k}} \hat{v}_k}{\rho_m} = \sum_{k=1}^{2} Y_k \hat{v}_k \tag{123}$$

Where Y_k is defined as the *mass fraction.* It is worth to note that all variables and properties can be expressed in the form of eq.(123)

3.4.4. OTHER VELOCITY FIELDS

According to Ishii and Hibiki (2010) different velocity fields can be defined in order to study different flows. The relative center of mass velocity is defined as

$$\boldsymbol{v_r} \equiv \hat{v}_2 - \hat{v}_1 \tag{124}$$

The volumetric flux, or following the definition a superficially velocity

$$\boldsymbol{j_k} \equiv \varepsilon_k \hat{v}_k \tag{125}$$

It is worth to note that for two phase flows the velocity $\boldsymbol{j_k}$ differs from the velocity $\boldsymbol{v_k}$ due to the different phase densities. Another velocity field centered on mass is the diffusion velocity

$$\boldsymbol{V_{km}} \equiv \hat{v}_k - v_m \tag{126}$$

And the drift velocity

$$\boldsymbol{V_{kj}} \equiv \hat{v}_k - j \tag{127}$$

3.4.5. FLUCTUATING COMPONENTS

In the same way as in turbulence, and due to the alternating phases and turbulence in a point $\boldsymbol{x_0}$, the instantaneous value is defined as a sum of a mean value and a statistical fluctuating value (ISHII; HIBIKI, 2010) for density, velocity and a generic field value ψ as

$$\rho_k = \overline{\overline{\rho_k}} + \rho_k' \; ; \quad \psi_k = \hat{\psi}_k + \psi_k' \; ; \quad v_k = \hat{v}_k + v_k' \tag{128}$$

As in the averaged analysis of turbulence the mean value of a fluctuation is equal to 0, then

$$\overline{\rho_k'} = 0 \; ; \quad \overline{\psi_k'} = 0 \; ; \quad \overline{v_k'} = 0 \tag{129}$$

Using the definition presented above, a mean of a convective quantity can be expressed as

$$\overline{\rho\psi v} = \rho_m \psi_m v_m + \sum_{k=1}^{2} \varepsilon_k \overline{\overline{\rho_k}} \hat{\psi} V_{km} + \sum_{k=1}^{2} \varepsilon_k \overline{\overline{\rho_k \psi_k' v_k'}} \tag{130}$$

Where the last term is the correlation of the phase and turbulence perturbation, the second term RHS is defined as

$$J^D = \sum_{k=1}^{2} \varepsilon_k \overline{\overline{\rho_k}} \hat{\psi} V_{km} = \frac{\overline{\overline{\rho_1 \rho_2}}}{\rho_m} \sum_{k=1}^{2} \varepsilon_k \hat{\psi} V_{kj} \tag{131}$$

Where the last term is expressed using the drift flux velocity. And

$$J_k^T = \varepsilon_k \overline{\overline{\rho_k \psi_k' v_k'}} \; ; \; J^T = \sum_{k=1}^{2} \varepsilon_k \overline{\overline{\rho_k \psi_k' v_k'}} \tag{132}$$

Therefore the average can be expressed in a short notation as

$$\overline{\rho\psi v} = \rho_m \psi_m v_m + J^D + J^T \tag{133}$$

Deriving eq.(130) in the Eulerian sense

$$\frac{\partial \overline{\rho\psi}}{\partial t} + \nabla \cdot (\overline{\rho\psi v}) = \frac{\partial \rho_m \psi_m}{\partial t} + \nabla \cdot (\rho_m \psi_m v_m) + \nabla \cdot (J^D + J^T) \tag{134}$$

for the mixture, and

$$\frac{\partial \overline{\rho_k \psi_k}}{\partial t} + \nabla \cdot (\overline{\rho_k \psi_k v_k}) = \frac{\partial \varepsilon_k \bar{\bar{\rho}}_k \hat{\psi}_k}{\partial t} + \nabla \cdot \left(\varepsilon_k \bar{\bar{\rho}}_k \hat{\psi}_k \hat{v}_k\right) + \nabla \cdot (\varepsilon_k J_k^T) \tag{135}$$

for the phases alone. Expanding both equation gives the general forms

$$\overline{\left(\frac{\partial \rho\psi}{\partial t}\right)} + \overline{\nabla \cdot (\rho\psi v)} \tag{136}$$
$$= \frac{\partial \rho_m \psi_m}{\partial t} + \nabla \cdot (\rho_m \psi_m v_m) + \nabla \cdot (J^D + J^T)$$
$$+ \frac{1}{\Delta t} \sum_j \frac{1}{v_{ni}} \sum_{k=1}^{2} [n_{k\cdot} \rho_k (v_k - v_i) \psi_k]$$

And

$$\overline{\left(\frac{\partial \rho_k \psi_k}{\partial t}\right)} + \overline{\nabla \cdot (\rho_k \psi_k v_k)} \tag{137}$$
$$= \frac{\partial \varepsilon_k \bar{\bar{\rho}}_k \hat{\psi}_k}{\partial t} + \nabla \cdot \left(\varepsilon_k \bar{\bar{\rho}}_k \hat{\psi}_k \hat{v}_k\right) + \nabla \cdot (\varepsilon_k J_k^T)$$
$$+ \frac{1}{\Delta t} \sum_j \frac{1}{v_{ni}} [n_{k\cdot} \rho_k (v_k - v_i) \psi_k]$$

3.4.6. COMPLETE BALANCE EQUATION FOR PHASES AND INTERFACE

Equations 136 and eq.(137) represent the eulerian balance on a volume centered on $\boldsymbol{x_0}$ for the phases and mixture only. However, it is necessary to derivate a balance considering the interface. According to Ishii and Hibiki (2010) the special balance equation for the initerface is

$$B_s = \frac{1}{\delta}\left\{\frac{d_s}{dt}\psi_a + \psi_a \cdot v_i - \frac{1}{\Delta t}\sum_{k=1}^{2}\frac{1}{v_{ni}}[\rho_k n_k \cdot (v_k - v_i)\psi_k + n_k \cdot J_k] + g_{ln}A^{\alpha\beta}(t_\alpha^n J_\alpha^l)_\beta - S^{\psi_a}\right\} = 0 \quad (138)$$

Where the term $g_{ln}A^{\alpha\beta}(t_\alpha^n J_\alpha^l)_\beta$ was obtained by Ishii and Hibiki (2010) in order to express J_α^l flux in the local coordinate of the moving interface. Defining a instantaneous balance equation for the mixture including diffusion flux J and a source term S^ψ gives

$$B_V = \frac{\partial \rho\psi}{\partial t} + \nabla \cdot (\rho\psi v) + \nabla \cdot J - \rho S^\psi \quad = 0 \quad (139)$$

Defining the total balance as

$$B = B_V + B_s \quad (140)$$

And taking the average, Ishii and Hibiki (2010) obtained the total balance equation for the mixture including the interface

$$\frac{\partial \rho_m \psi_m}{\partial t} + \nabla \cdot (\rho_m \psi_m v_m) + \nabla \cdot (\bar{J} + J^D + J^T) - \rho_m S_m^{\psi_m} + \frac{1}{\Delta t}\sum_j \frac{1}{v_{ni}}\left\{\frac{d_s}{dt}\psi_a + \psi_a \cdot v_i - S_a^{\psi_a}\right\} + \frac{1}{\Delta t}\sum_j g_{ln}A^{\alpha\beta}(t_\alpha^n J_\alpha^l)_\beta = 0 \quad (141)$$

Where $\bar{J}$, $J^D$and $J^T$are the fluxes due to the averaged molecular diffusion, the macroscopic phase diffusions, regarding the center of mass, and the contribution of the fluctuation turbulent effects, respectively. The term $\rho_m S_m^{\psi_m}$ is the volumetric mean source term and the latest two terms are balances at the interface. The eq.(141) states that the quantity ψ is conserved inside a volume centered in $\boldsymbol{x_0}$ considering the exchanges between the phases including the interface. For each phase and considering a source term and molecular diffusion

$$\frac{\partial \alpha_k \bar{\bar{\rho}}_k \hat{\psi}_k}{\partial t} + \nabla \cdot \left(\varepsilon_k \bar{\bar{\rho}}_k \hat{\psi}_k \hat{v}_k\right) + \nabla \cdot \varepsilon_k \left(\bar{\bar{J}}_k + J_k^T\right) - \varepsilon_k \bar{\bar{\rho}}_k \hat{S}_k^{\psi_k} + \frac{1}{\Delta t}\sum_j \frac{1}{v_{ni}}\left[n_k \cdot \rho_k (v_k - v_i)\psi_k + n_k \hat{S}_k^{\psi_k}\right] = 0 \quad (142)$$

Defining the interfacial source term for mixture

$$S_m^{\psi,I} = \frac{1}{\Delta t}\sum_j \frac{1}{v_{ni}}\left\{\frac{d_s}{dt}\psi_a + \psi_a \cdot v_i - S_a^{\psi_a}\right\} + \frac{1}{\Delta t}\sum_j g_{ln}A^{\alpha\beta}(t_\alpha^n J_\alpha^l)_\beta \tag{143}$$

And the interfacial source term for mixture

$$S_k^{\psi,I} = \frac{1}{\Delta t}\sum_j \frac{1}{v_{ni}}\left[n_k.\rho_k(v_k - v_i)\psi_k + n_k\hat{S}_k^{\psi_k}\right] \tag{144}$$

The general balance equations are

$$\frac{\partial \rho_m \psi_m}{\partial t} + \nabla\cdot(\rho_m\psi_m v_m) + \nabla\cdot(\bar{J} + J^D + J^T) - \rho_m S_m^{\psi_m} + S_m^{\psi,I} \tag{145}$$

And

$$\frac{\partial \varepsilon_k \bar{\bar{\rho}}_k \hat{\psi}_k}{\partial t} + \nabla\cdot\left(\varepsilon_k\bar{\bar{\rho}}_k\hat{\psi}_k\hat{v}_k\right) + \nabla\cdot\alpha_k\left(\bar{\bar{J}}_k + J_k^T\right) - \varepsilon_k\bar{\bar{\rho}}_k\hat{S}_k^{\psi_k} + S_k^{\psi,I} \tag{146}$$

eq.(145)154 and eq.(146)155 are the mixture balance equations and phase balance equations for the k^{th} phase respectively. According to Ishii and Hibiki (2010) combining the eq.(145)154 and eq.(146)155 yields the interfacial transfer condition

$$\sum_k\left(S_k^{\psi,I}\right) - S_m^{\psi,I} = 0 \tag{147}$$

As stated by Ishii and Hibiki (2010) eq.(145) is the mixture balance equation and allows the drift flux model to be defined. On the other hand eq.(146) describes the flow by means of two separate balances, one for each phase, and it is the base for the multi-phase fluid model. Both equations need constitutive laws as in the single phase model. However, in order to close the system of equations additional relations to satisfy eq.(147) are necessary. The latter equation is the macroscopic expression for the jump condition in a framework that considers that the two phases coexist at the same point and at the same time even with an interface. Macroscopic jump condition can be obtained from fundamental theories and/or by experimental correlations. For example, for the case of the important effect of momentum exchange between a solid-gas flow, the momentum transfer β is defined by means of the empirical correlation for the drag coefficient C_d.

3.4.7. KINETIC THEORY OF GRANULAR FLOWS

For low dense particle clouds, the Lagrangian approach is suitable and feasible from the point of view of the computational efforts. However, for dense particle clouds, apply the Lagrangian approach is not feasible, because is practically impossible to track a large quantity of particles and accounts for the particle-particle and gas-particle interactions. In order to address this disadvantages, the *kinetic theory of granular flows* (KTGF), uses kinetic theory of gases providing the closure equations to account for the internal process treating the dispersed particle phase as a cluster with random motions. According to Jakobsen (2008) the particulate cluster can be represented considering a collection of identical, smooth, rigid spheres, adapting a Boltzmann type of equation. Fluctuating motions can transfer momentum through the system and dissipate energy by means of inelastic collisions, being the two processes related to the solid pressure, bulk viscosity and shear stress, respectively. Similarly, in the kinetic theory of gases, an averaging procedure is performed over the particle system. It is worth to note that the averaging procedure provides averaged fluctuating terms for motions. Therefore, an additional turbulence modeling for low frequencies eddies is not necessary for granular phases (GIDASPOW, 1994, p. 229).

Following the kinetic theory of gases, In KTGF theory the one third mean value of the isotropic kinetic energy is

$$\Theta = \frac{1}{3}\langle \hat{c}^2 \rangle \tag{148}$$

due to a normal distribution of velocity. In Eq.157 $\langle c^2 \rangle$ is the averaged velocity and Θ is the granular temperature (GIDASPOW, 1994). The granular temperature is related to the hydrostatic pressure P by the following state equation

$$P = \rho\Theta \tag{149}$$

The kinetic energy of the particle system can vary in space and time. Therefore, the transport equation associated is

$$\frac{3}{2}\left[\frac{d}{dt}(\varepsilon_s\rho_s\Theta) + \nabla\varepsilon_s\rho_s v_s\Theta\right] = \sigma_s : \nabla v - \nabla\cdot q' - \gamma \tag{150}$$

Where the two terms on LHS are the transient and convection terms. The first term on the RHS is the stress tensor that relates the solid pressure, the solid bulk viscosity and

the solid shear viscosity. The second term is for the flux of fluctuating dissipation. The third term accounts for the collisional energy dissipation (GIDASPOW, 1994). Viscosity is given by the following equations

$$P_s = \varepsilon_s \rho_s [1 + 2(1+e) g_0 \varepsilon_s] \Theta \tag{151}$$

Where ε_s, ρ_s, e and g_0 are solid volume fractions, effective solid densities, elastic coefficient and radial distribution functions. For solid pressure p_s the following viscosities are

$$\mu_s = \frac{2\mu_{s,dill}}{(1+e)g_0}\left[1 + \frac{4}{5}(1+e) g_0 \varepsilon_s\right]^2 + \frac{4}{5}\varepsilon_s^2 d_s \rho_s g_0 (1+e)\left(\frac{\Theta}{\pi}\right)^{1/2} \tag{152}$$

For solid phase shear viscosity μ_s

$$\lambda_s = \frac{4}{3}\varepsilon_s \rho_s (1+e)\left(\frac{\Theta}{\pi}\right)^{1/2} \tag{153}$$

For the bulk viscosity λ_s . The diluted viscosity term is given by

$$\mu_{dill} = \frac{5}{96\sqrt{\pi}} d_s \rho_s \Theta^{1/2} \tag{154}$$

The flux of fluctuating energy is given by eq.(155)

$$q' = -k' \nabla \Theta \tag{155}$$

Where k is

$$k' = \frac{2k_{s,dill}}{(1+e)g_0}\left[1 + \frac{4}{5}(1+e) g_0 \varepsilon_s\right]^2 + 2\varepsilon_s^2 d_s \rho_s g_0 (1+e)\left(\frac{\Theta}{\pi}\right)^{1/2} \tag{156}$$

Where $k_{s,dill}$

$$k'_{s,dill} = \frac{75}{384}\sqrt{\pi}\rho_s d_s \Theta^{1/2} \tag{157}$$

The collisional energy dissipation γ

$$\gamma = 3(e^2 - 1)\varepsilon_s \rho_s g_o \Theta \left[\frac{4}{d_p}\left(\frac{\Theta}{\pi}\right)^{1/2} - \nabla \cdot v_s\right] \tag{158}$$

If particle collision is fully elastic i.e. $e = 1$, the dissipation is zero. The radial distribution is the ratio between the distance s between particles and the particle diameter d_p

$$g_0 = \left[1 - \left(\frac{\varepsilon_s}{\varepsilon_{s,max}}\right)^{1/3}\right]^{-1} = \frac{\Delta s + d_p}{\Delta s} \tag{159}$$

Where $\varepsilon_{s,max}$ is the maximum packing.

3.4.8. CONSERVATION EQUATIONS FOR GRANULAR PHASES

Conservation equations or balance equations describe the transport processes of mass, momentum and energy. In the case of multi-phase flows, conservation equations additionally account for the closure terms coupling the independent balances of mass, momentum and energy of each phase. These terms arise in conservation equations due to the interface balances presented in sections 3.4.2 and 3.4.6.

3.4.9. MASS CONSERVATION EQUATION

Mass conservation equation or continuity equation account for the principle that states that mass is not destroyed in a process. From the point of view of multi-phase flow, there is one equation for the whole system and one specific balance equation for each phase. In general, mass conservation equation is

$$\frac{\partial \rho_m}{\partial t} + \nabla \cdot (\rho_m v) = 0 \tag{160}$$

Where ρ_m is the mixture density in terms of averaged values. As can be seen in eq.(160), mass balance has no source term following the conservation of mass principle. In the case of mass balance for phases, the continuity equation can account for a source term that represents the mass transfer between phases (JAKOBSEN, 2008).

$$\frac{\partial (\varepsilon_k \rho_k)}{\partial t} + \frac{d}{dx_i} (\varepsilon_k \rho_k v_k) = S_k^{\rho} \tag{161}$$

Where ε_k, ρ_k,v_k and S_k^{ρ} are the phase volume fractions, the specific density, the physical velocity for phase k and the source term accounting for the mass transfer source term between phases, respectively.

3.4.10. SPECIES CONSERVATION EQUATION

In each phase, a species transport equation can be defined. For a specie i in phase k, the species conservation equation extracted from Turns (Turns, 1996) and modified here is

$$\frac{\partial(\varepsilon_k \rho_k Y_{k,i} \gamma_v)}{\partial t} + \nabla \cdot \left[\varepsilon_k \rho_k Y_{k,i} \gamma_v (v_k Y_{k,i} - D_{k,i} \nabla Y_{k,i})\right] = \gamma_v \mu_{k,i} \tag{162}$$

Where γ_v is the volume available for the total flow, if $\gamma_v = 1$ therefore, the species conservation equation is

$$\frac{\partial(\varepsilon_k \rho_k Y_{k,i})}{\partial t} + \nabla \cdot \left[\varepsilon_k \rho_k Y_{k,i} (v_k Y_{k,i} - D^*_{i,k} \nabla Y_{k,i})\right] = S^{\rho}_{k,i} \tag{163}$$

Where $S^{\rho}_{k,i}$ is the source term of the average of local volume-averaged mass from specie i in phase k per unit time and unit mixture flow volume (KOLEV, 2005). Term $Y_{k,i}$ is the mass fraction of a specie i in phase k. Term $D^*_{i,k}$ is the total diffusion coefficient for the specie i in phase k.

3.4.11. MOMENTUM CONSERVATION EQUATION

Acording to Newton's second law the momentum for the phse k is

$$\frac{\partial(\varepsilon_k \rho_k v_k)}{\partial t} + \nabla \cdot [\varepsilon_k \rho_k v_k v_k] = -\nabla(\varepsilon_k \bar{P}_k) + \nabla \cdot [\varepsilon_k (\bar{\tau}_k + \bar{\tau}^T_k)] + \varepsilon_k \rho_k \hat{g}_k + S^M_k \tag{164}$$

Where $\bar{P}_k$, $\bar{\tau}_k$ and $\bar{\tau}^T_k$ are the averaged phase pressure, averaged stress tensor and averaged turbulent stress tensor. The term $\hat{g}_k$ is the general body force field, that can include, among others, the effect of gravity or drag forces. Finally, the last term on the RHS S^M_k is the k^{th} source of momentum transfer at the interface.

3.4.12. ENERGY CONSERVATION EQUATION

In general, in fluid dynamics there is more than one form of energy equations i.e. the total energy and the mechanical energy. The former is a direct consequence of the first law of thermodynamics while the latter is obtained starting by means the dot product between the velocity and Newton's second law equation. The total energy conservation equation is (ISHII; HIBIKI, 2010).

$$\begin{aligned} &\frac{\partial}{\partial t}[\varepsilon_k \rho_k (\hat{e}_k + v_k^2/2)] + \nabla \cdot [\varepsilon_k \rho_k v_k (\hat{e}_k + v_k^2/2)] \\ &\qquad = -\nabla \cdot [\varepsilon_k (q_k + q^T_k)] + -\nabla \cdot (\varepsilon_k T_k \cdot v_k) + \varepsilon_k \rho_k g_k \cdot v_k + S^E_k \end{aligned} \tag{165}$$

Where $\hat{e}_k$ is the effective internal energy and q_k is the conduction heat flux. Furthermore, the term q_k^T accounts for the turbulent convection and turbulent mechanical work. T_k is the mean temperature of the phase k. S_k^E is the energy source term at the interface. On the other hand mechanical energy equation is presented in equation 175 (ISHII; HIBIKI, 2010)

$$\frac{\partial}{\partial t}[\varepsilon_k \rho_k (v_k^2/2)] + \nabla \cdot [\varepsilon_k \rho_k v_k (v_k^2/2)] = -v_k \cdot \nabla[\varepsilon_k \bar{P}_k] + v_k \cdot \nabla \cdot [\varepsilon_k (\bar{\tau}_k + \bar{\tau}_k^T)] + \varepsilon_k \rho_k \hat{g}_k \cdot v_k + S_k^M \cdot v_k - \frac{v_k^2}{2} S_k^{E\ kinetic} \quad (166)$$

In eq.(166)175 the first term on the RHS is the mechanical work done by pressure, and the second term is the mechanical work due to shear stress. The third term is the work owing to body forces that can include the drag forces, defined later. The fourth term is the work done by momentum source term at the interface. Finally, the last term on the RHS is the momentum due to mass transfer at the interface.

3.5. BASES OF FINITE VOLUME METHOD

The set of conservation equations presented in this chapter is difficult to be resolved, only for specific simple application it is possible to obtain an analytical solution. For a complex system that coupled the mass, momentum and energy equations the use of computational numerical methods are mandatory. Other complexity about the conservation equations is the non-linear nature due to the advection terms. Furthermore, chemical kinetics and radiation heat transfer incorporate additional source terms that depend on field variables.

In order to resolve such complex non-linear equation systems, the finite volume method (FV) has been developed.

3.5.1. DISCRETIZATION

The FV method is in nature conservative (MALISKA, 1995) due to its starting from the application of mass, momentum and energy balance in a control volume with a finite size. The basic idea of FV method is to divide the geometry of interest in a set of control

volumes or cells, named the mesh, that allows the solution of the conservation equation system considering a discrete set of field and properties values at the center of the cell. According to Maliska (1995) a generic transport equation can be expressed as

$$\frac{D}{Dt}(\rho\psi) = \nabla\left(\Gamma^{\psi}\nabla\psi\right) + S^{\psi} \tag{167}$$

In where the variable transported over the field is ψ. The term on LHS is the material derivative, the first term on the RHS is the diffusion term and the second is the source term. Diffusion term is characterized by a the diffusive property Γ^{ψ}. Using Einstein's notation to rewrite eq. (167) and expressing the material derivative in the Eulerian form gives the transport equation in conservative form

$$\frac{\partial}{\partial t}(\rho\psi) + \frac{\partial}{\partial x_i}(\rho v_i\psi) = \frac{\partial}{\partial x_i}\left(\Gamma^{\psi}\frac{\partial\psi}{\partial x_i}\right) + S^{\psi} \tag{168}$$

The first term on the LHS is the transient term and the second is the advective term. In order to apply the FV method eq.(168)201a must be expressed algebraically by discretization. The latter process consists in integrating eq.(168) over space and time and approximating the differential terms using interpolation schemes.

The integration is performed over a finite time interval $t + \Delta t$ and in space considering a finite volume. In the case of a two-dimensional field, the domain is divided into several finite volumes or cells and the integration is performed over it. Figure 62 shows the volume and it neighbors. In Figure 62 the integration is performed over volume P, where the limits are the interfaces with neighbor volumes. Integrating over the time and space for x component gives.

$$\begin{aligned}\int_{w}^{e}[(\rho\psi)^{t+\Delta t} - (\rho\psi)^{t}]\,dx + \int_{t}^{t+\Delta t}[(\rho v_x\psi)_e - (\rho v_x\psi)_w]\,dt \\ = \int_{t}^{t+\Delta t}\left[\left(\Gamma^{\psi}\frac{\partial\psi}{\partial x}\right)_e - \left(\Gamma^{\psi}\frac{\partial\psi}{\partial x}\right)_w\right]dt + \iint_{w.t}^{e,t+\Delta t} S^{\psi}\,dx\,dt\end{aligned} \tag{169}$$

Where at least one integral per term can be reduced using the fundamental theorem of integral calculus leaving eq.(169)201b. All the quantities in the integral arguments are for the point P in the volume. The first integral on the LHS has the actual value quantity $\rho\psi$ at time t and the unknown value at time $t + \Delta t$. The second integral has the

advective values at the interfaces w and e with the neighbor's volumes W and E respectively.The first integral on the RHS accounts for the flux of ψ exchanged with the neighbors due to diffusion.

Figure 62 – Finite volume *P* and the neighbor's volumes in a 2D space.

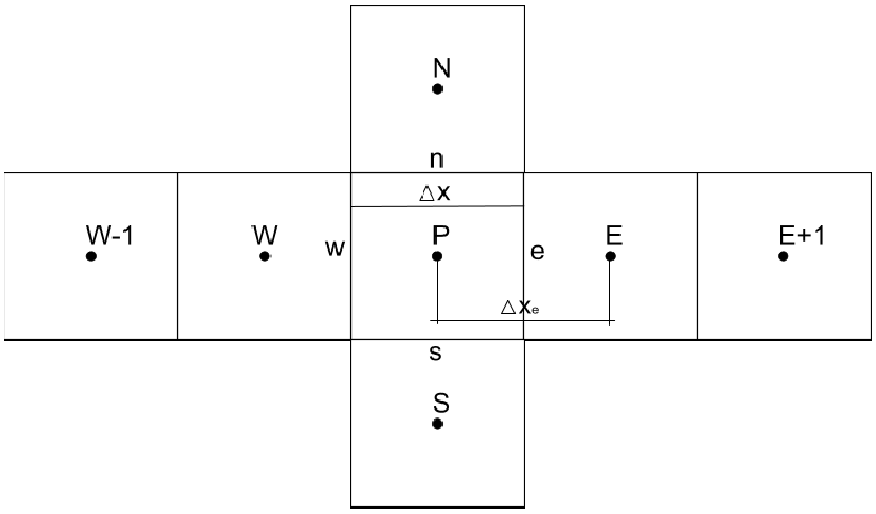

In order to integrate analytically eq.(169), it is necessary to know the distribution of the quantity $\rho\psi$ along dx. However, the approximate FV method only provides values for the field quantities at the central point of volumes. The most simple discretization scheme for the transient term is to consider that $\rho\psi$ is constant over the volume, then

$$\int_w^e [(\rho\psi)^{t+\Delta t} - (\rho\psi)^t]\, dx \approx [(\rho\psi)^{t+\Delta t} - (\rho\psi)^t]\, \Delta x \tag{170}$$

The second integral needs the values of the convective terms at the interfaces. These values can be obtained by interpolating the field values of $\rho v_x \psi$ from the points P and W and from the point P and E or considering more points such as $E+1$ or $W-1$, depending on the interpolation scheme order. According to Maliska (1995) the *central differencing scheme,* CDS, is appropriate owing is a second order interpolation scheme. The CDS relates the field values of volume *P* with its near neighbors volumes E and W. Therefore, the value at the interfaces can be determined. An additional simple approximation is to consider that the value of the advective term at the interface is constant. The conditions allow an algebraic approximation for the advective term

$$\int_t^{t+\Delta t} [(\rho v_x \psi)_e - (\rho v_x \psi)_w]\, dt \approx \int_t^{t+\Delta t} \left\{ \frac{1}{2}[(\rho v_x \psi)_E + (\rho v_x \psi)_P] - \frac{1}{2}[(\rho v_x \psi)_P + (\rho v_x \psi)_W] \right\} dt \tag{171}$$

Diffusion terms account for the derivative values at the interface, therefore, these quantities must be interpolated. First order scheme can be applied. The value of the derivative can be considered constant at the interface to maintain the simplicity.

$$\int_t^{t+\Delta t} \left[\left(\Gamma^{\psi} \frac{\partial \psi}{\partial x} \right)_e - \left(\Gamma^{\psi} \frac{\partial \psi}{\partial x} \right)_w \right] dt \approx \int_t^{t+\Delta t} \left[\Gamma_e^{\psi} \frac{\psi_E - \psi_P}{\Delta x_e} - \Gamma_w^{\phi} \frac{\psi_P - \psi_W}{\Delta x_w} \right] dt \tag{172}$$

Source term can depend on the field value ϕ. According to Maliska (1995) it is convenient to treat the source term in a linearized form of ψ. A linear approximation is shown in eq.(173)

$$S^{\psi} \approx S_p^{\psi} \psi + S_C^{\psi} \tag{173}$$

Where S_p^{ψ} is the derivative respect the field value ψ and S_C^{ψ} is a constant. The linearized source term can be considered a constant in time and space, therefore,

$$\iint_{w.t}^{e,t+\Delta t} S^{\psi}\, dx\, dt \approx \left(S_p^{\psi} \psi + S_C^{\psi} \right) \Delta x \Delta t \tag{174}$$

Approximation for convective and diffusive terms must be integrated over the time. The approximation can be explicit, totally implicit or implicit (MALISKA, 1995). In an explicit temporal scheme, the field values are evaluated at the current time t providing a fast and independent solution of each volume, since the only unknown in the equation is $\psi_P^{t+\Delta t}$. However, and according to Maliska (1995) instabilities and/or inconsistencies can arise. A more stable scheme is the totally implicit, that evaluates the field values at the next time step $t + \Delta t$. However, the equation has more unknowns $\psi_P^{t+\Delta t}$, $\psi_E^{t+\Delta t}$, $\psi_W^{t+\Delta t}$ coupling all of each volumes and boundary conditions, requiring a simultaneous solution each time. The implicit solution provides a mixture between the explicit and totally implicit schemes. By introducing a weighted function θ is possible to control the contribution of the current and the future field value and thus improve the stability. weighted function θ is defined by

$$\phi_P = \theta\psi_P^{t+\Delta t} + (1-\theta)\psi_P^t \tag{175}$$

Where θ is the weight factor. If $\theta = 0$ then the scheme turns explicit, on the other hand, if $\theta = 1$ the scheme is totally implicit. Any value for $0 < \theta < 1$ provides and implicit scheme.

Considering a totally implicit scheme for equation eq.(168) the resulting algebraic approximation for each volume is

$$\begin{aligned}[(\rho\psi)^{t+\Delta t} - (\rho\psi)^t]\Delta x \\ + \left[\frac{1}{2}[(\rho v_x\psi)_E + (\rho v_x\psi)_P] - \frac{1}{2}[(\rho v_x\psi)_P + (\rho v_x\psi)_W]\right]\Delta t \\ = \left[\Gamma_e^\psi \frac{\psi_E - \psi_P}{\Delta x_e} - \Gamma_w^\psi \frac{\psi_P - \psi_W}{\Delta x_w}\right]\Delta t + \left(S_p^\psi\psi + S_C^\psi\right)\Delta x\Delta t\end{aligned} \tag{176}$$

In problems where various fields are calculated terms such as ρ and v_x are also unknown. Therefore, a decoupling solution must be applied in order to solve the field value ψ considering the other values as constants. However, in each interation, an update step must be performed to account for the evolution of the other quantities. If $\Delta x_e = \Delta x_w = \Delta x$, and dividing eq.(176) by Δx and Δt and reducing terms gives

$$\begin{aligned}\left[\frac{\rho}{\Delta t} + \frac{\Gamma_e^\psi + \Gamma_w^\psi}{\Delta x^2} + S_p^v\right]\psi_P^{t+\Delta t} \\ = \left[\frac{\Gamma_e^\psi}{\Delta x^2} - \frac{1}{2\Delta x}(\rho v_x)_e\right]\psi_E^{t+\Delta t} + \left[\frac{\Gamma_w^\psi}{\Delta x^2} + \frac{1}{2\Delta x}(\rho v_x)_w\right]\psi_W^{t+\Delta t} \frac{(\rho\phi)^t}{\Delta t} \\ + S_C^\psi\end{aligned} \tag{177}$$

Equation 177 can be rewritten in a condensed form as

$$A_P\psi_P^{t+\Delta t} = A_E\psi_E^{t+\Delta t} + A_W\psi_W^{t+\Delta t} + A_0\psi^t + S_C^\psi \tag{178}$$

For all volumes considered, an equation such as the eq.(178) is placed. Since the totally implicit scheme has been applied, a system of equations may be obtained and it is necessary to solve them simultaneously. The equation system generates a matrix, generally, diagonally dominated, that is suitable for algorithms specially designed to invert them. However, coefficients A in eq.(178) varies in other fields, therefore, an

iteration process must be performed in order to update these coefficients as the solution proceeds.

3.5.2. DISCRETIZATION OF ADVECTION AND DIFFUSION TERMS

According to Maliska (1995) a fluid flow problem can be elliptic, parabolic or hyperbolic. In elliptic problems the information is transmitted in all directions, due to the dominant diffusive term. In parabolic and hyperbolic problems the information is transmitted in a preferred direction due to the dominant advective term. In problems with a strong advection and where diffusion terms are weaker, an alternative type of discretization schemes can be applied. As an example, in an advective dominant problem, instead of the use of CDS discretization the Upwind scheme may be suitable since it accounts for the fact that information is preferably transmitted from the up-stream to the down-stream. In the case of mixed problems, advection-diffusion, the *weighted up-stream differencing scheme*, WUDS, can be applied. The scheme has two factors α and β in order to balance the diffusion-advection coupling.

3.5.3. MESHING

The mesh is an important part in CFD. The mesh must cover the domain exactly providing a set of finite volumes in where the approximated conservation equations are evaluated and in each volume the values of the field variables are stored in its center. In order to obtain convergence in calculations, the mesh must be fine enough in order to approximate the true solution and to capture the flow characteristics. Maliska (1995) classifies the mesh as structured and unstructured mesh. The former is constructed following a specific rule and has a global coordinate system in which all internal cells has always the same number of neighbor. The latter does not have a global coordinate system and the number of neighbor cells can vary.

The advantage of structured mesh is that frequently generates diagonally dominated matrix and the disadvantage is that it is not always possible to fit complex domains. Quality of the mesh can be assessed by the following key criteria (ANSYS FLUENT 19.0):

- Smoothness: the transition of the cell size from cell to cell prevents errors due to truncation.
- Skewness: measures the deviation of a cell compared with an equilateral cell with the same volume. Skewness is a normalized quantity that ranges from 0 to 1. As a recommended rule, the value of the skewness factor for all cells must be lower than 0.95 and in average near 0.33 in order to facilitate convergence.
- Aspect ratio: is the ratio between the lengths of cell faces, high aspect ratio, which means that a stretched cell can produce stability problems.

Mesh effect on solution must be performed in all CFD simulation. Numerical calculation analysis can be performed over the spatial grid (mesh) or in time. Theoretically, as the mesh is refined the solution tends to converge asymptotically to the true numerical solution. According to NASA (1998) is necessary to distinguish the physical solution and the true numerical solution of a fluid dynamic problem. The former is defined as the asymptotic value when the characteristic cell length h is zero. On the other hand, the later is the true solution of the problem.

According to AIAA (1998) an acceptable solution of a fluid dynamics calculation may be in the *asymptotic range of convergence*, defined latter. A convergence analysis can be performed in order to assess the mesh effect verifying the solution until the difference of quantities tends to a minimal value. However, procedures applied to check convergence can vary from different authors. According to AIAA (1998), the methodology developed by Roche, referenced in the AIAA (1998) document, offers a formalized procedure to determine the suitable mesh size (for a desire level of accuracy) and a measure of the error band respect to the true numerical solution. A *grid refinement study*, according to the methodology of Roche, can be reported by *grid convergence index,* GCI that is defined as a measure of the percentage of discrepancy between the actual numerical solution with the *asymptotic numerical value.*

The *grid refinement study* developed by Roche and referenced in AIAA (1998) document is consist into relate different numerical calculations doubling the grid points, in all coordinates and using a second order method to discretized the field equations. Then, using the theory of generalized Richardson Extrapolation range of convergence

and GCI index are determined. In Chapter 4 are presented the complete methodology to perform a spatial grid refinement assessment based on the procedure described in the NASA (2008).

3.4.11.4. SOLUTION PROCEDURE FOR INCOMPRESSIBLE FLOWS

The solution procedure, a solver, is an algorithm that is composed of several steps that can solve a set of discretized conservation equations in an iterative sense. As stated by Maliska (1995) the solution procedure can be performed in a coupled or in segregated sense. Coupled solution procedure solves the entire set of conservation equations for each cell at a time, eliminating the coupling between variables. In the segregated solution, one variable is solved at a time for each cell. According to Maliska (1995) for a large number of cells, the segregated solution is better, however, it is necessary to update the field, and also, an evolution equation is necessary for each variable, including the pressure. Strong non-linear systems are forced into solving the FV matrix iteratively in steps, including a coupled solution procedure, in order to manage these non-linearities, updating the coefficients after each iteration step. In the case of incompressible flows, an additional issue is to treat the coupling between the pressure with the velocity fields in the momentum equation, since there is no an evolution equation for pressure, such as the state equation for compressible flows, thus one extra equation is necessary.

In order to address the coupling issue for incompressible flows, an evolution equation for pressure and a corrector equation for velocity has been developed named *Semi Implicit Linked Equations*, SIMPLE (MALISKA, 1995). The evolution equation for pressure is obtained by means of the concept that states the correct pressure P is equal to the sum of the actual predicted pressure P^* and a correction P'.

$$P = P^* + P' \tag{179}$$

Introducing the correct pressure P and the actual pressure P^* in the momentum conservation equation and calculating the differences and neglecting the term $v - v^*$, produce a correction equation for the velocity field that as is shown in eq.(180) for the x direction

$$v_P = v_P^* - \frac{\Delta v}{A_P}\frac{\Delta P'}{\Delta x} \tag{180}$$

Where A_P is an algebraic coefficient. Introducing the correction written for the cell faces in the mass conservation equation an evolution equation is obtained for P'

$$A_P P' = \sum A_i P_i - \nabla \cdot v^* \tag{181}$$

Where the divergence of the velocity vector field V^* is determined using the mass conservation equation. The algorithm to solve an incompressible flow with the SIMPLE method is depicted in Figure 63.

Figure - 63 SIMPLE algorithm described step by step.

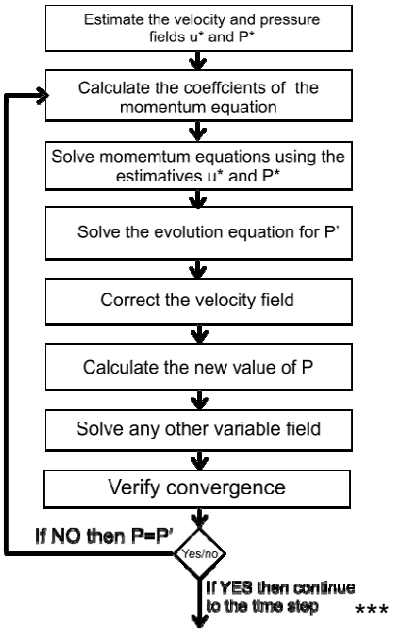

3.6. PHYSICAL PROPERTIES FOR MIXTURES

In multiphase flows, phases can be composed by more than one pure component; therefore, a combined mixture of physical properties can be calculated. Furthermore, if mass is transferred between phases and volumetric or superficial reactions are considered the averaged physical properties vary in space and time. An averaged physical property can be calculated as a function of the concentration of mass or molecules, for solid and gas phases respectively. In the case of gas phases an

averaged physical property can be calculated based the volume fraction. Being a generic physical property F_{ph} the averaged value of the mixture can be calculated with

$$F_{ph} = \sum_{i=1}^{N} \varepsilon_i \, F_{ph,i} \tag{182}$$

Where ε_i is the volume fraction and $F_{ph,i}$ is the physical property in volume basis of the component and N the number of components. In the case of solid phases an averaged property can be obtained by averaging based on the mass fraction Y_i

$$\psi_{ph} = \sum_{i=1}^{N} Y_i \, \psi_{ph,i} \tag{183}$$

3.7. STANDARD ENTHALPY OF FORMATION

For reacting systems, the heat of reaction can be obtained with the standard enthalpy of formation of each component as a property. If the standard heat of reaction is known, the enthalpy of formation for one component can be calculated with the following equation (ÇENGEL; BOLES; CÁZARES, 2006).

$$H_R^\circ = \sum_{i=1}^{N} \left(a_i \bar{h}_{f,i}^\circ\right)_{Products} - \sum_{i=1}^{M} \left(b_i \bar{h}_{f,i}^\circ\right)_{Reactants} \tag{184}$$

Where H_R, a_i and b_i, $\bar{h}_{f,i}^\circ$, N, and M are the standard heat of reaction, the stoichiometric coefficient, the standard molar enthalpy of formation, the total products and total reactants species respectively.

4. METHODOLOGY

This chapter presents all the procedures and methodologies that were used in order to obtain the multi-stage global reaction mechanism for the fast pyrolysis of *Chlorella Vulgaris* and its implementation in a CFD software to simulate a laboratory-scale semi-continuous fast pyrolyzer. The material is organized in two main sections. Additionally, the methodology used to obtain the mass fraction of carbohydrate, protein and lipid components is referenced. The first section is related with the methods and procedures specifically performed for the construction of the reaction mechanism and the second section, is dedicated to the CFD implementation in ANSYS Fluent 19.0 software package. Several details are specified in order to obtain the necessary additional information and parameters to construct the reaction mechanism and to set up the CFD simulation.

4.1. REACTION MECHANISMS FOR FAST PYROLYSIS OF CHLORELLA VULGARIS MICROALGAE

Considering the material presented in Chapter 2, a development of a detailed multi-stage reaction mechanism for microalgae is not feasible at the current time due to the fact that there is not enough data and research about specific mechanism and component analysis as a function of temperature or time. So far, there is only partial data and suggestions provided by few authors about the structure and possible paths of the thermal decomposition, mainly based on the data available for other substances such as cellulose.

Therefore, the development of a detailed reaction mechanism, for each microalgae component, without cross effects (all the components react independently) as in the case of lignocellulosic biomass (reviewed in Chapter 2) cannot be reached by using the current data of TG, DTG analysis without a deep understanding on how the principles of organic chemistry explain the structural characteristics, complex internal mechanics and kinetics.

In order to develop a mechanism for CFD applications, a procedure must be proposed with the objective of obtaining a useful mathematical model in accordance with the multi-phase flow theory equations. The proposition here is to develop a lumped multi-

stage mechanism by means of the data obtained from TG analysis. The latter can be achieved considering experiments with different heating rates to obtain the mass loss curve, final yields, the solid-gas evolution as a function of time, and to perform a regression procedure in order to determine the kinetic parameters with the methods and principles described in section 3.3. This chapter is divided in two sections which describe the whole methodology in order to obtain a reaction mechanism for *Chlorella Vulgaris* devolatilization and the CFD customary set up. Specifically, the first section accounts for the experimental methodology to obtain the mass rate and mass loss rate curves from the TG analysis, later, a formal proposition and application of hypothesis will be explained in order to obtain the kinetic triplet and therefore, the global multi-stage reaction mechanism. The second section describes the set up of the CFD application in ANSYS Fluent 19.0 that includes the definition of phases, sub models for the multi-phase flow, turbulence, boundary condition, physical properties, interpolation and discretization schemes and solution algorithm.

4.1.1. THERMAL ANALYSIS EXPERIMENTS

In order to obtain a global multi-stage reaction mechanism for the microalgae *Chlorella Vulgaris* using the methodology described in section 3.3, experimental runs must be made in order to obtain the mass loss and mass loss rate using a TG and DTG analysis. For the thermal responses, a Perkin Elmer Simultaneous Thermal Analyzer (STA) 6000 was used and is shown in Figure 64.

Figure 64 – Perkin Elmer Simultaneous Thermal Analyzer (STA) 6000 for TG, DTG and DSC analysis.

Powder of lyophilized *Chlorella Vulgaris* microalgae (Figure 65) used were obtained from PureBulk Inc. USA. For TG experiments a sample of 20 mg was used applying linear heating rates of 5, 10 and 20 °C/min. Heating process starts from room temperature 25°C to 1000°C. Pure nitrogen is used to sweep out the pyrolytic gases with a flow of 25 ml/min. It is worth to note that experimental conditions are the same that was used by Raheem et al. (2015). The sample of microalgae is loaded in an alumina ceramic crucible without a lid, in order to avoid secondary cracking reaction and interactions between the formed char and pyrolytic gases. The programmed heating rate is applied for each sample and the temperature of the sample and the reference is recorded.

Figure 65 – *Chlorella Vulgaris* powder obtained from PureBulk Inc. used in thermal analysis experiments.

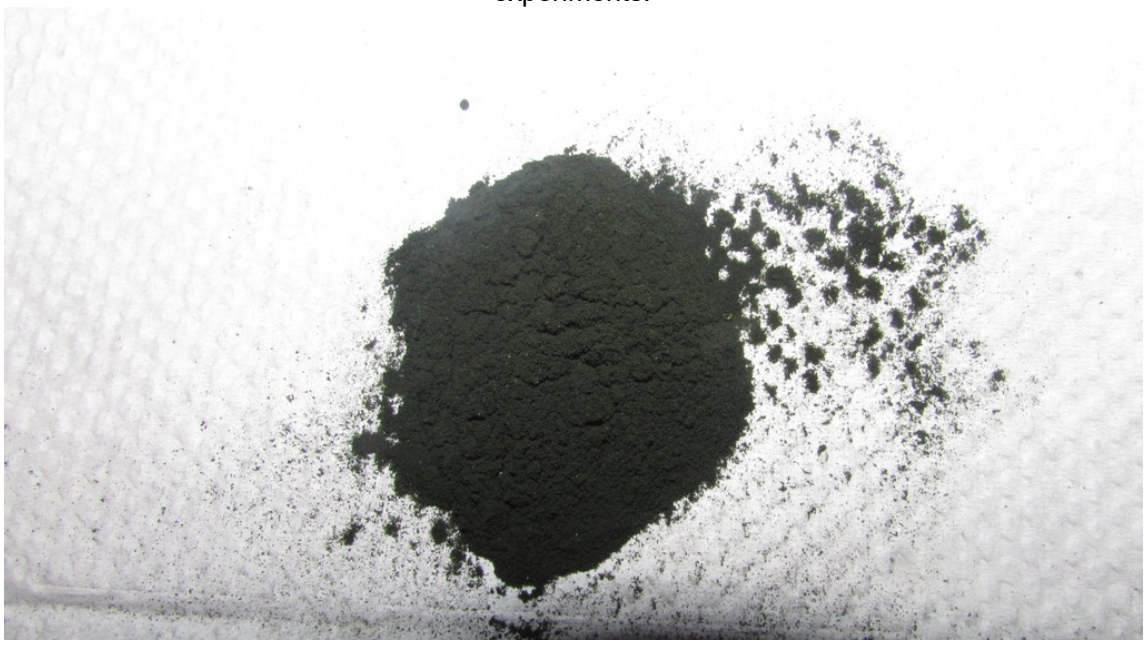

4.1.2. DATA TREATMENT

Mass loss from TG experiment is obtained for the three heating programs applied. The independent variable is time in minutes and the mass loss, program temperature, sample temperature and power for a DSC unit is measured in conjunction with other information to verify the correct operation of the apparatus. In order to study the different techniques for OHR and iso-conversional methods, the mass loss rate data (DTG) is obtained from the experimental mass loss data (TG) through differentiation of first order. Since noisy data is expected, a low band filter is applied taking a windows of

200 data points for smoothing since the expected volume of data varies from near 20000 to 9000. Normalized data sets are obtained using eq.(29) considering w_f, as the residual mass at the end of the experiment equal to 0. This modification accounts for that the kinetic parameters found are for the total gases released by each pseudo-component instead of the mass loss. Describing the devolatilization and char formation with only one global reaction implies that kinetics parameters are the same for the gas released and char formation, however no competitive approach is described and constitutes an additional hypothesis applied in this work related to the reaction mechanism. For iso-conversional method, that considers only the devolatilization of carbohydrates, proteins and lipids the value of w_f is set to 0, not accounting for the char gasification, and also, a match for the extent of conversion α is required between the data of the three heating rates. A new indexation as a function of α is performed using a linear interpolation of data. In order to produce a functional relationship between the extent of reaction and other data such as time, temperature and mass loss rate, different data points with the same values for α are eliminated. A code written in MatLab is developed for data treatment.

Iso-conversional differential method of Friedman, eq.(39), and integral methods of FWO, eq.(48), and KAS, eq.(53), including also the Starink method

$$ln\left(\frac{\beta_i}{T^{1.92}}\right) = constant\ - 1.0001\frac{E_\alpha}{RT_i} \tag{185}$$

are applied to the three treated data sets. Distributed activation energy is calculated trough linear regression between three sets of values in the interval for the extent of conversion α from 0.025 to 0.975. All treated data as a function on the extent of reaction is loaded by a code, specifically written in MatLab. Linear regression is calculated by using the *polyfit* MatLab function that gives the regression parameters. The linear regression coefficient and the sum of square error is calculated with the following equation

$$Z_{fit} = mU + n \tag{186}$$

Where Z_{fit}, m, X, n are fitted dependent values, the calculated slope, the independent data value and the calculated intercept. The residue is calculated by

$$Z_{resid} = Z - Z_{fit} \tag{187}$$

Where Z is the actual data value, for each data point. The sum of squares SS_{resid} is calculated with

$$SS_{resid} = \sum (Z_{resid})^2 \tag{188}$$

Sample variance is calculated with the following equation

$$S^2 = \frac{\sum (Z - \bar{Z})^2}{n - 1} \tag{189}$$

Where n is the number of samples. Finally, normalized coefficient of determination (R^2) is obtained using the eq.(190).

$$R^2 = 1 - \frac{SS_{resid}}{S^2} \tag{190}$$

To determine the pre-exponential factor *A,* the compensation effect presented in eq.(68) is used. The linear coefficients *a* and *b* are determined from values of the pre-exponential factor *A* and activation energy *E* obtained using linear regression of OHR method of eq.(34) for at least four reaction model listed in Table 26 and for the data set of 5°C/min. The mass loss rate calculated by differentiation is used in conjunction with the four methods mentioned. Normalized coefficient of determination is calculated with eq.(186) to eq.(190). A second linear regression is performed, in order to determine the compensation equation, using the pairs (*A,E*) from different reaction model tested, and again the normalized coefficient of determination with eq.(186) to eq.(190) is used.

The distribution of pre-exponential factor A and activation energy E obtained is analyzed and compared with the peaks of the mass loss rate calculated before presented as a function the extent of conversion α. Mean values of the pre-exponential factor A and activation energy E are used to characterize the apparent kinetic parameters associated with each peak. Uncertainty is calculated using the standard deviation of each pair of values.

4.1.3. REACTION MECHANISM STRUCTURE

Procedures for the development of reaction mechanisms based on thermal analysis data has been reported in the literature such as those provided by Di Blasi (1998, 2008)

and Di Blasi and Branca (2001). However, some methodologies have the disadvantage that large amounts of data and detailed characteristics about several reaction path are necessary. It is evident that the more detailed a mechanism is, more data and experiments are necessary. However, in the case of *Chlorella Vulgaris* and in general, for microalgae biomass, the availability of studies and experimental data for the thermal decomposition process are so far scarce and as a consequence the current development of a detailed reaction mechanism is unfeasible. Nonetheless, as starting point and proposed by this work is the development of a global reaction mechanism based on the TG and DTG analysis. The following section presents the methodology, procedures and assumptions in order to determine the kinetic parameters and additional data required for this purpose.

Considering the discussion of section 2.2 it is obvious that the development of a comprehensive reaction mechanism for biomass materials, even for pure cellulose is a challenging task. Furthermore, although the is an interest by researchers about the use of microalgae biomass as a raw resource for fuels and chemicals products obtained from fast pyrolysis is recent, the amount of data and hypothesis about the type of reactions and chemical species involved and chemical dynamics are not available in the detail so far in order to develop comprehensive chemistry model. However, a global single or multi-stage reaction mechanism is feasible by means the use and processing of the TG and DTG data for the mass loss and mass loss rate respectively. Hydrodynamics coupled with this type of reaction mechanism are not yet reported in the literature, and may be the starting point in order to study the physical behavior of the microalgae powder in the flow field inside a reactor environment allowing a first glance about the residence time, devolatilization timing, characteristic velocities, energy transfer, flow and one or multi stage, lumped and global reaction mechanisms can offer a quantitative measure about the mentioned different characteristics starting from the thermal analysis and combined with the multi-phase flow theory.

From the point of view of the reactants and products participating in a reaction the basic scheme is the *one stage lumped global reaction mechanism*, that considers two lumped materials: the biomass, that is composed, in the case of the microalgae biomass, by carbohydrates, proteins and lipids that can be considered a lumped component in which the thermal decomposition is governed by only one chemical reaction producing two

lumped products i.e. solid and gas. From the point of view of chemical kinetics, a set of three parameters may be obtained. Two of these parameters are belong to the Arrhenius term kinetic constant term i.e. the activation energy *E* and the pre-exponential factor *A*. The last parameter is related with the reaction model assumed to describe the thermal decomposition as reported by Vyazovkin (1996). The TG and or the DTG data are processed in order to perform a fitting calculation to obtain the kinetic parameters *E*, *A* ad *n.* The physical consistency of the kinetic parameters depends on the methodology utilized being the better the iso-conversional method that avoid the compensation effect. The *one stage lumped global reaction mechanism* offers a straightforward approach to determine kinetics in general however is not always applicable.

The description with only one reaction is not feasible for complex lignocellulosic or microalgae materials. The components i.e. cellulose, hemicellulose and lignin and carbohydrates, proteins and lipids, respectively, tend to be decomposed in stages instead in one whole step, therefore is evident that a one-stage reaction mechanism is not suitable. Evidences of the presence of several stages for the thermal decomposition of microalgae were presented in the literature review in Chapter 2, however the experimental data not evidences well separated stages for each component. The later observation introduces the concept of pseudo-component that is associated qualitatively with the effective components of the complex material, as in the case of *Chlorella Vulgaris* with the carbohydrates, proteins and lipids. As a consequence o more detailed description is necessary with more degrees of freedom. A separated description of the devolatilization of each pseudo-components, a multi-stage scheme, can capture in a better way the phenomena of thermal degradation. However, the later forces to the application of the first hypothesis about the devolatilization process applied here i.e. the application of the superimposed principle (MILLER AND BEJAN, 1997) that imposed independent reactions for each pseudo-components without cross effects. This principle is accepted and commonly used as a characteristic in the thermal decomposition modeling for lignocellulosic biomass and applied such as a hypothesis in this work. Procedure to determine the kinetic parameters for a multi-stage process require additional data processing especially if the iso-conversional method is applied. Several fitting processes are necessary for each pseudo-component, that can be more than the effective number of components, in order to determine three kinetic parameters for each

reaction. Also, despite that all reaction are considered independent, the mass fraction parameter for each pseudo-component must be determined coupling all equation.

With a multi-stage reaction mechanism is not always possible to discriminate the condensable from the non-condensable fraction, without a detailed gas phase description as in the TG and DTG analysis in where the species identification is not always available. Therefore, the condensation stage of the fast pyrolysis process will not be modeled in this study and the simulation performed will be only about the devolatilization reaction zone.

4.1.3.1. REACTION MODEL AND RATE EQUATIONS

Different peaks for each component of microalgae and moisture are expected according to literature reviewed in Chapter 2. Therefore, following the literature about pyrolysis of lignocellulosic biomass, the reaction mechanism proposed here will consider each peak and shoulders of the mass loss rate curve as an independent devolatilization process associated with each of the microalgae components: carbohydrates, proteins and lipids or its combination such as lipids-proteins pseudo-component.

The latter implies the use of the *superimposed principle* (MILLER AND BELLAN, 1997) with no cross effect between pseudo-components. Each of the peaks and shoulder detected in the DTG analysis is identified as a zone and in principle can be considered as a heterogeneous proto-reaction.

Figure 66 shows the reaction mechanism scheme defining the zone I as the process for moisture elimination that will be treated here as heterogeneous reaction. Following the definitions presented so far, this type of reaction mechanism can be classified as a *parallel multi-stage, global and lumped reaction mechanism.*

Parallel is defined due to the separated description of each pseudo-component, multi-stage due to the expected peaks and shoulders from the DTG analysis, global due to there is only one reaction for each pseudo-component and finally, lumped owing gas is considered a lumped pseudo-product.

Figure 66 – Set of reactions proposed for devolatilization in stages of *Chlorella Vulgaris microalgae.*

ZONE I (MOISTURE ELIMINATION)

$$MOISTURE \overset{k_W}{\Rightarrow} \text{WATER VAPOR}$$

ZONE II TO *M* (MICROALGAE PSUDO-COMPONENTS)

$$PC_1 \overset{k_1}{\Rightarrow} \text{GAS}_1 + \text{CHAR}_1$$
$$\vdots$$
$$PC_M \overset{k_M}{\Rightarrow} \text{GAS}_\text{M} + \text{CHAR}_\text{M}$$

Predictions given by a reaction mechanism model are sensitive to the reaction model, since provide the shape of the TG and DTG charts and physically is related to the physical process. In principle is necessary to avoid the arbitrary selection of the reaction model, nonetheless a structure can be chosen. In literature about devolatilization of lignocellulosic biomass, reaction mechanisms developed by authors, such as Diebold (1994) or Ranzi et al. (2008), account for frequently the Mampel first order reaction (Model 7 in Table 26). However, since the lack of a previous comprehensive reaction mechanism for *Chlorella Vulgaris*, there are no well-founded precedents to arbitrarily choose a model of first order, therefore the approach used here is to consider a more general model increasing the degree of freedom and improving the accuracy. The following n-order reaction model structure (eq.(191)), a modified *Sestak and Berggren model* (VYAVZOVKIN; GORYACHKO; LESNIKOVICH, 1991) is proposed and constitutes the second hypothesis assumed in this work

$$f(\alpha) = (1-\alpha)^n \tag{191}$$

4.1.4. FITTING PROCEDURE

As mentioned in Chapter 3 the iso-conversional methodology can provide the effective activation energy *E* and the pre-exponential *A* for a single step reaction independent of the reaction model. Also in the same Chapter it was presented the *simultaneous multi-stage optimization methodology* that finds the kinetic triplet for experimental curves directly for devolatilization of complex materials. However, as mentioned before, *simultaneous multi-stage optimization methodology* does not guarantee that the

effective activation energy *E* can be determined. Here, a combination of the iso-conversional method to determine *E* and *A* Arrhenius parameters and then apply a simultaneous multi-stage optimization using the IsoKin (http://www.cisp.spb.ru/isokin) software package in order to determine the coefficient n on eq.(191). Once the Arrhenius parameters are determined the following system with M rate equations must be optimized

$$\left(\frac{d\alpha}{dt}\right)_m = c_m A_m exp\left(\frac{-E_m}{RT}\right)(1-\alpha)^{n_m} \tag{192}$$

In where n_m and c_m must be simultaneously determined with the following mass conservation restriction

$$1 = \sum_1^M \int_0^t \left(\frac{d\alpha}{dt}\right)_m dt = \sum_1^M \int_0^t c_m A_m exp\left(\frac{-E_m}{RT}\right)(1-\alpha)^{n_m} dt \tag{193}$$

Since the definition of the extent of reaction α the integral eq.(193) must be equal to 1. The system of equation 192 has $2M$ degree of freedom and it is not expected that a solution of the optimization process fits well the experimental data. Hence, since the values of *E* and *A* has an inherent uncertainty due to the experimental measurements, and data treatment, a searching interval near the pre-determined values of *A* and *E* obtained for the iso-conversional method is applied to the optimization process. Therefore the degree of freedom is increases from $2M$ to $4M$.

4.1.5. ADDITIONAL PROPERTIES FOR REACTION MECHANISM

CFD application needs additional information in order to perform a simulation involving chemical reactions. The reaction mechanism must be closed with the enthalpy of reaction H_R for each reaction. Other physical properties such heat capacity, particle size and density of each component and char must be supplied. Also, a lumped-gas phase must be defined adding more physical properties.

Due to the lack of information for *Chlorella Vulgaris* microalgae in CFD calculations, parameters and properties must be obtained from literature or adapted from known materials. In the case of heat of reaction for moisture elimination, latent heat of steam h_{fg} is proposed and is determined by ASYS Fluent 19.0 fluids database. For carbohydrates thermal decomposition, considering the analysis made in Chapter 3, that

shows that it is composed by, among others substances, xylose monomers, the heat of reaction of hemicelluloses, that is described by the xylan properties, is used and obtained from the work of Mellin; Kantarelis and Yang, (2014) yields an endothermic heat of reaction for devolatilization of 951.0 kJ/kg. In the case of lipid component, the calculated value of heat of reaction for oleaginous biomass reported by Maddy (2014), whose adapt these parameters from the study of pyrolysis of *Chlorella Vulgaris*, is used with a value of 660.0 kJ/kg. For proteins, the heat of reaction of one of the main amino-acids presented in *Chlorella Vulgaris* as reviewed in the works of Ursu et al. (2014) and Kent et al. (2015), the *glutamic acid*, is used with an endothermic value of 822.4 kJ/kg obtained from the application of eq.(184) to the values of enthalpy of formation reported by Weiss et al. (2018).

Specific heat of each participating species must be supplied to ANSYS Fluent 19.0. For char pseudo-product the pre-defined material *Graphite* is chosen from the ANSYS Fluent 19.0 database, providing the specific heat capacity, the enthalpy of formation and also the thermal conductivity. Polynomial equation as a function of temperature or an averaged heat capacity for *Chlorella Vulgaris* or for other microalgae was not found in literature, therefore the heat capacity suggested by Maddy (2014) is used for each pseudo-component with a value of 1.7 kJ/kg/°C.

Table 27 – Specific heat capacity for Chlorella Vulgaris similar components.

Component	Specific heat capacity [kJ/kg/K]	Temperature [K]
Cellulose: Glucose	1.2 to 1.7[a]	300 to 400
Xylose: Xylan	1.17 to 3.44[b]	573 to 1123
Palmitic acid	1.80[c]	298
Aspartic acid	1.16[c]	298
Glutamic acid	1.19[c]	298
Alanine	1.37[c]	298

[a]Referenced by Thybring (2014), [b]Sampaio et al. (2016), [c]Obtained from NIST data base (https://webbook.nist.gov/chemistry, 2018).

It is worth to note that the value suggested by the later author is close to the values of the heat capacity of glucose (considered cellulose) and palmitic acid showed in Table 27, however significantly different for Xylose (used to describe the hemicellulose) and amino acids such as aspartic and glutamic acids and alanine.

Particle effective density is an important parameter for fluid dynamics calculations, and the value for microalgae biomass is seldom, however the bulk density used in this here was obtained from the work of Almeida et al. (2017) that reports a value of 525 kg/m^3. Finally, particle sizes are different according to different authors due to the selection of specified mean particle diameter in order to perform the thermal analysis or fast pyrolysis experiments. Raheem et al. (2015) reports a mean size of 100μm, Lopez-Gonzalez et al. (2014) a mean average value between 100 to 150 μm, Gong et al. (2013) performs thermal analysis with particle size ranging between 40 and 150 μm and finally, De Fillipis et al. (2015) has selected particles with values between 50 and 100 μm. A mean value based on a referenced author yields a value of near 100 μm. However, the value reported by Belotti et al. (2014), d = 150 μm, is used due to that the lab-scale fast pyrolyzer in their studies will be simulated here in order to assess the reaction mechanism.

4.2. CFD IMPLEMENTATION USING ANSYS FLUENT 19.0

ANSYS Fluent 19.0, from here, is probably the most used CFD software for simulating complex hydrodynamics systems. ANSYS Fluent 19.0 has capabilities to simulate and solve hydrodynamics, electrodynamics, solid stress analysis and ODE (Ordinary Differential Equations) systems and other engineering applications. Although ANSYS Fluent 19.0 is not totally flexible, such as OpenFoam (OpenFoam.org), the software has several built-in sub-models and methods ready to use being relatively easy to start simple fluid dynamics projects such as compressible and incompressible one phase, multi-phase and reacting flows. However, customization can be applied by means of the tuning of different sub-models and with an interaction with the main program through User Defined Functions (UDF) files. An additional advantage is that ANSYS Fluent 19.0 has generous user manuals that covering from some aspect of the theory up to semi-advanced tutorials, with specific guides for pre and post processing.

4.2.1. TUBULAR DROP REACTOR

As has been showed in Chapter 2 fast pyrolysis experiments can be performed using a Thermogravimetric apparatus and using a lab-scale fast pyrolyzer. The main difference between both processes is that in the former, and by definition, the transport effects must be avoided or diminishing to an order in where the net effects are negligible. In

other words discarding transport effects can reveal the pure kinetics about the thermal decomposition. Mass and heat resistances are the two main transport effects that may be avoided in TG experiments, in where species concentration and temperature gradients should not control the residence time inside the material and the rate of reaction, respectively. Mass and heat resistances is reduced using a suitable sample size in the order of milligrams, however, heat transfer is always controlled by the inherent thermal conductivity of a material, and the mass resistance is controlled by intra-particle hydrodynamics, that is related with characteristic geometry, viscosity of the gases that are released by heterogeneous reaction inside the particle.

On the other hand, heat transfer and macroscopic mass transfer must be enhancement in order to reach high heating rates and short residence time, respectively, in order to avoid secondary cracking reactions. However, large temperature gradients must be also avoided in order to maintain the homogeneity and produce char, gas and non-condensable substances in same conditions. Inside a lab-scale reactor homogeneity can be reached by means an intense mixing involving other physical properties of particle such as density, coalescence, shape and maximum packing. Three types of reactors are commonly encountered in literature i.e. the fluidized bed, the continuous fluidized bed and drop reactors. Fluidized and circulating fluidized bed reactors are similarly, and the difference is that on fluidized the char particles remains inside the reactor and in the later char can leave the reactor from the top. High heating rates can be reached by the use of an inert particles such as sand, and the intense mixing with a continuous injection from the bottom of an inert gas such as nitrogen. The residence time of particles is infinite in the case of fluidized bed reactor and can be controlled in the circulating fluidized bed. On-condensable and condensable gas is controlled by vertical length and with the volumetric rate of the inert gas. In drop reactors mass enters the reactors from top end and falls gravimetrically. Heat is transferred from the reactor walls and the devolatilization take place. As the produced gases are released flows towards the top of the reactor transferring additional heat to biomass. The residence time of particles can be controlled by the reactor tilt angle and the residence time of gases by volumetric flow rate of an inert gas injected from the bottom end of the reactor.

For these three reactors transport properties of particles and gases must be determined. Thermal conductivity of biomass is one of the fundamental property in order

to transfer heat for the devolatilization reaction. Particle stream properties are different than the gas phase properties. Frequently gas flows can be described by means a Newtonian fluid type rheology. Kinetic Theory of Granular Flows can be used to describe the particle flow as a continuum as was presented in Chapter 3. By means the equations of the KTGF the transport equations can be closed and the hydrodynamics can be predicted. However, properties of particles must be provided, such as particle thermal conductivity, density, size, maximum packing, particle-particle and particle-wall restitution coefficient. These particle properties in conjunction with KTGF allow the simulation of the pyrolysis in the framework of any of the lab- scale reactor described in this section.

Authors such as Gong et al. (2013), Yuan, Tahmasebi and Yu (2015) and Belotti et al. (2014) has been performed and reported fast pyrolysis experiments of *Chlorella Vulgaris*, as has been presented in Chapter 2. All the cited authors have reported yields of char and condensable and non-condensable gases as a function of the pyrolysis temperature. The carefully examination of these papers reveals feasibility to simulate the experiment conditions starting from the reactor parameters reported by the authors. Gong et al. (2013) and Yuan, Tahmasebi and Yu (2015) has performed the fast pyrolysis experiment using a fluidized bed quartz bed reactor. Geometrical information in both cases were not fully reported, specifically the height length. The later parameter is important when secondary reactions are in study, due to the higher the height higher the residence time. In this study the reaction mechanism not account for secondary reaction, therefore the height length can be deduced based on similar lab-scale reactor reported in other articles. For fluidized bed the particle residence time is virtual infinite, due to particle remains inside the reaction zone during the experiments. Therefore the experiment global time should be reported in order to run a simulation, however neither Gong et al. (2013), Yuan, Tahmasebi and Yu (2015) has been reported this process parameter being impossible to be deduced or estimated. Additionally, bed height and its relation with density and maximum packing size are important. Bed height was reported in both articles, however, maximum packing or density were not reported. The later properties, can be calculated based on *Chlorella Vulgaris* properties published in other articles, nonetheless introducing additional uncertainty in simulations.

Fast pyrolysis experiments performed by Belotti et al. (2014) was implemented in a tubular drop reactor showed in Figure 67. Reactor parameters are defined including, diameter, inlets and outlets and the height of the reaction zone. Also, biomass feeding rate and nitrogen volumetric flow rate are provided and particle residence time specified. Drop reactor is fully continuous and maximum packing data is not necessary due to it is not expected that particle phase volume fraction reach maximum packing value inside the reaction zone. Therefore, assumptions necessary to simulate the fast pyrolysis process of *Chlorella Vulgaris* are limited to the following unknown properties: thermal conductivity of biomass, restitution and specularity coefficients, effective particle density, and enthalpy of formation of pseudo-components.

Figure 67 – Lab-scale fast pyrolyzer used by Belotti et al. (2015) for *Chlorella Vulgaris* pyrolysis.

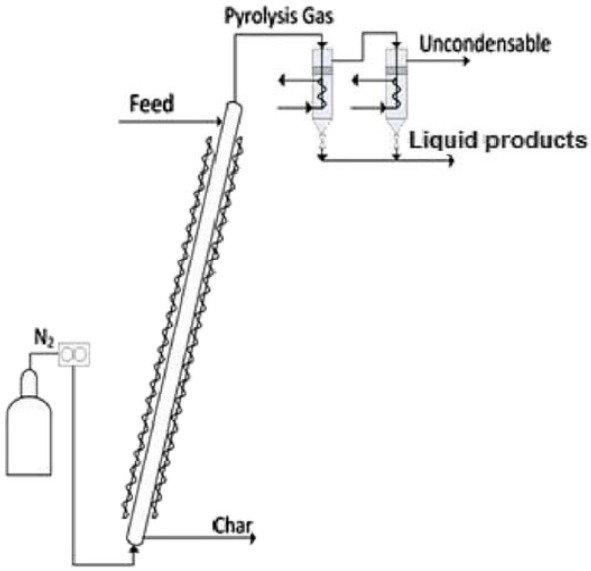

Source: Belotti et al. (2015).

4.2.1.1. REACTOR MODEL

Belotti et al. (2015) have provided geometric and size parameters and characteristics of the drop reactor as shown in Figure 68 being electrical heated, tubular, with 8 mm in diameter, 700 mm in length and with a tilt angle of 70 degrees with respect to the horizontal reference. Also, a mass feeding rate of 2.5E-5 kg/sec and a volumetric flow rate of nitrogen at normal conditions of 0.2 liters/min are reported indicating near 2 seconds for particle residence time. The authors state that the sliding effect on walls

produce a high heating rate in order to promote pyrolysis. Neither size nor shape of inlets i.e. biomass (at top) and nitrogen inlets nor gas and char (at bottom) outlet is reported.

From the point of view of CDF simulation, a two dimensional axisymmetric modeling, in the length axis, is proposed. However, the reactor meets the condition of axisymmetry only in geometry because of the effect of gravity produces a non-symmetric body force condition. To simulate the sliding effect inside the tubular reactor, an axisymmetric gravity force field will be assumed in order to promote the particle flow in contact with the reactor wall. Nitrogen inlet and gas outlet were assumed with a circular area with a diameter equal to the reactor diameter i.e. 8 mm. The biomass inlet was assumed as a lateral inlet with a length of 2 mm producing a cylindrical surface.

Figure 68 – Lab-scale fast pyrolyzer used by Belotti et al. (2015) for *Chlorella Vulgaris* pyrolysis with additional details.

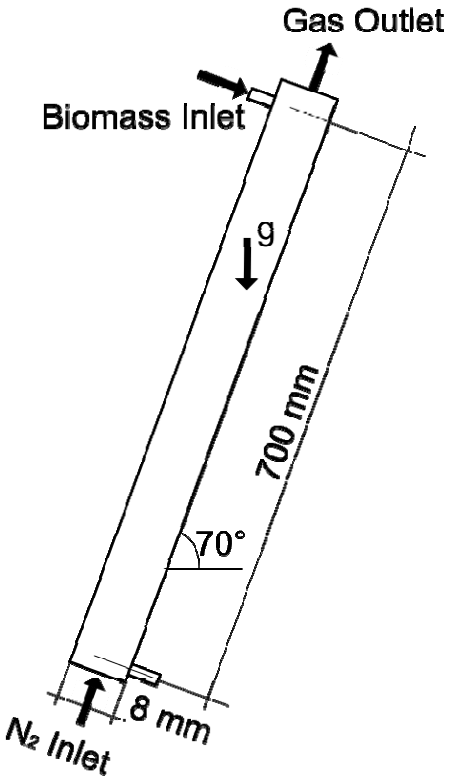

In ANSYS Fluent 19.0, the symmetry axis must be aligned with the *x* direction and the model must be drawn in the *xy* positive quarter. Therefore, the model was translated as is depicted in Figure 69 changing the direction of the gravity force. In Figure 69, gravity

points in the positive *y* direction to promote the sliding effect on the wall. The gravity acceleration components for the new orientation are:$\vec{g} = (-9.22, 3.36)\ [m/s^2]$.

In Figure 67, the outlet for char at bottom of the reactor is depicted. The mechanism for char removal was not reported in the article of Belotti et al. (2015). However, char can be removed by a screw that seals the reactor. Therefore, simulating the char outlet as a pressure outlet is not feasible since it affects the nitrogen flow field. Instead, an additional portion of tube is added in the bottom of the reactor in order to contain the residual biomass that has passed through the reaction zone maintaining the original length of the reactor.

This modification introduces an effect in simulations from the point of view of the heat transfer and from the drag force exerted by the gas on the biomass in the reaction zone. The biomass in the first 100 mm of the reactor would still be devolatilizing producing more gas, then, the volumetric flow rate will be higher increasing the heat transfer and drag. Therefore, this effect must be discussed in Chapter of results. Additionally, 100 mm is added on top of the reactor in order to avoid numerical issues related to back flow. This modification can affect the results significantly if secondary reaction is considered. However, the effects on hydrodynamic must be evaluated.

Figure 69 – Lab-scale fast pyrolyzer used by Belotti et al. (2015) for *Chlorella Vulgaris* pyrolysis.

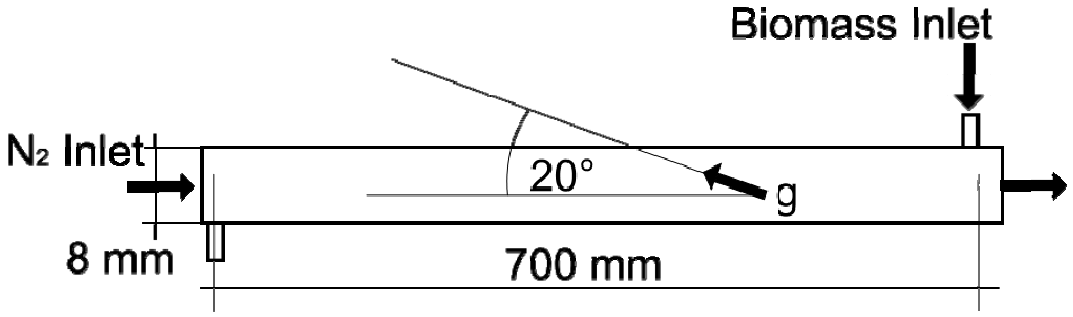

Figure 70 – Lab-scale fast pyrolyzer scheme for CFD simulations. In red the effective reaction zone. Symmetry axis is defined by dash line.

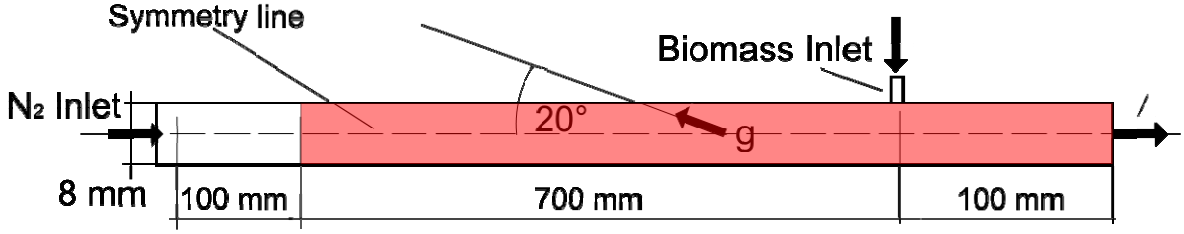

Figure 70 shows the model implemented in ANSYS Fluent 19.0, the part above the symmetry line, depicted in this figure will be simulated in calculations. The total reactor length is 900 mm, however, the effective reaction zone considers the original 700 mm, depicted in red in Figure 70.

4.2.1.2. BIOMASS CONVERSION INDEX

Biomass conversion is an objective variable in pyrolysis studies and is defined here as *the total mass of solid devolatilized during the pyrolysis*. Biomass conversion can be calculated *as the difference of the total solid residue that can include char and biomass components*. This quantity can be determined performing a mass balance over the effective reaction zone, including the back flow of pyrolytic gases and nitrogen from the extra length on the left part of the reactor scheme in Figure 70.

In order to determine the biomass conversion the Reynolds Transport Theorem (RTT) is used

$$0 = \frac{d}{dt}\left(\int_{CV} \rho dV\right) + \int_{CS} (\rho u \cdot \vec{n}) dA \tag{194}$$

In where CV, CS and $\vec{n}$ are: control volume, control surface and the local normal vector pointing to the outside of the control surface. Term ρdV and $\rho u \cdot \vec{n}$ refers to the total mass inside the control volume and the mass flow rate through boundaries. Considering a multiphase flow integrals terms can be separated for each components i.e. biomass, char and gases as

$$\begin{aligned} 0 = \frac{d}{dt}\left(\int_{CV} \rho_{BM} dV + \int_{CV} \rho_{char} dV + \int_{CV} \rho_{gas} dV\right) + \int_{CS} [(\rho u)_{BM} \cdot \vec{n}] dA \\ + \int_{CS} [(\rho u)_{char} \cdot \vec{n}] dA + \int_{CS} \left[(\rho u)_{gas} \cdot \vec{n}\right] dA \end{aligned} \tag{195}$$

Reaction rates over the control volume can be evaluated by means of the mass balance for each component as

$$\int_{CV} \dot{R}_i dV = \frac{d}{dt} \int_{CV} \rho_i dV + \int_{CS} [(\rho u)_i \cdot \vec{n}] dA \tag{196}$$

In where $\dot{R}$,is the local volumetric rate of reaction. Adding all components yields eq.(195). Because the simulation is the transaction type, mass balance must be performed over the total calculation time interval. Taking the time integral of eq.(195) yields the total mass considered in simulation.

Figure 71 – Mass balance over the effective reactor zone depicted in red (cv' is the difference between the total reactor volume and the effective reactor zone).

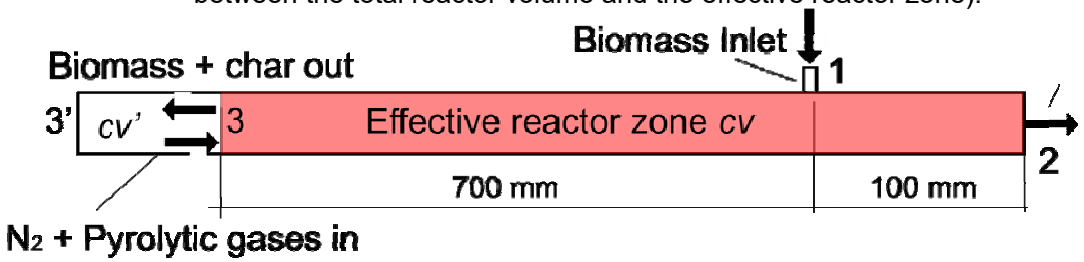

Biomass conversion is calculated as the ratio between the change of biomass inside the effective reactor zone and total biomass considered in calculations. Figure 71 shows the control volume in where mass balance is applied. Biomass conversion is calculated by eq.(197) based on RTT equation.

$$conv = 1 - \frac{\left[\int_{Reactor}(\alpha u)_s dV\right]_{t=T} + \int_T \left(\int_3 [(\rho u)_s \cdot \vec{n}]dA - \dot{m}_{PyGas}\right) dt}{\int_T \int_1 [(\rho u)_s \cdot \vec{n}]dA\, dt} \quad (197)$$

First term on numerator on RHS is the total mass of solid inside the effective reaction zone that include non-converted biomass and produced char at total time T. Second term accounts for the total mass flown to outside of the effective reaction zone integrated on the total time interval T. This term accounts for the pyrolytic gases produced outside of the effective reaction zone depicted in Figure 71. This term can be calculated performing a time integral over surface 3 for the gas phase subtracting the time integral of the nitrogen mass flux over the surface 3'

$$\dot{m}_{PyGas} = \int_3 [(\rho u)_g \cdot \vec{n}]dA - \int_{3'} [(\rho u)_g \cdot \vec{n}]dA \quad (198)$$

In eq.(198) second integral is performed over the nitrogen mass inlet boundary condition i.e. surface 3', therefore gas phase in this surface is comprised only by nitrogen. Second integral in eq.(198) are evaluated under the assumption of stationary regime of nitrogen flow.

Can be calculated by using the *volumeInt() function* of CFD-Post in ANSYS WorkBench post-processor. This function performs a numerical integration at each cell of a defined domain, in this case, the portion of the main domain corresponding to the effective reactor zone. Time integrals over surfaces in eq.(197) and eq.(198) are calculated in the following form. Firstly, overall time step data recorded during simulations mass fluxes are integrated over surfaces using the CFD-Post function *massFlow().* All the integral data acquired in the later step is stored in a spreadsheet as a function of time and numerically integrated using the trapezoid rule considering the local time step. Finally, all time integrated data is added resulting in the total mass flow over the surface.

4.2.2. MULTI-PHASE EULERIAN-EULERIAN FIELD EQUATIONS

The complete background for multi-phase flow equations were presented in Chapter 3. However, the balance equations are generic and the constitutive relations nor the macroscopic jump conditions were defined. In the following sections, the specific balance equations are introduced together with the selected models available in ANSYS Fluent 19.0. In general, all equations have been obtained from the *ANSYS Fluent 19.0 Theory Guide* (On line version https://ansyshelp.ansys.com) and the gas phase and the solid phase are identified with the subscript g and s. Once the generic equation used by ANSYS Fluent 19.0 is presented, the specific equation for the current application is also presented.

4.2.2.1. MASS CONSERVATION EQUATIONS

Conservation equation used in the multi-phase flow model is defined in Chapter 3 in a general way. However, closure and constitutive relations were not provided. Generic conservation equation for n phases in ANSYS Fluent 19.0 considers a mass transfer between the phases $\dot{m}_{pq}$ i.e. mass transfer from phase p to phase q, and additional user defined source term S_q^{ρ}.

$$\frac{\partial(\varepsilon_q \rho_q)}{\partial t} + \nabla \cdot (\varepsilon_q \rho_q v_q) = \sum_{1}^{n} (\dot{m}_{pq} - \dot{m}_{qp}) + S_q^{\rho} \tag{199}$$

In where ε_q is the volume fraction of phase q. The mass conservation equation for gas phase is:

$$\frac{\partial(\varepsilon_g \rho_g)}{\partial t} + \nabla \cdot (\varepsilon_g \rho_g v_g) = \dot{m}_{sg} \quad (200)$$

And for the solid phase

$$\frac{\partial(\varepsilon_s \rho_s)}{\partial t} + \nabla \cdot (\varepsilon_s \rho_s v_s) = -\dot{m}_{sg} \quad (201)$$

Mass transfer between phases is related with the devolatilization process which is an uni-directional process from the solid phase toward the gaseous phase, therefore only the term $\dot{m}_{sg}$ remain in eq.(200) and eq.(201). The mass transfer quantity in equation is generic as it is defined depending on the model used. In this case, only mass is transfer due to superficial reactions that represent the devolatilization process defined in the following sub-sections.

4.2.2.2. HETEROGENEOUS CHEMICAL REACTIONS

Pyrolysis process consists of the complex devolatilization of the solid phase by means of several internal and interface processes of the particles. From a global point of view, a net amount of mass is transferred from the solid to the gaseous phases during devolatilization and the process, can ideally, be modeled with a direct transfer into the gas phase by means of a heterogeneous superficial reaction. Two assumptions are implicit in the direct mass transfer approach. Firstly, ***devolatilization reaction is only defined on the surface of the solid phase,*** implying that intra-particle effects and gradients are not accounted for and no intermediate reactions are defined. Secondly, ***mass transfer at the interface does not depend on the interface concentration gradients of species***. Therefore, the net mass transferred between the phases depends on the chemical kinetics and on the interfacial area, which in ANSYS Fluent 19.0 for Eulerian-Eulerian description, can be modeled by two equations. The first interfacial area model, for spherical particles, is the *symmetric model* defined as

$$A_s = \frac{6\varepsilon_s(1-\varepsilon_s)}{d_s} \quad (202)$$

And the particle model defined as

$$A_s = \frac{6\varepsilon_s}{d_s} \quad (203)$$

In where the subscript *s* refers to the solid phase. Examination of these two equations shows that for very diluted phases both models tend to converge, however, for a higher value of ε_s the difference can be large as shown in Figure 72 (for $d_s = 1$).

Figure 72 – Comparison of two different models for the interface area defined in ANSYS Fluent 19.0 considering a particle diameter equal to 1.

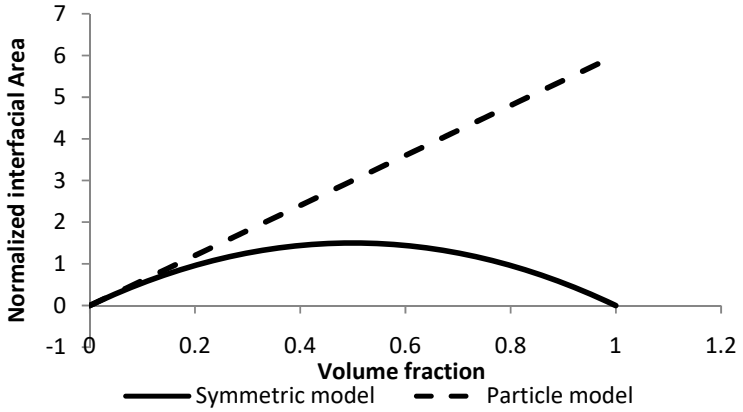

The advantage of eq.(202) is that it ensures that the interfacial area tends to 0 as the solid volume fraction ε_s tends to 1. In the simulation performed here, a low value for ε_s, is expected, however, the effect of the interfacial model may be evaluated.

Considering the first assumption, the bulk pyrolytic gas transferred to the gas phase corresponds to the gas released and measured in the TG and DTG analysis. In order to define a heterogeneous chemical reaction in ANSYS Fluent 19.0, a reaction equation and kinetic parameters consistent with the model provided by ANSYS Fluent 19.0 are necessary.

The contribution of gas released from each pseudo-component can be determined by the DTG analysis; however, contribution of char by each pseudo-component is not known starting from the thermal analysis. Therefore, an assumption about the char distribution must be defined. Considering an analysis of 1 kg of gas released, the mass of volatile of each pseudo-component is known through the parameter c_m of eq.(192). However, how much char was produced for each pseudo-component is not known due to the fact that a temporal analysis of the residue was not performed in the TG analysis. This is evident by performing the following analysis. Considering the mass fraction Y_i of any of the pseudo-component as the sum of the volatiles and char

$$Y_i = Y_{g,i} + Y_{c,i} \tag{204}$$

Where $Y_{g,i}$ and $Y_{c,i}$ are the volatile gas fraction, and the char mass fraction of the pseudo-component i, all in wet basis. Adding all Y_i including the moisture mass fraction $Y_{moisture}$ gives

$$1 = Y_{moisture} + Y_g + \sum Y_{c,i} \tag{205}$$

Where Y_g is the total volatile released (gases different of water vapor), in wet basis. It is worth noting that

$$Y_{moisture} + Y_g = \sum c_m \tag{206}$$

In where c_m (same parameter of eq.(192)) is mass fraction of pseudo-component present in the non-devolatilized biomass or in other word the initial mass fraction of the microalgae. Solving eq.(205) for $\sum Y_{c,i}$ gives

$$\sum Y_{c,i} = 1 - \left(Y_{moisture} + Y_g\right) \tag{207}$$

Therefore, there are infinite solutions for eq.(207), and an assumption must be made. The assumption proposed here is the following: ***the amount of char produced by each pseudo-component is proportional to the amount of gas released by the pseudo-component.*** The assumption implies the following corollary: ***the amount of pseudo-component is proportional to the amount of gas released in wet basis***. By expressing the assumption mathematically, the following equation is defined as

$$Y_i = Y_{g,i} + \Omega_i Y_c \tag{208}$$

In where Y_c is the total mass fraction of char in wet basis, produced during de devolatilization, obtained directly from the thermal analysis. The term Ω_i is the weighted factor proportional to the gas mass fraction. However, Ω_i is not directly equal to $Y_{g,i}$ since the factor has the following property: mass conservation provide the following equation

$$Y_{moisture} + \sum Y_i = 1 \tag{209}$$

Substituting eq.(208) in eq.(209)

$$Y_{moisture} + \sum Y_{g,i} + \sum \Omega_i Y_c = Y_{moisture} + \sum Y_{g,i} + Y_c \sum \Omega_i = 1 \quad (210)$$

Then $\sum \Omega_i$ must be equal to 1, and $\sum Y_{g,i}$ is not equal to 1 due to the fact of being in wet basis. Therefore $Y_{g,i}$ must be re-scaled with the following equation

$$\Omega_i = \frac{Y_{g,i}}{\sum Y_{g,i}} \quad (211)$$

Substituting eq.(211) in eq.(210) gives

$$Y_{moisture} + \sum Y_{g,i} + Y_c \sum \frac{Y_{g,i}}{\sum Y_{g,i}} = Y_{moisture} + \sum Y_{g,i} + Y_c \frac{1}{\sum Y_{g,i}} \sum Y_{g,i} \quad (212)$$

Then, the factors f_i are consistent. Therefore, the mass fraction of any component of the microalgae biomass, can be calculated from the thermal analysis and the assumption made about the char distribution, as the sum of the volatile part and the part that will be converted in char before the devolatilization as

$$Y_i = Y_{g,i} + Y_c \frac{Y_{g,i}}{\sum Y_{g,i}} \quad (213)$$

It is worth noting two facts in eq.(213). Firstly, Y_i is the mass fraction of the components. Therefore, it is the distribution of pseudo-components of *Chlorella Vulgaris*, and it is a necessary data for the mass inlet condition in a CFD calculation. Secondly, values of eq.(213) are in wet basis.

Equation 214 defines a normalized reaction in mass basis representing the global devolatilization process for any of the pseudo-components of the reaction mechanism.

$$Y_i \ COMP \overset{k}{\Rightarrow} Y_{g,i} GAS + Y_c \frac{Y_{g,i}}{\sum Y_{g,i}} CHAR \quad (214)$$

Assuming 1 kg of any component and multiplying by $1/Y_{g,i}$ gives

$$\frac{Y_i}{Y_{g,i}} COMP \overset{k}{\Rightarrow} \left(GAS + \frac{Y_c}{\sum Y_{g,i}} CHAR \right) \quad (215)$$

Equation 215 states that the stoichiometric coefficients for the global reaction are the same for all components, since the term $Y_c/\sum Y_{g,i}$ is constant, therefore the left part of the reaction eq.(215) must also be constant. The later is due to the assumption of proportionality respecting the gas release confirming the corollary. Therefore, only one global reaction must be calculated for all pseudo-components. It is worth verifying the consistency with the moisture elimination reaction that does not produce char.

$$\frac{Y_i}{Y_{g,i}} COMP \overset{k}{\Rightarrow} GAS \tag{216}$$

Since for moisture elimination Y_i must be equal to $Y_{g,i}$ eq.(216) is consistent for all reactions in the mechanism. Multiplying eq.(216) by a suitable factor, the following equation is obtained for 100 kg of any component

$$100\ kg\ COMP \overset{k}{\Rightarrow} g\ kg\ GAS + c\ kg\ CHAR \tag{217}$$

In eq.(217) k, g and c are: the kinetic coefficient, the stoichiometric coefficient of total gases released (condensable and non-condensable) and the stoichiometric coefficient of char. If a molar mass of 100 kg/kmol is arbitrarily chosen for $COMP$ and a gas distribution is assumed, the reaction equation in molar basis is

$$COMP \overset{k}{\Rightarrow} \bar{g}_1 GAS_1 + \bar{g}_2 GAS_2 + \cdots + \bar{g}_n GAS_n + \bar{c} CHAR \tag{218}$$

Frequently, the gas distribution in products is provided in volumetric fractions, while the component and char is provided in mass fraction. Reaction is calculated for 1 kmol of component. If the molar mass of the component is not known, that reaction equation is calculated in mass base. Therefore, the volumetric distribution of gases must be expressed in mass basis with the following equation

$$m_{GAS_i} = M_{GAS,i} V\% \tag{219}$$

Where m_{GAS_i}, $M_{GAS,i}$ and $V\%$ are; mass of the gas, molar mass of gas and the volumetric fraction. In order to determine the stoichiometric coefficients $\bar{g}_i$ a base of 100 kg of solid components, $COMP$, is considered. Therefore, mass of each gas must be scaled. The total amount of gas released for 100 kg of component is determined using the following conversion factor

$$f_{GAS-100kg} = 100(1-c)\left(\sum_{i=1}^{n} M_{GAS,i} V\%\right)^{-1} \quad (220)$$

Where $1-c=g$ is the global gas mass fraction about the total initial mass of all components released during the thermal decomposition. The later data is expressed in dry basis owing the moisture elimination to be considered apart. Dry-global gas mass fraction $g=1-c$ is obtained directly from the wet-global gas mass fraction data Y_{GAS} from TG analysis with the following equation for c

$$c = \frac{1-Y_{GAS}}{1-Moisture} \quad (221)$$

In where $Moisture$ is the moisture content of material in mass basis and it is obtained directly from the TG and/or DTG analysis. Since the distribution of gases in mass basis is known from eq.(219), then the mass distribution for 100 kg of component can be calculated with the following equation

$$m_{GAS_i-100kg} = \frac{f_{GAS-100kg}}{m_{GAS_i}} \quad (222)$$

Finally, the stoichiometric coefficient for any gas is given by

$$\bar{g}_i = \frac{m_{GAS_i-100kg}}{M_{GAS,i}} \quad (223)$$

A similar equation is defined for char stoichiometric coefficient

$$\bar{c} = \frac{100\left(1-Y_{gas}\right)}{M_{graphite}} \quad (224)$$

Where the molar mass of graphite is considered. Since the assumption made of the molar mass of the component is arbitrary, it is set to 100 kg/kmol.

ANSYS Fluent 19.0 uses the following equation to quantify an irreversible heterogeneous reaction at the surface of the solid phase (ANSYS Fluent 19.0).

$$R = k\left[\prod_{j=1}^{N}\left[\frac{Y_j \rho_{j,p} \varepsilon_{j,p}}{M_j}\right]^{st}\right]\left[\frac{kmol}{m^3\ sec}\right] \quad (225)$$

In where R, k, Y_j, $\rho_j, M_j, \varepsilon_{j,p}$ and st are the reaction rate of a particular specie, the Arrhenius kinetic coefficient, the mass fraction of reactant j, the effective density of specie j in phase p, the molar mass of the species j, the volume fraction and the rate of reaction exponent. For a reaction where there is only one reactant eq.(225) is

$$R = k\left(\frac{Y_j \rho_{j,p} \varepsilon_{j,p}}{M_j}\right)^{st} \left[\frac{kmol}{m^3\ sec}\right] \tag{226}$$

The term inside the parentheses is de molar concentration of the reactant. Comparing eq.(226) with eq.(227) reveals that a modification for the rate equations of the mechanism is necessary.

$$\left(\frac{d\alpha}{dt}\right)_m = c_m A_m exp\left(\frac{-E_m}{RT}\right)(1-\alpha)^{n_m} \tag{227}$$

Using the extent of reaction equation, eq.(29), using the total mass, TM, of volatiles instead w and considering $TM_f = 0$ (due to the rate equations of the reaction mechanism were obtained under this assumption) gives

$$\alpha = -c_m\left(\frac{TM(t) - TM_0}{TM_0}\right) = \left(\frac{COMP(t) - COMP_0}{COMP_0}\right) \tag{228}$$

The term c_m is used owing that determines the mass fraction of the component in reference with initial total mass. The temporal derivative is

$$\frac{d\alpha}{dt} = -\frac{1}{COMP_0}\frac{dCOMP}{dt} \tag{229}$$

And substituting in eq.(192) gives

$$\left(\frac{dCOMP}{dt}\right)_m = -COMP_0^{(1-n_m)} A_m exp\left(\frac{-E_m}{RT}\right) COMP^{n_m} \tag{230}$$

Where $COMP_0$ is the initial amount of mass of the component. Equation 192 is defined following a particle with 0 velocities. In order to calculate the rate of mass loss, the initial $COMP_0$ and the actual value $COMP$ is necessary. From the point of view of the Eulerian field description, there is no track over a specific particle. Therefore, eq.(192) or eq.(230) cannot be applied directly. The following reasoning is applied in order to

express the material equation in a suitable form to be applied in a transport equation. When an amount of mass of particle, $COMP_{t_0}$, enters into a fixed finite and small control volume in the space at x_0 point at $t = t_0$, its devolatilization may begin and the rate of reaction can be calculated with eq.(230), based with scale value $COMP_{t_0}$. In a finite interval Δt_1 part of the particle is devolatilized and an amount of gas is released and a residual char is created in the particle matrix. Therefore, the amount of mass of the component has changed and a new amount of mass of component $COMP_{t_0+\Delta t_1}$, different from the initial value, occupied the fixed control volume due to reaction, advection and diffusion. In the next finite interval Δt_2, and observing the same fixed control volume, the particle can continue its devolatilization and the rate of reaction in that volume can be calculated again with eq.(230). However, the amount of mass is $COMP_{t_0+\Delta t_1}$ instead of $COMP_{t_0}$. Therefore, from the point of view of the Eulerian description, that observes a fixed volume in space, the reaction rate is calculated by considering the current concentration in the fixed volume, then by applying this concept, results in a suitable equation for evaluating the rate of reaction given by the eq.(231), considering the limit in time and space

$$\left(\frac{dCOMP}{dt}\right)_m = -COMP^{(1-n_m)}(x_0,t)A_m exp\left(\frac{-E_m}{RT}\right)COMP^{n_m}(x_0,t) \tag{231}$$

Equation 231 is reduced to

$$\left(\frac{dCOMP}{dt}\right)_m = -A_m exp\left(\frac{-E_m}{RT}\right)COMP(x_0,t)\left[\frac{kg}{sec}\right] \tag{232}$$

a first order expression. Equation 232 specifies the units' dimensions, and it is necessary to express it in mass quantity per unit volume. Introducing the density, molar mass and considering a volume ΔV in eq.(232) gives

$$\left(\frac{1}{\Delta V}\frac{dN_{COMP}}{dt}\right)_m = -A_m exp\left(\frac{-E_m}{RT}\right)\frac{\rho_{COMP}}{M_{COMP}}\left[\frac{kmol}{m^3 sec}\right] \tag{233}$$

Comparing eq.(233) with eq.(234)

$$R = k\left(\frac{Y_j \rho_{j,p} \varepsilon_{j,p}}{M_j}\right)^{st}\left[\frac{kmol}{m^3\ sec}\right] \tag{234}$$

reveals that the second ratio on the RHS of the eq.(233) represents the same quantity that the second ratio term of the product on the RHS of eq.(234) i.e, the molar concentration of a reactant. The difference between the two expressions lies in the variables used for its calculation. In eq.(234) the variables used are those commonly available for hydrodynamics.

Comparing both equations in more detail yields that $st = 1$ and k is given by the pure kinetic term of eq.(192) both equations

$$k = -A_m exp\left(\frac{-E_m}{RT}\right)\left[\frac{1}{sec}\right] \tag{235}$$

In summary, in order to set up the heterogeneous model in ANSYS Fluent 19.0 it is necessary to provide the Arrhenius kinetic parameters A and E, the gas phase species and their respective stoichiometric coefficients.

4.2.2.3. MOMENTUM CONSERVATION EQUATIONS

The momentum conservation equation is defined in ANSYS Fluent 19.0 as follows in general notation for the continuous phase i.e. gaseous phase.

$$\begin{aligned}\frac{\partial(\varepsilon_q\rho_q v_q)}{\partial t} + \nabla\cdot(\varepsilon_q\rho_q v_q v_q) \\ = -\varepsilon_q\nabla P + \nabla\cdot(\tau_q) + \varepsilon_q\rho_q\vec{g} + \sum_1^n\left(R_{pq} + \dot{m}_{pq}v_{pq} - \dot{m}_{qp}v_{qp}\right) \\ + \left(\vec{F}_q + \vec{F}_{lift,q} + \vec{F}_{wl,q} + \vec{F}_{vm,q} + \vec{F}_{td,q}\right)\end{aligned} \tag{236}$$

Where $R_{pq}, \dot{m}_{pq}v_{pq}, \vec{F}_q, \vec{F}_{lift,q}, \vec{F}_{wl,q}, \vec{F}_{vm,q}, \vec{F}_{td,q}, \tau_q$ and ∇P are the interaction forces between phases, momentum transfer due to mass transfer, external body forces, lift force, wall lubrication force, virtual mass force, turbulent dispersion force, pressure gradient and the stress tensor, respectively. Stress tensor τ_q is shown in eq.(236)

$$\tau_q = \alpha_q\mu_q\left(\nabla u_q + \nabla u_q^T\right) + \alpha_q\left(\lambda_q + \frac{3}{2}\mu_q\right)\nabla\cdot u_q I \tag{237}$$

Following the article from Mellin; Kantarelis and Yang (2014) that performed a 2D simulation of lignocellulosic material in a fast pyrolyzer, current simulation, neither considered lift, virtual mass, lubrications, turbulent momentum dispersive nor other body

forces. The rest of the terms are presented in the following sub-sections. Momentum transfer equations for current simulation are, for gaseous phase.

$$\frac{\partial(\varepsilon_g \rho_g v_g)}{\partial t} + \nabla \cdot (\varepsilon_g \rho_g v_g v_g) = -\varepsilon_g \nabla P + \nabla \cdot (\tau_g) + \varepsilon_g \rho_g \vec{g} + R_{sg} + \dot{m}_{sg} v_{sg} \tag{238}$$

In where external body forces $\vec{F}_q$ accounts for only the acceleration of gravity and represented by the term $\varepsilon_g \rho_g \vec{g}$. For solid phase, ANSYS Fluent 19.0 provides a different structure due to the granular theory, however, with the same physical meaning

$$\begin{aligned} &\frac{\partial(\varepsilon_s \rho_s v_s)}{\partial t} + \nabla \cdot (\varepsilon_s \rho_s v_s v_s) \\ &\qquad = -\varepsilon_s \nabla P - \nabla P_s + \nabla \cdot (\tau_s) + \varepsilon_s \rho_s \vec{g} + K_{ls}(v_l - v_s) - \dot{m}_{sg} v_{sg} \\ &\qquad + \left(\vec{F}_s + \vec{F}_{lift,s} + \vec{F}_{vm,s} + \vec{F}_{td,s}\right) \end{aligned} \tag{239}$$

In where P_s, K_{ls} and $v_g - v_s$ are the solid pressure; the momentum exchange coefficient between the solid and gaseous phases; and the relative velocity between the phases, respectively. If other forces are not considered a resulting momentum conservation equation in this application is

$$\begin{aligned} &\frac{\partial(\varepsilon_s \rho_s v_s)}{\partial t} + \nabla \cdot (\varepsilon_s \rho_s v_s v_s) \\ &\qquad = -\varepsilon_s \nabla P - \nabla P_s + \nabla \cdot (\tau_s) + \varepsilon_s \rho_s \vec{g} + K_{gs}(v_g - v_s) - \dot{m}_{sg} v_{sg} \end{aligned} \tag{240}$$

In where momentum interface exchange is only due to drag and heterogenous chemical reaction effects. Constitutive equations for $-\nabla P_s$ and τ_s are presented in the following section and are obtained from the KTGF. Comparing eq.(238) and eq.(240) and considering the interaction force between phases, the term representing the drag force $K_{gs}(v_g - v_s)$ must be equal to $-R_{sg}$.

4.2.2.4. GAS-SOLID MOMENTUM EXCHANGE COEFFICIENT

The momentum exchange coefficient is K_{gs} depends on the model chosen. A general form is presented in eq.(241) 244. The exchange coefficient is

$$K_{gs} = \frac{\varepsilon_d \rho_s \hat{f}_s}{\tau_s} \tag{241}$$

Where $\hat{f}_s$ and τ_s are the drag function and the relaxation time of particles. The latter is calculated by

$$\tau_s = \frac{\rho_s d_s^2}{18\mu_g} \tag{242}$$

Where d_s^2 and μ_g are the particle diameter and the gaseous viscosity. Following the article from Mellin; Kantarelis, and Yang (2014) the momentum exchange model chosen and used here is the *Morsi and Alexander* model for biomass-gas mixture. Model equations are, for the drag function

$$\hat{f} = \frac{C_D Re}{24} \tag{243}$$

Drag coefficient is calculated by means

$$C_D = a_1 + \frac{a_2}{Re} + \frac{a_3}{Re^2} \tag{244}$$

In where the parameters a_1, a_2 and a_3 are provided as a function of the Reynolds Number according to the following Table 28

Table 28 – Parameters for drag coefficient of *Morsi and Alexander* model.

$\boldsymbol{Re}$ range	$\boldsymbol{a_1}$	$\boldsymbol{a_2}$	$\boldsymbol{a_3}$
$\mathbf{0} < Re < 0.1$	0	24	0
$\mathbf{0.1} < Re < 1$	3.690	22.73	0.0903
$\mathbf{1} < Re < 10$	1.222	29.1667	-3.8889
$\mathbf{10} < Re < 100$	0.6167	46.50	-116.67
$\mathbf{100} < Re < 1000$	0.3644	98.33	-2778
$\mathbf{1000} < Re < 5000$	0.357	148.546	-47500
$\mathbf{5000} < Re < 10000$	0.46	-490.546	578700
$\boldsymbol{Re} \geq \mathbf{10000}$	0.5191	-1662.5	5146700

However, according to the ANSYS Fluent 19.0 Theory Guide (https://ansyshelp.ansys.com), the Morsi and Alexander model can be instable, therefore, the *Symlal-O'Brien's* model used by Mellin; Kantarelis, and Yang (2014) for sand-gas interaction, can be used as an alternative for the gas-solid. Equation for the latter model is:

$$\hat{f}_s = \frac{\varepsilon_g C_D Re_s}{24 v_{r,s}^2} \tag{245}$$

In where C_D,Re_s and $v_{r,s}^2$ are the drag coefficient, solid Reynolds number and the terminal velocity. Drag coefficient is calculated from

$$C_D = \left(0.63 + \frac{4.8}{\sqrt{Re_s / v_{r,s}}}\right)^2 \quad (246)$$

And the Reynolds number for particles is

$$Re_s = \frac{\rho_d d_s |v_s - v_g|}{\mu_g} \quad (247)$$

Then, the momentum exchange coefficient between the solid and the gaseous phase is

$$K_{sg} = \frac{3\varepsilon_s \varepsilon_g \rho_g d_s}{4 v_{r,s} d_s} C_D \left(\frac{Re_s}{u_{r,s}}\right) |v_s - v_g| \quad (248)$$

Terminal velocity is determined by

$$v_{r,s} = 0.5\sqrt{A - (0.06Re_s)^2 + 0.12Re_s(2B - A) + A^2} \quad (249)$$

In where the model parameters *A* and *B* is determined as follows

$$A = \varepsilon_g^{4.014} \quad (250)$$

$$B = 0.8\varepsilon_g^{1.28} \quad (251)$$

If the gaseous volume fraction ε_g is less than or equal to 0.85, and

$$B = 0.8\varepsilon_g^{2.65} \quad (252)$$

If ε_g is greater than 0.85.

4.2.2.5. GRANULAR TEMPERATURE

From the point of view of the physical approximation of the discrete biomass phase, treated as a continuum, additional parameters for the KTGF must be defined in order to determine the parameterized rheology accounting for the stress tensor obtained from the granular temperature. Important parameters are those related to the particle-particle interaction, the wall particle interaction, specularity coefficient, radial distribution function and the maximum particle packing.

Due to the lack of information for microalgae biomass and particularly for *Chlorella Vulgaris* parameters used in this simulation are those parameters obtained from the literature specifically from the work of Benyahia et al. (2000). The latter authors have

performed a cold flow reactor simulation in a riser reactor a with flow regime similar to the regime described in the current work.

Partial differential transport equation for granular temperature is solved in order to determine the constitutive relation for the solid dispersed phase. ANSYS Fluent 19.0 provides the following equation:

$$\frac{3}{2}\left(\frac{\partial(\varepsilon_s\rho_s\Theta_s)}{\partial t}\right) + \nabla\cdot(\varepsilon_s\rho_s v_s\Theta_s) = (-P_s I + \tau_s):\nabla v_s + \nabla\cdot(\kappa_s\nabla\Theta_s) - \gamma_s + \varphi_{gs} \tag{253}$$

In where Θ_s is the granular temperature. The first term on the RHS corresponds to the generation of granular kinetic energy due to stress tensor, the second is the diffusion of granular energy term, in where κ_s is the diffusion coefficient, γ_s is the collision dissipation energy term and φ_{gs} is the exchange energy term between phases. ANSYS Fluent 19.0 provides other two algebraic equations for the granular temperature, however, under the assumption of balanced creation/dissipation energy condition.

4.2.2.6. SOLID PRESSURE

Solid phase pressure is determined by the following equation for incompressible regime, in where the solid packing value is lower than the maximum values, as expected in this simulation.

$$P_s = \varepsilon_s\rho_s\Theta_s + 2\rho_s(1-e_{ss})\varepsilon_s^2 g_{0,ss}\Theta_s \tag{254}$$

Where e_{ss} and g_0 is the particle-particle restitution coefficient and the radial distribution function. For the current simulation particle-particle restitution was obtained from Benyahia et al. (2000). Radial distribution function for spherical particles corrects the probability of collisions when the dispersed phase tends to the maximum packing limit. The function for one solid phase present is determined by

$$g_0 = \left[1 - \left(\frac{\varepsilon_s}{\varepsilon_{s,max}}\right)\right] \tag{255}$$

Where $\varepsilon_{s,max}$ is the maximum particle packing. The value defined in the current work is 0.62 taken from the book of Jakobsen (2008).

4.2.2.7. SOLID SHEAR STRESS

Constitutive closure for solid shear stress is obtained from the granular theory. It is composed by the shear and bulk viscosities. The former is given by the addition of the collisional, and kinetic viscosities

$$\mu_s = \mu_{s.col} + \mu_{s,kin} \tag{256}$$

Collisional viscosity is given by

$$\mu_{s.col} = \frac{4}{6}\varepsilon_s \rho_s g_{0,ss}(1+e_{ss})\left(\frac{\Theta_s}{\pi}\right)^{1/2}\varepsilon_s \tag{257}$$

Also, the kinetic viscosity is

$$\mu_{s.kin} = \frac{\varepsilon_s d_s \rho_s \sqrt{\Theta_s \pi}}{6(3-e_{ss})}\left[1+\frac{2}{5}(1+e_{ss})(3e_{ss}-1)g_{0,ss}\right] \tag{258}$$

It is worth to note that ANSYS Fluent 19.0 adds an additional viscosity to eq.(256) named frictional viscosity. However, it is not used here because it is an important term for dense phases such as packed bed modeling (ANSYS Fluent Theory Guide https://ansyshelp.ansys.com). On the other hand, similarly to the collisional viscosity, the bulk viscosity is given by

$$\lambda_s = \frac{4}{3}\varepsilon_s \rho_s d_s g_{0,ss}(1+e_{ss})\left(\frac{\Theta_s}{\pi}\right)^{1/2} \tag{259}$$

4.2.2.8. ENERGY CONSERVATION EQUATIONS

Energy conservation equation is coupled strongly with the momentum conservation equation. It also has terms related to mass transfer across the interfaces and source terms associated with chemical reaction. ANSYS Fluent 19.0 provides an energy conservation equation based on enthalpy

$$\frac{D\left(\varepsilon_q \rho_q h_q\right)}{Dt} = \varepsilon_q \frac{\partial P_q}{\partial t} + \tau_q : \nabla v_q - \nabla \cdot \vec{q}_q + \sum_1^n \left(\hat{Q}_{pq} + \dot{m}_{pq} h_{pq} - \dot{m}_{qp} h_{qp}\right) + S_q^h \tag{260}$$

Where transient and convective terms are expressed as the material derivative of h_q. On the RHS, first term is the mechanical work due to pressure, second term is work due to shear stress and the third term is the heat flux. Term $\hat{Q}_{pq}$ is the heat exchange

between phases and terms $\dot{m}_{pq}h_{pq}$ and $\dot{m}_{qp}h_{qp}$ are the energy transfers due to mass transfer being h_{pq} the interface enthalpy. Finally S_q^h is a source term that can be associated with chemical reactions. Equations for both phases are the same; however, pressure and stress terms change depending on the type of phase i.e. solid or gaseous.

The heat exchange between phases is modeled based on the local Nusselt number. Heat transferred between phases is

$$\hat{Q}_{pq} = \hat{h}_{pq}\bar{\bar{A}}_i(T_p - T_q) \tag{261}$$

Where $\hat{h}_{pq}$, $\bar{\bar{A}}_i$, T_p and T_q are the convection heat transfer coefficient, interfacial area concentration, local temperatures of phases, respectively. Interfacial area concentration for spherical particle dispersed phase is determined locally by using the following equation

$$\bar{\bar{A}}_i = \frac{6\varepsilon_p}{d_p} \tag{262}$$

Convection heat transfer coefficient is calculated with the following equation

$$\hat{h}_{pq} = \frac{\hat{k}_q Nu_p}{d_p} \tag{263}$$

Following Mellin; Kantarelis, and Yang (2014) the model chosen for the calculation of the particle Nusselt number Nu_p is the *Ranz-Marshall* correlation given by

$$Nu_p = 2.0 + 0.6Re_p^{1/2}Pr^{1/3} \tag{264}$$

Where Pr is the Prandtl number obtained from

$$Pr = \frac{(c_p)_q \mu_q}{k_q} \tag{265}$$

Reynolds number Re_p for the phase q is formulated from the relative velocity $|u_p - u_q|$ between phases

$$Re = \frac{\rho_q |v_p - v_q| d_p}{\mu_q} \tag{266}$$

4.2.2.9. SPECIES CONSERVATION EQUATIONS

A set of species conservation equation is defined for the gas phase.

$$\frac{D\left(\varepsilon^q \rho^q Y_i^q\right)}{Dt} = -\nabla \cdot \varepsilon^q j_i^q + \varepsilon^q \dot{R}_i^q + \varepsilon^q \dot{S}_i^q + \sum_1^n \left(\dot{m}_{p^i,q^j} - \dot{m}_{q^j,p^i}\right) + \dot{R} \tag{267}$$

Where Y_i^q, j_i^q, R_i^q, S_i^q, $\dot{m}_{p^i,q^j}$ and $\dot{R}$ are:mass fractions of species i in phase q, the diffusion coefficient for the species i in phase q determined solving the diffusion model chosen, the net rate of intra-phase production of specie i, the net rate of production of specie i from the dispersed solid phase, the heterogeneous reaction rate and the transfer rate of specie i in phase q.

4.2.2.10. AUXILIARY EQUATIONS

In order to close the system of equation it is necessary to define a state equation type for the gaseous phase. Ideal gas equation is chosen in ANSYS Fluent 19.0 with densities calculated based on volumetric concentration. Solid phase components are considered incompressible with constant densities and no functional relation with pressure.

Transport and thermodynamic properties must be provided in order to perform a simulation. In the case of the solid phase, transport properties, for momentum and energy are provided by means of the Kinetic Theory of Granular Flow (KTGF) (GIDASPOW, 1994). In the present work, the particle diameter is considered a constant and no distribution is defined. Transport and physical properties of continuum gas phase are obtained averaging the single species properties based on volume fraction relative to the gaseous phase. Particular values of properties for the gaseous phase as a function of pressure and temperature are obtained from the ANSYS Fluent 19.0 materials database.

4.2.3. MESHING

A central part of the numerical calculation in CFD, using the finite volume method, is the meshing process to produce the mesh or grid. In order to create and manipulate the grid for the pyrolyzer used in this simulation, the built-in meshing tool CM of ANSYS Fluent

19.0 is used. Boundary zones definition and mesh refinements are performed with CM tool. Mesh quality assess is performed inside ANSYS Fluent 19.0 application verifying the skew factor and the aspect ratio.

Four grids are constructed in order to analyze the solution and convergence. Benyahia et al. (2000) have used a cell grid length of 11.1 mm in the radial direction with a particle size of 76 μm and density of 1712 kg/m^3. The reactor zone consists of vertical tube with 200 mm in diameter and 14.2 m in height. Reynolds Number for gas in the work of Benyahia et al (2000) based on the reactor diameter and a air velocity of 5.2 m/s is Re = 71197. In the current work the same parameter for a nitrogen velocity of 0.066m/s (calculated based on reactor diameter and volumetric flow rate obtained from Belotti et al.) is Re = 36. A max grid length size of 1 mm is proposed as criteria to construct the grid. Finer grids are constructed applying a grid length ratio of 1.5 that gives the following maximum length grid criteria: 0.666 mm, 0.444 mm and 0.296 mm.Tetrahedral shape cells are considered and no refinement is applied on walls in order to perform the grid convergence analysis with a homogeneous grid length distribution over the domain.

4.2.3.1. GRID REFINEMENT STUDY

As mentioned in the theoretical framework in Chapter 3, a grid study is necessary to assess the accuracy of the numerical solution in CFD calculations with respect to the asymptotic numerical value when the grid spacing h equal to zero. Three numerical calculations are recommended (NASA, 2008) in order to perform the grid study, stating from a coarse mesh and halving the grid spacing in each coordinate using a second order discretization scheme. The error band for a numerical value, for a grid spacing h, is determined by the *grid convergence index*, GCI, that is calculated by the following equation (eq.(268))

$$GCI = \frac{F|e_a^{21}|}{r^p - 1} \tag{268}$$

Where F, e_a^{21}, r and p are a safety factor, the relative error, the grid refinement ratio and the effective order of convergence. The safety factor is 3 when only two grids are used. According with Celik; Ghia and Roache (2008) the safety can be equal to 1.5 if three grids is used. The relative error is a fraction obtained from two solution and given by eq.(269)

$$e_a^{21} = \frac{\hat{f}_2 - \hat{f}_1}{\hat{f}_1} \tag{269}$$

in where $\hat{f}$ is a solution quantity. As mentioned in NASA (2008), normally as a convention, the sub-index 1 is referred to values from finer grid. The grid refinement ratio is calculated with eq.(270).

$$r = \frac{h_2}{h_1} \tag{270}$$

For grids with different cell sizes the grid length can be calculated as described in Celik; Ghia and Roache (2008)

$$h = \left(\frac{1}{N} \sum_{i=1}^{N} \Delta \hat{A}_i \right)^{1/2} \tag{271}$$

In where N and ΔA_i are the total number of cells and the cell area. In axis-symmetric simulations in ANSYS Fluent 19.0 a grid is composed by volumes with different sizes due to the wedge geometry, therefore, the averaged length sizes can be calculated by (CELIK; GHIA; ROACHE, 2008)

$$h = \left(\frac{1}{N} \sum_{i=1}^{N} \Delta \hat{V}_i \right)^{1/3} \tag{272}$$

The effective order of convergence is different than the theoretic order of convergence of the method used and it is related with the global error E by the eq.(273).

$$E = \hat{f}(h) - \hat{f}_{exact} = Ch^p + H.O.T. \tag{273}$$

where $\hat{f}(h)$ is the current numerical solution, $\hat{f}_{exact}$ is the analytical solution, C is a constant independent of h and the last term on the RHS of eq.(273) are the higher order terms. An estimative of the order of convergence can be calculated by eq.(274) knowing three numerical solutions with different values for h

$$p = \frac{ln\left(\frac{\hat{f}_3 - \hat{f}_2}{\hat{f}_2 - \hat{f}_1}\right)}{ln(r)} \tag{274}$$

Equation 274 is for constant grid refinement ratio. Equation 275 provided by Celik; Ghia and Roache (2008) accounts for non-constant values of r.

$$\hat{p} = \frac{ln\left(\frac{\hat{f}_3 - \hat{f}_2}{\hat{f}_2 - \hat{f}_1}\right)}{ln(r_{21})} + ln\left(\frac{r_{21}^{\hat{p}} - s}{r_{32}^{\hat{p}} - s}\right) \tag{275}$$

In where r_{21} and $r_{32}^{\hat{p}}$ are the grid refinement ratio between two consecutive grids. Term s is calculated from the following equation Celik; Ghia and Roache (2008)

$$s = 1 \cdot sgn\left(\frac{\hat{f}_3 - \hat{f}_2}{\hat{f}_2 - \hat{f}_1}\right) \tag{276}$$

In where

$$s = \begin{cases} 1 & if\ \frac{\hat{f}_3 - \hat{f}_2}{\hat{f}_2 - \hat{f}_1} > 0 \\ 0 & if\ \frac{\hat{f}_3 - \hat{f}_2}{\hat{f}_2 - \hat{f}_1} = 0 \\ -1 & if\ \frac{\hat{f}_3 - \hat{f}_2}{\hat{f}_2 - \hat{f}_1} < 0 \end{cases} \tag{277}$$

Equation 275 is an implicit non-linear equation and must be solved numerically in order to determine the order of convergence. A short Matlab code was written in order to calculate the order of convergence $\hat{p}$.

A better solution can be obtained by means of the Richardson extrapolation method. The continuum value Φ_{ext21}, which is the value for the zero grid spacing (NASA, 2008) using the Richardson extrapolation by the following eq.(278)

$$\Phi_{ext21} \cong \hat{f}_2 + \frac{\hat{f}_1 - \hat{f}_2}{r^{\hat{p}} - 1} \tag{278}$$

The uncertainty of Φ_{ext21} is given by the GCI value calculated for the finer grid spacing. Finally, in order to check if all solutions provided for each grid are on the range of convergence, the following equation is used eq.(279)

$$GCI_{2-3} = r^{\hat{p}} GCI_{1-2} \tag{279}$$

In where GCI_{2-3} is the index calculated using the coarser grid 3 and the grid 2 with a half value of h_3, and, GCI_{1-2} is the index calculated using the finer grid 1 with the grid 2. According to Nasa (2008) if the ratio of eq.(280)

$$\frac{GCI_{2-3}}{r^p GCI_{1-2}} = Convergence\ range\ test \tag{280}$$

gives a value near to 1, then all three results are in the range of convergence.

4.2.4. BOUNDARY CONDITIONS

In order to provide closure to the conservation equation, different boundary conditions must be defined depending on whether the domain boundary is considered a wall, a mass inlet/outlet or a velocity inlet/outlet zone.

4.2.4.1. MASS PRESSURE-OUTLET

Outlet boundary condition is defined as using the *pressure outlet boundary condition* provided by ANSYS Fluent 19.0. The exterior pressure must be defined in conjunction with the back-flow values for field variables such as velocity (with direction), temperature, turbulence intensity, turbulent viscosity ratio and granular temperature.

4.2.4.2. MASS INLETS

In ANSYS Fluent 19.0 one of the boundary condition types is the *velocity inlet* in where physical velocity, volume fraction, species mass fraction, temperature, turbulent intensity and viscosity of each phase must be defined. ANSYS Fluent 19.0 offers three modes to define an inlet boundary: normal component with velocity magnitude, component velocities and component directions and velocity magnitude. Other conditions must be provided depending on the models chosen for the simulation. In this work, inlet flow condition is provided in terms of volumetric flow rate for nitrogen, in standard condition. For the case of biomass (*Chlorella Vulgaris* particles) the inlet condition is defined as mass rate. The *mass-flow-inlet boundary condition* in ANSYS Fluent 19.0 is defined. Parameters necessary to set up this boundary conditions are: mass flow rate, and the components on the global coordinate system of reference in order to determine the velocity vectors. Additionally, biomass components i.e. mass fraction of moisture and pseudo-components are defined here.

4.2.4.3. WALL AND SYMMETRY AXIS

Since the type axis-symmetric is used in the current work a symmetry line must be defined as a pseudo-boundary in ANSYS Fluent 19.0. The axial axis of the reactor is defined as the symmetry line. No additional parameters must be defined in ANSYS Fluent 19.0 for this type of boundary. All the parameters for wall boundary condition are specified in Table 29 in section 4.6 including the granular phase parameters.

4.3. SOLVER APPLIED

Since the flow is considered incompressible ANSYS Fluent 19.0 SIMPLE solver is chosen that it was reviewed in Chapter 3.

4.4. COMPONENTS OF CHLORELLA VULGARIS

Analysis of content of carbohydrates, proteins and lipids, expressed as mass fraction, was performed in this research in order to associate the different peaks of mass loss rate that have been calculated from TG analysis. *Chlorella Vulgaris* microalgae from PureBulk Inc. were used and the methodology to determine the amount of each component are described in detail in the paper of Muñoz et al. (2015). Proteins content was obtained suspending the microalgae in distilled water (water/microalgae 16:1).

As explained in Muñoz et al. (2015) mixture ph was adjusted to 11 using NaOH 2M and then protein was extracted under continuous stirring at 150 rpm along 13 minutes at room temperature. On the other hand lipid content was determined chemically by solvent separation using petroleum ether with an additional process to separate the solvent after extraction. Both final remnants of proteins and lipids were measured gravimetrically. Finally carbohydrate content was determined by difference using the following formula.

$$Carbohydrates = 100\% - (moisture + lipid + protein) \quad (281)$$

4.5. SUMMARY OF ASSUMPTIONS APPLIED TO CONSTRUCT THE REACTION MECHANISM

The following assumptions have been applied to construct the reaction mechanism that includes the rate equations the associated reactions.

1) The superimposed principle was applied. This assumption accounts for that each pseudo-component of the Chlorella Vulgaris reacts indecently without cross effects.
2) Each zones detected in the DTG analysis will be treated as a devolatilization reaction of a pseudo-component.

3) Each reaction is described by one rate equation with one set of kinetic parameters i.e. A, E and reaction model.
4) Reactions only produce Char and lumped gases. Condensable and non-condensable gases are not distinguishable.
5) Char is modeled as graphite with properties defined in ANSYS Fluent database.
6) The amount of Char produced by each reaction is proportional to the amount of the gas produced by same reaction.
7) The amount of pseudo-component present in virgin biomass (before the thermal decomposition or in other words the initial composition) is proportional to the amount of gas released, in wet basis, by each pseudo-component considered.
8) The Lagrangian rate equations obtained from the thermal analysis are adapted in a Eulerian form in order to be applied in the *heterogeneous reaction module* in ANSYS Fluent 19.0.
9) Gas phase will be defined considering a characteristic experimental gas phase distribution for Ch*orella Vulgaris* thermal decomposition obtained from the literature.
10) Enthalpy of formation its calculated starting from the heat of reaction for carbohydrates, proteins and lipids obtained from the literature.
11) Specific heat and thermal conductivity for pseudo-components are obtained from the literature. Specific heat is obtained from the work of Maddy (2014). A thermal conductivity of 0.173 W/m/K is obtained from the ANSYS Fluent 19.0 database corresponding to wood material.
12) Devolatilization reaction is only defined on the surface of the solid phase particle by a heterogeneous reaction.
13) Mass transfer at the interface does not depend on the interface concentration gradients of species, depends only on heterogeneous reactions.

4.6. PARAMETERS FOR SIMULATION

The following Table 29 and Table 30 present all the parameters used and defined in simulation of fast pyrolysis of *Chlorella Vulgaris* and a geometry that characterized the main properties of semi-continuous pyrolyzer.

Table 29 - Simulation parameters.

Type of simulation	**Transient multi-phase flow axis-symmetric 2-D**	
Number of phases	**2**	
Regime type	**Incompressible for both phases**	
Height length	900	[mm]
Base length	8	[mm]
Lateral mass Inlet	3	[mm]
Inlet and outlet diameter sizes	8	[mm]
Fluidizer gas	N_2	
Standard gas density	1.14	[kg/m^3]
Standard N_2 gas viscosity	1.79E-05	[kg/m/s]
Particle specific heat	1700	[J/kg/K]
Gas specific heat	Mixture averaged based on ANSYS ANSYS Fluent 19.0 database	
Gas phase	Incompressible gas phase	
Biomass phase	Granular phase (KTGF)	
Particle diameter	Constant 150	[µm]
Particle density	525	[kg/m^3]
Interfacial area	*Symmetric* type (ANSYS Fluent 19.0model)	
Drag model	Morsi-Alexander (ANSYS Fluent 19.0model)	
Granular temperature description	Partial differential transport Eq.	
Particle-particle restitution coefficient e	0.95	
Particle-wall restitution coefficient e_w	0.90	
Granular wall stress model (for e_w)	Johnson and Jackson (ANSYS Fluent 19.0model)	
Granular viscosity model	Symlal-O'Brien (ANSYS Fluent 19.0model)	
Granular bulk viscosity model	Lun et al. (ANSYS Fluent 19.0 model)	
Granular pressure model	Lun et al. (ANSYS Fluent 19.0 model)	
Granular conductivity model	Symlal-O'Brien (ANSYS Fluent 19.0 model)	
Granular radial model	Lun et al.	
Momentum specularity coefficient	0.5	
Particle-Gas heat transfer model	Ranz-Marshall (ANSYS Fluent 19.0 model)	
Solid packing limit	0.62	
Biomass thermal conductivity	0.137	
Discretization schemes		
Momentum	Second order UP-WIND	
Volume fraction	QUICK Scheme	
Granular temperature	Second order UP-WIND	
Energy	Second order UP-WIND	
Gas species conservation equation	Second order UP-WIND	
Solid species conservation equation	Second order UP-WIND	

Table 30 – Boundary and initial conditions.

BOUNDARY CONDITIONS		
Biomass inlet (lateral)	ANSYS Fluent 19.0 *mass-flow-inlet* type	
Temperature	300	[K]
Velocity direction	-*y* direction	
Mass flow	2.5E-5	[kg/s]
N_2 fluidizer inlet (bottom)	ANSYS Fluent 19.0 *velocity-inlet type*	
Temperature	Equal to pyrolysis temperature	
Velocity direction	*x* direction	
Velocity magnitude	0.066	[m/s]
Outlet	ANSYS Fluent 19.0 pressure outlet type	
Pressure	1	[atm]
Back flow conditions		
Solid volume fraction	0	
Gas volume fraction	1	
Gas mass fraction for N_2	1	
Temperature	Constant at pyrolysis temperature	[K]
Walls	ANSYS Fluent 19.0 *wall type*	
Temperature	Constant at pyrolysis temperature	[K]
Solid phase	Specularity and restitution coefficients defined before	
INITIAL CONDITION		
Granular temperature	1e-4	[m^2/s^2]
Pressure	1	[atm]
Temperature	Constant at pyrolysis temperature	[K]
Composition	Only N_2	
Gas and solid Velocities	0	[m/s]

5. RESULTS

Chapter 5 presents and discusses all the results obtained in this work. The discussion is organized in tow main parts. The first part describes the details about analysis of the microalgae components and the construction of the reaction mechanism, while the second part describes the definition of the reaction equations and its application in the reactor environment defined in chapter 4.

5.1. ANALYSIS OF MICROALGAE COMPONENTS

Valuable information is provided by analyzing the composition of the microalgae in order to start the understandings about the devolatilization process, hence, all the authors that have performed thermal analysis also have determined the carbohydrates, lipids and proteins contents. As has been reviewed in Chapter 2, authors Gong et al. (2013), De Filippis et al. (2015), Lopez-Gonzalez et al. (2013) et al. and Agrawal and Chakraborty (2014) have reported the characteristic microalgae contents for *Chlorella Vulgaris*. Figure 73 shows the composition of the microalgae obtained in this work in dry basis while Table 31 presents a comparison between the compositions obtained in this work with the results collected from the mentioned authors.

Figure 73 – Component mass fraction of carbohydrates, lipids and proteins in fry basis determined in this study.

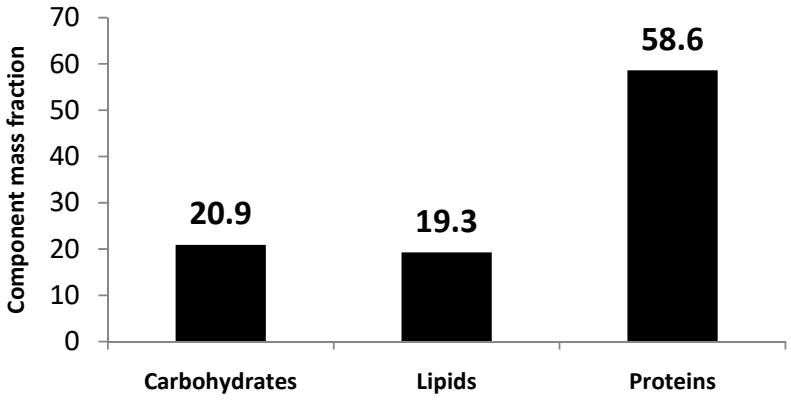

As can be seen in Table 31 values can vary significantly for carbohydrates and lipids from source to source. On the other hand, in the case of protein content, the results obtained here, are in agreement with those from literature, showing in general, that protein content has a lower variation. According to Chisti (2007) the differences in

carbohydrates and lipids content can be attributed to the growing rate of the culture and growing conditions such as level of solar radiation, temperature, nutrients affecting the composition.

Microalgae component distribution is necessary in order to help the identification of the characteristics zones in thermograms. As has been mentioned in the literature review, generally, the peaks and shoulders at lower temperatures are associated to the devolatilization of carbohydrates and proteins and at higher temperatures to lipids. Kebelmann et al. (2013) has shown this characteristic by means of the thermal analysis of extracted components. The results obtained here are, in general, in agreement with the referenced authors, allowing the identification of the zones in the thermal analysis charts that are presented in the next subsection.

Table 31 – Comparison of *Chlorella Vulgaris* components obtained in this study with values obtained from literature.

Author	Carbohydrates	Lipids	Proteins
Gong[a]	34.4	15.6	47.4
De Filippis[b]	38.2	16.2	45.6
Agrawal[c]	12.0	29.0	51.0
Lopez-Gonzalez[d]	12.4	13.5	58.1
Wang[e]	21.0	15.7	41.5
****Belotti**[f]	38.2*	16.2	45.6
This study	20.9	19.3	58.6

*Calculated here, from data of Belotti et al. (2014), by difference between lipids and proteins, in dry basis, with an estimated error of ±2%.
***Data from BG-11 species reported in Belotti et al. (2014).*
[a]Gong (Gong et al., 2013), [b]De Filippis et al. (2015), [c]Agrawal and Chakraborty (2013), [d]Lopez-gonzalez et al. (2014), Wang et al. (2013), [f]Belotti et al. (2014).

5.2. TG AND DTG ANALYSIS AND KINETIC PARAMETERS

Applying the methodology presented in Chapter 4, thermogravimetric experiments have been performed for *Chlorella Vulgaris* microalgae at three different heating rates. Figure 74 and Table 32 show the TG chart, stage and zones distribution with the relevant temperatures obtained directly from the apparatus described in the methodology Chapter.

As can be seen in Figure 74 devolatilization occurs in three stages. At the initial stage, as suggested by Peng et al. (2001) and Gong et al. (2013) near 5% of moisture is lost. A higher slope is observed between 200 and 500°C indicating the main devolatilization

stage. Further mass is lost starting from 500°C as char and carbonaceous residues thermal decomposition according to Wu et al. (2014).

Figure 74 – Experimental mass loss curves for heating rates of 5, 10 and 20 °C/min.

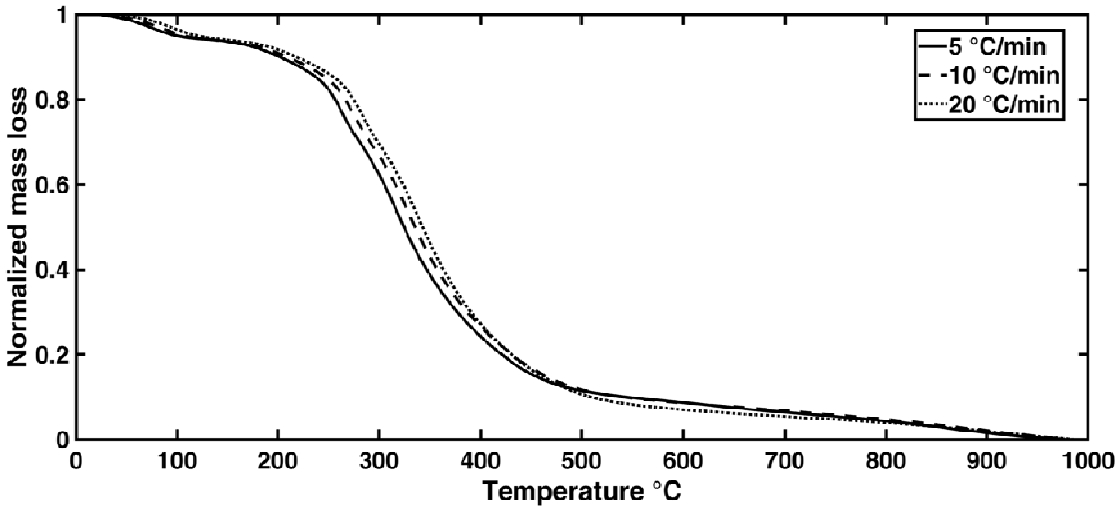

Table 32– Different devolatilization zones observed in TG experiments of *Chlorella Vulgaris*.

	Stage 1		**Stage 2**			**Stage 3**		
	Zone 1	Zone 2	Zone 3	Zone 4	Zone 5	Zone 6	Zone 7	
β **[°C/min]**				**Temperature [°C]**				**Mass**[b] (%)
5	79	193[a]	263	320	418[a]	644[a]	--	91.3
10	89	204[a]	274	331	456[a]	--	--	91.4
20	101	215[a]	285	343	487[a]	--	--	93.0

[a]estimated temperatures at peaks and shoulders, [b]Total mass loss at 100°C.

Figure 75 shows the calculated and filtered DTG chart as normalized mass loss rate and as a function of temperature. In this Figure, the three stages are very clear and there is an agreement with the results obtained by Raheem et al. (2015) for *Chlorella Vulgaris* obtained from the same source with the same heating rates used i.e. 5, 10 and 20 °C/min. Stages and zones depicted in Figure 75 are related to information in Table 32 that shows the temperature at the three observable peaks, the suggested peak (shoulders) of the overlapped zones, and the conversion at 1000°C where almost all the volatiles are released. According to literature (GONG et al., 2013) the shift of peak temperatures for all zones are obtained as expected for pyrolysis process.

The devolatilization starts with the moisture elimination on stage 1, followed by a main devolatilization process in stage 2. In addition of two clear peaks on stage 2, there are two shoulders at the beginning and at the final part of the stage, suggesting the

decomposition of additional two pseudo-components that are overlapped with the first and second peaks. Raheem et al. (2015) also reports two clear peaks at the main stage and also a shoulder aside the first peak. Considering the observable peaks, the unique difference between results obtained here is that in the work of Raheem et al. (2015) the first peak of stage 2 is higher than the second peak. Overlapping in stage 2 reveals a complex material decomposition as expected considering the literature review. This fact suggests the existence of more than one process simultaneously occurring during the thermal degradation and hence the presence of more than one one-step chemical reaction.

Figure 75 – Calculated and filtered mass loss rate curves from the TG analysis (Figure. 74) for heating rates of 5, 10 and 20 °C/min.

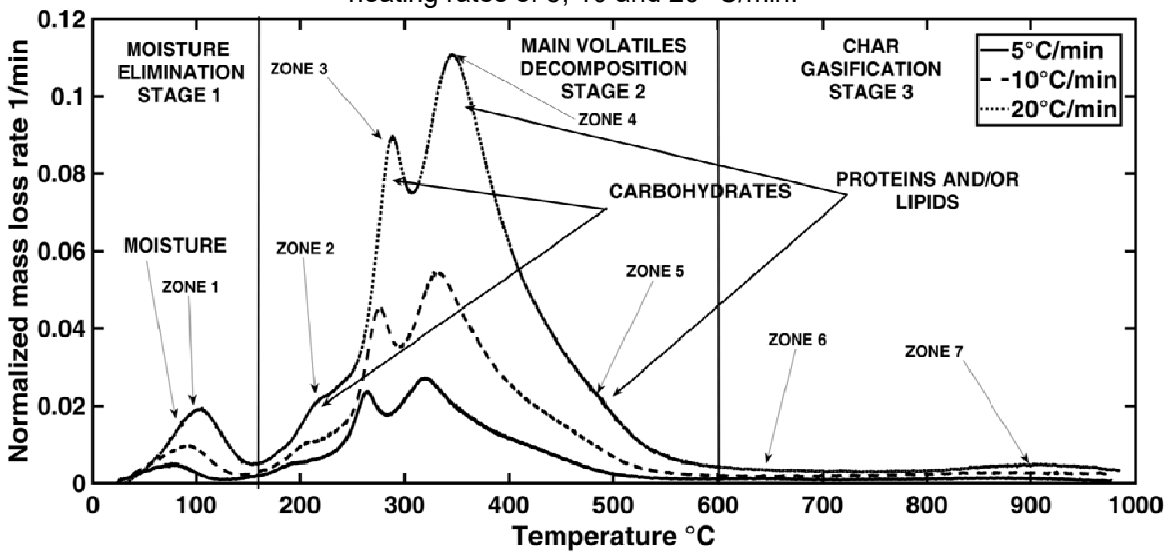

All the zones in Figure 75 can be related to the decomposition and volatile release from carbohydrates, proteins and lipids. Raheem et al. (2015) and Gong et al. (2013) state that the zones correspond, in ascending order by temperature, to the devolatilization of carbohydrates, proteins and lipids, while Agrawal et al. (2013) attribute these zones to the carbohydrates and protein devolatilization in the range of 150 to 350 °C degrees. Other researchers, Ferreira et al. (2015) report protein devolatilization at 300°C and lipids at 370°C. Furthermore, Lopez-Gonzalez et al. (2014) relate the shoulders appearing in thermogram for carbohydrates thermal decomposition. Finally, Kebelmann et al. (2013) has shown that the extracted and separated lipids and proteins of *Chlorella Vulgaris* are thermally decomposed near 400°C and between 350 to 360°C with a shoulder at 490°C respectively.

Considering the results obtained by the mentioned authors and the results presented in Section 5.1, a suggestion here is that the first shoulder (zone 2) and the first peak on stage 2 (zone 3) observed in Figure 75 can be attributed to devolatilization of carbohydrates followed by the thermal decomposition of proteins at the second peak (zone 4) of stage 2. And finally, the weak but significant shoulder on the right hand of stage 2 (zone 5) is attributed to lipid devolatilization. It is worth to note that zones 6 and 7 presented in Table 32 and depicted in Figure 75 may correspond to char residue gasification, process that is beyond the scope of fast pyrolysis, and thus it is not considered in the discussion.

Figure 76 – Iso-conversional method results from Friedman, FWO, KAS and Starink methods.

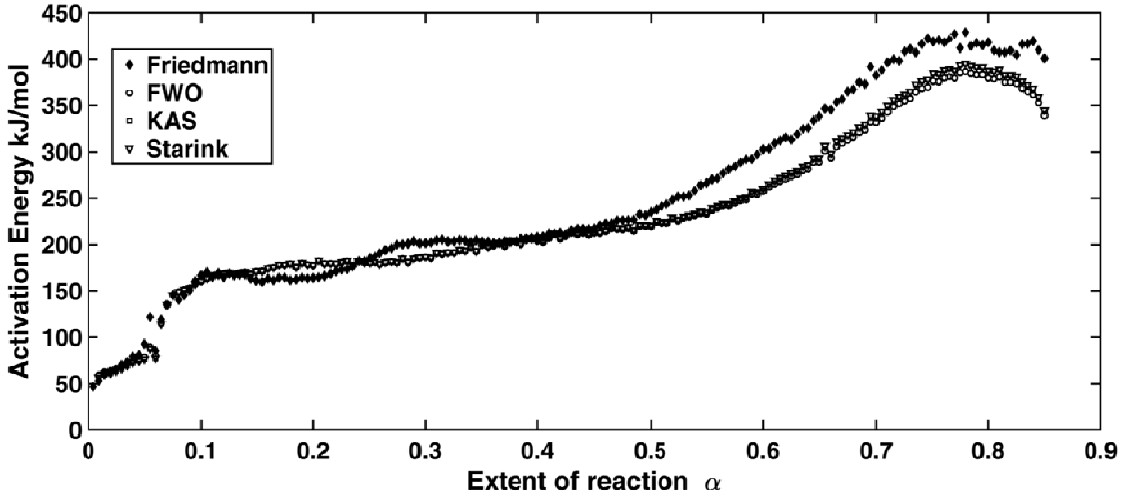

Figure 76 and 77 show the results of iso-conversional method applied resulting in the activation energy distribution and coefficient of determination *R,* respectively. Four estimations were applied, the differential method of Friedman and the integral methods FWO, KAS and Starink. Results from all the procedures reveal the devolatilization of a complex material due to the varying activation energy *E* obtained as a function of the extent of reaction α.The differential method of Friedman gives oscillating values for α from 0.15 to 0.40 and higher values above 0.40 in reference of the integral curves, a feature that is possible to observe according Vyazovkin et al. (1988) when comparing differential and integral methods.

On the other hand, integral method yields practically the same results for all values of α calculated and practically no oscillation. It is worth to note that in this work, the values calculated from the Friedman method for the activation energy distribution have been

obtained from numerical differentiation of the experimental values of mass loss (TG analysis, Figure 74), thus introducing noise, even when a smoothing procedure was applied. However, the integral method uses the values of mass loss directly obtained from the TG analysis, and as can be seen in Figure 74 these values have practically no noise.

Figure 77 – Coefficient of determination of iso-conversional Friedman, FWO, KAS and Starink methods.

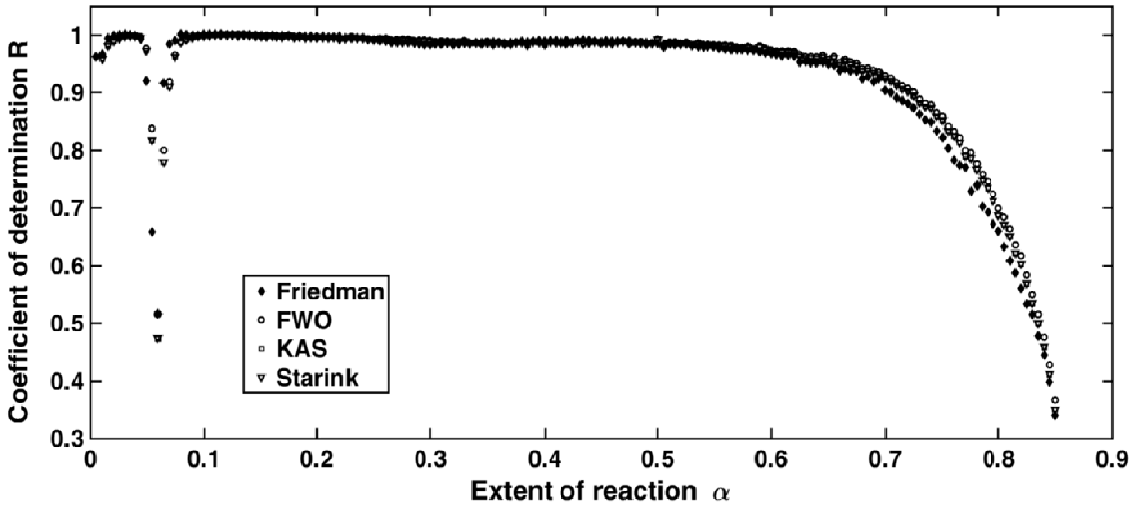

Details about the source data used for the construction of chart on Figure 76 can be seen in Figures 78 to 80 that show selected fitted lines for selected extent of reaction for the Starink, FWO and KAS methods, yielding the values of the slope that correspond to activation energy plotted in Figure 76.

As can be seen in these figures, a good fitting is achieving for α from 0.1 to 0.7 validating the estimation of the effective activation energy procedure. Following with the analysis, Figure 77 shows that the coefficient of determination *R* in the range of α from 0 to 0.7 has a good value close to one, validating the fitting procedure. However, between values of α near 0.05 to 0.1 and above 0.7 a poor coefficient has been obtained yielding uncertainty about the value of the activation energy in those zones.

By analyzing the distribution from Figure 76, a wide range of values for the activation energy have been obtained for α from 0 to 0.8 revealing and remarking again that more than one single thermal decomposition process is present in pyrolysis of *Chlorella Vulgaris.*

Figure 78 – Selected fitted lines of the regression procedure using the Starink method.

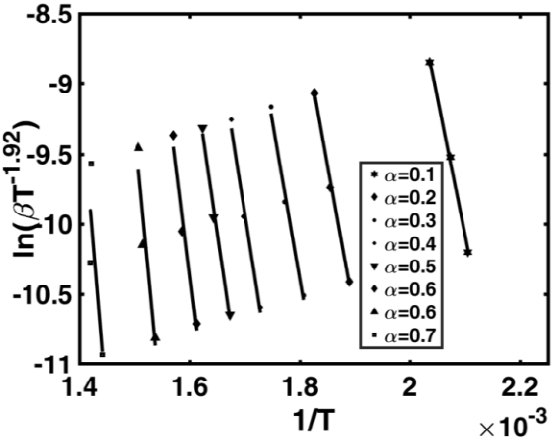

Figure 79 – Selected fitted lines of the regression procedure using the FWO method.

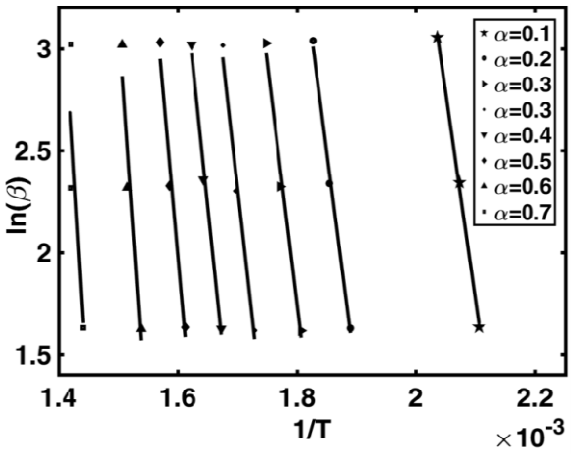

Figure 80 – Selected fitted lines of the regression procedure using the KAS method.

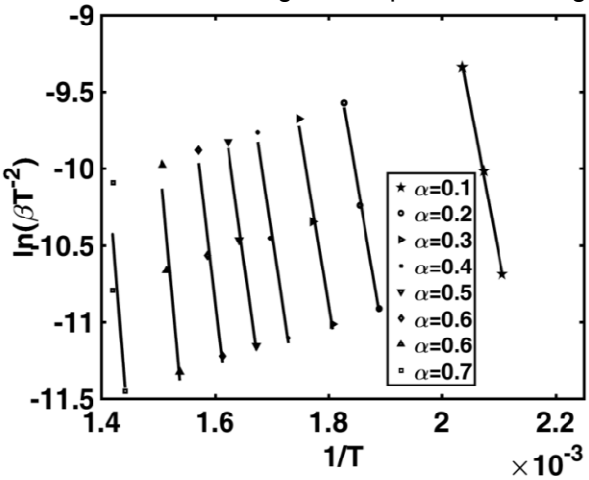

Authors such as Raheem et al. (2015), Gong et al. (2013), Agrawal and Chakraborty. (2013) and Yuan et al. (2015) also have performed iso-conversional and OHR analysis for pyrolysis of *chorella vulgaris,* obtaining in summary the result presented in the next paragraph.

Raheem et al. (2015), found in experiments a moisture elimination zone and a main devolatilization stage with two zones and reporting a unique value for the activation energy for each zone recognized. Values found by the author were 45.38, 61.20 and 97.22 kJ/mol, for moisture elimination and the two main zones, respectively. These results are very far from the values obtained here, considering that the values shown in Figure 76, lay in the range from 50 to above 400 kJ/mol. However, an important detail of the method used by the author, the Freeman-Carrol method, can be outlined. Raheem

et al. (2015) estimates the activation energy evaluating eq.(53), the KAS method at the temperature peaks. Methodologically, as presented in Chapter 3, this does not follow the concept of the iso-conversion analysis because of the value of the extent of reaction α is not necessarily the same at the peaks at different heating rates.

Gong et al. (2013) performed a thermal analysis for *Chlorella Vulgaris* at four heating rates, reporting the following unique activation energies for the overall process: 48.4, 45.2, 43.6 and 42.9 kJ/mol for 5, 10, 20 and 40 °C/min, respectively. Remarking that only one value for each heating rate run has been obtained by Gong et al. (2013) suggesting the use of a non-free model methodology, probably a OHR method, due to the fact that the author has considered an n-order model reaction. Therefore, results are not fully comparable with the results obtained here because of that the kinetic parameters were obtained using an arbitrary reaction model.

Agrawal and Chakraborty (2013) applied the FWO and KAS method to the data obtained at three heating rates and reported results at a selected extent of reaction values. Authors have defined different stages and zones. However, zone 1 of stage 2 is comparable with the results of this work due to the fact that main devolatilization occurs near the same peak temperatures 294, 305 and 318 for 5, 10 and 20 °C/min respectively. Other authors, Yuan; Tahmasebi and Yu (2015) performed a thermal decomposition experiment with the same microalgae at three heating rates 5, 10 and 20 °C/min. The thermogram reported by the author shows only one observable peak at the main devolatilization stage, however, with two shoulders in the DTG chart, at the beginning and at the end of the main stage.

The data reported by Agrawal and Chakraborty (2013), Yuan; Tahmasebi and Yu (2015) and the results obtained in this work are shown in Table 33. As can be seen in this Table, the activation energy obtained here, in general, differs significantly, in comparison with the results obtained by Agrawal et al. (2013) compared at the same extent of conversion value. However, by comparing the results from this work with the data calculated by Yuan; Tahmasebi and Yu (2015), in general, there are more agreements, and specifically, a similar result has been obtained for values of α from 0.4 to 0.5 using the FWO method, yielding activation energies of 204.13 to 219.18 kJ/mol

for this study and 207.04 to 206.73 kJ/mol by Yuan; Tahmasebi and Yu (2015) respectively.

Table 33 – Compared values for the activation energy obtained by Agrawal (Agrawal et al., 2013), Yuan (Yuan et al., 2015) using FWO and KAS methods.

	E from FWO [kJ/mol]			E from KAS [kJ/mol]		
	This study	**Agrawal**	**Yuan**	**This study**	**Agrawal**	**Yuan**
0.20	177.30	43.73	210.14	177.58	41.15	201.21
0.30	186.62	46.61	210.08	186.97	43.97	200.89
0.40	204.13	48.74	207.04	204.98	46.02	198.30
0.50	219.18	51.16	206.73	220.49	48.36	197.08
0.60	257.49	54.94	211.19	260.44	52.09	201.28
0.70	331.86	58.76	235.87	338.21	55.80	225.60
0.75	376.28	--	263.77	384.62	--	253.24
0.80	379.50	61.74	--	387.61	58.60	--

Compared analysis with other authors has shown that results can largely differ depending on the method used; iso-conversional or OHR, and also even when if the methods are the same, such as in the case of the latter analysis. However, similar results have been obtained in this study comparing them with the results reported by Yuan; Tahmasebi and Yu (2015), with the same method, giving consistency to the results of this investigation. The next step in the overall analysis is the definition of the reaction mechanism using the data obtained from the iso-conversional method presented so far.

Figure 81 shows a plot for the distribution of the activation energy obtained using the Starink method in conjunction with mass loss rate in order to relate the different zones, defined in Figure 75. This superposition of charts allow proposition of the set of reactions for the mechanism, considering the intervals between the vertical lines in Figure 81 as the domain for each reaction. A total of six independent reactions are defined in order to fit the experimental data. As can be seen in Figure 81, the proposed reaction R3 is the only one that practically has a constant value of the activation energy along the proposed interval. On the other hand, a wide range of activation energy values are attributed to the rest of the reactions R1, R2, R4, R5 and R6. Table 34 presents the values of the activation energy as a function of the extent of reaction α and the corresponding determination coefficient R^2. By observing the data in this Table it is worth noting that for reaction R6 there is no reliable information for the activation energy due to the lack of accuracy of the coefficient of determination, which is very low as the extent of reaction reaches the value of 1.

Figure 81 – Starink iso-conversional method results plotted in conjunction with the mass loss rate for 5 °C/min.

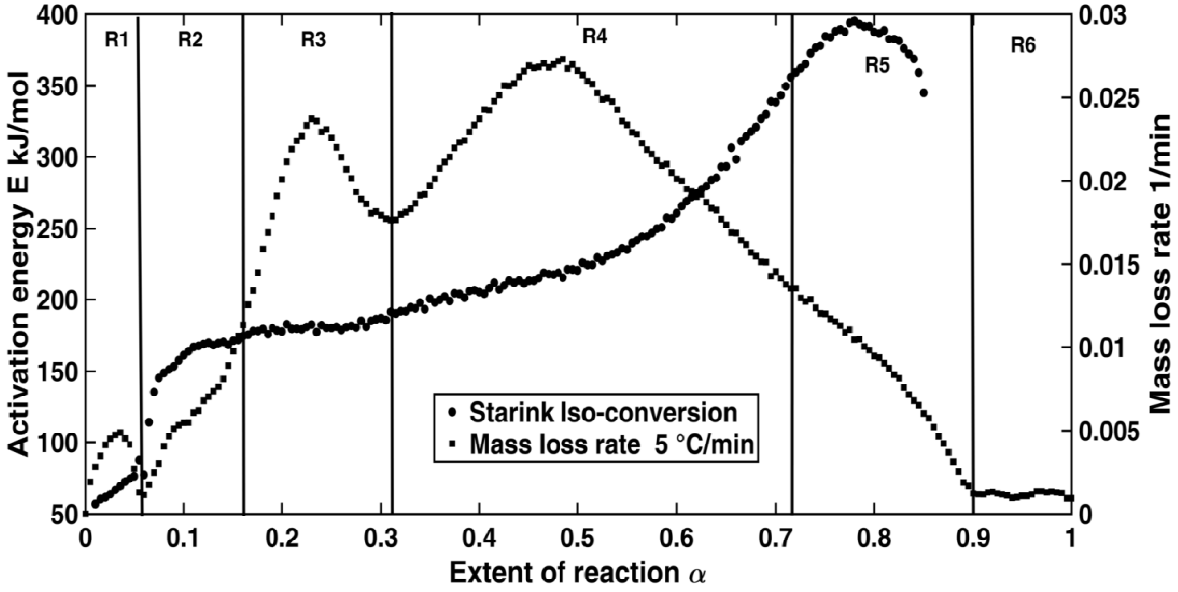

Table 34 – Results for the activation energy distribution obtained by using the Starink method.

α	Starink method	
	E [kJ/mol]	R
0.01	56.75	0.957
0.10	161.07	0.998
0.20	177.79	0.996
0.30	187.19	0.989
0.40	205.21	0.983
0.50	220.72	0.992
0.60	260.64	0.971
0.70	338.37	0.924
0.80	387.76	0.687
0.85	344.92	0.350

As has been defined in Methodology Chapter 4, the determination of the pre-exponential factor *A* is made by the use of the compensation effect. Figure 82 plots the linear regression estimation to determine the factors *a* and *b* for eq.(68) in order to obtain the compensation equation for zone 1 to zone 4 in where reliable data is available. Four reaction models have been evaluated with the OHR method using eq.(34) i.e the Mampel first order, one-dimensional boundary, two-dimensional boundary and second order models (Table 26), for zones 1, 3 and 4. In order to test other reaction models, additionally, power law reaction model for $n = 1/2$ and $n = 1/4$ were evaluated for zone 2.

As can be seen in Figure 82 a good fitting was obtained allowing the determination of the pre-exponential factor *A* as a function of the activation energy *E* and subsequently of the extent of reaction α. Values of factors *a* and *b* are presented for each zone in Table 35. The six devolatilization zones identified in Figure 75 are defined as a reaction from R1 to R6. Same compensation parameters are applied for reactions 4, 5 and 6 due to the lack of reliable data; however, the activation energy interval is different.

In table 35, in where every zone represents a reaction for the reaction mechanism, the range of activation energy E_i-E_f and neperian logarithm of the pre-exponential factor *A*, $LN(A)_i$-$LN(A)_f$, are presented as a function of extent of reaction α, and based on Figure 81. This is consistent with the methodology proposed in this study that includes as an optimization variable the activation energy *E* and the pre-exponential factor A in order to give more degrees of freedom and to improve the fitting procedure. An average value of the activation energy *E* for each zone is presented with the corresponding calculated average value for *ln(A)* obtained from the compensation parameters. Also, the coefficient of determination *R* for each interval is provided as an average for the compensation parameters.

Figure 82 – Compensation effect regression procedure results.

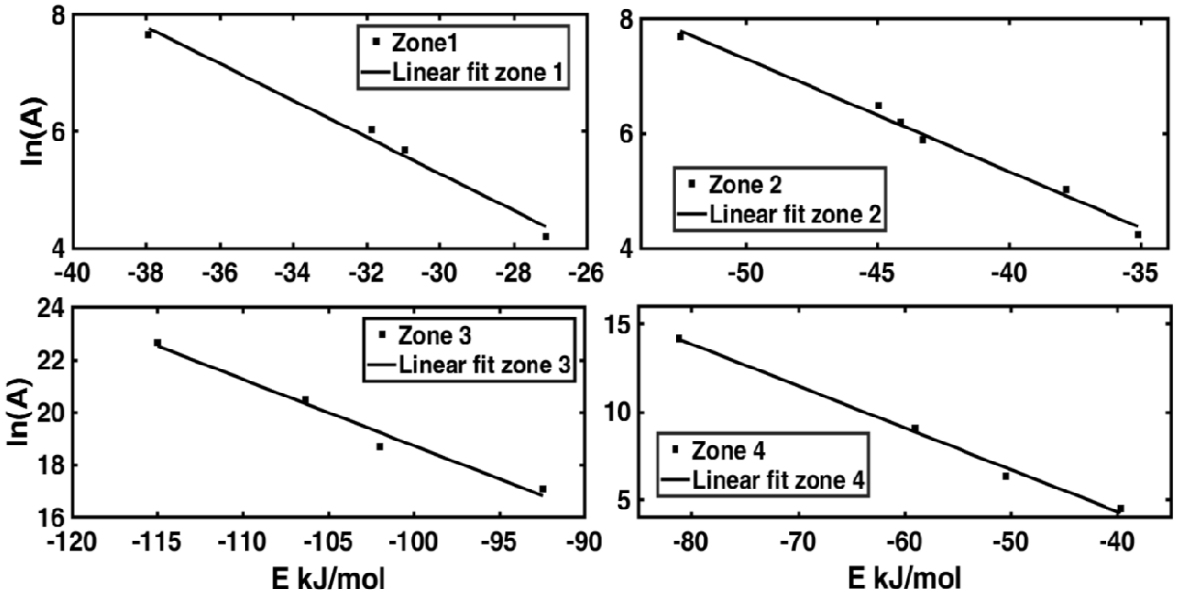

The range of the extent of reaction α_i - α_f provides an interval with a minimum and a maximum value for the activation energy and also an interval for the ln(A) value in where the optimized value will be searched.

Table 35 – Average kinetic parameters A and E and its search intervals to apply the simultaneous multi-stage fitting procedure.

	ISOCONVERSIONAL PARAMETERS			COMPENSATION PARAMETERS			
	α_i - α_f[a]	E_{avg} [kJ/mol]	E_i-E_f[b] [kJ/mol]	a-b[c]	R	LN(A)	$LN(A)_i$-$LN(A)_f$[d]
Zone 1 R1	0.001-0.06	71	56-87	0.314-4.150	0.987	14.8	13.6-23.4
Zone 2 R2	0.06-0.15	144	114-174	0.196-2.528	0.988	23.4	26.7-30.5
Zone 3 R3	0.15-0.31	182	174-191	0.250-6.566	0.976	38.3	36.7-40.8
Zone 4 R4	0.31-0.70	273	191-356	0.238-5.217	0.993	43.6	39.1-56.9
Zone 5 R5	0.70-0.90	370	344-395	0.238-5.217	0.993	77.2	58.1-89.0
Zone 6 R6	0.90-1.00	370	344-395	0.238-5.217	0.993	77.2	58.1-89.0

[a]Extent of reaction interval, [b]Activation energy E interval, [c]Compensation parameters Range, [d]Pre-exponential factor LN(A) range.

The parameters in Table 35*, E average*, E_i-E_f, *calculated Ln(A)* and $LN(A)_i$-$LN(A)_f$ are used to perform the simultaneous multi-stage optimization process in order to provide the parameters that fit the experimental data using as base the structure the n-order reaction model of eq.(191) and restriction of eq.(193). Parameters obtained from the optimization process have been used to numerically solve the non-linear equation system based on eq.(192) with a code written in MatLab, applying the experimental heating rates 5, 10 and 20 °C/min values, in order to verify the model predictions. The results of the optimization process against the experimental data are plotted together in Figures 83 and 84 for the mass loss and mass loss rate curves as a function of time and the values of the optimized parameters are presented in Table 36. The four parameters in the template eq.(192) are presented i.e. c_m, *E, A* and *n,* and also the calculated heat for reaction adapted from the literature and explained in the methodology Chapter 4. Further analysis about the information presented in Table 36 is presented in the next paragraphs.

Table 36 – Summary of the kinetic parameters obtained in this work by using the multi-stage simultaneously fitting process.

	c_m	E [kJ/mol]	A [1/s]	n
R1	0.050	64.9	2.42E7	2.00
R2	0.077	165.4	3.19E16	7.75
R3	0.193	195.3	6.60E16	3.55
R4	0.381	261.1	4.39E20	6.90
R5	0.042	300.0	2.58E21	5.00
R6	0.020	400.0	2.58E21	7.00
Total devolatilized mass	0.763			

Figure 83 – Rate of reaction of *Chlorella Vulgaris* at 5, 10 and 20 °C/min. Comparison of mass loss between simulated results and experimental data.

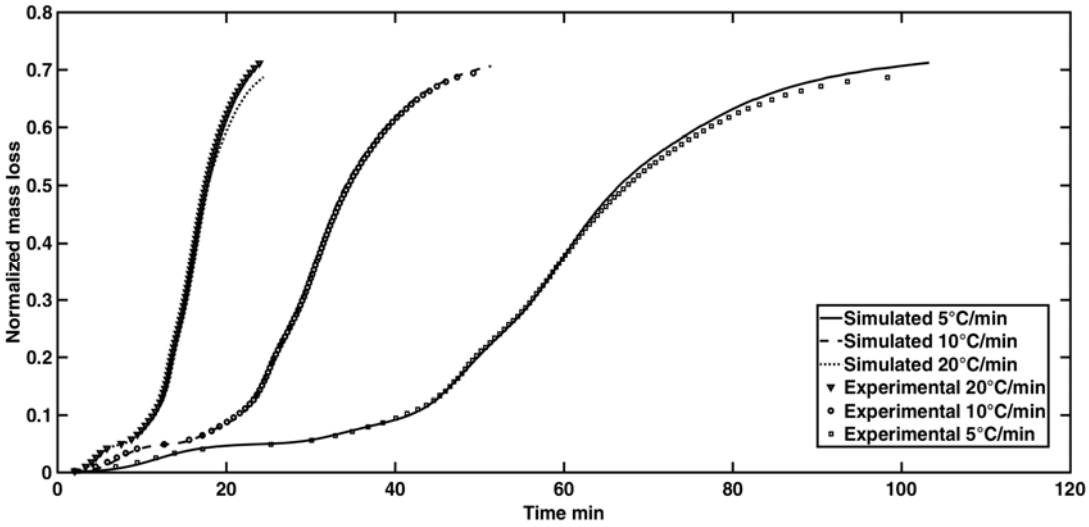

Figure 84 – Rate of reaction of *Chlorella Vulgaris* at 5, 10 and 20 °C/min. Comparison of mass loss rate between simulated results and experimental data.

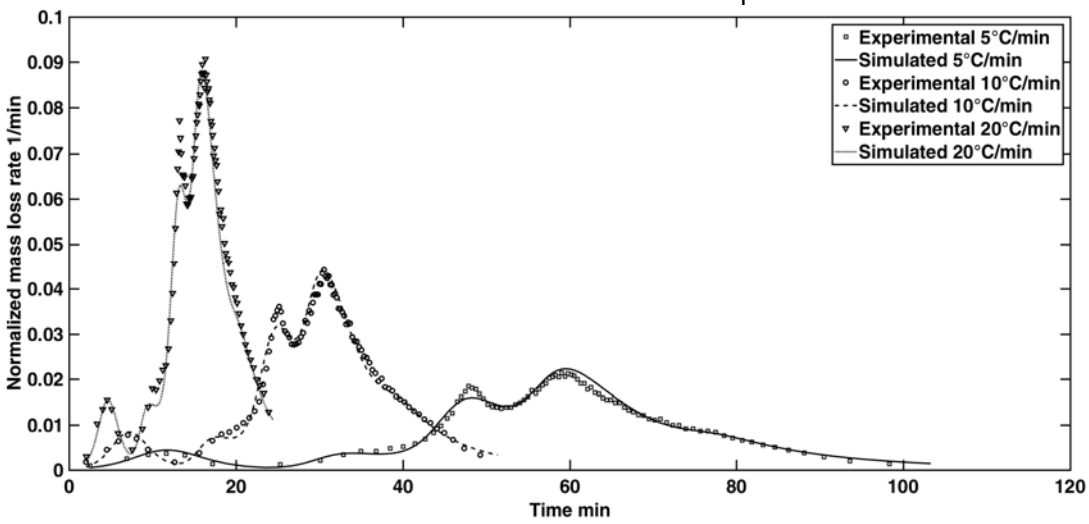

Figures 83 and 84 show a good agreement between the predicted values obtained from the reaction mechanism model compared with experimental TG and calculated DTG data. The prediction for heating rate of 5°C/min is slightly overestimated beyond 70 minutes. For 10 °C/min, the prediction is better and the model data fits the experimental data very well. In the case of the heating rate of 20 °C/min, the reaction mechanism sub-estimates the experimental data toward the end of the whole reaction. The over and sub-estimation predicted by the reaction mechanism differs more significantly from experimental data in a region beyond the zone 5 in where the solid char residuals start to be decompose. As a consequence, the reaction mechanism well predicts the main

devolatilization process of the volatile pseudo-components of the microalgae i.e. carbohydrates, protein and lipids, including the moisture.

The mass loss rate chart shows a good agreement for zones 1, 4 and 5 and an overestimation in zones 2 and 3 revealing a complex thermal decomposition, especially in the latter zones. The addition of reaction 5 and 6 is clearly necessary in order to extent the mass loss rate beyond the fourth reaction.

In order to relate the different zones defined in Figure 75 and reactions defined in Figure 81 and in Table 35, with *Chlorella Vulgaris* components analyzed in section 5.1, the results obtained here suggest the following: reaction R1 is for moisture elimination and reactions R2 and R3 can be attributed for carbohydrates pseudo-components. In the case of reactions R4, R5 and R6 and due to overlapping, a reasonable conclusion to whether can be associated with proteins or lipids is not possible in light of the evidence shown from the results. However, as a proposition suggested here and accounting for the analysis made by Kebelmann et al. (2013), reaction R4 can be attributed to proteins and reaction R5 to lipids leaving the reaction R6 only for char gasification.

Overall mass loss and mass loss rate predictions are presented in the first part of this section and the conclusion is that a good agreement is achieved; however, a detailed analysis about each reaction can be made in order to elucidate how the shape of each of each reaction contributes to the whole process.

Figure 85 shows the mass loss rate as a function of temperature detailing the contribution of each reaction compared with the whole experimental results for heating rate of 5 °C/min. As can be observed in this chart the first shoulder of the experimental data, near 220 °C, is not well covered by the simulated data because of the reaction R2 has a significantly asymmetry in order to try to replicate the results. Also the asymmetry of reaction R2 affect the predictions of reaction R3 that has a sharp shape as experimental result; however, the contribution of R2 results in an overall lesser sharp result.

Nonetheless, it is highlighted that the shoulder in the right hand side near 420 °C, which is predicted by reaction R5, is very well fitted by the model due to the asymmetry of R4. It is worth to note that in the range of temperature plotted in Figure 85, contribution of reaction R6 in negligible.

Figure 85 – Detailed rate of reaction of *Chlorella Vulgaris* at 5 °C/min.

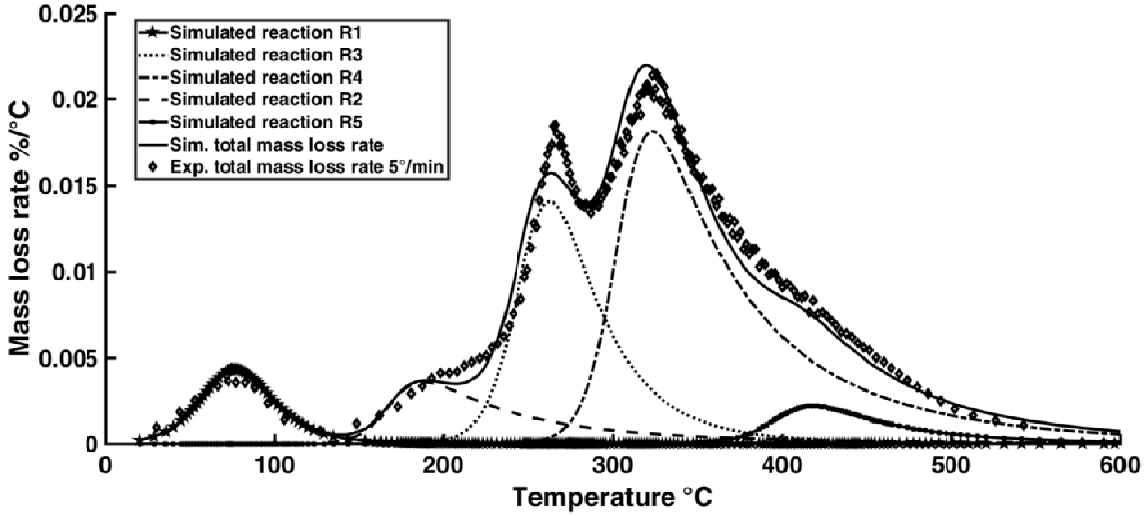

Figures 86 and 87 show in detail how the reactions determined in this work can predict the whole devolatilization process for heating rates of 10 and 20 °C/min. As can be seen, the accuracy obtained is also maintained for both heating rates. The prediction of the drying process by means of reaction R1 and the very good prediction of reaction R4 for proteins and the right shoulder of reaction R5 can be observed.

Figure 86 – Detailed rate of reaction of *Chlorella Vulgaris* at 10 °C/min.

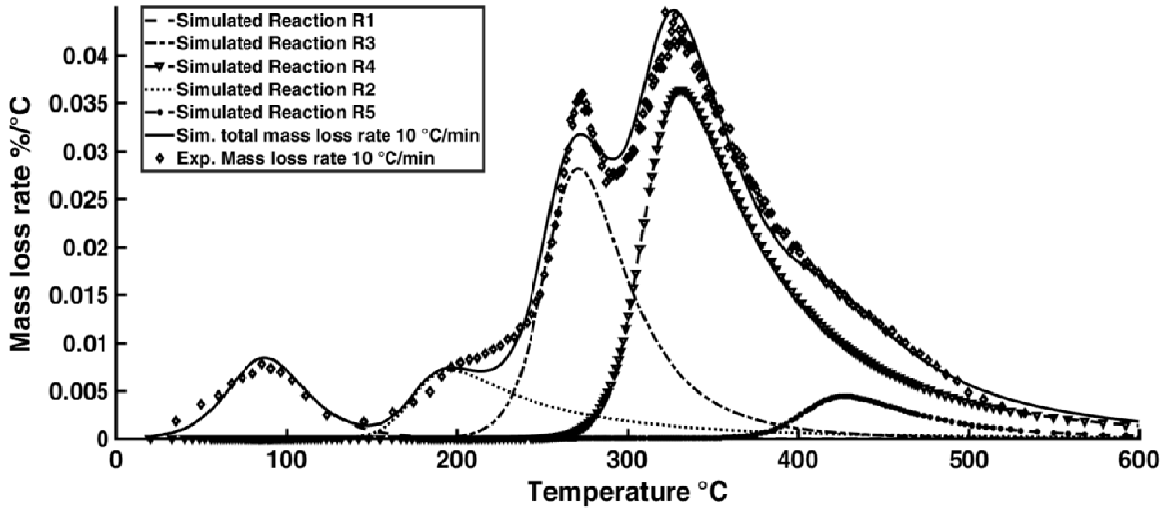

The deviations from the experimental data are present between reactions R2 and R3, and the peak over reaction R3 is still present. It is worth to note that these deviations can be covered with the addition of new reactions or by a post-optimization modification of the kinetic parameters of reaction R2. Nonetheless, the reaction mechanism

developed here has the objective of being used in CFD simulations, and, under this feature, it is important to take into account that further development of the reaction mechanism may integrate additional reactions, for cracking or gaseous phase recombination. Therefore, the less the reaction numbers for the devolatilization, the better the simulation detail, because computational resources can be released and used to analyze other processes such as hydrodynamics and gas phase kinetics. So, a fine balance between accuracy and feasibility may be considered in order to describe the devolatilization accurately, with minimum reactions as possible.

By observing each curve from Figures 85 to 87, the critical detail of the shift of temperature peaks is highlighted here. As can be observed by analyzing the results of the three heating rates, the shift of the devolatilization curves respect to the temperature, which is a common characteristic of the thermal decomposition (very clear in Figure 75), it is desirable and achieved by the reaction mechanism, even though it correspond of a thermal lag owing the heating rate or correspond of an inherent inertial process naturally presented in the thermal decomposition of *Chlorella Vulgaris*. The latter is discussible because of the shift can be explained by a thermal inertia effect caused by the heating rate, however, the reaction mechanism for cellulose developed by Bradbury; Sakai and Shafizadeh (1979) introduces a inertia effect by means the *activated cellulose* reaction explaining an observable delay in the devolatilization reaction not caused by the heating rate effect. Observing the reaction R1 for example, through the different heating rate processes, it is clear that the scheme in fact accounts for the shift characteristics. This desirable characteristic can be attributed to the iso-conversional method because of kinetic parameters, which control the shift, are obtained by covering the information through different heating rates providing a global sense, instead of the OHR method, that is straightforward, but with a local sense.

The analysis and discussion can be extended considering the scope of the reaction mechanism developed in this research. Figures 85 to 87 are truncated at 600°C, and as can be seen in figure 75, devolatilization is still present near 900°C. The process associated at this temperature is the reaction for zone 7 related to the char gasification. However this process is out of the scope of the fast pyrolysis mainly due to the following reason: long residence time is necessary to achieve gasification conditions, and longer residence times open the possibility of secondary cracking of large condensable organic

molecules. The latter is related with the specific objective of the fast pyrolysis, maximizing the condensable; therefore, a process or device designed for such a task may imperatively avoid high temperatures, specifically in this case, avoid hot spot above 600°C. As a consequence, the fast pyrolysis process may be finished at near 600°C and, as can be seen in the experimental results, only a little amount of char residue can be gasified if the temperature is not increased. The scope of the reaction mechanism is a clear prediction of moisture elimination and devolatilization of carbohydrates, proteins and lipids, therefore covering the predictions beyond 600°C is not necessary at this time.

Figure 87 – Detailed rate of reaction of *Chlorella Vulgaris* at 20 °C/min.

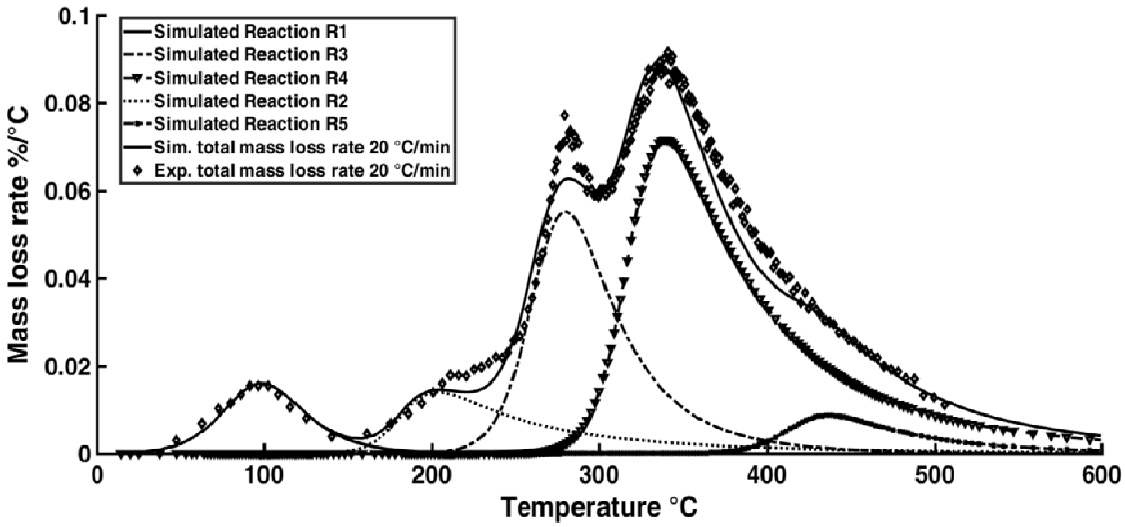

In closing this part of the analysis, it is important to mention an advantage when using a multi stage reaction mechanism. Specifically, detailed analysis can be made by means of a reactor CFD simulation in order to distinguish where and when moisture and the different components of the microalgae are thermally decomposed. The access to this information provides general lines in order to design a customized pyrolyzer with special features to improve specific requirements. Furthermore, the latter is one of the reasons why it is desirable to obtain the characteristic component distribution of the microalgae, task that was carried out by the current research.

Table 36 summarizes the final parameters for the global multi-stage reaction mechanism for pyrolysis of *Chlorella Vulgaris* which predict the experimental data shown in Figures 74 and 75 and in Figures 85 to 87. Model parameters include: the parameter c_m of eq.(192) of all pseudo-components, the activation energy *E*, the pre-

exponential factor *A* and the heat of reaction H_R. It is worth to note that the values for optimized activation energy fall inside regions or very close to the effective activation energy *E* interval obtained from the values calculated with the iso-conversional Starink method revealing an agreement with the inherent physics. Furthermore, it is outlined that larger deviation is for reactions R5 and R6 in where the reliability of data is not suitable (see Figures 76 and 77). However, it is also worth noting that the values of the optimized pre-exponential factor *A* do not fall in the compensation equation lines (eq.(68)), suggesting that the devolatilization process of *Chlorella Vulgaris* is very complex and needs further research.

Another fact is that the *n* order of reactions R2, R3, R4, R5 and R6 does not match the order of any reaction models with physical meaning presented in Table 26, thus reaffirming, again, that there is a complex process composed of more than one competitive or parallel reactions. However, reaction R1 for moisture elimination can very well predict the experimental data, as can be seen in Figures 85 to 87, with an order of reaction $n = 2$, suggesting a process of second order according to Table 26. Other approaches can be used in order to address the physical meaning of the reactions, such as the application of a distributed activation energy methodology (DE FILIPPIS et al., 2015) or estimating the kinetic parameters with a deconvolution technique (PEREJÓN et al., 2011).

In order to use the reaction mechanism parameters given in Table 36, in addition to the heat of reaction, specific heat and density collected and calculated in section 5.3.1 in a CFD application such as ANSYS Fluent 19.0 or OpenFoam, gas phase products must be determined. A gas phase can be defined starting from the data reported by Raheem et al. (2015) and by Raheem et al. (2017) who assume a total cracking of devolatilized products yielding a mixture of H_2O, CO, CO_2 and CH_4 gases for air-gasification of *Chlorella Vulgaris*. Then, applying the latter information and using the eq.(217) to eq.(224) from the Chapter 4, the reaction mechanism can be closed by incorporating the stoichiometric coefficients of the devolatilization reactions in addition to the kinetic parameters. However, for a more detailed scheme, considering macro-molecules release direct from the solid phase and cracked in a second stage, the addition of a mixture of chemical species reported in the literature such as those presented by

Kebelmann et al. (2013), Gong et al. (2013), Yuan; Tahmasebi and Yu (2015), Grierson et al. (2013), Wang et al. (2013) for *Chlorella Vulgaris* pyrolysis can be adapted.

5.3. APPLICATION OF THE REACTION MECHANISM IN THE DROP REACTOR SIMULATION

The following section shows the applicability of the reaction mechanism in a complex CFD simulation accounting for a gas phase and a dispersed solid phase composed by the *Chlorella Vulgaris* powder including: mass and heat transfer, heterogeneous chemical reactions and granular motions for the dispersed phase. The objective is not to study in detail the hydrodynamics inside the pyrolyzer reactor even when its geometry and main characteristics have been reproduced. Instead, the objective is to present the applicability of the reaction mechanism developed here allowing the analysis of the evolution of the moisture and pseudo-components i.e the biomass conversion, and its interactions with the physical processes considered.

Before starting the analysis the maximum Reynolds number has been calculated with respect to the reactor and particle diameters considering the maximum absolute and relative velocities. Maximum velocity for the gas phase at simulation time t = 2.36 seconds was 0.9596 m/s and the maximum relative velocity between the gas and particles was 1.0754 m/s. Local density and viscosity was calculated for the gas giving: ρ = 1.137 kg/m^3 and μ =1.72E-5 kg/m/s. The respective Reynolds number values were: Re_{abs} = 488 and Re_{rel} = 10.02 for the gas respect to the reactor diameter and respect to the particle diameter respectively. Both values allow the calculation assuming a laminar flow.

The reactor has been modeled in two dimensions as an axis-symmetric type as described in the methodology Chapter 4. A total of 4 simulations were performed for the GCI calculation considering a reactor temperature of 673 K. Kinetic parameters for the reaction mechanism were presented in the last Section 5.2 of this Chapter, however, gaseous solid phase and its stoichiometric coefficients are presented in this section and calculated following the methodology. Parameters and sub-models for the granular theory are specified in section 4.6 being the particle-particle restitution coefficient obtained from the work of Benyahia et al. (2000) who have performed a cold flow riser

reactor simulation in where no packed bed inside the reaction zone was considered. Two additional simulations were performed changing specific granular parameters and the reactor wall temperature in order to verify its influence on the biomass overall conversion.

5.3.1. BIOMASS SOLID PHASE COMPOSITION AND REACTION EQUATION

Reaction equation may be defined as the gas phase is defined. In this study a non-condensable gaseous phase distribution is chosen in order to represent the volatiles. Pyrolytic gas distribution was taken from the work of Raheem et al. (2017) who performed air-gasification experiments using *Chlorella Vulgaris* microalgae and using a continuous reactor. Although, there are other substance distributions reported in literature for fast pyrolysis of *Chlorella Vulgaris* microalgae, such as in the work of Kebelmann et al. (2013), the specific substances and/or its quantity were not determined, being difficult to use as a base gas distribution. In the case of gasification the main pyrolytic gases correspond to the non-condensable fraction due to the fact that gas generation is the objective of this type of process. In the case of the work of Raheem et al. (2017) the amount of the non-condensable fraction was higher than 80% providing a preliminary representative data about the gas phase. Also, the distribution of gases was presented as a function of temperature for 700, 750, 800, 850 and 900°C being the distribution for 750°C is chosen here.

It is worth to note that for gasification reactions more energy is necessary compared to fast pyrolysis in order to break the bonds of heavier macromolecules. As were presented in the methodology Chapter 4, the enthalpy of formation calculated using eq.(184) is based on the literature values reported for fast pyrolysis of lipids, carbohydrates and specific proteins. The implicit assumption here is that the heat of reaction to decompose the microalgae in fast pyrolysis conditions, in where a significant amount of condensable is present in the gaseous phase, it is energetically related to a gaseous phase with a predominant presence of non-condensable gases.

From the point of view of energy, this fact may not be relevant due to the fact that the heat of reaction is consistent and according to experimental observations made by the authors that report the respective data. However, from the point view of the sequence of

the pyrolytic reactions there is a difference. The current reaction mechanism is of the global type; therefore, the whole devolatilization process occurs in one whole step accounting for the heat of reaction assumed here. However, the type of reaction to produce primary condensable gases is a heterogeneous reaction, ideally over the particle surface, and part of the subsequent cracking to produce non-condensable gases corresponds to volumetric reactions and may takes place in the gaseous phase. Therefore, the total energy for pyrolysis may be provided in different steps and in different regions and conditions i.e. inside the particle, in the particle surface or completely in the gaseous phase.

In this study, the gaseous phase is passive from the point of view of chemical reactions and all the energy necessary to produce pyrolytic gases are consumed in regions in where the solid phase is present. If the pyrolysis reactions are described in one whole step the energy consumed by devolatilization may produce an over-estimated sink of heat affecting the local temperature, a fact that must be considered in the discussions.

The gas distribution, in volumetric basis, reported in the work of Raheem et al. (2017) for non-condensable gases, obtained from air-gasification of *Chlorella Vulgaris* and performed at 750°C are presented in Table 37. It is worth to note that the sum of the volume fractions in Table 37 is not equal to 1, therefore the difference is arbitrarily added to the hydrogen volume fraction.

Table 37 – Gaseous species distribution obtained from Raheem et al. (2017) used as gas phase in simulation.

Gaseous species	Volumetric concentration*	Molar Mass [kg/kmol]	$\overline{\Delta h_f}^{\circ}$ [J/kmol]
H_2	25.7 (26.8)**	2.01	0
CO_2	29.6	40.01	-3.935E8
CH_4	20.2	16.04	-7.490E7
CO	23.4	28.01	-1.105E8
Total	98.9 (100)		

* From Raheem et al. (2017)
**Volumetric total is not equal to 1, then the difference are added to hydrogen.

Since the assumption made in section 4.2.2.2 about the relation between the amount of gas produced by each microalgae pseudo-component, the factors g and c of eq.(217) can be determined independently from the pseudo-component distribution but dependent from the total gas released (in wet basis) during pyrolysis. From Table 36 the

total gas released in wet basis was $Y_{GAS} = 0.763$ and the moisture content was $Moisture = 0.05$, then using eq.(221) the factor c can be calculated. Then, using eq.(222) to eq.(224) the $\bar{g}_i$ and $\bar{c}$ were calculated, based on volumetric distribution presented in Table 37, giving the following reaction equation, considering a molar mass for char of 12.01 kg/kmol.

$$COMP \overset{k}{\Rightarrow} 1.02\ CO_2 + 0.80\ CO + 0.69\ CH_4 + 0.88\ H_2 + 2.08\ CHAR \tag{282}$$

Using eq.(184), the heat of reaction presented in section 3.7 and the enthalpy of formation of gases in Table 37 yield the apparent heat of formation of each pseudo-component necessary for calculations in ANSYS Fluent 19.0. Values of enthalpy of formation of gases were obtained from the NIST website (https://webbook.nist.gov). Table 38 shows the enthalpy of formation calculated from the data collected and with reaction equation of eq.(282).

Table 38 – Enthalpy of formation for each pseudo-component of the reaction mechanism for *Chlorella Vulgaris*.

	H_R [kJ/kg]	M* [kg/kmol]	$\overline{\Delta h_f^\circ}$ [kj/mol]
Comp 2	951	100	8.534E8
Comp 3	951	100	8.534E8
Comp 4	822	100	8.663E8
Comp 5	822	100	8.663E8
Comp 6	660	100	8.825E8

*Molar mass is defined arbitrarily in order to be consistent with the devolatilization reaction eq.(282) that was defined for 100 kg of biomass.

In Table 38 index of component start from 2 in order to be consistent with reactions numbers on Table 36. Each component has the corresponding Arrhenius kinetic parameters *A* and *E* in Table 36 and the kinetics parameters for reaction R1 correspond to moisture elimination. For moisture elimination the following reaction is defined from eq.(216)

$$Moisture \overset{k}{\Rightarrow} H_2O\ (gas) \tag{283}$$

Finally, using the coeffiecient C_m of Table 36 and eq.(213) the mass fraction of pseudo-components in biomass calculated and presented in Table 39, being a necessary data to define the biomass at inlet of the reactor. Reaction eq.(282) and eq.(283) in conjunction with the enthalpy of formation presented in Table 39 and additional properties presented in the methodology Chapter 4 closes the reaction mechanism and it is completed in order to be applied in a CFD simulation.

Table 39 – Pseudo-component mass fraction of *Chlorella Vulgaris* microalgae obtained from the thermal analysis.

Biomass pseudo-component	Mass Fraction
Moisture	0.050
Comp2	0.103
Comp3	0.257
Comp4	0.508
Comp5	0.056
Comp6	0.027
Total	1.000

Table 40 present a summary of all parameters and properties necessary to perform the CFD simulation, for the solid and gaseous phases.

Table 40 – Summary of physical, chemical kinetics properties and parameters of *Chlorella Vulgaris* microalgae, pseudo-components and gaseous species used in simulation.

BIOMASS PSEUDO-COMPS.	Y	ρ [kg m^{-3}]	k [W m^{-1}K^{-1}]	c_p [J kg^{-1} K^{-1}]	μ 1E-5 [kg m^{-1}s^{-1}]	M [kg kmol^{-1}]	$\overline{\Delta h}_f^{\circ}$ [J kmol^{-1}]	Arrhenius kinetic parameters		
								E [kJmol^{-1}K^{-1}]	A [s^{-1}]	n
Moisture	0.050	998.2[a]	0.6[a]	4182[a]		18.02[a]	-2.86E8[a]	64.9	2.42E7	
Comp 2	0.103						8.53E8	165.4	3.19E16	
Comp 3	0.257						8.53E8	195.3	6.60E16	
Comp 4	0.508	525[b]	0.173[c]	1700[d]		100[e]	8.66E8	254.0*	1.0E20*	1
Comp 5	0.056						8.66E8	300.0	1.70E21	
Comp 6	0.027						8.83E8	400.0	1.70E21	
PRODUCTS										
Gas phase										
H_2		0.0819[a]	0.1672[a]	model[f]	84.1[a]	2.01[a]	0[a]			
CO_2		1.7878[a]	0.0145[a]	model[f]	1.37[a]	40.01[a]	-3.94E8[a]			
CH_4		0.6679[a]	0.0332[a]	model[f]	1.09[a]	16.04[a]	-7.49E7[a]			
CO		1.1233[a]	0.0250[a]	model[f]	1.75[a]	28.01[a]	-1.11E8[a]			
H_2O (vapor)		0.0261[a]	0.0261[a]	model[f]	1.34[a]	18.02[a]	-2.42E8[a]			
Solid phase Char (Graphite)		2000[a]	0.33[a]	model[f]		12.01[a]	7.17E8[a]			
INERT										
N_2		1.138[a]	0.0242[a]	model[f]	1.66[a]	28.01[a]	0[a]			

[a]ANSYS Fluent 19.0 data base, [b]from Almeida et al. (2017), [c]conductivity of wood from ANSYS Fluent 19.0 data base, [d]from Madi (2014), [e]arbitrarily chosen to be consistent to with rate of reaction equation, [f]Polynomial ANSYS Fluent 19.0 model.

*Pre-exponential factor A is modified for reaction R4 (compensated) due ANSYS Fluent 19.0 does not accept values higher than 1E20 for A, then a calculation was performed compensating the values of the activation energy in order to obtain the same activation of reaction R4 in the temperature interval of experiments.

It is worth to nota that in Table 40 the Arrhenius kinetic parameters for reaction R4 are different from those shown in Table 36. This modification is made because ANSYS Fluent 19.0 does not accept values greater than 1E20 for the pre-exponential factor *A*.

Using this maximum value of 1E20, the value of activation energy *E* has been compensated to obtain the same response giving a value of 254 kJ/mol/K.

5.3.2. GRID CONVERGENCE STUDY

In order to analyze the results of numerical calculations as the grid element size is reduced, the GCI methodology is applied to 4 grids. These grids are constructed in the *Meshing Tool module of ANSYS Fluent 19.0* based on the reactor model domain that was discretized as a wedge under the axis-symmetric assumption by a set of tetrahedral volumes. Four length sizes $\bar{h}$ for cell edges are defined starting from 1 mm. The line over $\bar{h}$ is defined here as a *criteria size* since it is the *maximum length* parameter used in the Meshing Tool module software to construct the mesh and it is not the length parameter to calculate the grid refinement ratio in eq.(270). A grid refinement ratio (GRR) of 1.5 is assumed to determine the subsequent sizes $\bar{h}$, a ratio that is above 1.3, the minimum GRR suggested by Celik; Ghia and Roache (2008). Table 41 shows the calculated values for $\bar{h}$ together with the grid information, including the effective grid length size obtained from eq.(270) and the averaged cell area and volume. Values of effective h based on area and the respective grid refinement ratio r are used in calculating the GCI index. A code written in Matlab is used in solving the implicit non-linear eq.(275) to determine the effective order of convergence $\hat{p}$.

In order to test the convergence, an Eulerian-Eulerian transient laminar simulation was set up and run in ANSYS Fluent 19.0 including heat and mass transfer, heterogeneous chemical reactions, applying the KTGF to the biomass solid particle phase and reproducing ideally the geometry of reactor, applying experimental conditions obtained from Belotti et al. (2014) and for a reactor temperature of 400°C (673 K). All the parameters used in simulations are the same as presented in Table 29 and Table 30 of Chapter 4. It is worth to note that the article of Belotti et al. (2014) does not specify where the temperature was measured, and then, the experimental temperature set point (400°C (673 K)) is applied, here in this study, as a *wall temperature boundary condition*. Additionally, in the same article, the temperature of fluidizer nitrogen gas is explicitly defined as in standard conditions; therefore the nitrogen inlet boundary condition is defined in simulations as 1 atm and 300 K.

The four grids detailed in Table 41 were used in simulations. Owing that the large aspect ratio of the tubular reactor, the representation of the entire model in one whole image (900 mm x 4mm) is difficult. Instead, Figure 88 shows only a part of the wedge volume for the different grids sizes. Second order spatial discretization schemes for all variables and simulation parameters were presented in Table 29 and Table 30; and applied without any change for all grids. Time discretization was applied as follows: in order to reach convergence at initial steps the solid phase transport equations were not solved, instead only the gas phase since at the beginning there is only nitrogen inside the reactor. A fixed time step of 1.0E-4 seconds is used and the solver runs 50 time steps in where the nitrogen flow field was stabilized. Then the time step was changed to a fixed 2.5E-3 seconds and solid phase transport equation was enabled. Based on previous tests performed in this research the latter time step guarantees that the calculations can converge at least for an elapsed of 2.36 seconds after the start.

Table 41 – Grid parameters for four grid refinements used to perform the grid convergence analysis.

Grid ID	**4**	**3**	**2**	**1**
Criteria parameter $\bar{h}$ [mm]	1	0.666	0.444	0.296
GRR		1.5	1.5	1.5
Number of cells	3408	7866	17276	41132
Minimum Orthogonal quality	0.9999	0.9996	0.9239	0.9958
Skewness	100% under 6.29E-3	88% under 6.81E-3	97% under 2.95E-3	88% under 5.88E-3 and 7% between 5.88E-3 and 1.17E-2
Maximum Aspect Ratio	1.4264	1.4605	2.5717	1.5071
Cell Area (min/max) [m^2]	9.99E-7 1.00E-6	4.22E-7 4.29E-7	1.79E-7 2.21E-7	7.99E-8 8.14E-8
Percentage of cells	100%	18%	100%	17%
		4.29E-7 4.35E-7		8.14E-8 8.29E-8
		37%		32%
		4.35E-7 4.42E-7		8.29E-8 8.44E-8
		45%		52%
Averaged cell area [m^2]	**1.00E-6**	**4.30E-7**	**1.98E-7**	**8.27E-8**
h based on area [mm]	1.000	0.656	0.445	0.288
r based on area		**1.52**	**1.47**	**1.55**

In order to perform the grid analysis convergence six field variables are chosen according to its relevance in the current work. Variables are: Solid volume fraction, Solid temperature, Char mass fraction, Moisture elimination reaction R1 rate, R2 reaction rate for Comp 2 and R3 reaction rate for Comp 3. Reaction rates of R1, R2 and R3 are

chosen due to is expected that at 400°C these reactions may be activated and deplete almost all of moisture, Comp 2 and Comp 3 pseudo-components. Since a stationary regime is not expected to be reached in simulations, because of the solid mass will be accumulated in the final part of the reactor (the left part in white in Figure 89), the GCI was calculated at a specific elapsed time. The first option to calculate the GCI is when the solid phase reaches the *reactor end zone* showed in Figure 89.

Figure 88 – Grid used in GCI analysis. (a) $\bar{h} = 1.00\ [mm]$, (b) $\bar{h} = 0.666\ [mm]$, c) $\bar{h} = 0.444\ [mm]$ and (d) $\bar{h} = 0.296\ [mm]$.

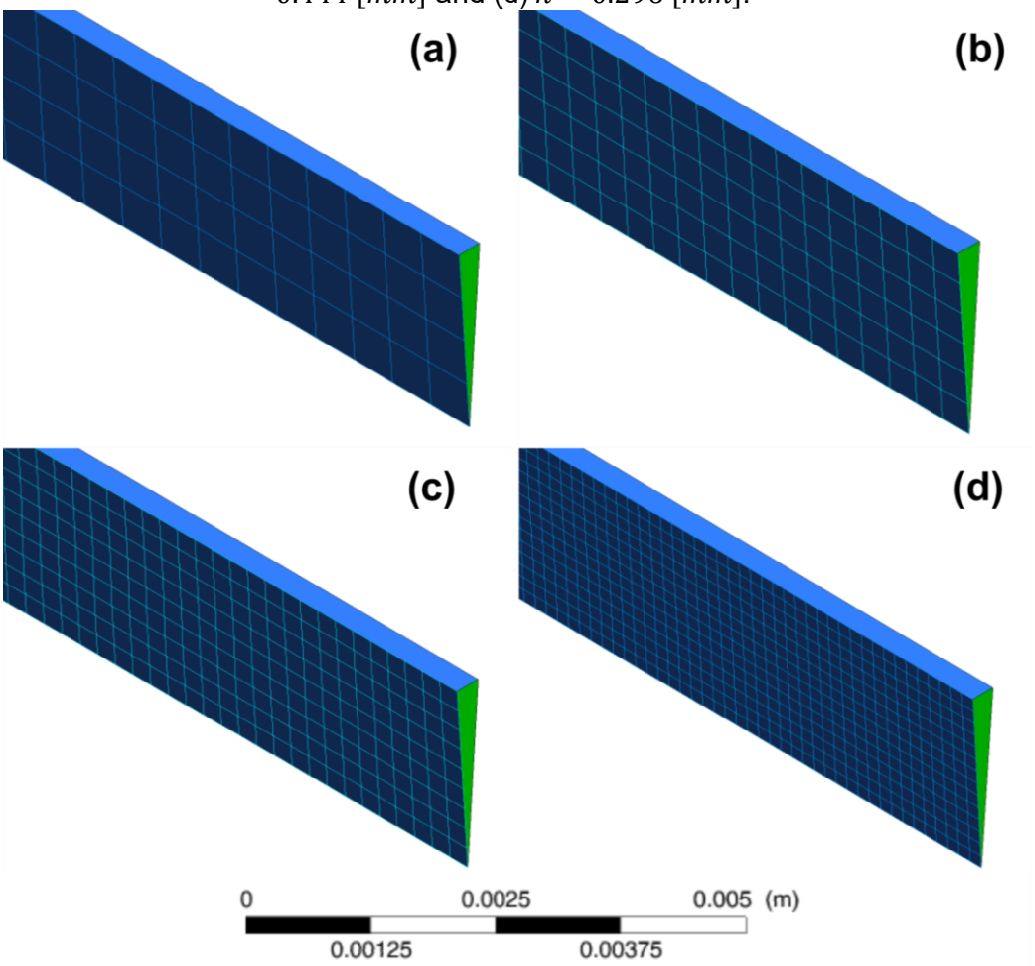

Figure 89 – Reactor end zone, the limit of the effective reaction zone, and also in red the effective reactor zone.

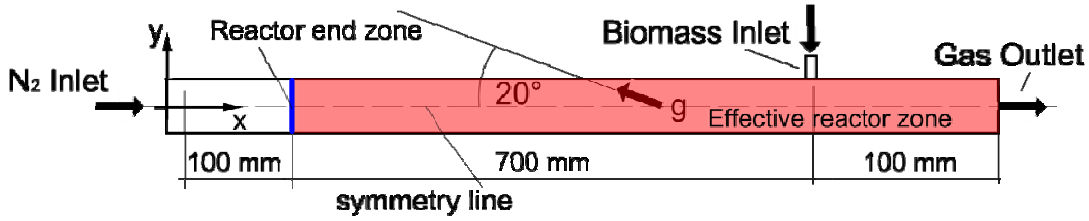

However, as can be seen in Figure 90 simulations preformed using the four different grids show different elapsed times to reach *reactor end zone*. It is worth to note that the grid with the smaller length size reaches the reactor end zone near 2.06 seconds accordingly to the value for particle residence time reported by Belotti et al. (2014). Although, the author has not precisely reported how the residence time was defined, however, the value obtained here is a suitable approximation in order to compare the results.

Figure 90 – Axial position of the solid phase initial tip for simulations using each of de different grid sizes.

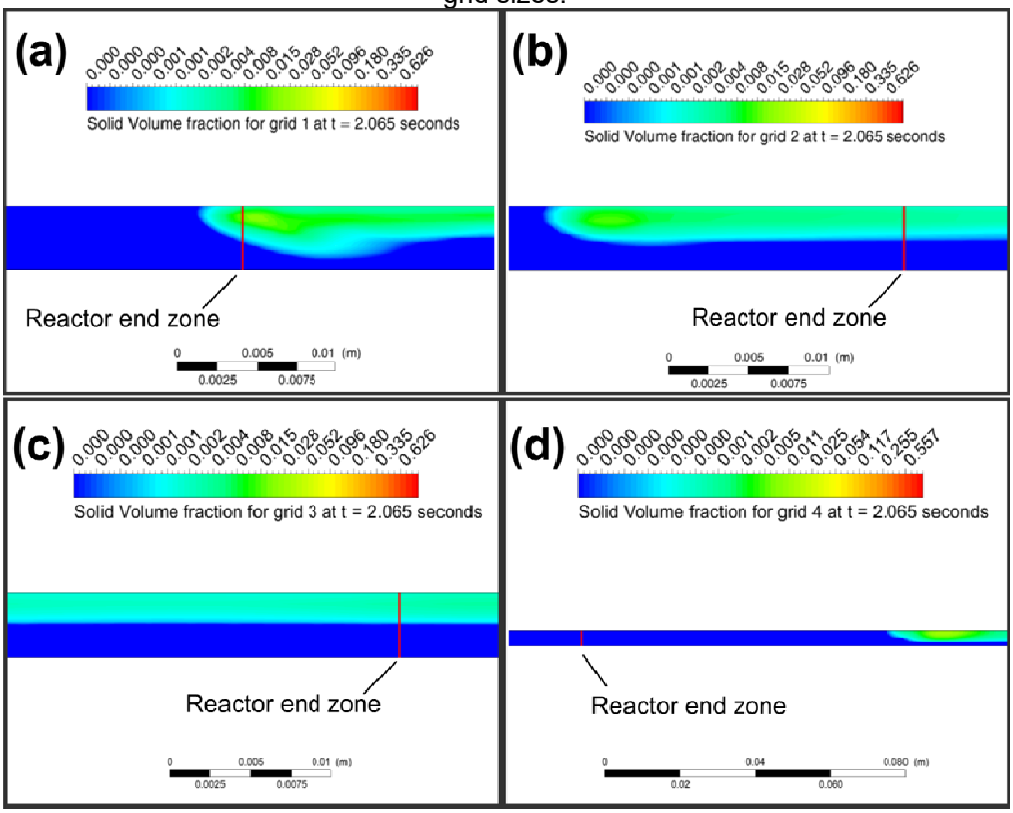

(a) Grid 1 (finer) $h = 0.288\ [mm]$, (b) Grid 2 $h = 0.445\ [mm]$, (c) Grid 3 $h = 0.656\ [mm]$, (d) Grid 4 (coarser) $h = 1.000\ [mm]$.

As can be seen in Figure 90, at time interval of 2.06 seconds after the start, the stream tips of the solid phase have reached different axial positions with respect to the reactor end zone. However, the minimum difference in length is for grid 1 and 2. Figure 90 suggests that as the grid size is smaller; starting from the grid 3, the time interval to reach the reactor end zone is higher. More details about the position respect to the reactor end zone (at x = 100 mm) of the solid volume fraction streams can be viewed in Figure 91 in where the axial profiles for each grids are plotted considering 200 sample

points in the axial direction and at a distance of 3.0 mm from the reactor symmetry axis. In this Figure, the tip of the stream can be identified as the spike of the volume solid fraction in the interval of x = [0.0 m,0.2 m]. Both, the relative distance to the reactor end zone in x = 0.1 m and the magnitude of the volume fraction are closer for simulations using grids 1 and 2. This observation suggests a tendency to convergence as the length of the grid tends to zero.

Another fact that can be observed in Figure 91 is the increase of fluctuations of the solid volume fraction as grid length is smaller evidencing that as the grid length is smaller, the simulation can capture in a better way the fluctuating nature of the granular phase, a feature that is not observable in the simulation using the coarser grid 4.

Figure 91 – Axial profile of solid volume fraction at t = 2.06 seconds obtained from y = 3 mm from the symmetry line.

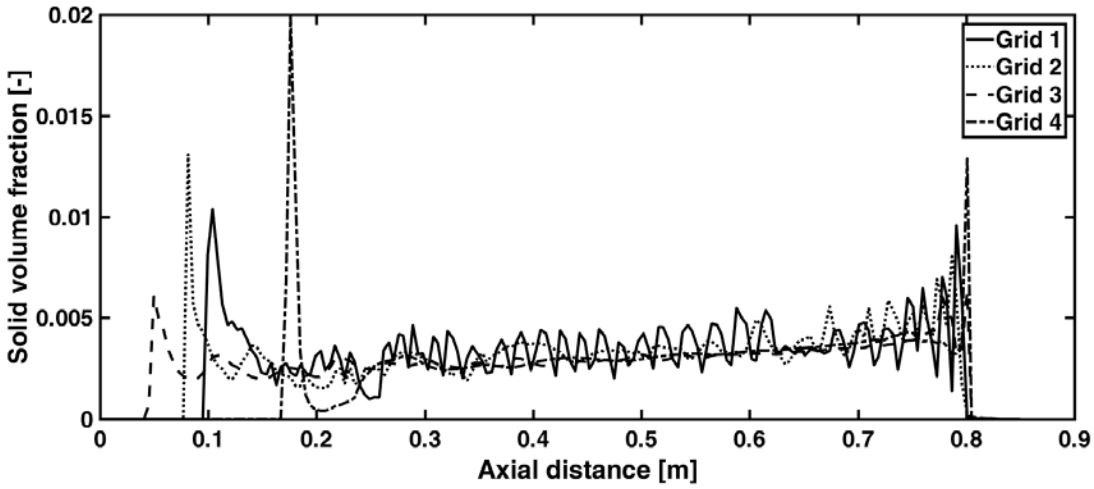

The GCI of relevant variables may be evaluated at the point (x,y,t) =(0.1 m, 0.003 m, 2.06 seconds) just over the reactor end zone. However, as mentioned before, as can be seen in Figure 91, in the case of solid volume fraction, at this point, a large difference is obtained between different grids.

Although in the same Figure, it is also possible to observe that the difference between solutions is smaller as the axial distance is closer to 0.8 m, even when there are strong fluctuations for the solutions for grids 1 and 2. In the light of this evidence, a space averaged variable instead a single local value is proposed in order to calculate the GCI index and using only the first three grid lengths due to the fact that the solution of the grid 4 seems to be very inaccurate and does not capture the granular fluctuations.

Additionally, in order to avoid the large difference caused by the stream tips, the GCI will be evaluated at a lower elapsed time defined by the numerical solution with the lesser final simulation time i.e. at t = 2.36 seconds corresponding to the final simulation time of grid 1. Figure 92 shows the solution for the three first grids at the mentioned elapsed time.

In Figure 92 it is possible to observe a better coincidence between different solutions. Therefore, the GCI index will be calculated averaging the relevant variables over the entire reactor i.e. a volumetric integral over the tubular reactor. Table 42 shows the effective grid length based on the criteria $\bar{h}$, the average cell areas and the effective grid refinement ratio (GRR). It is worth to note that the resulting GRR obtained using the methodology presented by Celik; Ghia and Roache (2008) is very close to the ratio of the criteria $\bar{h}$ ratio that is defined as 1.5.

Figure 92 – Axial profile of solid volume fraction at t = 2.36 seconds obtained from y = 3 mm from the symmetry line.

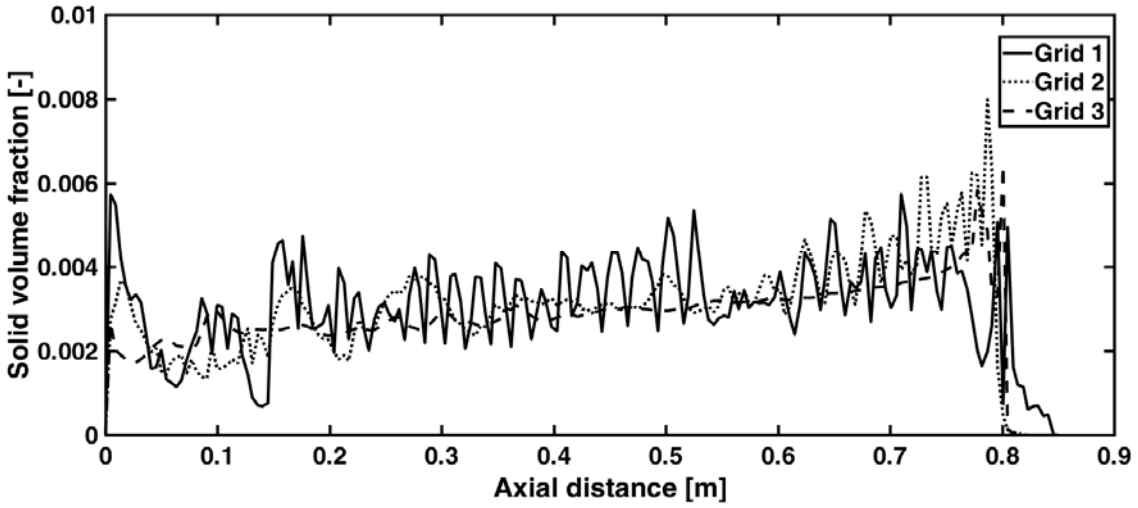

Table 42 – Grid parameters for GCI calculation considering only the three first grids.

Grid ID	**1**	**2**	**3**
Criteria $\bar{h}$ [mm]	0.296	0.444	0.667
Average Cell Area [m^2]	8.27E-8	1.98E-7	4.30E-7
Effective grid length h [mm]	0.288	0.445	0.656
GRR r		r_{21} 1.55	r_{32} 1.47

Table 43 shows the averaged values of the relevant field variables calculated by means of a volumetric integration over the entire reactor. Comparing the results in this Table,

large differences between averaged values of grids 1 and 2 are evident compared with values of grid 3 for Char mass fraction, and for rate of reactions.

Table 43 – Averaged field variables over the entire reactor at t = 2.36 sec.

	Grid ID		
Averaged variables	**1**	**2**	**3**
Solid volume fraction [-]	1.24E-3	1.36E-3	1.31E-3
Solid temperature [K]	626.2	620.2	629.5
Char mass fraction [-]	0.379	0.349	0.483
Moisture rate of reaction [mol/m^3/s]	1.037	1.217	0.447
Comp 2 rate of reaction [mol/m^3/s]	0.407	0.450	0.745
Comp 3 rate of reaction [mol/m^3/s]	0.773	0.795	0.121

However, in the case of temperature and solid volume fraction averaged values of grid 3 are closer to those values of grid 1 than of the values of grid 2. Table 44 shows the parameters calculated following the methodology described in section 4.2.3.1. As defined in the methodology section in Chapter 4, all the field equations has been solved performing a discretization of a second order with a rate of convergence equal to 2, however, effective order of convergence $\hat{p}$ for reaction rate of Comp 3 and Comp 2 are larger than this value.

Table 44 – Effective convergence ratio for averaged field variables at t = 2.36 seconds.

Variable	$^*\hat{\varepsilon}_{21}$	$^*\hat{\varepsilon}_{32}$	$\hat{\varepsilon}_{32}/\hat{\varepsilon}_{21}$	$\hat{p}$	Φ_{ext21}	e_a^{21}	e_a^{ext}
Solid Volume fraction [-]	1.17E-4	-5.30E-5	-0.453	**1.87**	1.15E-3	0.094	0.079
Solid Temperature [K]	-6.00	9.30	-1.55	**1.03**	636.6	0.010	0.016
Char mass fraction [-]	-0.029	0.134	-4.577	**3.62**	0.386	0.077	0.019
Moisture rate of reaction [mol/m^3/s]	0.180	-0.770	-4.278	**3.46**	0.987	0.174	0.051
Comp 2 Rate of reaction [mol/m^3/s]	0.043	0.295	6.888	**4.61**	0.401	0.105	0.016
Comp 3 Rate of reaction [mol/m^3/s]	0.022	-0.674	-31.041	**8.25**	0.772	0.028	0.001

*In where $\hat{\varepsilon}_{21}$ and $\hat{\varepsilon}_{32}$ are the difference of numerical results for the relevant variables between grids 2 and 1; and between grids 3 and 2, respectively (CELIK; GHIA; ROACHE, 2008).

Table 45 shows the extrapolated values calculated applying the Generalized Richardson Extrapolation method obtaining the asymptotic numerical solution when the grid length is equal to zero. For the case of temperature, the extrapolated value is closer to the value of grid 3 while the solutions obtained applying grids 1 and 2 deviate more. This characteristic can be attributed to the sign of the ratio $\hat{\varepsilon}_{32}/\hat{\varepsilon}_{21}$ that according to Celik; Ghia and Roache (2008) it suggests an oscillatory convergence when this ratio is lower than zero. Additionally, observing the third column in Table 44 all values of the ratio$\hat{\varepsilon}_{32}/\hat{\varepsilon}_{21}$, excepting for Comp 2 rate of reaction, are lower than zero suggesting an

oscillatory dominated rate of convergence for the whole solution at the elapsed time equal to 2.36 seconds.

Table 45 – Extrapolated solution obtained using the effective order of convergence $\hat{p}$ at t = 2.36 seconds.

Averaged variables	Extrapolated solution Φ_{ext21}	Grid ID 1	2	3
Solid volume fraction [-]	1.15E-03	1.24E-3	1.36E-3	1.31E-3
Solid temperature [K]	636.6	626.2	620.2	629.5
Char mass fraction [-]	0.386	0.379	0.349	0.483
Moisture rate of reaction [mol/m^3/s]	0.987	1.037	1.217	0.447
Comp2 rate of reaction [mol/m^3/s]	0.401	0.407	0.450	0.745
Comp3 rate of reaction [mol/m^3/s]	0.772	0.773	0.795	0.121

Table 46 and Figure 93 show the GCI results and the charts of all averaged field values including the extrapolated values. Table 46 shows a deviation above 5% from the asymptotic numerical value for Solid volume fraction and for Moisture reaction rate. The index value for Solid phase temperature, Char mass fraction, Comp 2 and Comp 3 rate of reaction are on the acceptable range of accuracy, defined in this work as 5%.

Table 46 – GCI calculated for relevant averaged field variables considering the grid length of ID 1, 2 and 3.

Variable	CGI_{21}
Solid Volume fraction [-]	9.19%
Solid Temperature [K]	2.08%
Char mass fraction [-]	2.46%
Moisture rate of reaction [mol/m^3/s]	6.03%
Comp 2 Rate of reaction [mol/m^3/s]	1.98%
Comp 3 Rate of reaction [mol/m^3/s]	0.09%

Solutions using the different grids are plotted in Figure 93 including also the solution for the coarser grid (grid 4). On the horizontal axis the normalized values for the grid refinement length are used. These values have been calculated relative to the finer grid length and using the effective order of convergence $\hat{p}$ to calculate the values for grids 2 and 3 and the ratio based on the criteria value $\bar{h}$ in the case of grid 4. Chart a) in Figure 93 depicts the solution for the Solid volume fraction. In this chart the solution of the coarser grid is closer to the asymptotic value than to the other solutions. However, the value of the asymptotic solution has been calculated only with results of the first three grids. Starting from the grid 3, an oscillatory convergence is obtained since the solution of grid 2 is higher than the solution of grid 3 and the finer solution is lower than grid 2

and grid 3 solutions. Also, it is possible to see that the relative difference between solutions of grid 2 and 3 is smaller than the difference between solutions of grids 1 and 2. Rate of convergence for Solid volume fraction is close to but smaller than 2 due to the fact that there is a relative error ratio (e_a^{21}) of 0.094 (9.4%) between solutions of grid 1 and 2. The case of temperature, depicted in chart b), is similar to the case of Solid volume fraction, there is an oscillatory convergence, but with a smaller rate of convergence, due to the relative error ratio, e_a^{21}, equal to 1.0% between solutions of grid 1 and 2, however, this relative error is almost one order of magnitude lower than in the case of Solid volume fraction, and as a consequence the GCI is better.

Figure 93 – Relevant averaged field variables plotted as a function of normalized grid length for simulation using grid ID 1,2,3 and 4 and at t = 2.36 seconds.

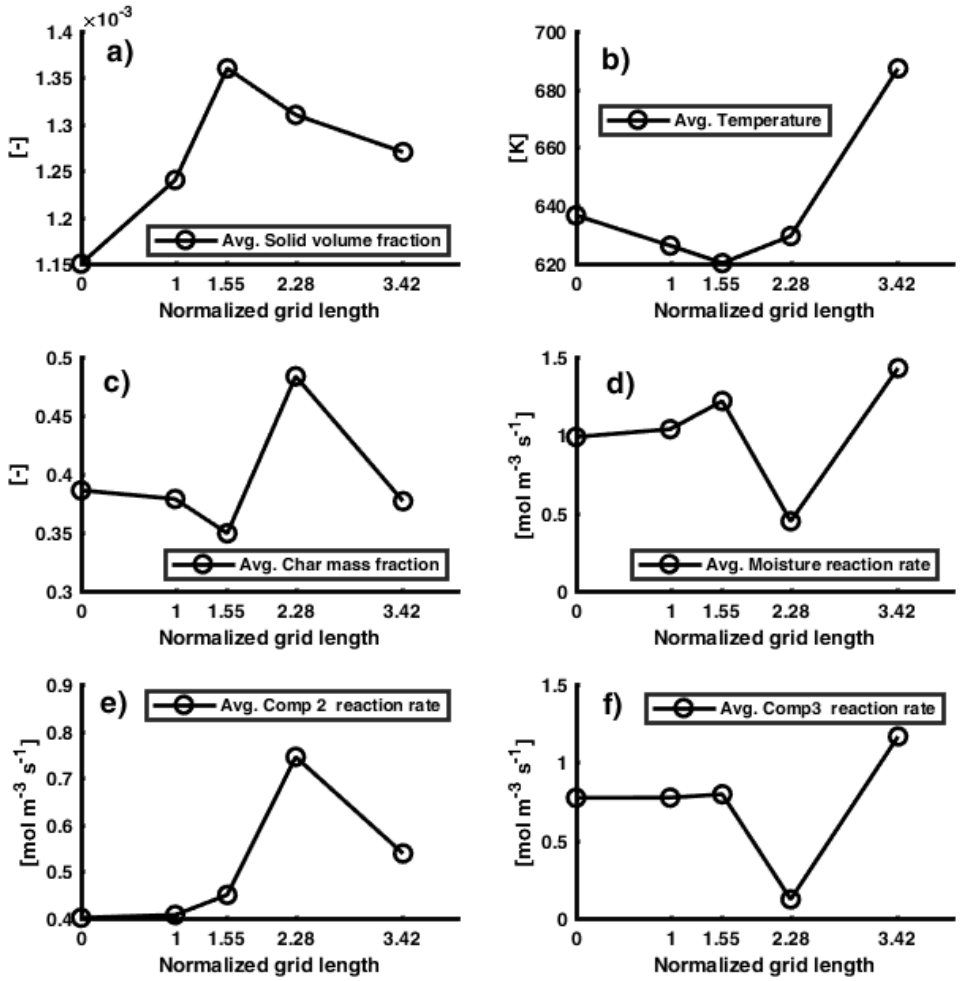

In charts *c), d) e)* and *f)* solutions for Char mass fraction, Moisture, and Comp 3 behave similarly, except for Comp 2 (chart (e)) that converges without oscillations for the three first grids. Effective order of convergence is rather larger than the values for a) and b) cases. This characteristic is due to the fact that solutions tend to reach the asymptotic numerical values faster when the grid changes from normalized length 2 to1 than when it changes from 3 to 2. This characteristic is very clear in the mentioned charts, and the consequence is a lower GCI. It is worth to note that the GCI for Moisture reaction rate is over 5% and this is due to the fact that the relative error ratio e_a^{21} is larger i.e. 17.4%.

The fast convergence is evident in chart *f)*, for the rate of reaction of Comp 3, in where the relative error ratio of grids 1 and 2 compared with the relative error of grid 1 and the asymptotic numerical solution is minimal, 2.8% and 0.1% respectively. It is worth to note that there is close relation between the Char mass fraction and the rate of reaction of Comp 2 and Comp 3 due to the total averaged mass fraction of Char depends on the rate of depletion of biomass pseudo-components. Because of this a similar convergence characteristics of Char mass fraction is expected. Furthermore, the oscillatory rate of convergence of Char mass fraction, suggestively, is due to the oscillatory behavior of reaction rate of Comp 3. However, there are also two more reactions, for Comp 4 and Comp 5, that could affect the rate of convergence of Char mass fraction, nonetheless, as can be discussed in the next section, these reactions were not fully activated at elapsed time t = 2.36 seconds, then the net effect can be assumed as negligible.

Finally and in summary, asymptotic numerical results for the relevant field variables obtaining from the Richardson Extrapolation method are presented in Table 47 in conjunction with the respective uncertainty interval equal to the GCI index.

Table 47 – Asymptotic numerical values of relevant field variables and uncertainty interval for solution at elapsed time t=2.36 seconds

Averaged variables	Extrapolated solution Φ_{ext21}	Uncertainty
Solid volume fraction [-]	1.15E-3	9.19%
Solid temperature [K]	636.6	2.08%
Char mass fraction [-]	0.386	2.46%
Moisture rate of reaction [mol/m^3/s]	0.987	6.03%
Comp 2 rate of reaction [mol/m^3/s]	0.401	1.98%
Comp 3 rate of reaction [mol/m^3/s]	0.772	0.09%

5.3.3. BIOMASS CONVERSION

In this section results of the simulation performed at a reactor temperature of 673 K and using the smallest characteristic grid length i.e h = 0.2875 [mm], are presented and discussed. Section starts presenting the biomass conversion, a result that is analyzed as a function of other variables. Also, the relation between results and GCI analysis relating to the effect of the grid on prediction of different field variables appears as a necessary base to explain the results of the simulation performed here.

Conversion of biomass in fast pyrolysis to produce char is an important parameter due to the fact that it is directly related with the total gases released during the process. Biomass conversion is also a direct effect of chemical kinetics describing the devolatilization. However, transport processes also play a fundamental role because of it affects the mass and heat transfer to supply energy for devolatilization reactions. Locally, heat transfer is affected by the thermal conductivity but observing the macro-scale heat transfer could be limited and controlled by the mass transfer. These effects, chemical kinetics, heat and mass transfer and its relation with the KTGF will be discussed in this section in order to explain the results of simulation.

Calculating eq.(197) over the whole reactor and balancing the mass over the surface defined as the *reactor end zone*, depicted in Figure 89, yields the overall biomass conversion at elapsed time t = 2.36 seconds. As was explained in the methodology section 4.2.1.2, conversion calculation is performed over the total simulation time since stationary conditions can not be reached due to the accumulation and continuous devolatilization of biomass at the bottom of the reactor (the part at the left side of effective reactor zone). Table 48 shows the results of the volume and surfaces integrals while Table 49 shows the quantities to calculate the overall biomass conversion. Based on this data, the overall conversion of biomass reached in simulation was 17.8%.

Table 48 – Total mass quantities for calculation of biomass conversion at t = 2.36 [s].

Total solid mass inside reactor	4.84E-05	[kg]
Total biomass that entered the reactor	5.92E-05	[kg]
Total mass of gases passed through reactor end zone surface	9.11E-06	[kg]
Total N_2 mass that entered and left the reactor	8.93E-06	[kg]

Table 49 – Biomass conversion in wt% basis.

Total solid mass inside reactor	Total pyrolytic gases through reactor end surface	Effective mass remaining inside reactor	Conversion %wt
4.84E-5 [kg]	1.78E-7 [kg]	4.86E-5 [kg]	17.8%

Table 50 presents reference values obtained from literature for fast pyrolysis of *Chlorella Vulgaris* using lab-scale pyrolyzers at 400°C. Result from the current simulation shows a significant deviation from experimental results. The simulation was performed modeling the geometry and process condition based on the tubular reactor used by Belotti et al. (2014) whose has obtained a conversion about 75%. In order to extent the comparison Table 50 are also presented in the results obtained by Gong et al. (2013) and Yuan, Tahmasebi and Yu (2015) for fast pyrolysis experiments of *Chlorella Vulgaris.*

Table 50 – Solid mass fraction recovered in fast pyrolysis of *Chlorella Vulgaris* from: Gong et al. (2013), Yuan Yuan, Tahmasebi and Yu (2015) and Belotti et al. (2014).

	Solid mass fraction recover		
Temperature [°C (K)]	Gong	Yuan	Belotti*
400 (673)	66.0±9.7	56.54	Close 75%
500 (773)	72.0±3.2	70.72	80 to 75%

**Data from BG-11 specie reported in Belotti et al. (2014).*

Results from the simulation open the discussion about the lower biomass conversion obtained here. In order to start the analysis four factors must be taken into account and discussed i.e. chemical kinetics, thermal conductivity of biomass, mass and heat transport and the energy necessary for devolatilization. Chemical kinetics is obviously the first factor to be analyzed, since it directly controls the rate of conversion, and in the light of the first result, it seems that the reaction mechanism cannot well predict the devolatilization rate at higher heating rates. However, for devolatilization and in general for pyrolysis, energy is necessary and the rate at which it is supplied can also limit and may control the reaction rate. In order to determine if pure chemical kinetics, described by the reaction mechanism, is the main factor that causes this under-estimated biomass conversion, an isolated analysis, independent of energy, can be performed solving the set of non-linear ordinary differential equations. The isolation of kinetics from the energy and also mass transport effects can be made by solving the system of rate equations (eq.(192)) considering a perfect stirred reactor, which considers instantaneous mixing

and an infinitely fast heat transfer process i.e. without resistances. Therefore, without these limiting processes pure kinetics effect can be evaluated.

5.3.3.1. ANALYSIS OF CHEMICAL KINETICS EFFECTS

The mentioned set of non-linear ordinary differential equations (ODE) is the system described by a set of equations of the type of eq.(192), one equation for moisture and each component. A total of 6 independent non-linear ODE's were solved in Isokin software package that uses a solver based on high order Runge-Kutta method. System of equation has been solved considering a total integration time of 2.0, 2.5 and 3.0 seconds as the residence time and constant process temperature of 400 and 500°C. Time interval near of 2.0 seconds is mentioned in Belotti et al. (2014) as the experimental residence time, however, higher time intervals of 2.5 and 3.0 seconds were also used in calculations in order to evaluate the sensibility. Table 51 shows the results of the pure chemical kinetics analysis providing the biomass conversion

Table 51 – Overall biomass conversion predicted by the reaction mechanism developed here and considering a perfect stirred reactor simulations.

Temperature [°C (K)]	**Integration time interval [s]**		
	2.0	2.5	3.0
400 (673)	51.8%	52.7%	53.2%
500 (773)	68.8%	69.5%	70.0%

Table 52 presents a comparison between the simulated overall conversion and literature data for a pyrolysis process at 400°C. As can be seen in this Table, predicted values, considering only pure chemical kinetics, can reach conversions closer to those experimental fast pyrolysis results published by Gong et al. (2013) and Yuan, Tahmasebi and Yu (2015), specially with the latter. However, by comparing the results with the published data provided by Belotti et al. (2014), results still deviate. Several considerations can be made about the results.

Firstly, microalgae composition can affect the biomass conversion. As can be seen in Table 31 composition of *Chlorella Vulgaris* used by Belotti et al. (2014) differs significantly from the protein and carbohydrates content determined in this work. Therefore, the overall rate of reaction as a function reaction temperature can also differ significantly. As can be seen in Figure 75, zone 2 (reaction R2) and zone 3 (reaction

R3), that is associated here with carbohydrates, has its main devolatilization rate between 200 and 300°C, while proteins (zone 4 and associated to reaction R4) from 300 to 400°C.

Table 52 – Comparison of simulated results, performed at 400°C (673 K) considering a perfect stirred reactor simulation, with selected literature values.

	This study		
Residence time	2.0 [s]	2.5 [s]	3.0 [s]
Conversion	51.8%	52.7%	53.2%
Residence time	ns* [s]	ns* [s]	Near 2 [s]
Conversion	66.0±9.7%	56.5%	Close 75%
	Gong	**Yuan**	**Belotti****

*ns: particle residence time was not specified. **Data from BG-11 specie reported in Belotti et al. (2014). References: Gong et al. (2013), Yuan Yuan, Tahmasebi and Yu (2015) and Belotti et al. (2014).

On the other hand, as can be seen in Table 31, the carbohydrates content, reported by Belotti et al. (2014) is 82.7% higher than the content determined here. The latter comparison can suggest that devolatilization rate of *Chlorella Vulgaris* microalgae used by Belotti et al. (2014) (the BG-11 specie in Belotti et al. (2014)) tends to thermally decompose faster at lower temperatures due to the higher contents of carbohydrates.

Additionally, in Belotti et al. (2014) the specific point in where the temperature was measured was not well given. That methodology states that once the reactor temperature reached the pre-defined experimental temperature the microalgae injection has started. However, the place where the temperature was measured was not specified, it could be on reactor walls or fully immersed into the nitrogen flow. Facing this lack of information, simulations here were performed with a constant temperature on walls equal to the experimental temperature set point (400°C in simulation performed here). As a consequence and as can be seen in Table 47 the averaged Solid temperature was 363.6°C (636.6 K), 36.4°C below the experimental temperature.

To analyze the latter in more detail a new simulation is carried out with this temperature (363.6°C), and considering again a perfect stirred reactor, giving the result shown in Table 53. These calculations show that a reduction of temperature from 400 to 363.6°C can decrease the biomass conversion near 16% (reduction percentage of the percentage of conversion) evidencing the sensitivity of the conversion with respect to

temperature and showing that it could be an important factor in explaining the difference in results.

Table 53 – Biomass conversion predicted by reaction mechanism considering a perfect stirred reactor at 363.6°C.

	Integration time interval [s]		
Temperature [°C (K)]	2.0	2.5	3.0
363.6 (636.6)	44.3%	45.2%	45.9%
400.0 (673.0)	51.8%	52.7%	53.2%
Difference	7.5%	7.5%	7.3%

However it is worth to note that there is an observation about the perfect stirred reactor calculations. System of equation solved in the perfect stirred reactor calculations are considered following a particle, nonetheless, CFD simulation was performed using the Eulerian instance, eq.(232), for moisture and component equations. The main difference between both descriptions is the order of the reaction model. However, reaction model affect the shape of the rate of reaction instead of modifying significantly the temperature at which the reaction take place. This is evident performing the following numerical calculation considering the kinetic parameters of reaction R3 of the mechanism: *A = 6.6E16 [1/s]*, *E = 195.3 [kJ/mol/K],* initial value for reactant $W_0 = 1$, and reaction model order *n = 3.55*. Conversions are calculated for the following equations: following a particle with velocity equal to zero i.e. Lagrangian approach (as in thermal analysis)

$$\frac{dW}{dt} = 1^{-2.55}(6.6E16.)exp\left(\frac{-195.3}{RT}\right)W^{3.55} \tag{284}$$

this equation has the same form of eq.(230); and Applying the Eulerian approach to eq.(284)

$$\frac{dW}{dt} = -(6.6E16)exp\left(\frac{-195.3}{RT}\right)W \tag{285}$$

Solving, numerically, eq.(284) and eq.(285) with the Euler Simple method for ordinary differential equations with a time step of 1 second, initial temperature of 300 K, and considering a integral time of 150 minutes, gives the solutions depicted in Figure 94. As can be seen in this Figure the shape of the conversion and reaction rate curves are different evidencing that the shape is losses in the transformation from the Lagrangian to the Eulerian description.

Figure 94 – Comparison between Eulerian and Lagrangian rate equation solutions. (a) Conversion; (b) rate of reaction

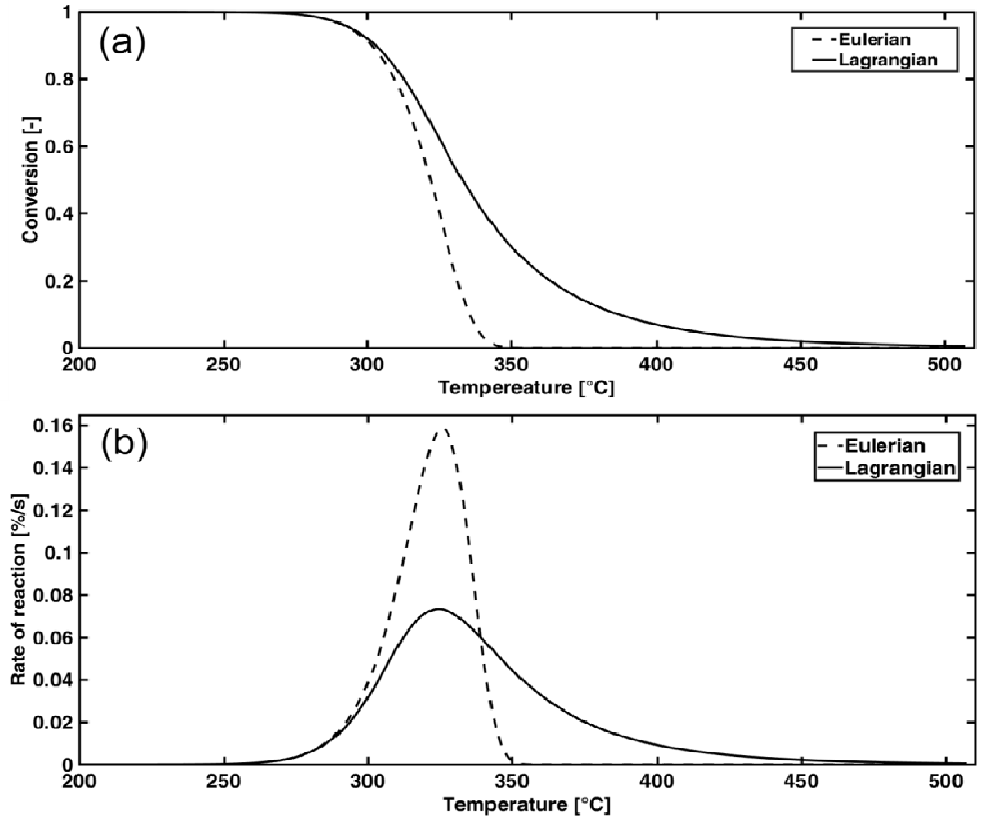

However the temperature of the maximum rate of reaction does no change significantly 325.8 °C and 324.4 °C for Eulerian and Lagrangian description respectively. From the point of view of the results obtained in simulation the prediction using the Eulerian approach does not affect the reaction temperature and further the rate of reaction is largely faster than the Lagrangian rate. Therefore, although there is a deviation in shape respect the Lagrangian reaction mechanism the temperature in where the reaction take place are the same and even at higher rate and not explain the difference in conversion observed in the simulation performed here.

It is clear that an additional parameter is necessary to implement the reaction mechanism in ANSYS Fluent 19.0. However the standard module of the software does not provide a way to introduce the additional parameter. This additional parameter is the $W_0^{(1-n)}$ which may be introduced together multiplying the pre-exponential factor. However, the shape of the curves is a consequence of the history of the devolatilization process and if the particle phase is described as a continuum (Eulerian description) tracking of particles is not possible. Therefore an alternative form is to evaluate the

history as a function of local properties, a module that must be implemented with an UDF script in ANSYS Fluent 19.0.

Although averaged reactor Solid temperature can be the causality of the deviation with respect to the data published by Belotti et al. (2014), the deviation in results may not obey only of a chemical kinetic effect due to temperature. As a consequence, the analysis and the discussion can be moved toward the analysis of the transport properties of the flow.

5.3.3.2. ANALYSIS OF HYDRODYNAMICS EFFECTS

As was demonstrated in the latter section, temperature plays a significant role in the overall biomass conversion. The local value of temperature depends on the mass and heat transport processes, and heat transport described by the energy conservation equation is coupled to the momentum equation that describes the advective mass transport. The latter mechanism is in general more important than the molecular mass transport inside a continuous fluidized reactor. The rate at which the energy is consumed locally by the heterogeneous reaction can decrease, also locally, the temperature. If the mass and heat advection transport processes are weak the chemical reactions will reduce its rate of reaction, therefore the devolatilization will be controlled by hydrodynamics instead kinetically. As a consequence the hypothesis proposed is that because of the coupling between the energy equation with the momentum equation, the solid mass transfer can control the heat transport, therefore an analysis observing mass transfer properties of the granular flow are necessary.

As stated in Belotti et al. (2014) the main source of heat to promote the devolatilization in the experimental apparatus used are the reactor walls. This heat is subsequently transported by convective and random motions inside the flow field. Under this statement the analysis of solid radial velocity is necessary. Solid phase radial velocity depends on the random motions of particles in a direction perpendicular to the reactor axial axis, which in turn depends on the granular temperature (KTGF) equations. The development of KTGF is based on the pseudo-microscopic averaging of discrete particles, similar to how turbulent mixing theory is developed. Random motions that are described by the granular temperature Θ can transport the heat to increase the temperature inside the flow away from the wall. Random motions, very close to wall,

can be damped, or completely reduced, forming a no-slip boundary condition. As random motions are smaller at the walls, the greater the influence of heat transported by conduction, thus controlling the overall heat flux. In the KTGF the intensity of motion at walls is defined by an interaction property that depends on the effective rheology of the particle flow, that in the case of microalgae particle flows is unknown or not reported so far.

The interaction properties aforementioned in KTGF are the particle-wall restitution coefficient and the specularity. The former is a measure of how much momentum is dissipated at the walls and accordingly with Benyahia et al. (2000) this parameter has a predominant influence in the apparent rheology of granular phase inside the flow and in boundaries. High dissipation i.e. coefficient equal to zero, means non-elastic collision, and tends to generate a no-slip boundary condition, and as a consequence the local heat transfer may be dominated by the molecular thermal conductivity of the solid phase. If the momentum dissipation is lower, the particles tend to have a velocity magnitude different from zero and the heat transfer can be enhanced. The latter, the specularity coefficient is related to the resultant direction of a particle after it collides with a wall and with the lateral momentum dissipation (ANSYS Fluent 19.0 Theory Guide http://ansyshelp.ansys.com). Specularity coefficient equal to zero corresponds to a condition of zero stress at the wall. In this work the particle-wall restitution coefficient was obtained from the work of Benyahia et al. (2000) who simulated a cold flow of particles in a raiser, and provided a value of 0.90. On the other hand the specularity coefficient was chosen equal to 0.5.

In order to analyze the heat and mass transfer, the radial velocity field near the wall is presented in Figure 95. Restitution coefficient of 0.9 means that a particle tends to maintain its momentum when colliding with the wall. According to Benyahia et al. (2000), for particle-particle restitution coefficient, a change from 0.90 to 0.99 introduces a reduction of an order of magnitude in dissipation, since the term related with the coefficient is of second order. For the boundary condition, used in ANSYS Fluent 19.0 (*Johnson and Jackson boundary condition* for granular flows (JOHNSON; JACKSON, 1987)), the particle-wall restitution coefficient is also a second order term parameter a change of 0.09 can introduce a significant dissipation. On the other hand, specularity coefficient is present in the shear force term in the granular temperature boundary

condition (also in ANSYS Fluent 19.0 set of equations) however it is a linear term, but also can introduce significant dissipation of granular temperature at wall.

As can be seen in Figure 95 the velocity fluctuations at 0.19 [mm] from the wall (3.81 [mm] from the symmetry line) are almost equal to zero along the axial direction.

Figure 95 – Axial profiles of solid phase radial velocities at different distance from the symmetry line at elapsed time t = 2.36 [s].

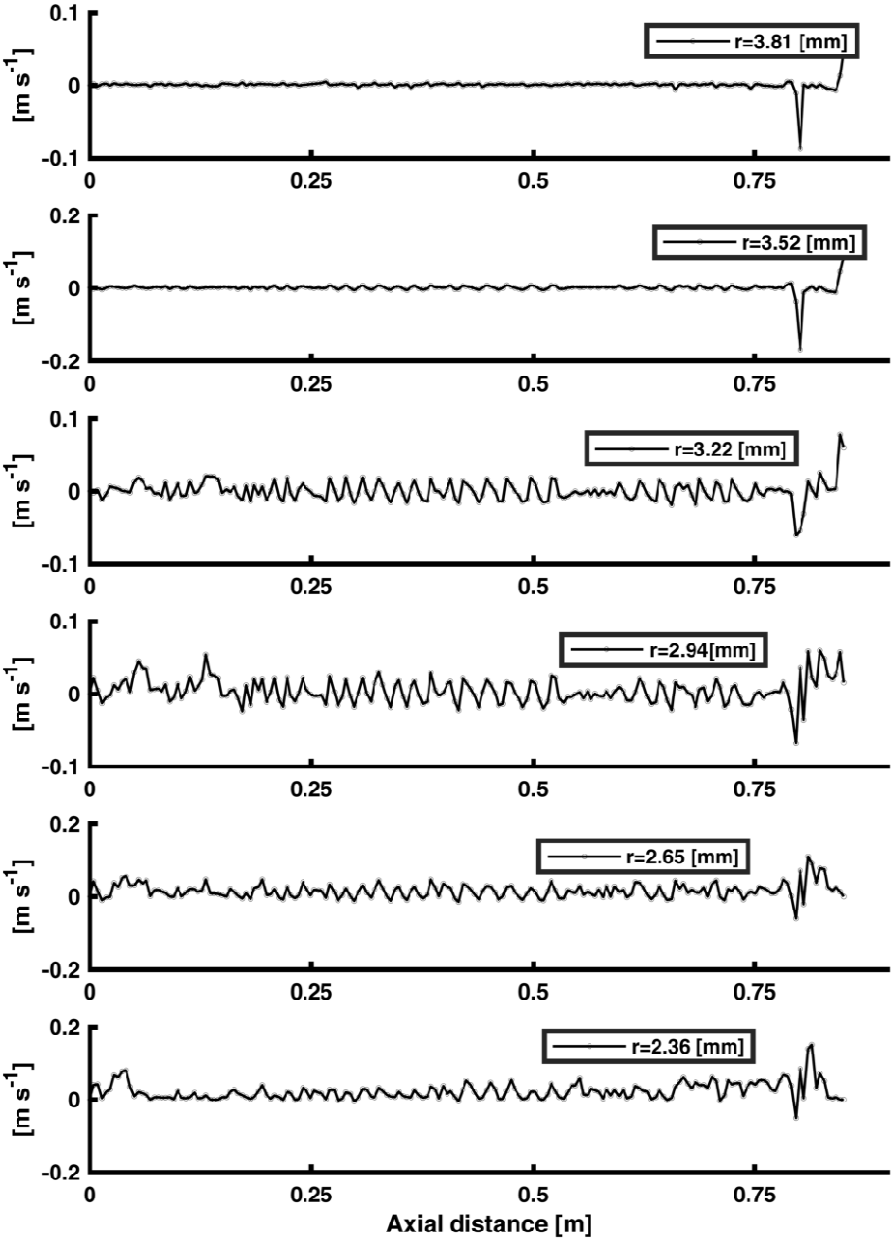

However, as the radial distance is increased, the velocity fluctuation is also increased up to 1.06 [mm] from the wall (2.94 [mm] from the symmetry line). In terms of mass transfer there is a zone with practically zero radial velocity due to the specularity and restitution coefficient parameters applied, producing a resistance layer for heat transfer in where thermal conductivity of solid particles limits and controls the heat transfer. Starting near r = 3.22 [mm] (measured from the symmetry line) there is an intense radial velocity that can transfer heat to flow field, however, this amount of heat is primarily controlled by the resistance layer. Specularity and particle-wall restitution coefficients are not reported in literature for microalgae powders. This fact is expected due to the fact that CDF simulations of pyrolysis of microalgae materials has not been performed or has not been reported so far neither for cold flow experiments nor in conjunction with chemical kinetics.

In the light of the discussion presented, the large deviation of conversion observed in Section 5.3.3 may not to be attributed at all to a miss-prediction of the reaction mechanism, owing that it was demonstrated that pure chemical kinetics predictions are close to the observed biomass conversions in the literature. Nonetheless it is also necessary to analyze the hydrodynamic effects of mass and heat transfer in order to discard or not this factor. Flow properties analysis can be started from the particle phase conduction property. The thermal conduction chosen here, in absence of literature data, was the value provided by ANSYS Fluent 19.0 database for wood. In simulations of pyrolysis of lignocellulosic biomass these parameters behave well, therefore can be discarded as a limiting parameters of heat transfer.

As suggested by the radial velocity profile near the wall, the derived hypothesis is that the layer formed generates a thermal resistance layer diminishing the heat transfer in this zone and therefore controlling the process by thermal conduction. However, under the assumption that the thermal conduction is adequate the lack of the efficiency to distribute can be attributed to the mass and heat transport processes that depends on to the rheology granular parameters.

If this hypothesis is true, the devolatilization reactions of microalgae components are not supplied with enough energy to maintain the rate of reaction and the process temperature. This limiting bottleneck produces that reactions R1, R2 and R3, as can be

seen in Figure 96, have one and two orders of magnitude higher than the rate of reaction R4, respectively.

Figure 96 – Averaged reaction rate over the radial direction plotted along the axial direction at elapsed time t = 2.36 [s].

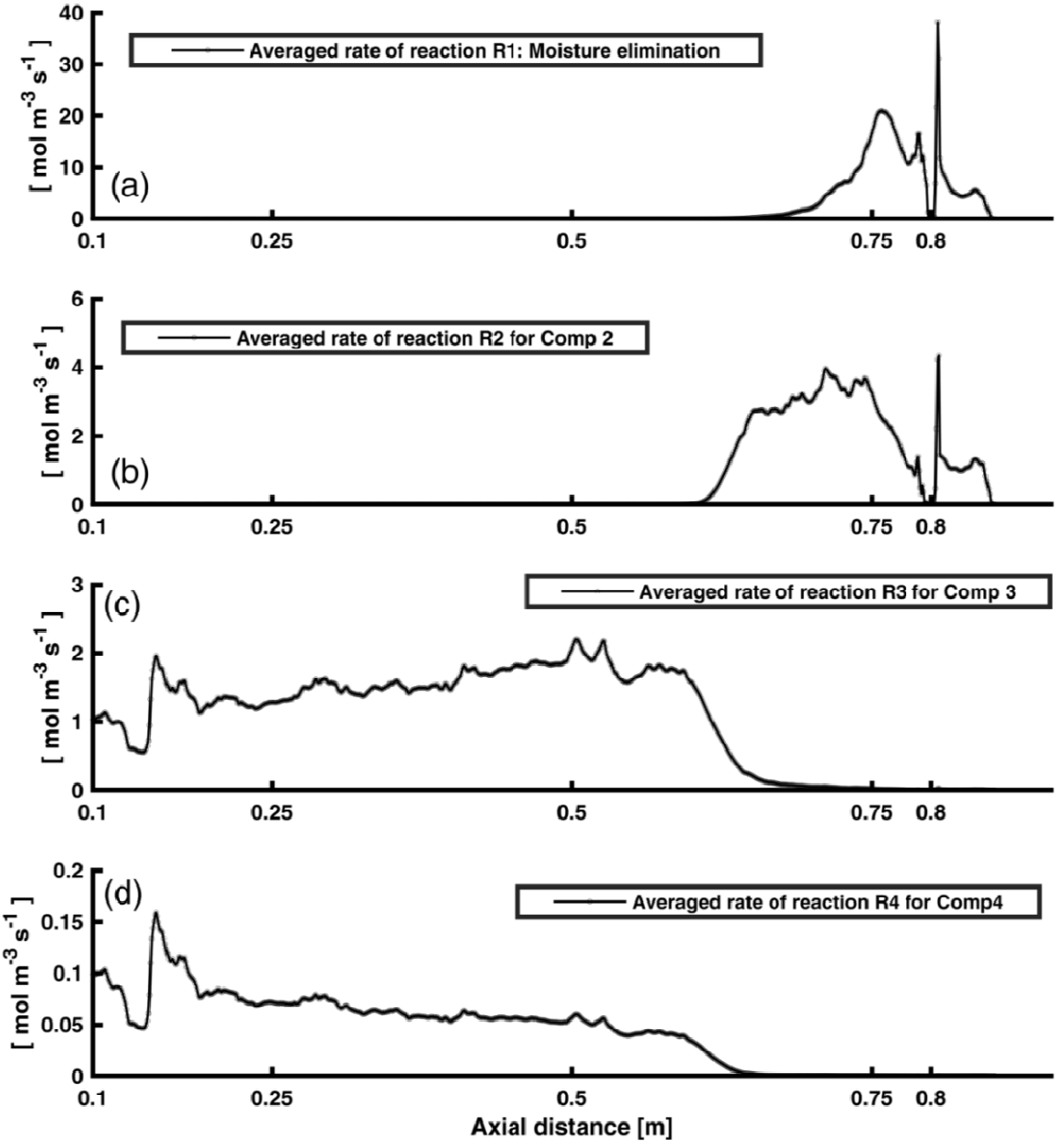

Since Comp 4 has the higher mass fraction in the *Chlorella Vulgaris* specie, 50.8% of the total mass in wet basis, the overall conversion is largely influenced by temperature and subsequently from the transport processes. Apart from the hypothesis and the current analysis, it its worth to mention also the following. In Figure 96 it is also possible

to see the steps of microalgae devolatilization distributed in space, which is one of the main reasons in describing the process with a multi-step reaction mechanism when it is combined with a hydrodynamic simulation. This feature of the chemistry scheme developed in this study is of much importance due to the fact that it helps the design of process or fast pyrolyzers units and also allows the heat balance in order to assess for example the feed-back of energy from the combustion of char.

Continuing in the same Figure 96 and as expected, moisture is eliminated much earlier inside the reactor in the first 10 centimeters. Comp 2 that can be attributed to carbohydrates are eliminated earlier and it is depleted at 0.6 m. The reaction rates of comp 3 and comp 4 effectively start near 0.60 and 0.65 m respectively, however, it tends to evolve to a constant reaction rate owing the lower temperature. In consequence, these components are poorly devolatilized.

Figure 97 shows the radial distributions of Solid phase temperature and Solid phase volume fraction at different positions along the *x* direction. As can be seen in charts where the solid volume fraction is higher, the temperature is lower, suggesting local energy consumption by reactions. A gradient of temperature is also presented on the left side of the charts due to the fact that there is a heat transfer from the gas phase that flows on the axial stream core in counter flow configuration.

Heat transferred from the gas phase also contributes to devolatilization and the mixing causes a decrease in temperature. On the other hand, near the wall, the temperature gradient is higher. This gradient can enhance the conductive heat transfer from the walls, nonetheless for fast pyrolysis, the molecular mechanism alone is not enough to sustain the process in short time intervals. For a distance from 3.6 to 4.0 mm from the symmetry line, the radial velocity fluctuations are very low as can be seen in Figure 95 limiting the energy transfer due to the significant momentum loss near the boundary.

It is worth to note that Figure 97 reveals that the concentration of particles in the wall is lower than in the middle zone of the solid flow. This feature seems to be unrealistic because the force of gravity should tend to agglomerate more particles in this zone. This fact suggests that the study of the rheology requires greater attention.

Figure 97 – Radial distribution of solid volume fraction and Solid temperature at elapsed time t = 2.36 [s].

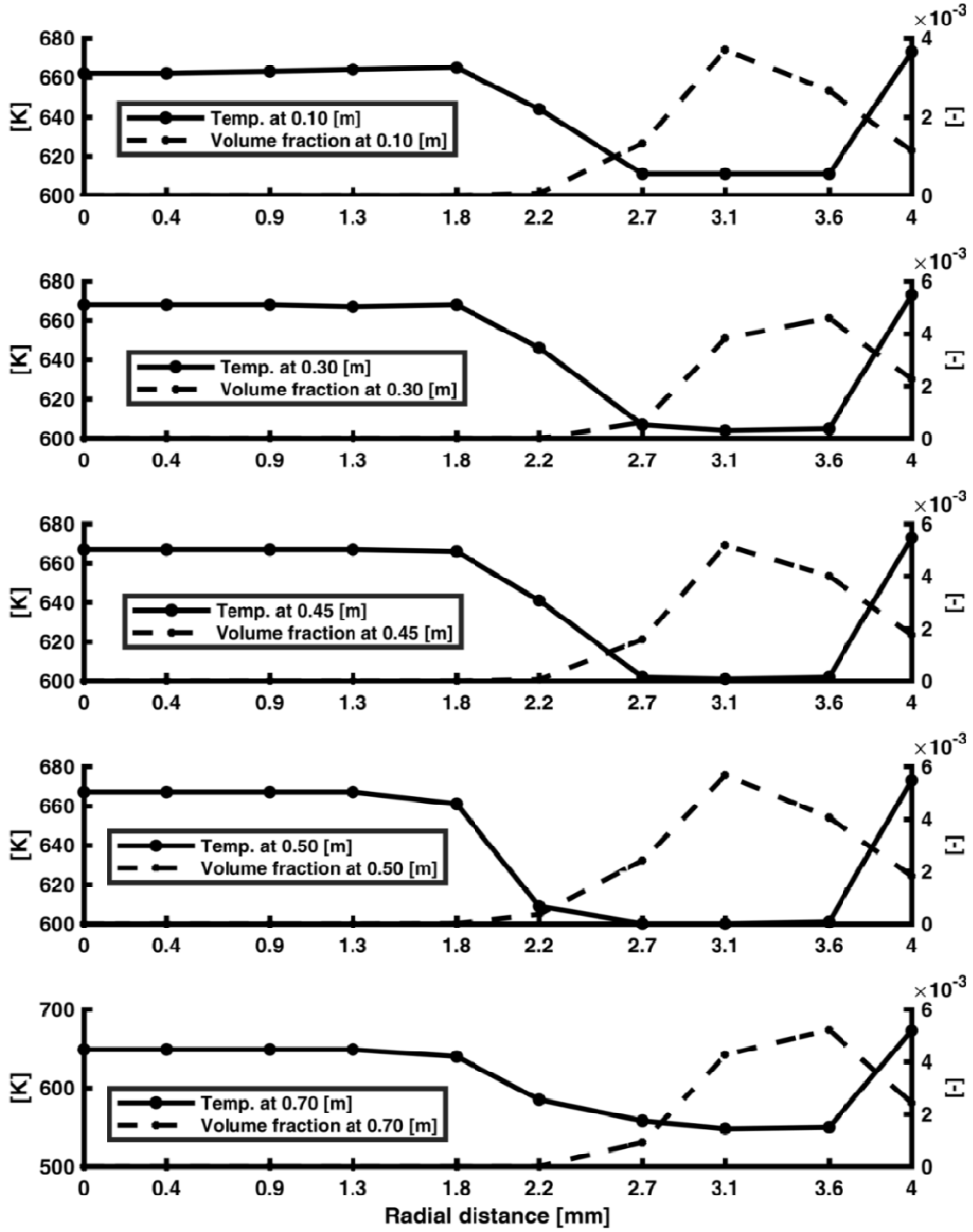

Finally, Figure 98 shows the absolute mass fraction of Char calculated performing the product of the Solid volume fraction with the Solid phase mass fraction of char. This Figure shows that the higher concentration of char is in a zone where the temperature is lower. The latter fact implies that the energy consumed by devolatilization in an interval

Δr = [1.8 mm, 4.0 mm] is not supplied at a fast enough rate to maintain the process temperature and therefore, the rate of reaction of components with higher activation i.e. Comp 3 and Comp 4, are not fast enough in being able to produce a higher biomass conversion. However, there is no enough evidence to attribute this behavior to the mass transport process due to an inadequate selection of granular parameters.

Figure 98 – Radial distribution of Absolute char mass fraction and Solid temperature at elapsed time t = 2.36 [s].

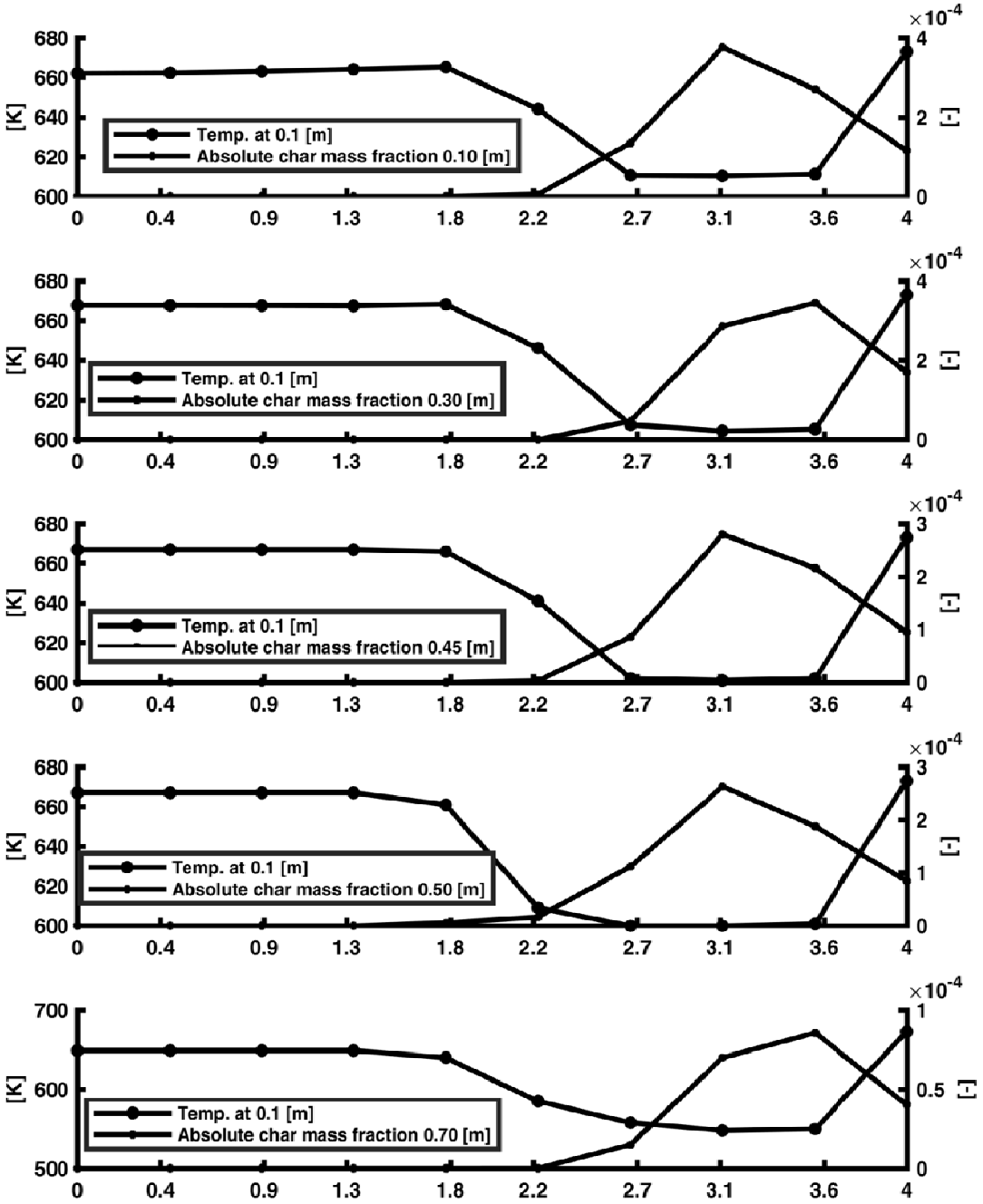

Also, the local decrease in temperature due to devolatilization is caused by the endothermic heat of reaction that depends of the heat of formation calculated for pseudo-components. If the heat of reaction is excessively high it can produce also a large decrease in local temperature. As was explained in the methodology section, the enthalpy of formation was calculated starting from literature values of pyrolysis of carbohydrates, proteins and lipids. Considering that the literature values of heat of reaction used here are similarly to those for lignocellulosic biomass (as can be seen in Mellin; Kantarelis and Yang (2014)) the energy balance for reactions are well bounded in a range typically for thermal decomposition for biomasses and can be discarded as reason of the lower conversion obtained in simulations.

Since the hypothesis of a weak mass transfer could not be discarded so far an a additional simulation was performed in order to evaluate the influence of the granular parameters at the wall on the transport processes.

5.3.3.3. ANALYSIS OF GRANULAR TEMPERATURE EFFECTS

An additional simulation was performed, changing the specularity coefficient and the particle-wall restitution coefficient to 0.1 and 1, respectively in order to reduce the momentum dissipation near the walls and thus promoting the radial transport of mass and heat. All the other simulation parameters were held constant. Flow time for this simulation was 1.24 seconds. From here on in, results of the first simulation are identified as a *reference* and the simulation results of the current new calculations will be identified as the *modified* values.

Figure 99 shows the spread of the solid phase in the domain for the reference and modified simulations. Reference simulation shows a wider spread in axial direction while less spread in the radial direction. Driving force in promoting the motion is the gravity and results on Figure 99 suggest that the kinetic energy of the flow provided by this source is more preferably distributed in the axial direction for the reference simulation than in the modified simulation. Therefore, radial velocity may be higher in the modified simulation, thus incrementing mass transport in this direction.

Figure 99 – Solid volume fraction from x = 0.40 m to x = 0.55 m for reference and modified simulations at t = 1.24 seconds. (a) reference; (b) modified

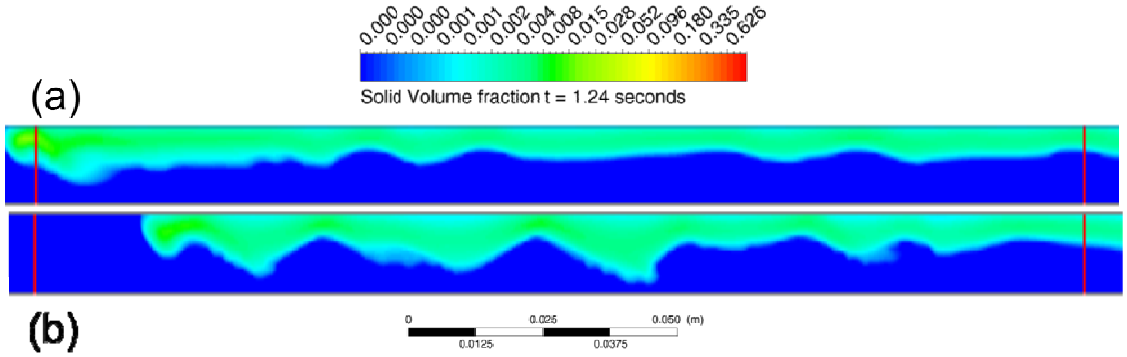

*Red line at left is for x = 0.40 m and; red line on the right is for 0.55 m.

Figure 100 and 101, show a comparison between the reference and modified results for the radial velocities and granular temperature at 0.2 mm (r = 2 mm) from the wall respectively. Figure 100 confirms that the radial velocity magnitude is higher in the modified simulation than the radial velocity in the reference simulation. Figure 100 also shows a preferred higher radial velocity magnitude in the negative *y* direction, toward the symmetry line. Higher radial velocity promotes a higher spread of the solid phase in this direction for the modified case as a result of the lesser momentum dissipation at the walls.

Figure 100 – Axial distribution radial velocity for reference and modified simulation at t = 1.24 seconds.

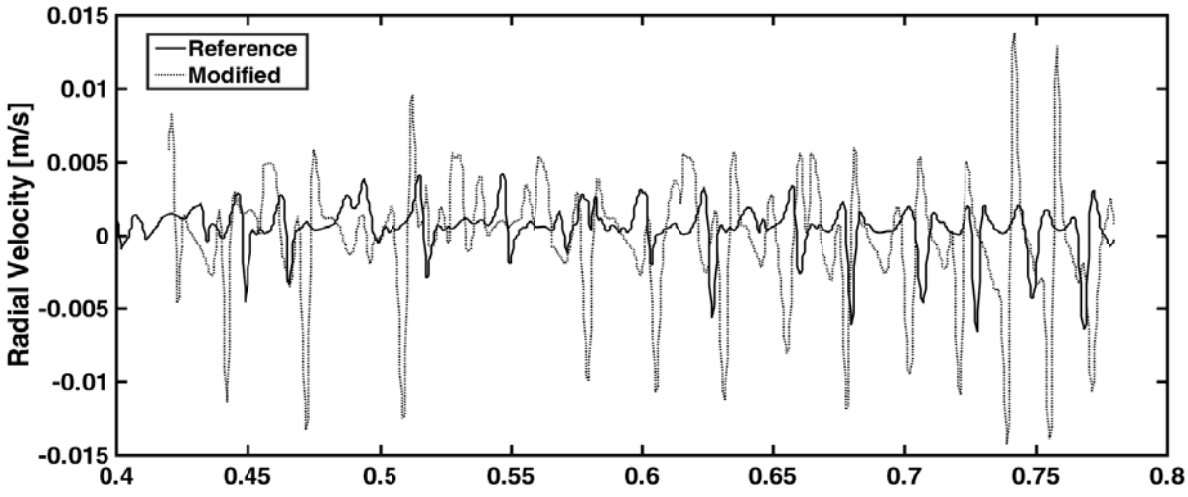

Figure 101, shows the granular temperature at the same distance of 2 mm from the reactor wall. Chart shows a significantly higher intensity of the random motions of particles resulting in a higher radial velocity for the modified case. It is worth to note that

the axial frequency of the radial velocity is similar in both cases. The net effect of the changes in the parameters specularity coefficient and particle-wall restitution coefficient has produced an increase in the solid mass transport in the radial direction, as can be seen in Figures 100 and 101, revealing the significant influence of these parameters on the flow characteristics.

Figure 101 – Axial distribution Granular temperature for reference and modified simulation at t = 1.24 seconds.

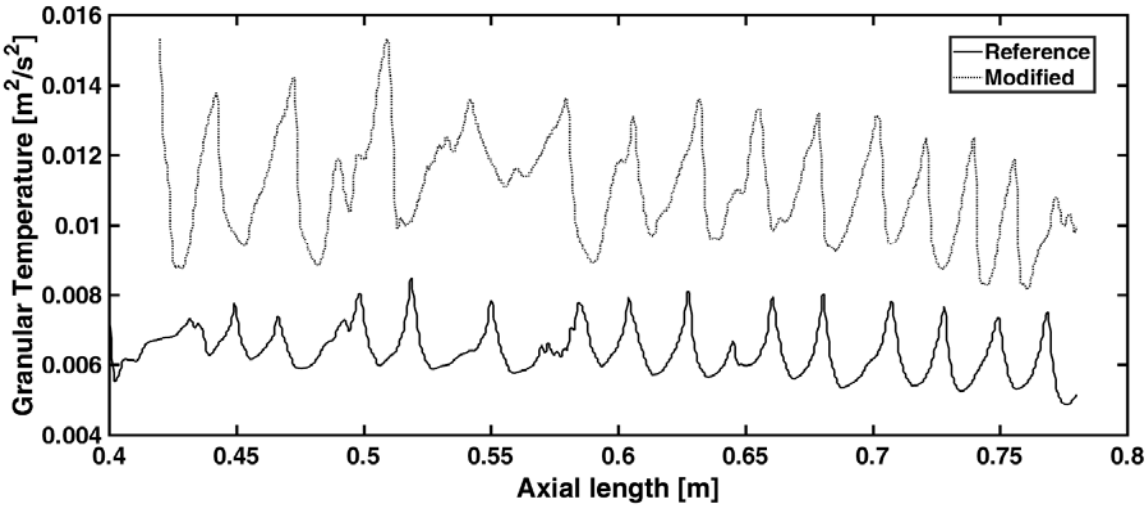

Despite of the increase in intensity of the granular temperature and the radial velocity, the particle layer immediately adjacent to the wall, still offers the same thermal resistance because in this zone, the heat transfer is mainly controlled by the thermal conductivity.

Figure 102 – Axial of Wall heat flux for reference and modified simulation at t = 1.24 seconds.

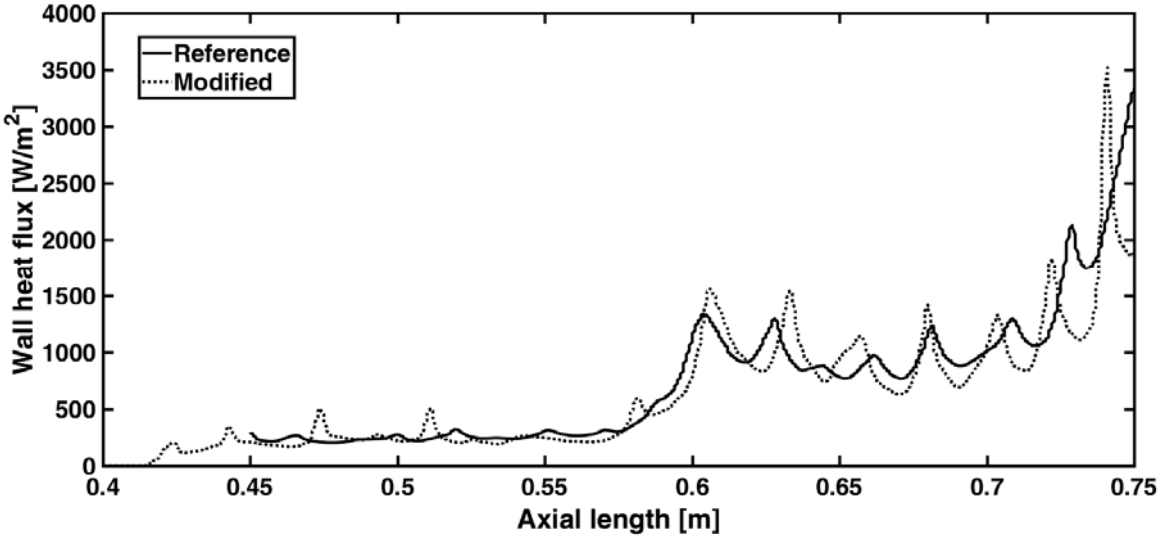

This can be clearly seen in Figure 102, where it is possible to see the same profile of heat flux on reactor walls. The latter evidence shows that considering a rheology that implies less dissipation of momentum in the wall does not radically influence heat transfer from the wall, and consequently, the energy available for the chemical reactions is the same.

Figure 103, shows the places and the intensity of the rate of reaction of R2. First, it can be verified that the reaction rate is similar for the two cases, with a maximum reaction rate close to 13 mol/m^3/s. Second, the increase in the intensity of the velocity in the radial direction produces oscillations with higher amplitudes in the modified case compared with reference case.

Figure 103 – Reaction rate intensity for R2 reaction for reference and modified simulation at t = 1.24 seconds. Red line on the right denotes the biomass inlet.

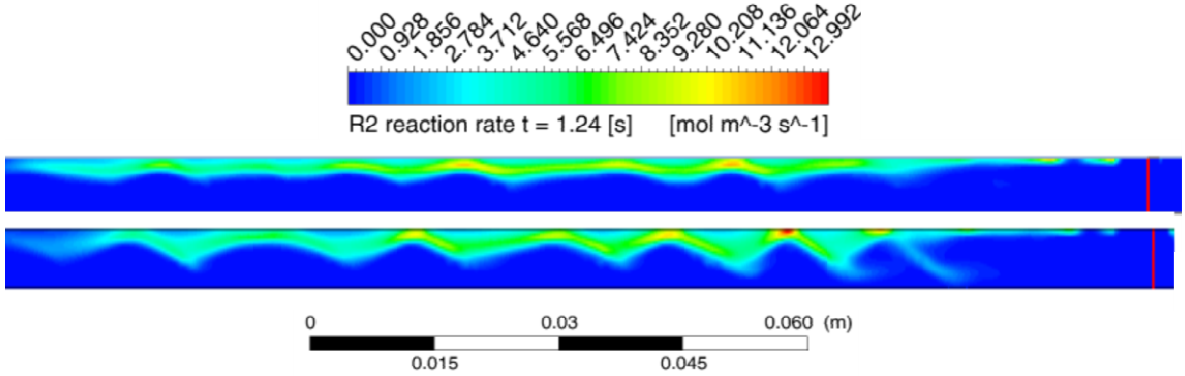

This implies that the decrease in the momentum dissipation causes in consequence a lesser contact with the reactor walls. The foregoing can be clearly seen in Figure 104, where the reaction rate of R2 close to the reactor walls presents large oscillations changing from very high reaction rates to rates significantly lower than those in the reference case.

It can also be observed that only at the beginning, near the biomass inlet at x = 0.8 m, the reaction rate is higher for the modified case, however, the magnitude of the spikes of reaction rate is similar in both cases starting from x = 0.73 m in where the contact of the particles with the wall decreases as a result of the increase in the amplitude of the oscillations.

Figure 104 – R2 rate of reaction at the reactor walls (r = 4 mm) for reference and modified simulation at t = 1.24 seconds.

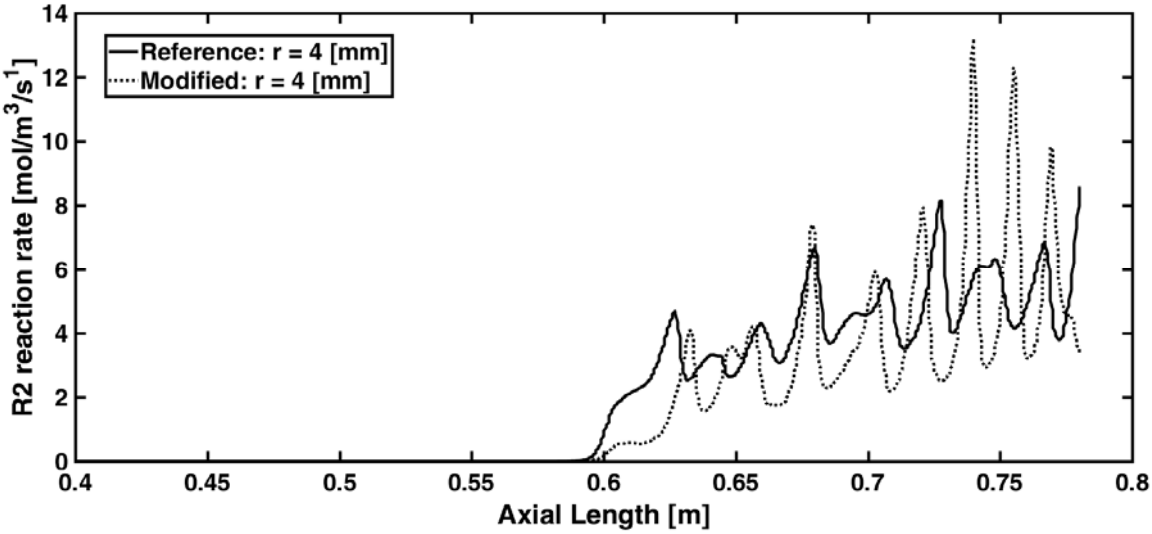

Figure 105, shows the profile of the reaction rate R2 in the axial direction at a 2 mm from the wall. The lower dissipation of momentum results in an increase in the reaction rate of R2 in the modified case while the oscillations are similar in both cases. This shows the improvement of the mass transfer due to the changes in granular parameters at the wall.

Figure 105 – R2 rate of reaction at r = 2 mm for reference and modified simulation at t = 1.24 seconds.

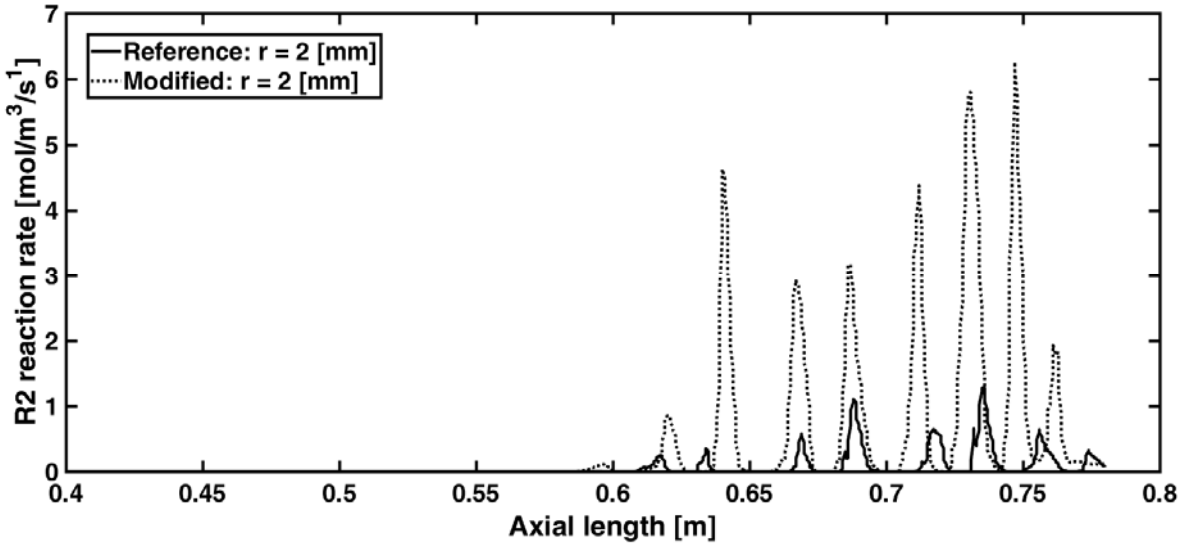

In summary, changes in the parameters, specularity and restitution coefficients result in an increase in the maximum reaction rates but also in a decrease in the minimum reaction rates. To verify the overall effect, the specific average reaction rate and the overall reaction rate must be calculated. Table 53, shows these features in both cases.

As can be seen in this Table, the specific heat flux is higher for the modified case; however, the total heat power is practically the same in both cases, therefore, the energy available to decompose the biomass is the same.

Table 54 – Specific and averaged values for heat flux, heat power, reaction rate and averaged temperature for reference and modified simulations at t = 1.24 seconds.

	Average Wall heat flux [W/m^2]	**Total Wall heat power [W]**
Reference	939.8	20.12
Modified	949.9	20.34
	Average R2 reaction rate [mol/m^3/s]	**R2 total reaction rate [mol/s]**
Reference	0.610	2.61E-5
Modified	0.584	2.50E-5
	Average Solid Temperature [K]	
Reference	625.9	
Modified	622.0	

Averaged reaction rate of R2 is higher for the reference case; however, the total reaction rate is very similar in both cases. This can be explained because of the average temperature of the solid phase, that for the reference case, it is slightly higher, as can be seen in Table 54.

In summary, the change of parameters on the wall has produced an increase in mass transport in the radial direction, causing a greater dispersion and a decrease in the averaged temperature of the solid phase. In turn, the reaction rate of R2, and the other reactions, have increased its maximum reaction rate but also decreased the minimum rate, compensating both effects resulting in a similar global reaction rate, all because the heat power from walls is practically the same in both cases.

Although the average temperature of the solid phase is 625 K at t = 1.24 seconds for th reference case, the average temperature in where the highest concentration of particles is found is lower, as can be seen in Figure 97. The average temperature of the solid phase in the axial direction in the interval r = [2.7, 3.6] mm is 584 K. Figure 106, shows the solution of the rate equation R4 with kinetic parameters of E = 254 kJ/mol/K and A = 1E20 1/s at constant temperature equal to 548 K.

Calculations were made performed using the Lagrangian equation. These results clearly show that reaction R4 does not evolve at a fast enough rate at 584 K in order to produce a significant conversion. In fact, sub-chart (b) shows that the conversion considering 2.5 seconds is very low near 0.5%. However, Figure 96, shows a significant rate of reaction compared with the 0.5%, but it is due to the fact that reaction R4 is calculated with the Eulerian rate equation giving a higher reaction rate. Figure 106, shows the rate of reaction for R4 considering a constant temperature of 673 K.

Figure 106 – R4 conversion at constant temperature T = 584 K.

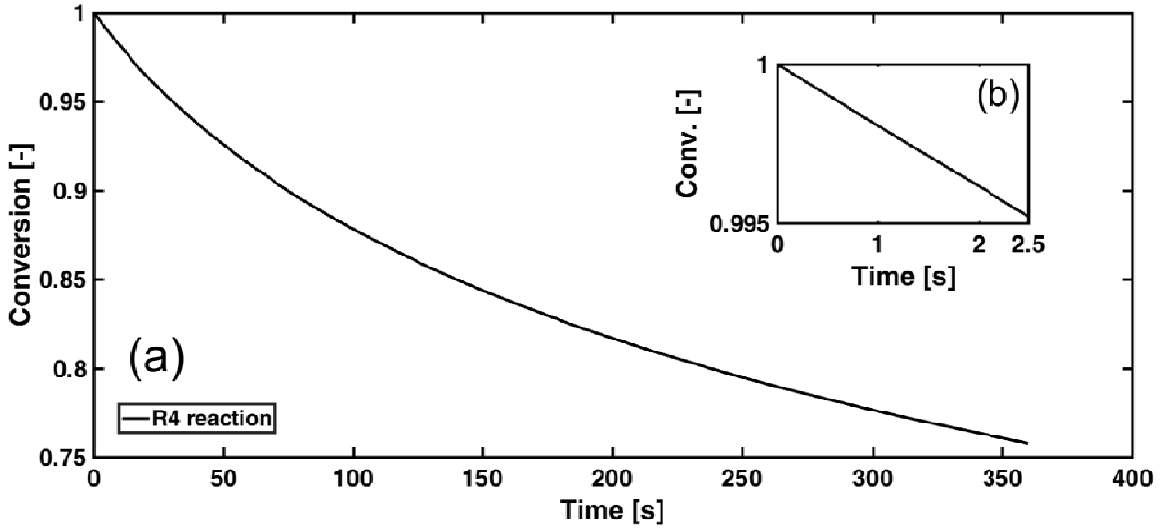

Figure 107 – R4 conversion at constant temperature T = 673 K.

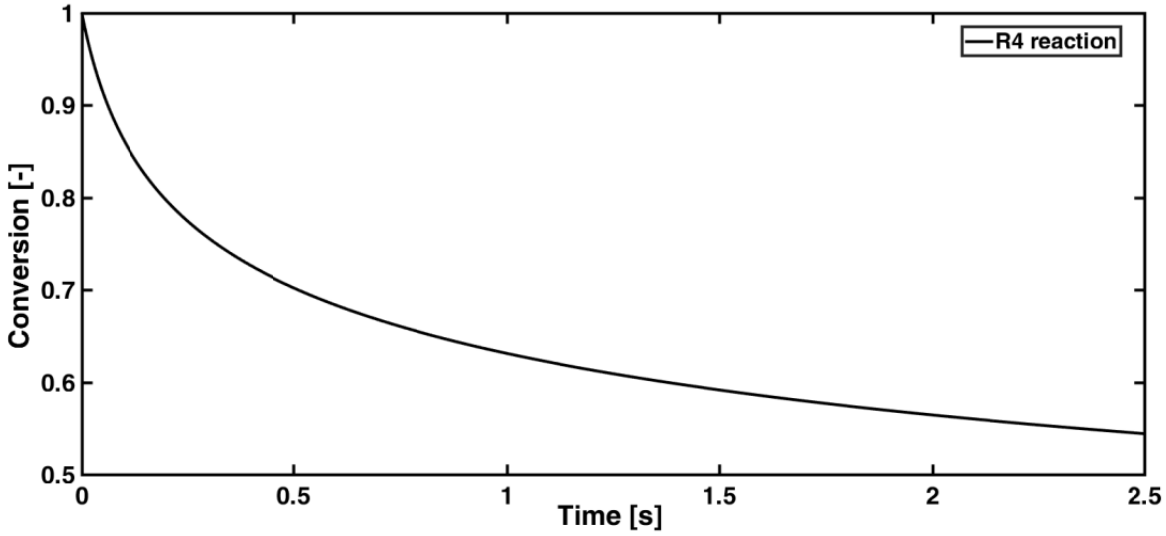

As can be seen in Figure 106, the rate of reaction of R4 is significantly higher at 673 K and the conversion can reach 55% between 2 and 2.5 seconds.

Analyzing the results, again is necessary to comment that the experimental temperature of 400 ° C (673 K) applied in the experiments of Belotti et al (2014) was reproduced in the present simulation as a boundary condition applied to the reactor wall. The foregoing was due to the fact that the author did not specify in methodology the place where the temperature was measured. The last information is important because the response of an automatic control will be different if the temperature is measured on the reactor wall or for example, immersed on the gas flow. The response of an automatic control also depends on the internal energy accumulated by the reactor and must be taken into account. If the internal energy of the reactor is large compared to the energy required for reactions and to increase the temperature of the gases and biomass, then, it would not be necessary to significantly increase the wall temperature. On the other hand, if the thermal resistance offered by the particle layer formed on the reactor wall is significant, the measured flow temperature would be lower and the automatic control would have to react increasing the temperature of the reactor wall possibly at a temperature higher than that of set point temperature, increasing the heat flow to the biomass. In view of this fact, new simulations must be carried out in the future, considering the average temperature of the biomass as the reference temperature and defining the wall boundary condition as an additional variable in time and along the axial direction in order to provide the heat flux necessary to reach experimental temperature.

This simulation was not carried out in the present work, nonetheless an additional simulation was performed with a higher wall temperature of 773 K, with the same parameters of the reference case in order to evaluate the effect of the wall boundary condition on the mass conversion.

5.3.3.4. ANALYSIS OF WALL TEMPERATURE EFFECTS

The simulation considering a wall temperature of 773 K is identified as the wall modified case while the comparison is made with the same reference case. As mentioned before, all the simulation parameters different than the wall temperature is the same as the reference case and using the finer grid 1. Figure 108 depicts the advance of the volume fraction tip at t = 1.24 seconds. As can be seen in the Figure the axial position for both cases is practically the same, being the difference attributed to the wall temperature.

The thickness of the volume fraction is different than the modified case discussed in section 5.3.3, however similar than the reference case.

Figure 108 – Comparison of volume fraction distribution between reference and wall modified cases.

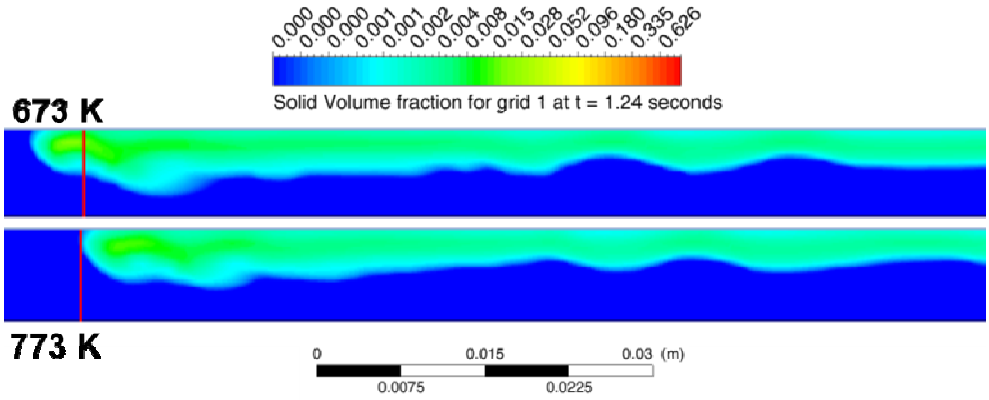

*Red line indicate the axial position of x = 0.4 m

Figure 108 evidences that for the same wall granular parameters but with different wall temperature the axial transport of mass is not significantly affected, however a detailed analysis may be performed in future simulations. Figure 109 shows the axial distribution of rate of reaction of R1, R2, R3 and R4 at the wall in r = 4 mm.

In this Figure is very clear, in general, the influence of wall temperature on the rate of reaction of all pseudo-components. For the case of moisture elimination, the axial profile of the reaction rate is similar in both cases, almost completely consuming this pseudo-component at x = 0.7 m. However, both the maximum and the minimum reaction rates in the first 3 cm from the inlet of biomass into the reactor is significantly higher. Therefore the moisture is completely eliminated from the biomass at x = 0.7 m for the wall modified case. Reaction R2 shows a significant change due to the change in wall contour condition. As can be seen in Figure 109 the reaction rate is consistently higher in the first 2 cm of the reactor, which has as a consequence that comp 2 is completely devolatilized around x = 0.70 m. Reaction R3 shows two significant changes. The first is that the devolatilization reaction begins 10 cm earlier in the wall modified case. While the second difference is that in general the consumption rate of Comp3 is higher for the wall modified case. Which in general would imply a greater conversion for the second most important pseudo-component of the microalgae. The component Comp 4 is the most important in the microalgae, which has been attributed to proteins. In the reference

case, the reaction rate of this pseudo-component was low and therefore did not contribute significantly to the overall conversion. However, as can be seen in the Figure, the pseudo-component 4 begins its devolatilization 10 cm before and with a significantly higher rate in the wall modified case compared to the reference case.

Figure 109 – Comparison of axial reaction rates distribution at walls (r = 4 mm) between reference and wall modified cases.

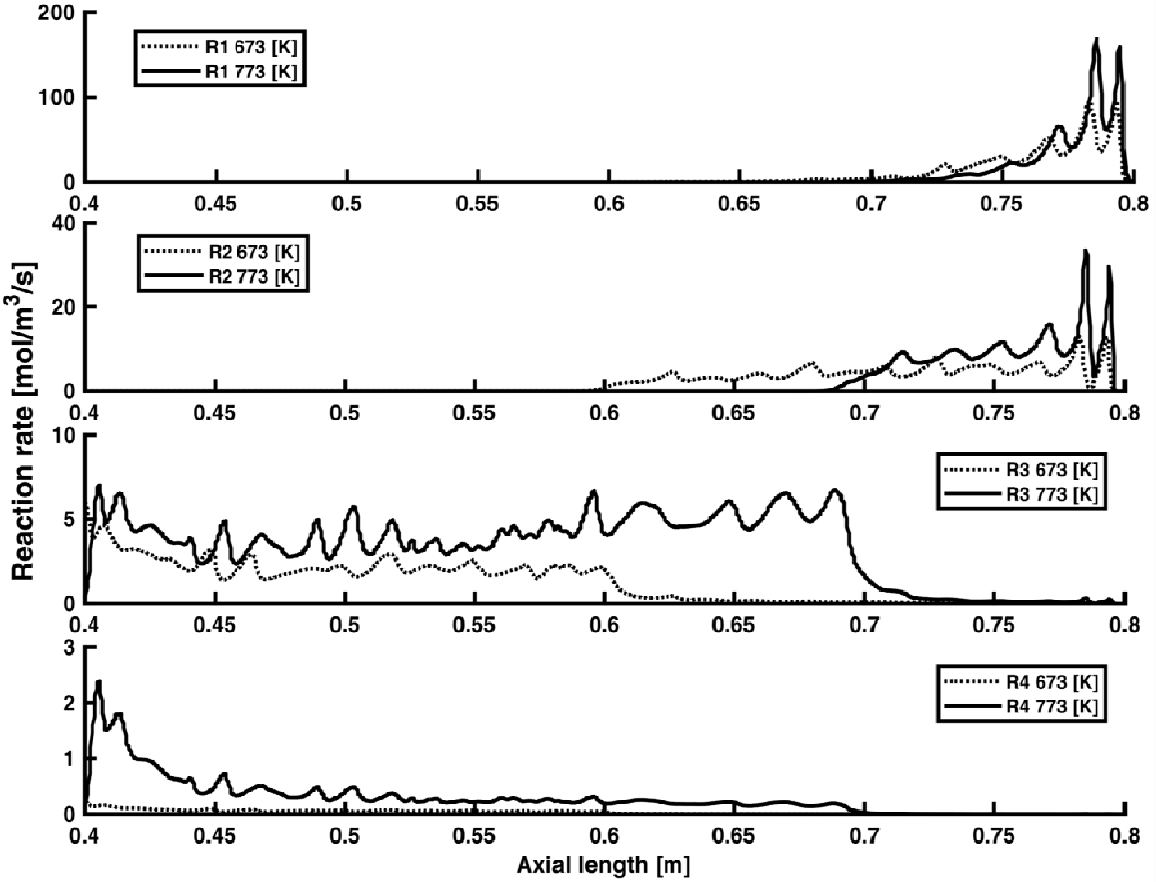

In order to evaluate the overall influences of the wall temperature in Table 55 are presented several averaged and total values of heat flux and reaction rates.

As can be seen in the Table, both the heat flow and the power is greater for the wall modified case as expected. The most important information presented in this table is the volumetric reaction rate and the total reaction rate for pseudo-components 3 and 4. As can be seen in the table, the volumetric reaction rate for both components is an order of magnitude greater for the wall modified case and the total reaction rate of the pseudo-component 4 is an order of magnitude greater for the same case. As a consequence,

the biomass conversion at t = 1.24 seconds is 51% higher due to the averaged temperature largely higher in the wall modified case.

Table 55 – Specific and averaged values for heat flux, heat power, reaction rates, averaged temperature and biomass conversion for reference and wall modified simulations at t = 1.24 seconds.

	Average Wall heat flux [W/m^2]	**Total Wall heat power [W]**
Reference	939.8	20.12
Wall modified	1154.0	24.70
	Average R2 reaction rate [mol/m^3/s]	**R2 total reaction rate [mol/s]**
Reference	0.609	2.61E-5
Wall modified	0.601	2.57E-5
	Average R3 reaction rate [mol/m^3/s]	**R3 total reaction rate [mol/s]**
Reference	0.534	2.29E-5
Wall modified	1.317	5.64E-5
	Average R4 reaction rate [mol/m^3/s]	**R4 total reaction rate [mol/s]**
Reference	0.014	6.21E-7
Wall modified	0.115	4.91E-6
	Average Solid Temperature [K]	
Reference	625.9	
Wall modified	699.8	
	Biomass conversion [%]	
Reference	11.7%	
Wall modified	17.7%	

The analysis of the results presented and discussed in this Chapter are sufficient in order to come by with conclusions about the effectiveness of the reaction mechanism developed in this work and for the determining the causes of the low conversion observed Considering the effects of the granular parameters on the wall and the effect of the average reaction temperature, and considering also that, kinetically, the reaction mechanism predicts well the conversion at a higher heating rate, it is evident that the average temperature of the reactor is the factor that exerts the greater influence in the global conversion of biomass.

6. CONCLUSIONS

This doctoral research was started with the objective of developing an engineering tool in order to assess the applicability of the fast pyrolysis for the *Chlorella Vulgaris* microalgae in the concept of the BioRefinery scheme. The approach chosen was the mathematical modeling of the chemical kinetics from the TG and DTG thermal analysis thus providing a sub-model applicable in the use of computational fluid dynamics. The fact that this work is related to a doctoral research is because, in the scientific literature, there are no complete or usable reaction mechanisms for fast pyrolysis of microalgae biomass for the use in CFD applications. This was evident in the discussion where the first scientific reports about the topic had been analyzed and compared with the current work, outlining the differences in the obtainment of the kinetic parameters and concluding that the direct application of the cited works in CFD is not straightforward. Furthermore, a fundamental difference with the partial reaction mechanisms for microalgae reported in the literature is that the scheme developed here preserves the value of the effective activation energies determined by the iso-conversional method thus giving a proper realistic characteristic inherent to the devolatilization process without excessive parameter compensation.

Due to this lack of reaction mechanisms reported in the literature, in general for microalgae biomasses, and in the requirement of such mathematical models to study the fast pyrolysis in CFD, this work specifically proposed the construction of a multi-stage global reaction mechanism for devolatilization of *Chlorella Vulgaris*. As a result, a good agreement was achieved comparing the experimental TG and DTG data performed at different heating rates, for the mass loss and mass loss rate. Thus, with additional development, this work can provide the tool to start parametric studies in continuous fluidized bed reactors (CFB) in order to evaluate: final char, gas released, temperature distribution, energy requirements, residence time, particle distribution and velocity profiles.

In relation with kinetics itself, the TG and calculated DTG has shown a complex thermal decomposition in three stages with four zones in the main devolatilization stage two. Under the light of the evidence presented in Chapter 5 and considering the order of the reaction model and the values of the pre-exponential factor found it is possible to conclude that zones 2, 3, 4 and 5 are composed by more than one single step reaction,

being difficult to make an accurate prediction with only basic simple Mampel's reaction model. Nonetheless, in the case of moisture elimination, the second order model listed in Table 26 fits very well the experimental data, suggesting that this zone is dominated by a single one step reaction of order two. Other features can be mentioned here as conclusions. First, the mechanism accounts for the characteristic shift as a function of temperature commonly observed in the thermal decomposition of complex materials. Secondly, the multi-stage feature and the knowledge of the *Chlorella Vulgaris* components identified in this work, allow the design reactors or processes with a specific focus on any of the components or its devolatilized products. The latter immediately calls the attention for further development in the direction of identifying in detail the different components released during the pyrolysis. Closing this paragraph it is worth to remark that the reaction mechanism developed here has wide applicability and a straightforward implementation in software for chemical kinetics due to the use of the Arrhenius parameters. However, and for future developments, the chemical kinetic description is not closed because of the fact that it is necessary to known related physical properties of biomass and discriminate the condensable from the non-condensable gases identifying its particular kinetic parameters, parallel competitions with the char production; and at least an averaged compounds distribution.

The second part of this work has shown that the direct application of the reaction mechanism in CFD is possible and thus coupling the hydrodynamics. In order to complete this objective, first, the reaction mechanism was adapted from its Lagrangian version to the Eulerian form to be applied in the heterogeneous reactions module of ANSYS Fluent 19.0. This transformation implied the loss of the order of the reaction model (the *n* parameter of eq.(192)), causing in turn also the loss of the shape of the curve of the reaction rate and a significant increase of it. However, this technical detail is completely solvable by developing an UDF script in ANSYS Fluent 19.0 incorporating the characteristic reaction order to simulations.

Before the analysis of results, the GCI was calculated for 3 different meshes calculating the effective grid lengths based on the averaged cell areas. Then and based on the effective length, the simulation order of convergence was calculated for the following relevant variables: Solid volume fraction, Solid temperature, Char mass fraction and reaction rates for Moisture, Comp 2 and Comp 3. GCI was determined based on the

volume averaged values of these field variables for an elapsed time equal of 2.36 seconds. Results from the grid convergence study show an oscillatory convergence for all variables except for the rate of reaction of Comp 2. GCI determined here gives a value below 5% for Solid temperature, Char mass fraction and Comp 2 and Comp 3 reactions rates, while 9.19% for Solid volume fraction and 6.03% for moisture reaction rate. The conclusion of the analysis is that the smaller grid length is sufficient to achieve accurate results in order to analyze the reaction mechanism. However, local refinements are necessary in order to reduce the GCI of the Solid Volume fraction.

The analysis of results was performed by processing the data provided by the use of the mesh with the smaller grid length and was started by the calculation of the biomass conversion using the reactor model and process parameters described in methodology. A conversion of biomass of 17.8% was achieved in simulations calculated when the initial tip of solid stream reached the reactor bottom in an elapsed time of 2.36 seconds. The value of biomass conversion deviates significantly from the values reported in the literature i.e. between 56 to 75%. The evidence exposed and discussed in Chapter 5 suggests two main conclusions about this result. First, the simulated devolatilization process is not controlled kinetically and the reaction mechanism behaves well for high heating rates. Second, the local solid temperature, as expected, plays a fundamental role affecting the rate of reaction which in turn is strongly determined by the wall boundary condition and to a lesser extent from the rheology parameters of the granular model not known for the *Chlorella Vulgaris* powder.

First conclusion is supported by the energy-independent calculations and analysis performed solving only the set of rate equations considering a perfect stirred reactor model. These calculations have shown that the biomass conversion at 400°C can achieve values very close to those reported in the literature, and the error range observed can be attributed to the microalgae composition and to the averaged process temperature.

In the light of evidence, and discarding the chemical kinetic effect, the analysis performed in the final part of Chapter 5 has shown that the significant difference between the conversion obtained in this simulation and the experimental results obtained by Belotti et al. (2014) are not due to the kinetics predicted by the reaction mechanism. Instead,

the low conversion observed in simulation is caused by the low temperature in the area where the concentration of biomass particles is higher. This low temperature is due to boundary temperature conditions at the reactor wall, and to a lesser extent caused by the rheological properties of the solid phase defined in the simulation. The transfer of heat from the wall depends, in part, on the thermal conductivity of the particles. The value used in this simulation was 0.173 W/m/K the default value for wood in ANSYS Fluent 19.0. The value for this property is even higher, one order of magnitude, than the one for carbohydrates, proteins and lipids, but still within the expected value for biological materials. A higher value could be used in future simulations considering the value of 0.3 W/m/K given by Xiong et al. (2014) for cellulose. However, the heat transfer should not be noticeably different because the Fourier equation is linear with respect to thermal conductivity and the value of cellulose is only 42.3% higher. Heat transfer in a multi-phase flow depends also on volume fraction of the particle phase, therefore, depending on the rheology. By observing Figure 97, it is possible to verify that the concentration of particles on the wall is lower than that in the middle zone of the solid flow. This feature seems to be unrealistic because the force of gravity should tend to agglomerate more particles in that zone, and therefore, the study of the rheology requires greater attention to better developing the application of the reaction mechanism and the study of the pyrolysis in reactors.

As a final conclusion about the low conversion of biomass observed in the reference simulation, is possible to state that the low temperature obtained in the reference simulation is mainly due to the boundary condition for temperature defined for the reactor wall, which was established as a function of the experimental temperature applied by Belotti et al. (2014) i.e. 400°C (673 K). This condition did not allow the average temperature to be high enough in order to activate the R4 reaction and consequently the devolatilization rate of the main pseudo-component of the *Chlorella Vulgaris* was low, as was demonstrated by performing the separate analysis of this reaction. But in addition, the same analysis in turn showed that for an average temperature, equal to the experimental temperature, the aforementioned reaction would significantly be activated in the residence time of 2 seconds yielding a conversion near 55%. In the light of this observation a new simulation was carried out in order to evaluate the influence of the wall temperature in the biomass conversion. As a result, all the reactions showed a significant increase in the reaction rate, but especially the most

important reaction, R4. This significant increase resulted in an increase in the overall conversion of 51%, with respect to the reference case, showing that the reaction mechanism developed in this study is adequate and predicts well the devolatilization of the microalgae and that the average reaction temperature has a greater influence on the total conversion than the rheology of the granular phase.

7. BIBLIOGRAPHY

AGRAWAL, A., & CHAKRABORTY, S. (2013). A kinetic study of pyrolysis and combustion of microalgae *Chlorella Vulgaris* using thermo-gravimetric analysis. Bioresource technology, 128, 72-80.

AHMAD, A. L., YASIN, N. M., DEREK, C. J. C., & LIM, J. K. (2011). Microalgae as a sustainable energy source for biodiesel production: a review. Renewable and Sustainable Energy Reviews, 15(1), 584-593.

ALMEIDA, H. N., CALIXTO, G. Q., CHAGAS, B. M., MELO, D. M., RESENDE, F. M., MELO, M. A., & BRAGA, R. M. (2017). Characterization and pyrolysis of Chlorella vulgaris and Arthrospira platensis: potential of bio-oil and chemical production by Py-GC/MS analysis. Environmental Science and Pollution Research, 24(16), 14142-14150.

ALI, S. A. M., RAZZAK, S. A., & HOSSAIN, M. M. (2015). Apparent kinetics of high temperature oxidative decomposition of microalgal biomass. Bioresource technology, 175, 569-577.

ARSENEAU, D. F. (1971). Competitive reactions in the thermal decomposition of cellulose. Canadian Journal of Chemistry, 49(4), 632-638.

ARSHAD, M. A., MAAROUFI, A., BENAVENTE, R., & PINTO, G. (2017). Kinetics of the thermal degradation mechanisms in urea-formaldehyde cellulose composites filled with zinc particles. Journal of Materials Science: Materials in Electronics, 28(16), 11832-11845.

BANYASZ, J. L., LI, S., LYONS-HART, J., & SHAFER, K. H. (2001). Gas evolution and the mechanism of cellulose pyrolysis. Fuel, 80(12), 1757-1763.

BASU, P. (2010). Biomass gasification and pyrolysis: practical design and theory. Academic press.

BENYAHIA, S., ARASTOOPOUR, H., KNOWLTON, T., & MASSAH, H. (2000). Simulation of particles and gas flow behavior in the riser section of a circulating fluidized bed using the kinetic theory approach for the particulate phase. Powder Technology, 112(1), 24-33.

BELOTTI, G., DE CAPRARIIS, B., DE FILIPPIS, P., SCARSELLA, M., & VERDONE, N. (2014). Effect of *Chlorella Vulgaris* growing conditions on bio-oil production via fast pyrolysis. Biomass and Bioenergy, 61, 187-195.

BLUMREISINGER, M., MEINDL, D., & LOOS, E. (1983). Cell wall composition of chlorococcal algae. Phytochemistry, 22(7), 1603-1604.

BRADBURY, A. G., SAKAI, Y., & SHAFIZADEH, F. (1979). A kinetic model for pyrolysis of cellulose. Journal of Applied Polymer Science, 23(11), 3271-3280.

BRANCA, C., & DI BLASI, C. (2003). Kinetics of the isothermal degradation of wood in the temperature range 528–708 K. Journal of Analytical and applied Pyrolysis, 67(2), 207-219.

BRIDGWATER, A. V., & BOOCOCK, D. G. B. (EDS.). (2013). Developments in Thermochemical Biomass Conversion: Volume 1 (Vol. 2). Springer Science & Business Media.

CABALLERO, J. A., CONESA, J. A., FONT, R., & MARCILLA, A. (1997). Pyrolysis kinetics of almond shells and olive stones considering their organic fractions. Journal of Analytical and Applied Pyrolysis, 42(2), 159-175.

CAREY F., A. (2006). Química Orgánica. Editorial Mc Graw Hill, México.

CELIK, I. B., GHIA, U., & ROACHE, P. J. (2008). Procedure for estimation and

reporting of uncertainty due to discretization in CFD applications. Journal of fluids Engineering-Transactions of the ASME130(7).

ÇENGEL, Y. A., BOLES, M. A., & CÁZARES, G. N. (2006). TERMODINÁMICA (NO. QC311 C4 1996.). MCGRAW-HILL.

CHIA, M. A., LOMBARDI, A. T., & MELAO, M. D. G. G. (2013). Growth and biochemical composition of *Chlorella Vulgaris* in different growth media. Anais da Academia Brasileira de Ciências, 85(4), 1427-1438.

CHISTI, Y. (2007). Biodiesel from microalgae. Biotechnology advances, 25(3), 294-306.

CHOI, S. A., LEE, J. S., OH, Y. K., JEONG, M. J., KIM, S. W., & PARK, J. Y. (2014). Lipid extraction from *Chlorella Vulgaris* by molten-salt/ionic-liquid mixtures. Algal Research, 3, 44-48.

CHOI, S. S., & KO, J. E. (2011). Analysis of cyclic pyrolysis products formed from amino acid monomer. Journal of Chromatography A, 1218(46), 8443-8455.

CHOIX, F. J., DE-BASHAN, L. E., & BASHAN, Y. (2012). Enhanced accumulation of starch and total carbohydrates in alginate-immobilized Chlorella spp. induced by Azospirillum brasilense: II. Heterotrophic conditions. Enzyme and microbial technology, 51(5), 300-309.

COSTA, J. A. V., & DE MORAIS, M. G. (2011). The role of biochemical engineering in the production of biofuels from microalgae. Bioresource technology, 102(1), 2-9.

CUOCI, A., FARAVELLI, T., FRASSOLDATI, A., GRANATA, S., MIGLIAVACCA, G., RANZI, E., & SOMMARIVA, S. (2007). A General Mathematical Model of Biomass Devolatilization Note 1. Lumped kinetic models of cellulose, hemicellulose and lignin. In 30th meeting of the Italian section of the

Combustion Institute.

DAVIS, M. E., & DAVIS, R. J. (2012). Fundamentals of chemical reaction engineering. Courier Corporation.

DE FILIPPIS, P., DE CAPRARIIS, B., SCARSELLA, M., & VERDONE, N. (2015) Double Distribution Activation Energy Model for microalgae pyrolysis.

DEBDOUBI, A., & COLACIO, E. (2005). Production of fuel briquettes from esparto partially pyrolyzed. Energy conversion and management, 46(11), 1877-1884.

DEMIRBAS, A. (2010). Use of algae as biofuel sources. Energy conversion and management, 51(12), 2738-2749.

DI BLASI, C. (1998). Comparison of semi-global mechanisms for primary pyrolysis of lignocellulosic fuels. Journal of Analytical and Applied Pyrolysis, 47(1), 43-64.

DI BLASI, C. (2008). Modeling chemical and physical processes of wood and biomass pyrolysis. Progress in Energy and Combustion Science, 34(1), 47-90.

DI BLASI, C., & BRANCA, C. (2001). Kinetics of primary product formation from wood pyrolysis. Industrial & engineering chemistry research, 40(23), 5547-5556.

DI BLASI, C. (2002). Modeling intra- and extra-particle processes of wood fast pyrolysis. AIChE journal, 48(10), 2386.

DIEBOLD, J. P., & BRIDGWATER, A. V. (1997). Overview of fast pyrolysis of biomass for the production of liquid fuels. In Developments in thermochemical biomass conversion (pp. 5-23). Springer Netherlands.

DIEBOLD, J. P. (1994). A unified, global model for the pyrolysis of cellulose. Biomass and Bioenergy, 7(1-6), 75-85.

DU, Z., HU, B., MA, X., CHENG, Y., LIU, Y., LIN, X., & RUAN, R. (2013). Catalytic pyrolysis of microalgae and their three major components: carbohydrates, proteins, and lipids. Bioresource technology, 130, 777-782.

FERREIRA, A. F., DIAS, A. S., SILVA, C. M., & COSTA, M. (2015). Evaluation of thermochemical properties of raw and extracted microalgae. Energy, 92, 365-372.

FONT, R., MARCILLA, A., VERDU, E., & DEVESA, J. (1990). Kinetics of the pyrolysis of almond shells and almond shells impregnated with cobalt dichloride in a fluidized bed reactor and in a pyroprobe 100. Industrial & engineering chemistry research, 29(9), 1846-1855.

GAI, C., ZHANG, Y., CHEN, W. T., ZHANG, P., & DONG, Y. (2013). Thermogravimetric and kinetic analysis of thermal decomposition characteristics of low-lipid microalgae. Bioresource technology, 150, 139-148.

GIDASPOW, D. (1994). Multiphase flow and fluidization: continuum and kinetic theory descriptions. Academic press.

GONG, X., ZHANG, B., ZHANG, Y., HUANG, Y., & XU, M. (2013). Investigation on pyrolysis of low lipid microalgae *Chlorella Vulgaris* and Dunaliella salina. Energy & Fuels, 28(1), 95-103.

GRIERSON, S., STREZOV, V., ELLEM, G., MCGREGOR, R., & HERBERTSON, J. (2009). Thermal characterisation of microalgae under slow pyrolysis conditions. Journal of Analytical and Applied Pyrolysis, 85(1), 118-123.

HO, S. H., HUANG, S. W., CHEN, C. Y., HASUNUMA, T., KONDO, A., & CHANG, J. S. (2013). Characterization and optimization of carbohydrate production from an indigenous microalgae *Chlorella Vulgaris* FSP-E. Bioresource technology, 135, 157-165.

HU, M., CHEN, Z., GUO, D., LIU, C., XIAO, B., HU, Z., & LIU, S. (2015). Thermogravimetric study on pyrolysis kinetics of Chlorella pyrenoidosa and bloom-forming cyanobacteria. Bioresource technology, 177, 41-50.

HURT, R. H., & CALO, J. M. (2001). Semi-global intrinsic kinetics for char combustion modeling. Combustion and flame, 125(3), 1138-1149.

ISHII, M., & HIBIKI, T. (2010). Thermo-fluid dynamics of two-phase flow. Springer Science & Business Media.

JAKOBSEN, H. A. (2008). Chemical reactor modeling. Multiphase Reactive Flows, Berlin, Germany: Springer-Verlag.

JOHNSON, P. C., & JACKSON, R. (1987). Frictional–collisional constitutive relations for granular materials, with application to plane shearing. Journal of fluid Mechanics, 176, 67-93.

KEBELMANN, K., HORNUNG, A., KARSTEN, U., & GRIFFITHS, G. (2013). Intermediate pyrolysis and product identification by TGA and Py-GC/MS of green microalgae and their extracted protein and lipid components. Biomass and bioenergy, 49, 38-48.

KENT, M., WELLADSEN, H. M., MANGOTT, A., & LI, Y. (2015). Nutritional evaluation of Australian microalgae as potential human health supplements. PloS one, 10(2), e0118985.

KIM, S. S., LY, H. V., KIM, J., LEE, E. Y., & WOO, H. C. Pyrolysis of microalgae residual biomass derived from Dunaliellatertiolecta after lipid extraction and

carbohydrate saccharification. Chemical Engineering Journal, 263 (2015), 194-199.

KOLEV, N. I. (2005). Multiphase flow dynamics 1: fundamentals. Springer.

LIAO, Y. F., WANG, S. R., & MA, X. Q. (2004). Study of reaction mechanisms in cellulose pyrolysis. Preprints of Papers-American Chemical Society, Division of Fuel Chemistry, 49, 407-411.

LIN, R., ZHU, Y., & TAVLARIDES, L. L. (2013). Mechanism and kinetics of thermal decomposition of biodiesel fuel. Fuel, 106, 593-604.

LÓPEZ-GONZÁLEZ, D., FERNANDEZ-LOPEZ, M., VALVERDE, J. L., & SANCHEZ-SILVA, L. (2014). Pyrolysis of three different types of microalgae: Kinetic and evolved gas analysis. Energy, 73, 33-43.

LYON, R. E. (1997). An integral method of non-isothermal kinetic analysis. Thermochimica Acta, 297(1-2), 117-124.

MADDY, B. (2014). Pyrolysis Strategies for Effective Utilization of Lignocellulosic and Algal Biomass. Phd Thesis of University of Toledo – Spain.

MALISKA C. R. (1995). Transferência de calor e mecânica dos fluidos computacional. ISBN 8521613962. 2ª Edição–2004. LTC.

MANYA, J. J., VELO, E., & PUIGJANER, L. (2003). Kinetics of biomass pyrolysis: a reformulated three-parallel-reactions model. Industrial & engineering chemistry research, 42(3), 434-441.

MARONGIU, A., BOZZANO, G., DENTE, M., RANZI, E., & FARAVELLI, T. (2007). Detailed kinetic modeling of pyrolysis of tetrabromobisphenol A. Journal of Analytical and Applied Pyrolysis, 80(2), 325-345.

MARONGIU, A., FARAVELLI, T., & RANZI, E. (2007). Detailed kinetic modeling of the thermal degradation of vinyl polymers. Journal of analytical and applied pyrolysis, 78(2), 343-362.

MELLIN, P., ZHANG, Q., KANTARELIS, E., & YANG, W. (2013). An Euler–Euler approach to modeling biomass fast pyrolysis in fluidized-bed reactors–Focusing on the gas phase. Applied Thermal Engineering, 58(1-2), 344-353.

MELLIN, P., KANTARELIS, E., & YANG, W. (2014). Computational fluid dynamics modeling of biomass fast pyrolysis in a fluidized bed reactor, using a comprehensive chemistry scheme. Fuel, 117, 704-715.

MILLER, R. S., AND J. BELLAN. "A generalized biomass pyrolysis model based on superimposed cellulose, hemicelluloseand liqnin kinetics." Combustion science and technology 126.1-6 (1997): 97-137.

MOLDOVEANU, S. C. (1998). Analytical pyrolysis of natural organic polymers (Vol. 20). Elsevier.

MUÑOZ, R., NAVIA, R., CIUDAD, G., TESSINI, C., JEISON, D., MELLA, R., & AZÓCAR, L. (2015). Preliminary biorefinery process proposal for protein and biofuels recovery from microalgae. Fuel, 150, 425-433.

NASA (2008). Tutorial on CFD Verification and Validation. On line guide https://www.grc.nasa.gov/www/wind/valid/tutorial/tutorial.html.

NEMCOVA, Y., & KALINA, T. (2000). Cell wall development, microfibril and pyrenoid structure in type strains of Chlorella vulgaris, C. kessleri, C. sorokiniana compared with C. luteoviridis (Trebouxiophyceae, Chlorophyta).(With 14 figures in the text). Archiv fur Hydrobiologie-Supplementband Only, 136, 95-106.

OPDAL, O., AND O. SKREIBERG. Production of synthetic biodiesel via Fischer-Tropsch synthesis biomass-to-liquids in Namdalen, Norway project report by Olav A. (2006).

PENG, W., WU, Q., TU, P., & ZHAO, N. (2001). Pyrolytic characteristics of microalgae as renewable energy source determined by thermogravimetric analysis. Bioresource Technology, 80(1), 1-7.

PEREJÓN, A., SÁNCHEZ-JIMÉNEZ, P. E., CRIADO, J. M., & PÉREZ-MAQUEDA, L. A. (2011). Kinetic analysis of complex solid-state reactions. A new deconvolution procedure. The Journal of Physical Chemistry B, 115(8), 1780-1791.

PARK, W. K., MOON, M., KWAK, M. S., JEON, S., CHOI, G. G., YANG, J. W., & LEE, B. (2014). Use of orange peel extract for mixotrophic cultivation of *Chlorella Vulgaris*: Increased production of biomass and FAMEs. Bioresource technology, 171, 343-349.

RAHEEM, A., SIVASANGAR, S., AZLINA, W. W., YAP, Y. T., DANQUAH, M. K., & HARUN, R. (2015). Thermogravimetric study of Chlorella vulgaris for syngas production. Algal Research, 12, 52-59.

RAHEEM, A., DUPONT, V., CHANNA, A. Q., ZHAO, X. VUPPALADADIYAM, A. K., TAUFIQ-YAP, Y. H., & HARUN, R. (2017). Parametric Characterization of Air Gasification of *Chlorella Vulgaris* Biomass. Energy & Fuels, 31(3) (2959-2969).

RANZI, E., CUOCI, A., FARAVELLI, T., FRASSOLDATI, A., MIGLIAVACCA, G., PIERUCCI, S., & SOMMARIVA, S. (2008). Chemical kinetics of biomass pyrolysis. Energy & Fuels, 22(6), 4292-4300.

REN, Q., ZHAO, C., CHEN, X., DUAN, L., LI, Y., & MA, C. (2011). NOx and N_2O precursors (NH_3 and HCN) from biomass pyrolysis: co-pyrolysis of amino acids and cellulose, hemicellulose and lignin. Proceedings of the

Combustion Institute, 33(2), 1715-1722.

ROSTAMI, A. A., HAJALIGOL, M. R., & WRENN, S. E. (2004). A biomass pyrolysis sub-model for CFD applications. Fuel, 83(11), 1519-1525.

SALMON, E., VAN DUIN, A. C., LORANT, F., MARQUAIRE, P. M., & GODDARD III, W. A. Thermal decomposition process in algaenan of Botryococcusbraunii race L. Part 2: Molecular dynamics simulations using the ReaxFF reactive force field. Organic Geochemistry, 40(3) (2009), 416-427.

SAMPAIO I.,MORAIS E., JUNQUEIRA T., GOUVEIA V., BONOMI A. (2016). Components databank for the industrial simulations in the virtual Sugar Cane biorefinery (VSB). Centro Nacional de Pesquisa em Energia e Materiais, Laboratório Nacional de Ciência e Tecnologia do Bioetanol - Brasil

SÁNCHEZ, R. A., SOLSVIK, J., & JAKOBSEN, H. A. (2012). Modeling and simulation of cold flow fluidized bed reactors. Energy Procedia, 26, 22-30.

SHAFIZADEH, F. R. E. D., & CHIN, P. P. (1977). Thermal deterioration of wood. In ACS Symposium Series American Chemical Society.

SHARARA, M. A., HOLEMAN, N., SADAKA, S. S., & COSTELLO, T. A. Pyrolysis kinetics of algal consortia grown using swine manure wastewater. Bioresource technology, 169 (2014), 658-666.

SHARMA, R. K., CHAN, W. G., & HAJALIGOL, M. R. (2006). Product compositions from pyrolysis of some aliphatic α-amino acids. Journal of analytical and applied pyrolysis, 75(2), 69-81.

SHEN, D. K., GU, S., & BRIDGWATER, A. V. (2010). Study on the pyrolytic behaviour of xylan-based hemicellulose using TG–FTIR and Py–GC–FTIR. Journal of analytical and applied pyrolysis, 87(2), 199-206.

SHUPING, Z., YULONG, W., MINGDE, Y., CHUN, L., & JUNMAO, T. (2010). Pyrolysis characteristics and kinetics of the marine microalgae Dunaliella tertiolecta using thermogravimetric analyzer. Bioresource Technology, 101(1), 359-365.

SYAMLAL M., ROGERS W. AND. O'BRIEN T. J. MFIX Documentation: Volume1, Theory Guide. National Technical Information Service, Springfield, VA. DOE/METC-9411004, NTIS/DE9400087, 1993.

TAKEDA, H. (1988a). Classification of Chlorella strains by cell wall sugar composition. Phytochemistry, 27(12), 3823-3826.

TAKEDA, H. (1988b). Classification of Chlorella strains by means of the sugar components of the cell wall. Biochemical systematics and ecology, 16(4), 367-371.

TEGELAAR, E. W., DE LEEUW, J. W., & HOLLOWAY, P. J. (1989). Some mechanisms of flash pyrolysis of naturally occurring higher plant polyesters. Journal of Analytical and Applied Pyrolysis, 15, 289-295.

THURNER, F., & MANN, U. (1981). Kinetic investigation of wood pyrolysis. Industrial & Engineering Chemistry Process Design and Development, 20(3), 482-488.

THYBRING, E. E. (2014). Explaining the heat capacity of wood constituents by molecular vibrations. Journal of materials science, 49(3), 1317-1327.

TRENDEWICZ, A., BRAUN, R., DUTTA, A., & ZIEGLER, J. (2014). One dimensional steady-state circulating fluidized-bed reactor model for biomass fast pyrolysis. Fuel, 133, 253-262.

URSU, A. V., MARCATI, A., SAYD, T., SANTE-LHOUTELLIER, V., DJELVEH, G., & MICHAUD, P. (2014). Extraction, fractionation and functional properties of

proteins from the microalgae *Chlorella Vulgaris*. Bioresource technology, 157, 134-139.

VARHEGYI, G., ANTAL JR, M. J., SZEKELY, T., & SZABO, P. (1989). Kinetics of the thermal decomposition of cellulose, hemicellulose, and Sugar Cane bagasse. Energy & Fuels, 3(3), 329-335.

VARHEGYI, G., ANTAL JR, M. J., JAKAB, E., & SZABÓ, P. (1997). Kinetic modeling of biomass pyrolysis. Journal of analytical and Applied Pyrolysis, 42(1), 73-87.

VYAZOVKIN S. (2015). Isoconversional Methodology. In: Isoconversional Kinetics of Thermally Stimulated Processes. Springer, Cham, 27-62.

VYAZOVKIN, S., & LINERT, W. (1995). False isokinetic relationships found in the non-isothermal decomposition of solids. Chemical physics, 193(1-2), 109-118.

VYAZOVKIN, S. V., & LESNIKOVICH, A. I. (1988). Estimation of the pre-exponential factor in the isoconversional calculation of effective kinetic parameters. Thermochimica acta, 128, 297-300.

VYAZOVKIN, S., & WIGHT, C. A. (1998). Isothermal and non-isothermal kinetics of thermally stimulated reactions of solids. International Reviews in Physical Chemistry, 17(3), 407-433.

VYAZOVKIN, S., & DOLLIMORE, D. (1996). Linear and nonlinear procedures in iso-conversional computations of the activation energy of nonisothermal reactions in solids. Journal of chemical information and computer sciences, 36(1), 42-45.

VYAZOVKIN, S. V., GORYACHKO, V. I., & LESNIKOVICH, A. I. (1991). An approach to the solution of the inverse kinetic problem in the case of complex processes: Part II. Thermochimica acta, 176, 49-56.

WALLIS, G. B. (1969). One-dimensional two-phase flow. Fifth Edition, McGraw-Hill Inc, New York.

WANG, K., BROWN, R. C., HOMSY, S., MARTINEZ, L., & SIDHU, S. S. (2013). Fast pyrolysis of microalgae remnants in a fluidized bed reactor for bio-oil and biochar production. Bioresource technology, 127, 494-499.

WANG, Q. D., WANG, J. B., LI, J. Q., TAN, N. X., & LI, X. Y. (2011). Reactive molecular dynamics simulation and chemical kinetic modeling of pyrolysis and combustion of n-dodecane. Combustion and Flame, 158(2), 217-226.

WANJUN, T., CUNXIN, W., & DONGHUA, C. (2006). An investigation of the pyrolysis kinetics of some aliphatic amino acids. Journal of analytical and applied pyrolysis, 75(1), 49-53.

WEISS, I. M., MUTH, C., DRUMM, R., & KIRCHNER, H. O. (2018). Thermal decomposition of the amino acids glycine, cysteine, aspartic acid, asparagine, glutamic acid, glutamine, arginine and histidine. BMC biophysics, 11(1), 2.

WU, K., LIU, J., WU, Y., CHEN, Y., LI, Q., XIAO, X., & YANG, M. (2014). Pyrolysis characteristics and kinetics of aquatic biomass using thermogravimetric analyzer. Bioresource technology, 163, 18-25.

WURZENBERGER, J. (2001). A combined packed bed and single particle model applied to biomass combustion. Dissertation Technische Universitat Graz.

XIONG, Q., ARAMIDEH, S., PASSALACQUA, A., & KONG, S. C. (2014). BIOTC: an open-source CFD code for simulating biomass fast pyrolysis. Computer Physics Communications, 185(6), 1739-1746.

XU, Q., MA, X., YU, Z., & CAI, Z. (2014). A kinetic study on the effects of alkaline

earth and alkali metal compounds for catalytic pyrolysis of microalgae using thermogravimetry. Applied Thermal Engineering, 73(1), 357-361.

XUE, Q., HEINDEL, T. J., & FOX, R. O. (2011). A CFD model for biomass fast pyrolysis in fluidized-bed reactors. Chemical Engineering Science, 66(11), 2440-2452.

YU, X., MAKKAWI, Y., OCONE, R., HUARD, M., BRIENS, C., & BERRUTI, F. (2014). A CFD study of biomass pyrolysis in a downer reactor equipped with a novel gas–solid separator — I: Hydrodynamic performance. Fuel processing technology, 126, 366-382.

YUAN, T., TAHMASEBI, A., & YU, J. (2015). Comparative study on pyrolysis of lignocellulosic and algal biomass using a thermogravimetric and a fixed-bed reactor. Bioresource technology, 175, 333-341.

ZHOU, D., SCHMITT, E. A., ZHANG, G. G., LAW, D., WIGHT, C. A., VYAZOVKIN, S., & GRANT, D. J. (2003). Model free treatment of the dehydration kinetics of *nedocromil sodium trihydrate*. Journal of pharmaceutical sciences, 92(7), 1367-1376.